Cy. 4

ORNL-4520
UC-25 – Metals, Ceramics, and Materials

FUELS AND MATERIALS DEVELOPMENT PROGRAM

QUARTERLY PROGRESS REPORT

FOR PERIOD ENDING DECEMBER 31, 1969

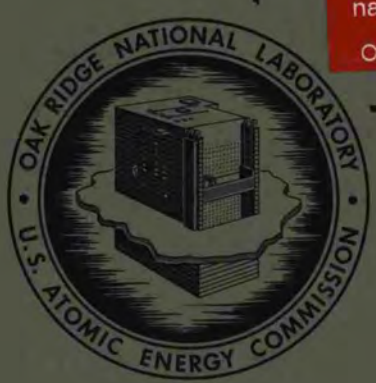

OAK RIDGE NATIONAL LABORATORY
operated by
UNION CARBIDE CORPORATION
for the
U.S. ATOMIC ENERGY COMMISSION

Printed in the United States of America. Available from Clearinghouse for Federal
Scientific and Technical Information, National Bureau of Standards,
U.S. Department of Commerce, Springfield, Virginia 22151
Price: Printed Copy $3.00; Microfiche $0.65

ORNL-4520

Contract No. W-7405-eng-26

METALS AND CERAMICS DIVISION

FUELS AND MATERIALS DEVELOPMENT PROGRAM QUARTERLY PROGRESS REPORT FOR PERIOD ENDING DECEMBER 31, 1969

Compiled by

P. Patriarca

Edited by

D. J. Rucker

MAY 1970

OAK RIDGE NATIONAL LABORATORY
Oak Ridge, Tennessee
operated by
UNION CARBIDE CORPORATION
for the
U.S. ATOMIC ENERGY COMMISSION

FOREWORD

This quarterly progress report describes research and development on nuclear fuels and materials performed at the Oak Ridge National Laboratory for the U.S. Atomic Energy Commission. This work is either sponsored by or of particular interest to the Fuels and Materials Branch of the Division of Reactor Development and Technology.

Progress on these programs is reported for the three major divisions of the work — Fast Reactor Technology, Space Power Technology, and General Reactor Technology — under the appropriate AEC activity titles listed below.

AEC Activity Title	AEC Activity Number
PART I. FAST REACTOR TECHNOLOGY	
FUELS	
DEVELOPMENT OF LMFBR OXIDE FUELS	04 40 02 01 1
DEVELOPMENT OF HIGH-PERFORMANCE LMFBR FUELS	04 40 02 01 1
EFFECT OF POWER CYCLING ON LMFBR FUEL-CLADDING BEHAVIOR	04 40 02 01 1
LMFBR FUEL ELEMENT DESIGN AND MODEL DEVELOPMENT	04 40 02 01 1
CLADDING AND OTHER STRUCTURAL MATERIALS	
MECHANICAL PROPERTIES OF ALLOYS IN REACTOR ENVIRONMENTS	04 40 02 03 1
DEVELOPMENT OF LMFBR CLADDING AND STRUCTURAL MATERIALS	04 40 02 01 1
FABRICATION DEVELOPMENT FOR LMFBR STAINLESS STEEL TUBING	04 01 61 01 5
WELDING DEVELOPMENT FOR LMFBR VESSELS AND COMPONENTS	04 40 02 04 1
SHIELDED METAL-ARC WELDING FOR LMFBR COMPONENTS	04 01 61 01 5
NONDESTRUCTIVE TESTING TECHNIQUES FOR LMFBR	04 40 02 04 1
SODIUM CORROSION STUDIES	04 40 02 02 1
DEVELOPMENT OF FAST-REACTOR NEUTRON-ABSORBER MATERIALS	04 40 02 02 1

*Research sponsored by Division of Space Nuclear Systems.

CONTENTS

CLADDING AND OTHER STRUCTURAL MATERIALS

PART II. SPACE POWER TECHNOLOGY

FUELS

CLADDING AND OTHER STRUCTURAL MATERIALS

PART III. GENERAL REACTOR TECHNOLOGY

FUELS

CLADDING AND OTHER STRUCTURAL MATERIALS

SUMMARY

PART I. FAST REACTOR TECHNOLOGY

FUELS

1. DEVELOPMENT OF FAST-REACTOR OXIDE FUELS

A total of 1.2 kg of Pu sol and 9.5 kg of 93% enriched U sol was prepared to meet the demands of the fast-reactor oxide fuels program. About 1.5 kg of dense microspheres containing $(U,Pu)O_2$ were prepared for loading into fuel pins for the Experimental Breeder Reactor-II (EBR-II). Five Sphere-Pac fuel pins and three pellet fuel pins were completed, all with 3-in.-long fuel columns and all to be irradiated in the Engineering Test Reactor (ETR). Detailed plans were developed for fabricating 19 unencapsulated fuel pins for irradiation in a 37-pin subassembly in the EBR-II. Planning, scheduling, and procurement of hardware and raw materials were the principal activities during the quarter. We also developed procedures for loading the microspheres and for fabricating the pellets.

We previously observed gas releases as high as 0.5 cm^3/g. Further work on control of gas release and the ratio of O:metal indicates that cooling in an atmosphere of pure Ar after adjustment of the ratio of O:metal decreases the susceptibility of the fuel to reabsorbtion of gas and therefore results in a lower measured gas release.

A sol-gel Sphere-Pac capsule that contained $(U,Pu)O_2$ attained a calculated burnup of 8.5 fissions per initial actinide metal atom (FIMA) in the ETR, and the irradiation of the capsule is continuing at a peak heat rate of 15 kw/ft with a target of 10% FIMA burnup. The third instrumented capsule for irradiation in the Oak Ridge Research Reactor (ORR), which contains one Sphere-Pac fuel pin and one sol-gel pellet fuel pin of the same composition and smear density, was completed and installed into the ORR. It began operation late in the quarter.

Six fuel pins that contain unirradiated sol-gel-derived $(U,Pu)O_2$ pellets or Sphere-Pac microspheres were subjected to power transients at the Transient Reactor Test Facility (TREAT). No failures occurred

even though two Sphere-Pac pins were subjected to a transient that probably melted 50 to 60% of the fuel in the peak power regions. The capsules from the experiments in TREAT were neutron radiographed, and postirradiation examination of the fuel pins was started.

Encapsulated Sphere-Pac $(U,Pu)O_2$ fuel pins were tested in subassembly X050 in the EBR-II to a peak burnup of 3.4% FIMA. We received approval in principle for the series II unencapsulated tests, which are to be shared with the Babcock and Wilcox Company, and we submitted a design for the ORNL fuel pins to the personnel of the EBR-II project for their review.

Another interesting highlight of the work for this quarter was the observation of the location of Cs in a white, crystalline deposit on the surface of a metallographic specimen prepared from an irradiated fuel pin. This white, crystalline deposit formed on irradiated $(U,Pu)O_2$ fuel when unmounted sections cut from the fuel pins were allowed to stand several days before mounting and polishing. Gamma spectrum analysis of the white material revealed ^{134}Cs and ^{137}Cs activity only.

2. DEVELOPMENT OF HIGH-PERFORMANCE LMFBR FUELS

We compared the sinterability of (U,Pu)N powders derived from an alloy with that of powders derived from mechanical mixtures of UN and PuN. With proper pretreatment, the mechanically mixed materials can be sintered to reasonably dense structures that have microstructures and precision lattice parameters identical to those obtained from powder synthesized from a U-Pu alloy of the same molar composition. We had difficulty in synthesizing nitride powders from the alloy in that they tend to contain small concentrations of free metal after synthesis is apparently complete. We are now studying the effects of annealing upon the lattice parameter of PuN and the phases derived when powders are synthesized from U-Pu alloy.

Vanadium and V_2N were found to be stable in the presence of UN, but not in the presence of U_2N_3. A new phase, UVN_2, was found to be stable in the presence of U_2N_3, UN, VN, or V_2N, but not in the presence of V or

U. The UN-V_2N-V and UN-UVN_2-V_2N three-phase regions form good buffering systems for use of nitride fuels with stainless steels.

3. EFFECT OF POWER CYCLING ON LMFBR FUEL-CLADDING BEHAVIOR

We are designing a series of reactor experiments for studying the effects of power cycling and power transients on the behavior of oxide fuel and the interactions of fuel and cladding. We made the calculations necessary to establish the geometry of the capsules so that a preliminary design and cost estimate may be made for the first experiment.

4. LMFBR FUEL ELEMENT DESIGN AND MODEL DEVELOPMENT

The FMØDEL computer code was used to study the performance characteristics of a typical liquid-metal-cooled fast breeder reactor (LMFBR) fuel pin. Radial temperature distributions and linear heat rates were calculated for different positions along the axis of the pin, and gap closure kinetics were examined by use of different assumptions regarding fuel strength and neutron flux. The stress-strain distribution in the cladding was also examined with respect to cladding thickness.

Work was begun to improve available analytical models for predicting fuel swelling and gas release. Electron microscopy was used to examine irradiated mixed oxide fuel to determine the size and density distribution of bubbles of fission gas.

We developed an equation, based on British data, that describes the creep rate of type 316L stainless steel out-of-reactor at 600 to 700°C that we will use in our modeling studies of British irradiation tests.

CLADDING AND OTHER STRUCTURAL MATERIALS

5. MECHANICAL PROPERTIES OF ALLOYS IN REACTOR ENVIRONMENTS AND DEVELOPMENT OF LMFBR CLADDING AND STRUCTURAL MATERIALS

Samples of austenitic stainless steel are being irradiated in the Oak Ridge Research Reactor (ORR), the High Flux Isotope Reactor (HFIR), and the Experimental Breeder Reactor-II (EBR-II). Experiments have

been designed for each reactor to obtain the desired exposure temperatures.

Type 304 stainless steel specimens were injected with 20×10^{-6} atom fraction He in a cyclotron before irradiation in the EBR-II at 390°C to a fast fluence of 8.5×10^{21} neutrons/cm^2. A duplicate specimen that did not contain He was irradiated under identical conditions, and the resulting samples were examined by transmission electron microscopy. The voids were smaller and more numerous in the sample injected with He. The calculated changes in density were about the same.

Our accumulated observations from electron microscopy studies of several irradiated metals, including Al, Ni, V, Fe, and austenitic stainless steels, have revealed that void formation generally is not homogeneous. When we view materials irradiated at very high fluences, the inhomogeneous nature of the void formation is quite often masked, and these observations have led to the proposal of nucleation mechanisms that predict homogeneous nucleation. However, the current observations favor inhomogeneous nucleation mechanisms.

Some comparative samples of type 304 stainless steel in the cold-worked and annealed conditions were irradiated in EBR-II at 400°C to a fluence of 2.8×10^{22} neutrons/cm^2. The measured change in density and the observed density of voids were smaller in the cold-worked samples.

Samples of type 316 stainless steel were irradiated in the ORR to a fluence of 1.4×10^{21} neutrons/cm^2 (> 1 Mev). Postirradiation tensile and stress-rupture properties show that the rupture life and the fracture strain were reduced by irradiation.

The biaxial stress-rupture properties of annealed specimens without defects from the second batch of 0.2% Ti-modified type 304L stainless steel tubing fabricated at ORNL were determined:

1. Planetary-swaged and cold-drawn tubing, annealed 1 hr at 925°C, have essentially the same rupture times; however, the planetary-swaged material tends to exhibit slightly higher uniform and total circumferential strain.

2. Annealing planetary-swaged tubing at either 925 or 1038°C produces rupture lives and ductilities that are indistinguishable from each other.

3. A very large fraction of the total circumferential strain exhibited by this tubing is due to uniform straining of the tubing before local wall thinning, or necking, occurs.

4. The minimum observed ductilities of these tubes, which were essentially free from discontinuities that could be determined ultrasonically, are higher than those observed earlier on tubes that contained discontinuities.

6. FABRICATION DEVELOPMENT FOR LMFBR STAINLESS STEEL TUBING

We fabricated ultrafine grained type 316 stainless steel tubing (0.250 in. in outside diameter by 0.016 in. in wall thickness) from two heats of materials that had 0.06 and 0.04% C, respectively. The tubing process, developed as a consequence of evaluating the temperatures of heat treatments between passes, also results in a nearly random distribution of carbide precipitate. Although this tubing is stronger at room temperature, it is weaker at 650°C than tubing processed conventionally.

The biaxial stress-rupture life of the fine-grained 20% cold-worked type 316 stainless steel tubing with carbide precipitates was shorter at 650°C than that of standard tubing from the same heat that was cold-worked 10 to 15%. The differences in the slopes of the stress-rupture curves may be due to interactions between C and dislocations. The fine-grained cold-worked tubing exhibits higher rupture strains (13 to 25%) than does the standard cold-worked tubing (generally only a few percent).

The origin and significance of natural defects in tubing are being examined. Machined surfaces with a rating of 125×10^{-6} in. can result in longitudinal bore defects in the final tubing. Fabrication procedures are being devised for artificially generating flaws that resemble natural defects. We can produce realistic defects by electro-discharge machining notches into the tubing and then drawing it.

7. WELDING DEVELOPMENT FOR LMFBR VESSELS AND COMPONENTS

We investigated the effect of heat treatment after welding on the creep-rupture properties of typical austenitic stainless steel weld metal.

Studies of bead-on-plate welds showed that a wide range of macroscopic growth patterns and microscopic substructural details are attainable with the submerged-arc process. Weldments in 1-in.-thick plate are being prepared to investigate the effects of these variables on creep-rupture properties at 650°C. Scanning electron microscopy showed a correlation between fracture appearance and the solidification substructure present in weld metal. About 15 ft of weldment made by the submerged-arc process in 1-in.-thick plate is being prepared for use in a program sponsored by the Atomic Energy Commission at the U.S. Naval Research Laboratory.

8. SHIELDED METAL-ARC WELDING FOR LMFBR COMPONENTS

We made 14 shielded metal-arc weldments with type 308 stainless steel electrodes, each of which had a slightly different electrode coating. In three of these, only the basic types of commercial coatings (lime, lime-TiO_2, and TiO_2) varied. The deposit compositions of the remaining electrode batches (all with lime-TiO_2 coatings) were adjusted so that we might study the effect on the mechanical properties at elevated temperatures of high and low amounts of the following elements: Si, P, S, C, and B. In all cases, the deposit analyses reflect subtle differences in the electrode coatings and are within reasonable composition limits to conform to American Society for Testing and Materials (ASTM) specifications.

Metallographic examination and extensive studies of bead-on-plate welds proved that there are few, if any, distinguishing features in any of the electrode batches as to their deposition performance and bead appearance. Stress-rupture data, however, indicated a definite influence of electrode coating. At this point, only the three batches of standard electrodes and the low-Si batch of electrodes have been tested. Stress-rupture data were recorded at 650°C and stress levels of 25,000, 20,000, and 18,000 psi. The weld made with the lime-coated electrode showed a comparatively shorter rupture time than the welds from the other three batches (all of which contained some TiO_2 in the coating). All welds showed severe loss of ductility for the tests for longer times. Welds made with the standard electrodes with lime-TiO_2 coatings were

characterized by a plot for ductility versus rupture time significantly lower than that for either of the other two standard batches. The low-Si weld showed the best ductility.

9. NONDESTRUCTIVE TESTING TECHNIQUES FOR LMFBR

We are developing new methods, techniques, and equipment for nondestructively evaluating materials for liquid-metal-cooled fast breeder reactors (LMFBR) with emphasis on measuring cold work in stainless steel tubing.

We are developing an eddy-current instrument to measure both size and depth of defects and are using a Hg model to aid the design studies. Several stainless steel welds that contain intentional flaws were prepared for use with the schlieren system.

Because of the good results we obtained by measuring permeability caused by cold working stainless steel sheet, we designed and began constructing a prototype system for tubing. Using our mathematical models, we determined the optimum design parameters by computer calculations. The calculations indicate that we can measure relative permeability to within ±50 ppm, which corresponds to less than 1% change in cold work.

10. SODIUM CORROSION STUDIES

We conducted capsule tests of various V alloys to determine the effect of alloying on the reactivity of V with O in Na. As indicated by weight changes at 600°C, Cr additions to the V markedly reduced the uptake of O by the metal. Tests of V alloys in low-pressure O_2 also showed a lower contamination rate with increasing Cr content in the alloy. These latter tests indicate that the O_2 pressure has a greater effect on contamination rate than does temperature between 500 and 700°C.

The oxidation of 300 series stainless steels in contact with thermal insulation at 760°C is being tested in N_2 + 1% O_2 + 100 ppm H_2O. We observed that both types 304 and 316 stainless steel form highly protective scales after a few hours in contact with this gas mixture. In a related study, we examined the effect of a Na leak on the oxidation

behavior of type 304 stainless steel in contact with insulation and this same gas mixture. When Na was allowed to leak through a 0.060-in.-diam hole at 760°C, we observed enlargement of the hole and extensive oxidation of the surfaces of the stainless steel exposed to the N_2 mixture. Smaller leaks, however, plugged soon after the release of Na, and much less oxidation resulted. The thermal insulation reacted with the leaking Na to essentially the same extent in all tests.

11. FAST-REACTOR NEUTRON ABSORBER MATERIALS

The structural changes that result from annealing of B_4C powders are being investigated. Boron carbide powders that have a B:C ratio of 3.62 undergo a maximum reduction in density of 5% when they are annealed at 2000°C. Previously reported unidentified phases in experimental B_4C powders produced by arc melting have been shown to be W and Cu.

Thermal irradiation testing of B_4C powders in the Oak Ridge Research Reactor (ORR) has begun. The initial experiment was removed from the reactor late in this reporting period, and postirradiation testing is now in progress.

Pellets are being prepared from specific types of B_4C powders for irradiation in the Experimental Breeder Reactor-II (EBR-II) later in 1970 after the reactor goes to higher power.

PART II. SPACE POWER TECHNOLOGY

FUELS

12. DEVELOPMENT OF URANIUM MONONITRIDE FUELS

The middle fuel pin of capsule UN-3 failed after 5800 hr of operation at a temperature of 1370°C at the surface of the cladding. Several short cracks were visible in the cladding over the fueled region of the pin. Visual examination and dye-penetrant tests established that the claddings of the top and bottom fueled pins remained sound during the irradiation test. Each of the three fuel pins was examined by gamma scan; no unusual characteristics were revealed. Measurement of the pin diameters with an

opposed dial gage profilometer showed that each pin was reduced in diameter during irradiation testing; the range was from 0.001 in. for the bottom pin to 0.003 in. for the top pin. The nondestructive evaluation of these pins was completed, and we are now sectioning the failed (middle) pin to investigate the cause of failure.

CLADDING AND OTHER STRUCTURAL MATERIALS

13. CLADDING MATERIALS FOR SPACE ISOTOPIC HEAT SOURCES

We determined the time and temperature parameters of embrittling-aging reactions in the superalloys Hastelloy N, Haynes alloy No. 25, and Haynes developmental alloy No. 188 by impact testing of specimens aged at 650 to 900°C for times to 5000 hr. Hastelloy N was embrittled least. We also evaluated the results of our study of the evaporative losses of elements with high vapor pressures (i.e., Cr and Mn) from these alloys at 800 to 1050°C in 10^{-9} torr vacuum. These losses resulted in microstructural damage such as the formation of voids and solutioning of precipitates as well as changes in the morphology of the surfaces.

In an effort to develop alloys that are strong and resistant to oxidation for containing radioisotopes in advanced thermoelectric generators for space applications, we are investigating alloys that contain Pt. The formation of long-range order in the alloy Pt_3Cr (alloy S-19) results in an exceptionally low primary creep rate and also reduces the steady-state creep rate by a factor of 25, indicating the superior properties of such structures. The lower stress exponent of 3 that characterizes the ordered alloys (versus 5 for unordered alloys) is also a desirable feature in applications that require resistance to high applied stress. Comparisons of the time to produce 1% strain in vacuum at 900°C and a stress of 10,000 psi showed alloy S-19 to be superior to Haynes alloy No. 25 by about two orders of magnitude. At about 1000°C, the evaporative resistance is also vastly superior to that of Haynes alloy No. 25, and the oxidation resistance is greatly superior to that of the refractory alloys.

14. PHYSICAL AND MECHANICAL METALLURGY OF REFRACTORY ALLOYS

Potential problems associated with use of refractory alloys in advanced isotopic heat sources were defined: (1) interaction of liners with oxide fuels, (2) contamination of refractory alloys with degassed interstitials, (3) plugging of nonselective vents with decomposed gases, and (4) hydriding of Nb and Ta alloys after reentry into water.

An apparatus for creep testing Ta alloys in low-pressure N_2 is being installed to simulate the interaction of Ta alloys with the N of nitride fuels. The aging characteristics of equimolar Ta-Hf alloys were determined. These studies suggest a simple β, $(\beta + \alpha)$, α sequence of phases with increasing Hf rather than a miscibility gap. Several quasi-chemical models for spinodal decomposition were applied to real solutions. A model based on clustering and nonrandom configurational entropy qualitatively predicts the experimental observations. The electrical resistivity and absolute Seebeck coefficient of Nb—10% W to 1700°K were determined. A direct heating apparatus for measuring these properties and thermal conductivity is being evaluated. Stress-rupture properties of electron-beam welds of TZM and W—25% Re at 1400, 1650, and 2000°C were determined.

The remelt temperature of Ti—48% Zr—4% Be braze alloy on Ta was 75°C below its original melting temperature, and that for the Ti—46% Zr—8% Ge alloy was higher by 20 to 40°C. Six techniques for producing leak-tight joints of Pt and Ta—10% W were investigated. A three-tube joint with a W transition layer was leak-tight after 500 hr at 1200°C but not after 1000 hr.

15. TUNGSTEN METALLURGY

We determined that the creep rate of W at 1800°C increases significantly with increasing O_2 pressure between 1.1×10^{-7} and 1.9×10^{-5} torr primarily due to the sublimation of volatile oxides. Our recent long-time creep data on arc-melted W-Re alloys and chemically vapor deposited W are presented and compared for primary and secondary design criteria for nuclear applications. Additional tests on powder-metallurgy W—25% Re

confirmed that at 500 psi this material has a lower creep rate at 2200°C than at 1650°C. Electron fractography on creep specimens of powder-metallurgy W at low strains showed that grain-boundary cracks grow by the merger of small voids. We are determining the optimum welding conditions for gas W-arc welding of W—25% Re sheet with and without Mo—50% Re filler metal. Continued efforts to eliminate nodules completely from chemically vapor deposited W—5% Re by interrupted deposition were not successful.

16. FAST-NEUTRON IRRADIATION EFFECTS ON ELECTRICAL INSULATORS

Four commercial types of alumina were irradiated in the Engineering Test Reactor (ETR) at various temperatures from 400 to 1230°C and at various fluences from 1 to 7×10^{21} neutrons/cm^2 (> 1 Mev). The irradiation assembly was identical to a short-term assembly that was irradiated to fluences from 0.4 to 3.1×10^{21} neutrons/cm^2. More specimens fractured in the long-term assembly than in the short-term assembly. For both assemblies, alumina of higher purity was damaged less than alumina of lesser purity. Specimens in the long-term assembly expanded in volume by about twice as much as those in the short-term irradiation. Part of the additional expansion is undoubtedly an increase in grain volume, which occurs almost linearly with increasing fluence above 10^{21} neutrons/cm^2, but some of it is probably a result of additional separation at grain boundaries caused by the increase in grain volume.

17. CORROSION STUDIES OF ADVANCED REFRACTORY METALS

We began operation of a Li forced-circulation loop to evaluate the corrosion properties of T-111 in a flowing, nonisothermal system. The loop has operated 344 hr with a 1370°C maximum Li temperature. A replacement test section being fabricated for this loop will be inserted after 3000 hr of testing with the current test section. This second test section includes specimens of W as well as Ta alloys.

PART III. GENERAL REACTOR TECHNOLOGY

FUELS

18. FISSION-GAS RELEASE AND PHYSICAL PROPERTIES OF FUEL MATERIALS DURING IRRADIATION

Irradiation of a cylinder of large-grained UO_2 was terminated when it began cracking before temperatures reached the level for grain growth. Thermal data obtained from the specimen have not been processed because the mathematical methods first used did not give satisfactory results. New theories and processes developed to deal with the data appear very promising. Irradiation of sol-gel $(U,Pu)O_2$ microspheres has begun.

19. DEVELOPMENT OF FUEL ELEMENT FABRICATION

Evaluation and design of an instrumented facility for irradiation of fuel plates in the High Flux Isotope Reactor (HFIR) is continuing. The experimental apparatus for testing flux and fission density was built and will be inserted next quarter.

Postirradiation examination of fuel plates irradiated during fiscal year 1969 in the G-12 loop at the Engineering Test Reactor (ETR) provided further evidence that fabrication voids reduce the swelling of Al-base dispersions. Aluminum-base fuel plates produced by normal fabrication techniques and containing the burned grade of U_3O_8 had the largest amount of fabrication voids for a given volume fraction of fuel compound, and, hence, irradiation swelling was lower for this material than for the high-fired grade of U_3O_8 or UAl_x. A 50 wt % high-fired U_3O_8 plate was irradiated to a burnup of 2.24×10^{21} fissions/cm^3 without failure.

Our study of the effect of variations in process parameters during the chemical cleaning of type 6061 Al on bonding during rolling was completed with encouraging results. However, extended use of the etching solution, extreme deviations in the etching temperature, use of cold water as a rinse, and extended storage of cleaned billets before rolling can deteriorate the bonding.

Parametric studies of the deformation of UAl_x-Al and U_3O_8-Al dispersions are continuing. With respect to plate characteristics that influence irradiation performance, compacting pressure or compact density does not influence the amount of fabrication voids in the final composite plate, but the amount of cold rolling does affect the void content.

The effect of variations in the size of fuel particles on the x-ray attenuation calibration curve is being studied. Investigations of the use of scattered and fluorescent radiation for measuring the thickness of cladding are under way with ^{241}Am and ^{147}Pm radiation sources.

The influence of the variables in the electron-beam welding process during the joining of simulated fuel plates to side plates is being evaluated statistically.

CLADDING AND OTHER STRUCTURAL MATERIALS

20. BEHAVIOR OF REFRACTORY MATERIALS UNDER IRRADIATION

Irradiated specimens of refractory-metal carbides are being thermally annealed out-of-reactor to aid in defining damage mechanisms. Thermal annealing of displacements produced by fast neutrons in the carbides of Ti, Zr, Ta, Nb, and W was found to become significant at temperatures between 500 and 700°C.

A high-temperature (1000°C) assembly and a low-temperature (150°C) assembly containing depleted UN, $U^{15}N$, and UN-UC (50-50 mole %) were constructed and inserted into the Engineering Test Reactor (ETR). The results of these irradiation experiments will determine the effect of He gas generated within nitride fuels through the $^{14}N(n,\alpha)^{11}B$ fast-neutron reaction.

Preliminary design work was started on a comprehensive experiment in which B_4C will be irradiated in row 7 of the Experimental Breeder Reactor-II (EBR-II) to evaluate B_4C with different ratios of B:C and different void densities as a neutron absorber for control of reactivity in fast reactors.

21. JOINING RESEARCH ON NUCLEAR MATERIALS

We made welds in 1/8-in.-thick Incoloy 800 sheet with filler wires prepared from experimental alloys. We also used two recommended filler metals, Inconel 62 and Inconel 82, and an electroslag remelted heat of commercial Incoloy 800. The sheet was fully restrained during welding. Cracking was observed in those welds made with the experimental alloys that nominally contained high S (0.015% S).

The austenitic stainless steel experimental alloys were tested magnetically in the as-cast conditions. Homogenizing the alloys at 1150°C for 1 hr reduced considerably the magnetic character of the alloy. The effect of the presence of the high-temperature ferritic phase (ferrite) on the diffusionless transformation of austenite to martensite is being investigated.

The shielded metal-arc welds were chemically analyzed. A comparison between the requested percentage of ferrite in an electrode and the percentage of ferrite predicted on the basis of chemical analysis of the weld metal indicates that high ferrite levels are difficult to achieve. The welding conditions (travel speed, current, and voltage) control the chemical composition of the deposit.

Results from the study of the effect of defects showed that the yield strength at room temperature of sound weld metal was 10% higher than that of the base metal in which the fusion zone was made. Ultimate tensile strength was about 10% lower. Where evidence of discontinuities in the weld metal were revealed by radiographic examinations, the tensile properties were drastically reduced. A similar behavior was noted in short-time stress-rupture tests at 815°C.

22. NONDESTRUCTIVE TESTING

Newly developed computer programs now allow instrument simulation to determine the effect of instrument instabilities on test results. Other new programs now provide construction details for desired eddy-current coils.

We developed techniques for recording on motion picture film sequences in our ultrasonic schlieren system. Experimental and mathematical studies on frequency analysis of ultrasonic spectra demonstrated the feasibility of measuring flaw size by means of spectral variations despite changes in signal amplitude due to differences in acoustic impedance or other variables.

Studies in x-ray attenuation demonstrated the ability to measure physical density in graphite with an accuracy of better than 0.5%. The study of scattered and fluorescent radiation for measurement of cladding thickness is continuing on Pb and Al specimens. An improved goniometer is now being used.

23. IMPROVEMENT OF HASTELLOY N AND RELATED COMPOSITIONS

We concentrated on optimizing the concentrations of Nb, Ti, Zr, and Hf in modified Hastelloy N to give good mechanical properties after irradiation. Small heats of alloys containing up to 2% of each element were prepared for study. Aging studies at 650 and 760°C showed that the tensile and yield strengths were reduced and that the fracture strains ranged from 19 to 45%. These property changes in the absence of irradiation are not thought to be serious. Some of these modified alloys were irradiated, and those alloys that contained finely dispersed carbides of the MC type had good postirradiation properties. Scale-up studies on 50-lb heats revealed some porosity in welds in an alloy that contained 1% Ti and 1% Hf and some cracking of the weld metal in an alloy that contained 0.5% Hf and 2% Nb.

Surveillance samples from the Molten Salt Reactor Experiment (MSRE) have made it possible to study the changes that occur in the mechanical properties of standard Hastelloy N as a result of irradiation. The fracture strain reaches a minimum at a strain rate of about 0.1%/hr. Thermal irradiations that produce only 1 ppm He in the alloy reduce the fracture strain from 30% to about 2%. Further irradiation results in fracture strains as low as 0.5% when the He concentration reaches 40 ppm.

24. ADVANCED MATERIALS FOR STEAM GENERATORS

Isothermal corrosion testing in superheated steam at 595°C for 8000 hr indicated the following ratings of weldments between similar metals (in order of decreasing resistance to general corrosion in the finish-ground condition): (1) Hastelloy X and Inconel 625 welded with themselves and Incoloy 800 welded with Inconel 82 (total scale thickness less than about 2 μm); (2) IN-102 welded with itself and type 304 stainless steel welded with type 308 stainless steel; and (3) Inconel 600 welded with Inconel 82 filler metal. The relative resistances of weldments to corrosion by superheated steam at 650°C were (1) IN-102, Inconel 625, and Hastelloy X welded with themselves (total scale thicknesses less than 3 μm); (2) Incoloy 800 welded with Inconel 82 and type 304 stainless steel welded with type 308 stainless steel; and (3) Inconel 600 welded with Inconel 82.

Weldments between dissimilar metals – Hastelloy X, Inconel 625, and IN-102 joined to Incoloy 800 with themselves and Inconel 82 as filler metals – exhibited excellent resistance to corrosion by steam at 595 and 650°C; the extent of corrosion was explainable by the corrosion properties found for the individual alloys that comprised the weldments. Inconel 82 filler metal and Inconel 625, Hastelloy X, and IN-102 used as filler metals were remarkably resistant to corrosion. Hastelloy W filler metal was inferior to the others, especially when cold worked.

All of the weldments tested in superheated steam were free of any preferential corrosion in the area of the fusion line after 8000 hr at 595 and 650°C.

PART I

FAST REACTOR TECHNOLOGY

FUELS

1. DEVELOPMENT OF FAST-REACTOR OXIDE FUELS

P. Patriarca A. L. Lotts

The objective of this program is to obtain an economically optimized $(U,Pu)O_2$ fuel cycle for a liquid-metal fast breeder reactor (LMFBR) by extending the performance capability and advancing the fabrication technology of oxide fuels. These fuels have the most advanced technology and greatest potential for reliable operation in first-generation LMFBR's. They have been tested in fast-flux environments but as yet have not been exposed under actual prototypic conditions. Currently, the burnup and heat rate are limited to about 50,000 Mwd/metric ton and 16 kw/ft, respectively, based on irradiation experiments with fuels that are not necessarily optimized for thermal, chemical, and mechanical performance.

The capability of oxide fuels can possibly be improved by adjusting structures or void distribution in the fuels. We emphasize irradiating fuels derived from the sol-gel process with thoroughly characterized structures and void distributions different from those of the oxide fuels irradiated heretofore. These include fuels fabricated by Sphere-Pac, vibratory compaction, extrusion, and pelletization. We compare the performance of these with the performance of reference fuels such as pellets derived from mechanically blended powders and coprecipitated material. The development of computer programs to assist in the analysis of test results and the development of a mathematical model to predict the performance of a fuel pin are integrated with the test program.

Preparation of $(U,Pu)O_2$ Fuel Materials

W. T. McDuffee[1]

Preparation of PuO_2 Sol

We prepared eight lots of standard PuO_2 sol totaling 1.2 kg Pu. About half of this material was blended with 93% enriched UO_2 sol, and

the mixed sol was used to prepare $(U_{0.8},Pu_{0.2})O_2$ pellet fuel for the series II irradiation experiments in the Experimental Breeder Reactor-II (EBR-II). The remaining mixed sol is being used to form dense oxide microspheres that are to be loaded by the Sphere-Pac technique into irradiation specimens that also are to be included in the series II experiments in the EBR-II.

Preparation of Enriched UO_2 Sol

We prepared 29 batches of 93% enriched UO_2 sol totaling 9.4 kg U to meet the current demands for development studies. Part of this material was used to prepare the fuel for the series II test capsules for irradiation in the EBR-II. For these, the fuel is a $(^{235}U_{0.8},Pu_{0.2})O_2$ mixture that is obtained by blending standard PuO_2 sol with $^{235}UO_2$ sol that is free of sediments to produce a mixed sol that is either converted into pellet fuel or formed into microspheres. We prepared satisfactory UO_2 sol that contained a total of 2.2 kg ^{235}U for blending with standard PuO_2 sol and converting into pellet fuel. Another batch of sol that contained 2.9 kg ^{235}U was prepared for blending with standard PuO_2 sol and forming into dense microspheres, as previously stated.

During preparation of the early batches, we corrected several difficulties previously encountered in both the reduction of U(VI) to U(IV) and in the precipitation, washing, and peptization steps. These early sols were of poor quality, and the yield of useful product was low. When the refinements developed during this period were incorporated into the final flowsheet, we were routinely able to prepare UO_2 sols with a product yield that exceeded 90%.

Preparation of Dense Microspheres

About 1.5 kg (heavy-metal content) of dense microspheres are scheduled for Sphere-Pac loading into the series II specimens for irradiation in the EBR-II. About one-third of these are to be less than 44 μm in diameter; the rest are to be 250 to 600 μm in diameter. All of the coarse fraction has been prepared, and the smaller material is being prepared.

Preparation of the microspheres includes forming the mixed sol into droplets in a drying solvent (2-ethyl-1-hexanol) in which the droplets gel. Oxide spheres are obtained by further drying the gel beads in a current of mixed steam and Ar at 170°C and firing the dried gel beads in Ar–4% H_2 to 1200°C. After cooling in Ar, the dense oxide product is classified by screening and shape separation.

Yields of round microspheres, free of pits or cracks, varied from 25 to 90%, but most were about 70%. Possible differences in composition are difficult to determine because of the inherent problem of representative sampling of the batches of microspheres, and the difficulty in obtaining reproducible analytical data for Pu and U in the high-density product.

The particle density of the 250- to 600-μm-diam microspheres, as determined by Hg porosimetry, was greater than 96% of the theoretical value. Despite this, the tap density was 59 to 60% instead of the desired 62 to 63% of the theoretical value. We believe, however, that the tap density will increase to the desired level during adjustment of the O:metal ratio at 1450°C, as previously observed.

Development of Fabrication Processes

J. D. Sease

Fast reactors that operate at high specific powers will require fuel pins of small diameter with fuel ranging from 80 to 90% of theoretical density and a high fissile loading. Our work is to develop procedures for Sphere-Pac and pelletization and for fabricating irradiation capsules.

Sphere-Pac (C. R. Reese)

Sphere-Pac is a process for compacting microspheres into fuel pins by means of vibration. The objective of our effort to develop Sphere-Pac is to investigate variables of the material and processing that will allow use of the Sphere-Pac process in a production facility. A comparative study of methods for determining the curve for distribution of

particle sizes showed close correlation between various techniques. The time required to infiltrate the fine microspheres into the coarse bed was found to vary with the diameter of the fuel bed. Experiments were performed in an effort to predict and control the density of the total bed by controlling the density of the coarse bed.

Thoria microspheres from 700 to 1000 μm in diameter were separated into lots according to size by means of sieves. From these sized lots, we mixed experimental batches, each with a different weight percentage of the various sizes of microspheres. We loaded these batches by the Sphere-Pac process to determine the effect of various distributions of particle sizes in the coarse fraction upon the density of the coarse bed. We observed no significant effect.

We investigated whether the density of the coarse bed could be controlled by varying the mean size of the particles in the coarse fraction. Preliminary tests of batches with mean particle sizes between 250 and 535 μm showed that the density of the coarse bed increased as the mean size of the particles decreased. We mixed batches of coarse microspheres in which the mean size of the particles varied but the distribution spread (the ratio of the maximum particle diameter to the minimum particle diameter, $D_{max}:D_{min}$) was held constant at 1.5. These batches were loaded into a stainless steel pin 16 in. long by 0.245 in. in outside diameter and infiltrated with fine microspheres 30 to 44 μm in diameter. Table 1.1 indicates that the density of the coarse bed increased slightly as the mean diameter of the particles decreased. However, the infiltrated total density decreased as the mean size decreased. The particles in the fine fraction are too large to allow efficient packing when the mean size of the coarse fraction is reduced. Precursory results obtained by infiltrating the thoria coarse bed with urania microspheres 15 to 25 μm in diameter indicate that the packing efficiency increases greatly with a decrease in the size of the particles in the fine fraction. We requested thoria microspheres 5 to 25 μm in diameter from the Chemical Technology Division for further work we have planned to investigate the effect of the size of the particles in the fine fraction upon the total density.

Table 1.1. Effect of the Average Size of Particles in the Coarse Bed on the Density of the Coarse Bed and on Total Density

Average Size of Particle[a] (μm)	Density, % of Theoretical	
	Coarse Bed	Total
540	60.2	82.0
420	60.6	80.9
280	60.7	62.3[b]

[a]The average size of particles was determined by the following formula:

$$D_{min} + 4/5\ (D_{max} - D_{min}) = \text{average size of particles,}$$

where D is diameter. The ratio D_{max}:D_{min} was constant at 1.5.

[b]The fine fraction could only be infiltrated into the coarse bed slowly and with great difficulty.

Pelletization of Sol-Gel $(U,Pu)O_2$ (R. A. Bradley, W. H. Pechin)

Irradiation capsules 43-120 and 43-121 for the Engineering Test Reactor (ETR) will each contain two fuel pins loaded with $(U_{0.80},Pu_{0.20})O_2$ microspheres by the Sphere-Pac process and two pins loaded with 84% dense sol-gel $(U_{0.80},Pu_{0.20})O_2$ pellets. For both the pellets and microspheres, the ratio of O:metal must be 1.98 ± 0.01, and less than 0.10 cm^3/g (preferably less than 0.05 cm^3/g) of gas may be released. We have fabricated the pellets for the capsules, adjusted the ratio of O:metal in the microspheres, and characterized the fuel.

Experimental Procedure. — We prepared a 1300-g batch (ET3) of urania-plutonia powder by blending UO_2 and PuO_2 sols and drying to a gel at 100°C with an Ar purge. The product was ground in a fluid-energy jet mill, sieved through a 325-mesh screen, and subdivided into 100-g batches (designated ET3A through ET3M) of powder for calcination. Samples of the blended sol, dried gel shards, jet-milled powder, and the fines collected in the dust bag of the jet-mill exhaust were analyzed for U and Pu. The bulk density and surface area of the dried gel shards

and the surface area of the jet-milled powder and the fines were also determined. The results of all these analyses are summarized in Table 1.2.

Two batches, ET3A and ET3B, were calcined in Ar and Ar–4% H_2, respectively, according to the conditions shown in Table 1.3. The results of sintering tests on each of these batches are summarized in Table 1.4. After analyzing the results of these tests, we decided to calcine the remainder of the powder for the ETR pellets in Ar–4% H_2, since powder from this treatment appeared to have slightly better pressing characteristics. The calcined powder was characterized by visual appearance (primarily color), and the green density of pellets formed at an arbitrarily selected pressure. The results of this characterization are summarized in Table 1.3.

A sintering test was performed on each of the seven batches of calcined powder by pressing three pellets from each batch at 55,000 psi and sintering according to the schedule described in Table 1.4. The results of this test are given in Table 1.5. All seven batches were then blended to form a uniform batch of powder (ET3N) for fabricating the ETR pellets. After the powder was blended, a final sintering test was made to determine the pressure required to produce 84% dense pellets. The forming pressures, green densities, and sintered densities of these

Table 1.2. Summary of Analyses on Blended Sol, Dried Gel Shards, and Jet-Milled Powder for Batch ET3

Material Form	Uranium Content	Plutonium Content	Ratio Pu:(U+Pu)	Bulk Density (g/cm^3)	Surface Area (m^2/g)
Blended sol	199.4 $\frac{mg}{ml}$	47.7 $\frac{mg}{ml}$	0.193		
Dried gel shards	68.56%	15.33%	0.183	4.40[a] 4.48[b]	36.2
Jet-milled powder	67.32%	16.13%	0.193		44.2
Jet-milled fines	64.45%	14.76%	0.186		51.3

[a]Determined by Hg porosimetry at atmospheric pressure.

[b]Determined by Hg porosimetry at 10,000 psi.

Table 1.3. Characterization of Urania-Plutonia Powder Calcined for Pellets for Engineering Test Reactor

Powder Batch	Heat Treatment	Calcining Conditions				Surface Area (m^2/g)	Ratio O:Metal	Green Density at 55,000 psi (% Theoretical)	Appearance
		Heating Rate (°C/hr)	Maximum Temperature (°C)	Time at Temperature (hr)	Atmosphere				
ET3A	H95	300 Cool	520	4	Argon CO_2	7.63	2.226	53.9	Black
ET3B	H96	400 Cool	520	4.1	Ar–4% H_2 CO_2	26.7	2.365	49.3	Brown
ET3C	H97	360 Cool	520	4.1	Ar–4% H_2 Ar–4% H_2	35.5	2.441	47.4	Yellowish brown
ET3D	H98	360 Cooling Hold Cool	600 600–520 520	0 0.5 3.25	Ar–4% H_2 Ar–4% H_2 Ar–4% H_2 CO_2			47.7	Color between ET3B and ET3C
ET3E	H99	380 Cool	520	4	Ar–4% H_2 CO_2			46.0	Color between ET3B and ET3C
ET3F	H100	380 Cool	520	4	Ar–4% H_2 CO_2			46.1	Color between ET3B and ET3C
ET3G	H101	360 Cool	520	4	Ar–4% H_2 CO_2			45.9	Color between ET3B and ET3C
ET3N[a]	H95–H101					33.0	2.404	47.3	Color between ET3B and ET3C

[a]Blend of batches ET3A-H95–ET3G-H101.

Table 1.4. Summary of Densities and Shrinkages for Sintering Tests on Powder Batches ET3A-H95 and ET3B-H96

Sintering Run	Pressure (psi)	Average Density, % Theoretical		Average Shrinkage, %[b]	
		Green	Sintered[a]	Length	Diameter
	$\times 10^3$				
		Powder Batch ET3A-H95			
99	20	46.6	73.0	$12.9^{+1.0}_{-0.7}$	$15.4^{+0.0}_{-0.0}$
99	30	48.8	78.0	$14.1^{+0.6}_{-0.7}$	$15.4^{+0.0}_{-0.0}$
99	40	50.5	81.0	$14.3^{+0.1}_{-0.0}$	$15.4^{+0.0}_{-0.0}$
99	50	52.2	83.6	$14.3^{+0.2}_{-0.1}$	$15.4^{+0.0}_{-0.0}$
100	45	51.3	82.4	$13.8^{+0.9}_{-1.3}$	$15.8^{+0.0}_{-0.0}$
100	50	51.8	83.9	$14.1^{+0.3}_{-0.3}$	$15.8^{+0.0}_{-0.1}$
100	55	53.2	85.9	$13.9^{+0.3}_{-0.3}$	$15.6^{+0.0}_{-0.0}$
100	60	53.3	85.5	$14.1^{+0.2}_{-0.4}$	$15.4^{+0.1}_{-0.0}$
		Powder Batch ET3B-H96			
100	30	43.3	79.2	$18.1^{+0.2}_{-0.2}$	$19.1^{+0.1}_{-0.1}$
100	40	44.6	81.5	$17.9^{+0.1}_{-0.1}$	$19.2^{+0.0}_{-0.0}$
100	50	46.5	83.0	$17.5^{+0.1}_{-0.1}$	$18.8^{+0.2}_{-0.2}$
100	60	49.7	89.4	$17.2^{+0.1}_{-0.2}$	$18.5^{+0.0}_{-0.0}$

[a]Sintered in Ar–4% H_2 by heating at 300°C/hr to 1450°C and holding for 10 hr.

[b]Plus and minus values indicate maximum and minimum values for each group of three pellets.

Table 1.5. Summary of Densities and Shrinkages for Sintering Tests of Seven Calcining Batches

Powder Batch	Pellet Number	Density, % Theoretical				Shrinkage, %	
		Green[a]	Average[a] Green	Sintered[b]	Average[b] Sintered	Length	Diameter
ET3A-H95	1105	53.7		85.1		13.7	15.5
	1106	53.5	53.9	85.2	85.3	13.9	15.5
	1107	54.4		85.5		13.6	15.4
ET3B-H96	1108	49.3		81.5		17.5	15.4
	1109	49.3	49.3	81.5	81.4	17.2	15.5
	1110	49.2		81.1		16.9	15.4
ET3C-H97	1111	47.4		90.2		18.7	20.3
	1112	47.2	47.4	89.1	89.4	19.1	19.9
	1113	47.7		89.0		18.6	19.9
ET3D-H98	1114	45.9		86.2		22.7	17.9
	1115	c	47.7	c	86.2	c	c
	1116	49.6		86.1		16.5	17.8
ET3E-H99	1117	45.5		81.7		17.8	19.0
	1118	46.0	46.0	84.8	84.8	18.0	19.4
	1119	46.4		84.9		17.9	19.3
ET3F-H100	1120	46.7		86.5		18.3	19.5
	1121	45.0	46.1	82.5	84.7	17.5	19.7
	1122	46.6		85.1		17.6	19.3
ET3G-H101	1123	45.4		82.4		19.4	20.0
	1124	45.9	45.9	85.2	84.8	18.3	19.7
	1125	46.3		86.7		18.5	19.8

[a]Pressed at 55,000 psi.

[b]Sintered in Ar–4% H_2 at 1450°C for 10.5 hr.

[c]Broke pellet before sintering.

pellets are given in Table 1.6. This test indicated that a forming pressure of 41,500 psi would yield 84% dense pellets; therefore, four batches of 40 pellets each were pressed at that pressure and sintered by the schedule previously described. Three additional batches were formed by pressing at 41,000 psi. To aid in reducing the ratio of O:metal, we placed a roll of Ta foil upstream and adjacent to the pellets to serve as a getter in the first four sintering runs but not in the last three.

Table 1.6. Results of Sintering Test of Blended Powders[a]

Forming Pressure (psi)	Density, % Theoretical[b]	
	Green	Sintered
$\times 10^3$		
40	45.1	83.4
45	45.9	85.2
50	46.9	86.1
55	47.3	87.7

[a]Batch ET3N obtained by blending batches ET3A-H95—ET3G-H101.

[b]Based on theoretical density of 11.06 g/cm^3.

Six control pellets, two each at the left end, center, and right end of the boat, were dimensionally inspected to determine green and sintered densities. These densities are given in Table 1.7. The moisture level in the effluent gas from the furnace was monitored to aid in controlling the ratio of O:metal. One pellet from each sintering run was analyzed for ratio of O:metal. After the pellets were ground to the required diameter on a centerless grinder, the ratio of O:metal and the gas released were determined for each sintering run. The H_2O in the effluent gas, the ratio of O:metal before and after grinding, and the gas released for each of the sintering runs are summarized in Table 1.8.

Results and Discussion. — The ratio of Pu to heavy metal (U + Pu) in the blended sol was 0.193; however, in the dried gel shard, the ratio was 0.183 (see Table 1.2). Since only one analysis was made of the shards, the results are not conclusive, but there is a possibility of some segregation of Pu and U during drying. The jet-milled powder contained 0.193 weight fraction Pu; this indicates that the effects of any segregation that might occur during drying are no longer evident after the material has been blended in the grinding operation. The fines collected in the dust bag of the jet-mill exhaust contained 0.186 weight fraction Pu. The exhaust dust was analyzed to determine if there were any gross segregation of Pu and U during grinding. The results indicate

Table 1.7. Densities of Pellets Sintered in Seven Production Runs for Engineering Test Reactor

Sintering Run	Density, % Theoretical[a,b]						Average (%)
	Green			Sintered[c]			
	Left	Center	Right	Left	Center	Right	
103	44.3	44.5	45.1	83.4	84.1	81.4	83.0
104	45.0	45.0	45.2	82.2	86.7	84.6	84.5
105	45.3	45.4	45.5	83.1	85.5	84.3	84.3
106	45.3	45.3	45.4	83.9	85.2	83.3	84.1
107	46.0	45.5	45.4	81.7	84.6	84.0	83.4
108	45.6	45.4	45.5	82.8	84.1	83.6	83.5
109	45.4	45.8	45.6	82.4	84.9	84.5	83.9

[a] Based on theoretical density of 11.06 g/cm^3. (Ratio of O:metal).

[b] Designations left, center, and right indicate position of sample in sintering boat.

[c] Average of two pellets from each position in boat.

Table 1.8. Moisture in Effluent Gas, Ratio of Oxygen to Metal, and Gas Release of Pellets from Seven Production Runs

Sintering Run	H_2O in Effluent Gas (ppm)	Ratio O:Metal		Gas Released (cm^3/g)
		Before Grinding	After Grinding	
103	28	1.991	1.946	0.91
104	27.5	1.974	1.940	1.00
105	17	1.967	1.952	1.8
106	24	1.963	1.943	0.81
107	31.5	1.988		0.67
108	30.5	1.990		0.70
109	37.8	1.986		0.03

that the amount of separation, if any, is very small. Measurements on the dried gel shards by Hg porosimetry show the bulk density at atmospheric pressure to be 4.40 g/cm^3 and the density at 10,000 psi to be only 4.48 g/cm^3. Since a pressure of 10,000 psi is sufficient to force Hg into 170-A openings, the measurement at 10,000 psi indicates that either

1. the porosity is closed,
2. the pores are less than 170 A in diameter or at least that the passages connecting the pores are less than 170 A, or
3. the crystal density is 4.48 g/cm^3.

By means of Hg porosimetry alone, one cannot determine which of these is correct; however, measurements by Hg porosimetry in conjunction with measurements of the Brunauer-Emmet-Teller (BET) surface area, can resolve the uncertainty. The surface area of the dried gel shards is about 36 m^2/g, which corresponds to a particle size of 100 to 200 A. This indicates that the dried gel shards are made up of agglomerates of 100- to 200-A crystallites with interconnected porosity of less than 170 A.

The surface area of the jet-milled powder was about 44 m^2/g; this indicates that the basic character of the particles was not changed during grinding; the particles were only reduced in size. This is the first time that we have observed an increase in surface area during jet-milling; normally it decreases slightly. The higher surface area of the fines (51.3 m^2/g) is consistent with previous observations.

The sintering tests on the two batches of powder calcined in Ar (ET3A-H95) and in Ar–4% H_2 (ET3B-H96) indicated that either type of powder could be used for making 84% dense powder. The green densities were lower and shrinkages higher for pellets pressed from the powder calcined in Ar–4% H_2; however, since we were able to press this powder slightly better, we selected it for further work.

The surface area of the powder calcined in Ar was about what we expected, about 8 m^2/g; however, the surface area of the first two batches calcined in Ar–4% H_2 was much higher than we expected, 27 to 35 m^2/g. Analysis of the batch ET3N, obtained by blending seven batches of calcined powder, again showed the surface area to be high (33 m^2/g); therefore, the results appear to be correct. The ratio of O:metal in the powder, from 2.22 to 2.44, is a little higher than the 2.15 to 2.25

we were attempting to achieve. The higher surface area would account for this because a powder with high surface area would oxidize more readily when cooled in CO_2. One batch (ET3C-H97) was inadvertently cooled in Ar–4% H_2 instead of CO_2. After a small amount of handling in the Ar-purged (but not high-purity atmosphere) glove box, this material had a yellowish-brown color that indicated considerable surface oxidation. All other powder calcined in Ar–4% H_2 was brown, while that calcined in Ar was black.

The results of the sintering test of the seven individual batches of calcined powder before they were blended indicated that five of the seven batches would be suitable for making 84% dense pellets (Table 1.5). The pellets from batch ET3B-H96 were only 81.4% dense. No explanation could be found for the lower density of these pellets. The pellets from batch ET3C-H97 were 89.4% dense; however, this was probably due to the increased surface oxidation of this powder that resulted because it was not stabilized in CO_2. We decided to blend all seven batches, expecting that the low density obtained with batch ET3B-H96 would compensate for the high density in batch ET3C-H97.

The test sinter of the blended batch of powder (ET3N) produced pellets with sintered densities (Table 1.6) about 1 to 2% higher than we had expected based on the results of sintering individual batches. A different die was used in pressing these pellets, but this does not appear to have been the cause of the variation in density, since the green densities of the pellets corresponded closely with those of pellets pressed from the individual batches. The source of variation might have been additional oxidation of the powder as it was handled. If this was the case, our stabilization treatment was not effective. We will continue to investigate this.

The average densities of the six control pellets in the seven production runs varied from 83.0 to 84.5% of theoretical (Table 1.7). In each run, density varied with position in the boat; density was 2 to 3% lower at each end of the boat than it was in the center. We attribute this variation to the nonuniform temperature profile of the furnace. After the pellets had been ground on a centerless grinder to the required diameter for loading into fuel pins, the densities of all pellets were

calculated. The percentage yields of pellets in three density ranges are summarized in Table 1.9. The low yield of pellets with 84.0 ± 1.0% of theoretical density is primarily due to our inability to position the boat so that all of the pellets were in the zone of uniform temperature.

Table 1.9. Yield of Pellets in Various Density Ranges for Seven Sintering Runs

Sintering Run	Pellet Yield in Indicated Density Range, %		
	83.5–84.5% of Theoretical	83.0–85.0% of Theoretical	82.5–85.5% of Theoretical
103	17	40	69
104	48	71	91
105	60	89	97
106	61	74	97
107	28	52	66
108	54	74	89
109	24	47	76

The ratio of O:metal was determined on pellets from each sintering run both before and after the pellets were ground on a centerless grinder. Table 1.8 shows that the ratio of O:metal of pellets from the first four sintering runs was significantly lower after grinding on a centerless grinder. The reasons for this are not understood at this time, but we are investigating.

Although the pellets were stored in a closed container that was evacuated and backfilled with dry Ar, the gas release from pellets from the first six sintering runs was extremely high (0.67 to 1.8 cm^3/g). After an extensive investigation[2] of the problem of gas release, we reduced the gas release from pellets from the final sintering run to 0.03 cm^3/g by cooling them from 850°C in Ar.

Capsule Fabrication

Capsules for Irradiation of Mixed Oxide Fuels in ETR (M. K. Preston). — As our next thermal-flux irradiation test of mixed oxide fuels, we are

planning four relatively simple instrumented capsules for the ETR. The fuel will be contained within two claddings bonded with NaK for transfer of heat. Thermocouples will be used to monitor the temperatures at the surfaces of the claddings. In two of the capsules, the fuel column will consist of four separate fuel pins with 3-in. fuel sections; the total height of the stack of four fuel pins will be 34 in. In each of the other two capsules, the fueled section will be a single fuel column 20 in. high. The cladding for the fuel pins will be the same as that we plan to use in our series II experiments in the EBR-II, 0.250-in.-OD × 0.015-in.-wall-thickness type 316 stainless steel.

We completed capsule components for development of welding, for fabrication of a dummy capsule for checking procedures, and for fabrication of the two stacked 3-in. fuel units. Welds were developed to comply with the ETR standards.

Equipment was assembled for loading NaK-44 (44% K) into the capsules. The equipment was checked for leaks, and practice runs will probably be made on dummy assemblies early in January.

Assembly procedures were prepared, along with data sheets, for the capsules with the stacked 3-in. fuel sections. These are being or have been reviewed and checked on dummy hardware.

The following subassemblies were fabricated and inspected: (1) the fuel-pin subassemblies, consisting of the tubing and bottom end plug; (2) the bottom capsule subassembly, consisting of the bottom end plug with the NaK fill tube, the internal sleeve, and the outer capsule tube; and (3) the capsule top end plug subassembly with the eight thermocouples brazed in place.

Five Sphere-Pac fuel pins and three pellet fuel pins, all with 3-in.-long fuel columns, were completed and accepted. Two pellet fuel pins are being rebuilt due to faulty welds. These will be completed the first week in January.

Series II Unencapsulated Fuel Pins for Irradiation in the Experimental Breeder Reactor-II (R. B. Pratt, M. K. Preston). — During fiscal year 1970 we plan to fabricate 19 unencapsulated fuel pins for irradiation in a 37-pin subassembly of the EBR-II shared with the Babcock and Wilcox Company. Eighteen positions will be used by Babcock and Wilcox Company, and 19

positions will be used by ORNL. Each site is responsible for fabrication, inspection, shipping, and postirradiation examination of its own fuel pins. Our test pins will be fueled with pelletized and Sphere-Pac fuel produced by the sol-gel process. Planning, scheduling, and procurement of hardware and raw materials have been the principal activities during the past quarter.

For our initial planning of fabrication, we created a critical-path schedule that shows the sequences and interaction of more than 1000 fabrication activities. The computer output predicted completion in May 1970. We have received approval-in-principle from the Division of Reactor Development and Technology (RDT) to begin fabricating fuel pins. The design of the fuel pin is being reviewed by EBR-II personnel.

A preliminary design of the fuel pin for the series II irradiations in EBR-II was completed.[3] The 40-in.-long fuel pin is clad with 0.250-in.-OD × 0.015-in.-wall-thickness type 316 stainless steel. A 1/16-in.-OD capillary tube is installed in the upper end fitting for the purpose of introducing gaseous He and Xe. The pin contains 5 7/8 in. of UO_2 blanket pellets and 13 1/2 in. of $(U,Pu)O_2$ fuel along with ThO_2 insulator pellets, fiberfrax pads, a Ni neutron shield, an extensometer, and a plenum spacer tube. The outside of the cladding tube is to be wrapped with spacer wires by operations personnel at the EBR-II.

Laboratory management recently instituted a more formal program of quality assurance. The program for fabricating the series II fuel pins was selected to participate in this program. We are now accumulating material and specifications for each type of raw material. In cases where RDT specifications were not available, other suitable specifications [such as American Society for Testing and Materials (ASTM), Military (MIL), Aerospace, and Metallurgy (MET) specifications] were substituted. We are in the process of qualifying our material to meet the appropriate specifications. All raw materials for mechanical components are on hand; archive samples were stored, and chemical samples were submitted for analysis. Considerable effort has been spent for inspections of the 700 ft of 0.250-in.-OD × 0.218-in.-ID type 316 stainless steel seamless tubing that is to be used for cladding. Longitudinal and transverse ultrasonic

inspections were made, and the results were compared to the signal from a 0.001-in.-deep × 0.004-in.-wide × 0.030-in.-long standard. Tubing with flaws less than the standard is acceptable for use in the EBR-II.

Specifications for the EBR-II $(U,Pu)O_2$ fuel pellets are being prepared. Four batches of Pu sol were received and blended with U sols. These batches were tray dried, and the resulting shards were blended and are being comminuted in a fluid-energy mill.

The initial output of the critical-path schedule showed that preparation of UO_2 blanket pellets was the critical path. To alleviate this situation, 200 pellets and 2 kg of UO_2 powder were obtained from the Battelle Memorial Institute Pacific Northwest Laboratory (BNWL). Receipt of the UO_2 material and pellets reduced the estimated number of days for this activity sufficiently to remove it from the critical path. Approximately 380 pellets are being prepared by the Ceramic Process Development Group. To date, a number of pellets have been test sintered and are being analyzed. A pressing die was designed and is being fabricated. Experiments with ThO_2 for the insulator pellets showed that the die sized for the blanket pellets is also suitable for pressing the insulator pellets.

The critical path presently concerns Sphere-Pac and pellet fabrication activities. Specifications for both coarse and fine microspheres are being prepared. The Chemical Technology Division is successfully preparing $(U,Pu)O_2$ microspheres.

During fabrication of the fuel pins, at least 1 cm^3 of Xe tagging gas must be introduced into each pin. Drawings for equipment and procedures for Xe tagging were received from BNWL and the EBR-II site. At General Electric and Argonne National Laboratory, a device similar to a hypodermic needle is used to puncture a septum and withdraw Xe gas, which is then ejected into individual fuel pins. At BNWL the He and Xe gases are mixed beforehand and then admitted through valves into each fuel pin. Each system seems to have some drawbacks. Therefore, we have prepared a conceptual design for a third system in which each fuel pin is evacuated, the free volume is determined, and the fuel pin is then evacuated once more before introducing into the pin, through valves, first a measured amount of Xe and then a measured amount of He. The resultant mixture is at a pressure

slightly above atmospheric. The gases are introduced through a capillary that is later pinched shut, cut, flattened, and welded. This does not require the use of cryogenic or Hg Toepler pumps nor handling of a cumbersome, 4-ft-long "hypodermic" needle. Information and procedures for the conceptual design are being transmitted to the EBR-II site for review and approval.

Characterization of $(U,Pu)O_2$ Fuels

J. M. Leitnaker D. L. McElroy C. S. Morgan

The development of sol-gel fuel fabrication requires characterization of both the chemical composition and physical properties of the material to control the process and to interpret meaningfully the irradiation behavior. Thermodynamic studies will contribute to the development of the process for producing the fuel and will aid in predicting fuel performance for both irradiation testing and model studies.

Analytical Chemistry (W. H. Pechin)

The Analytical Chemistry Division procured equipment for analyzing water sorbed on the mixed oxide fuel at desorption temperatures to 1000°C. This equipment should be installed, tested, and placed in service in time for use on the fuel for the series II irradiations in the EBR-II. The moisture analysis will ensure the capability for characterizing $(U,Pu)O_2$ fuels in accordance with the specification. This analysis is also required in conjunction with the problem of gas release, as discussed previously,[2,4] since moisture may contribute to the gas release. In this case it would probably be detected as H_2, which would confuse the problems of retention of H during heat treatment and adsorption of water after heat treatment.

Control of Gas Release and Ratio of Oxygen to Metal (W. H. Pechin, R. A. Bradley)

Specifications for nuclear fuels normally include a maximum volume of gas to be evolved by the fuel at elevated temperature. The current

specification for the Fast Flux Test Facility allows not more than 0.05 cm^3 of gas (STP) per gram of fuel and, additionally, a maximum of 30 ppm by weight of H_2O. Using the gas release technique described previously[5] we have often observed values in excess of 20 times the desirable limit. Table 1.10 lists the ratio of O:metal and gas release measured on pellets prepared for the ETR capsules. During the period covered by this report we have concentrated our efforts on determining the source of evolved gas and on finding means of controlling it.

We had previously observed that the amount of gas released increased with the time since final heat treatment. We attributed this behavior to adsorption of moisture by the pellets. Accordingly, we handled the pellets from subsequent sintering runs in such a manner as to minimize exposure to the atmosphere of the glove box and stored them in desiccators containing less than 1 ppm moisture.

Even with these precautions, however, the gas release from the fuel may be as high as 0.50 cm^3/g. This and the fact that mass spectrographic analysis of the evolved gas has always shown it to be largely H_2 indicated that the gas was probably H_2 being retained from the heat treatment in Ar–4% H_2. Therefore, we performed several experiments in the production sintering furnace with its associated moisture monitor to determine if this were the case.

These experiments are described in Table 1.10. All of these runs were made with pellets that had previously been sintered; the heating rates were 300°C/hr, and gas flow rates were 2.5 ft^3/hr. We dried all gases to a moisture content of less than 1 ppm before we admitted them to the furnace. Between the heating cycles of a given heat treatment, the furnace was not opened to the atmosphere of the glove box.

In the first run, as illustrated in Fig. 1.1(a), the pellets were heated in Ar–4% H_2 to 1425°C and held at that temperature until the effluent moisture dropped to 30 ppm. This level corresponds to an O:metal ratio of about 1.97. The very large moisture peak observed in this heating cycle was probably not due to reduction of the pellets but rather to the fact that the furnace system had been saturated with CO_2 in the previous run. The pellets were cooled to room temperature, and

Table 1.10. Heat Treatments 110 and 111

Heat Treatment	Heating Atmosphere	Gas Equivalent of Low-Temperature Peak (cm^3/g)	Final Moisture Level (ppm)	Cooling Atmosphere	Measured Gas Release at 1600°C (cm^3/g)
110A	Ar–4% H_2	0.0	28.5	Ar–4% H_2	
110B	CO_2-600°C, Ar–4% H_2	0.035	26.7	Ar	
110C	CO_2-600°C, Ar–4% H_2	0.0	28	Ar–4% H_2	
110D	CO_2-600°C, Ar–4% H_2	0.013	27.5	Ar	0.03
111A	Ar	0.0	15	Ar–4% H_2	
111B	Ar	0.0	12	Ar–4% H_2	
111C	CO_2-600°C, Ar–4% H_2	0.072	34.5	Ar–4% H_2	
111D	CO_2-600°C, Ar–4% H_2	0.025	18	Ar–4% H_2	
111E	CO_2-600°C, Ar–4% H_2	0.024	10	Ar–4% H_2	
111F	CO_2-600°C, Ar–4% H_2	0.019	23.5	Ar–4% H_2, Ar from 850°C	
111G	CO_2-600°C, Ar–4% H_2	0.0	10	Ar–4% H_2	0.49
116C	Air-400°C, Ar–4% H_2	0.17	30	Ar–4% H_2	
116D	Air-400°C, Ar–4% H_2	0.22	30	Ar–4% H_2	

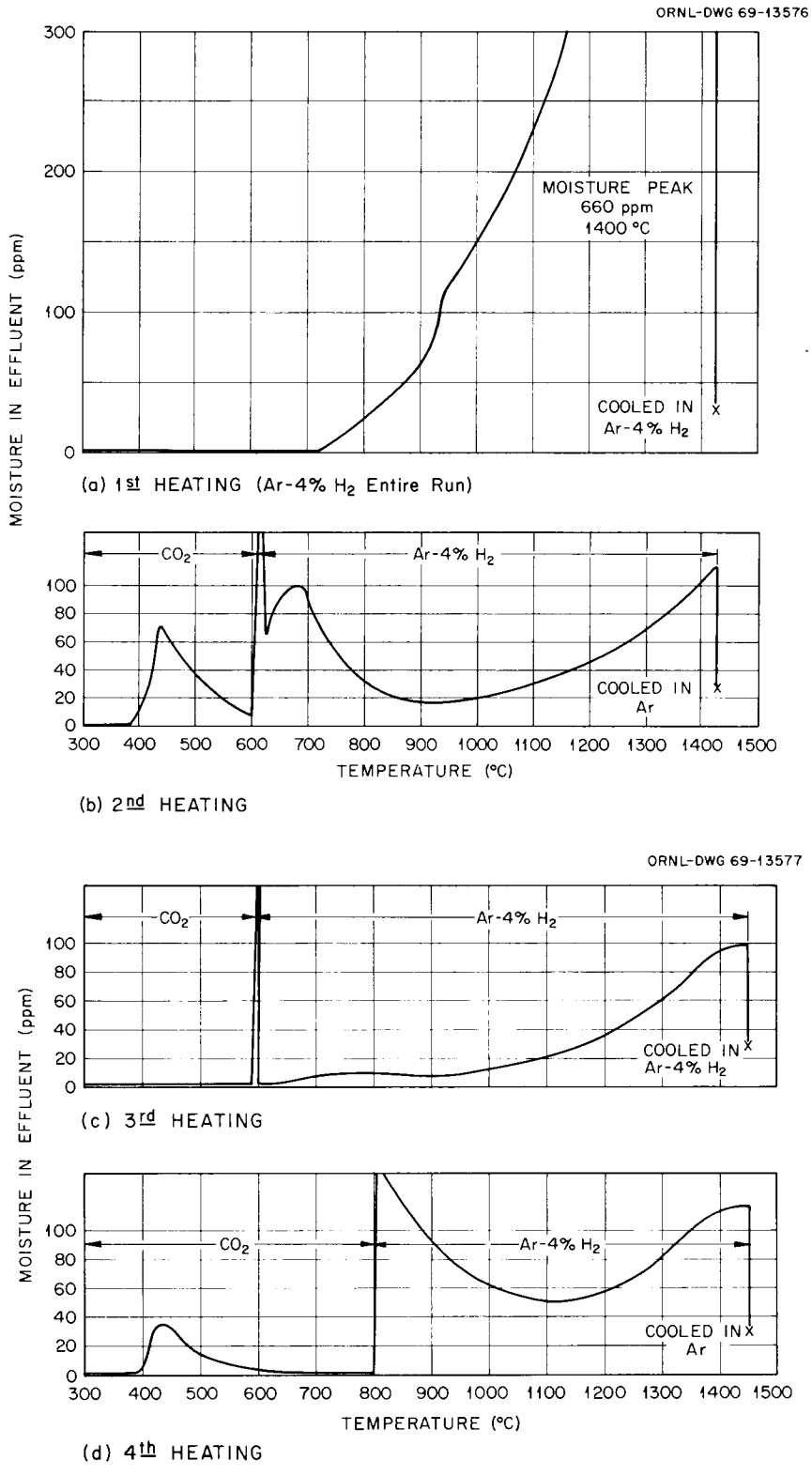

Fig. 1.1. Effluent Moisture During Heat Treatment of $(U,Pu)O_2$.

the second heating was begun in CO_2, as illustrated in Fig. 1.1(b). During this heating, we observed a moisture peak that began at about 380°C and reached a maximum of about 75 ppm. We hesitate to ascribe this peak directly to moisture, since the pellets had previously been equilibrated to a much lower moisture level. We believe that this peak is caused by the evolution of H_2 from the pellets. The evolved H_2 reacts with the CO_2 atmosphere to form water. After the peak appeared to be complete, we switched the atmosphere in the furnace to Ar–4% H_2 and heated the pellets to 1425°C. Again, the moisture in the effluent was reduced to about 30 ppm. The pellets were then cooled to room temperature in an Ar atmosphere. During the third heating [Fig. 1.1(c)], which was again in a CO_2 atmosphere, there was no peak at low temperature. This indicates that cooling in an Ar atmosphere prevented the fuel from picking up H_2. The pellets were again reduced to about 30 ppm moisture at 1425°C and cooled in Ar–4% H_2. The fourth heating [Fig. 1.1(d)] indicated that the peak at low temperature was again present. The pellets were again reduced to 30 ppm moisture at 1425°C in Ar–4% H_2. After this fourth heating, the pellets were cooled in Ar and removed from the furnace.

The pellets that received heat treatments 110 and 111 (Table 1.10) were similar. The amount of reduction of the pellets was varied between 10 and 35 ppm moisture. The trend seems to be that greater reduction caused a greater peak at a low temperature but that repeated temperature cycling reduced the size of the peak. The gas equivalents in Table 1.10 indicate the number of grams per cubic centimeter of H_2 released by the pellets that would be required to cause a moisture peak of the magnitude observed. The number was calculated from a graphical integration of the peak, the known weight of pellets in the furnace, and the known flow rate of the furnace gas.

Our experiments showed that H_2 can be retained by the fuel during heat treatment and that this retention can be avoided by cooling in Ar. The magnitude of the retention demonstrated in heat treatments 110 and 111 is considerable compared to the fuel specification, but is not great enough to explain the amount of gas released, about 1.0 cm^3/g. A possible explanation is that not all the H_2 evolved in conjunction with the peaks observed at low temperature in heat treatments 110 and 111 was

oxidized to H_2O. To determine if this were the case, we ran the same type of experiment (heat treatment 116) in air instead of CO_2 while heating through the low-temperature peak. With the air atmosphere, the peak content at low temperature was 0.17 to 0.22 cm^3/g. This represents from 25 to 50% of the amount of gas typically found in these pellets after cooling in Ar–4% H_2 and indicates that the H_2 was not completely oxidized in heat treatments 110 and 111. Since the H_2 may not be completely oxidized even in air, we have installed a catalytic unit in the effluent line ahead of the moisture monitor to ensure that the reaction between H_2 and O_2 is complete before the gas reaches the moisture monitor.

Table 1.10 shows that cooling in Ar reduces the gas released at 1600°C and also eliminates the moisture peak at low temperature. It is not practical to measure the gas released at temperatures as low as 400°C in our present apparatus; however, one sample that had been cooled in Ar–4% H_2 was analyzed at an estimated temperature of 600°C and found to release 0.65 cm^3/g. The sample was heated to 1600°C and released only an additional 0.03 cm^3/g, showing that nearly all the gas was released at or below 600°C. The results of mass spectrographic analysis of the gas released by this sample at 600°C are given below:

Species	Vol %
H_2	98.8
H_2O	0.7
H_2 + CO	0.3
CO_2	0.1

A control sample from the same batch that was analyzed at 1600°C in the usual manner released 0.55 cm^3/g.

One-half the pellets from heat treatments 110 and 111 were exposed to the atmosphere in the glove box while the other half of each run was placed in a metal desiccator with molecular sieve desiccator. Samples from each portion will be sent for analysis of gas release at intervals to determine the effect of exposure on gas release. Preliminary results from this experiment are listed in Table 1.11. Pellets cooled in Ar release less gas than those cooled in Ar–4% H_2. In addition, the rate

Table 1.11. Effect of Furnace Atmosphere During Cooling and Length of Exposure on Gas Release of $(U,Pu)O_2$ Pellets

Heat Treatment	Exposure Condition	Exposure Time (Days)	Gas Released (cm^3/g)
110 cooled in Ar	Glove box	0	0.03[a]
	↓	2	0.03
	↓	6	0.04
	↓	13	0.05
	↓	18	0.05
	Desiccator	5	0.05[a,b]
	↓	6	0.02
	↓	18	0.05
111 cooled in Ar–4% H_2	Glove box	0	0.49[a]
	↓	2	0.86
	↓	7	0.98
	Desiccator	7	0.91

[a]Average for two pellets.

[b]Diameter reduced by 0.010 in. by grinding on a centerless grinder under an Ar atmosphere.

of gas release from pellets cooled in Ar–4% H_2 apparently increases with time after cooling while the rate for pellets cooled in Ar does not.

As shown in Table 1.8, a significant difference in the ratio of O:metal was seen in sintering runs 103 through 106 before and after the pellets were ground on a centerless grinder. This indicates a steep gradient in O:metal ratio with a high value at the surface and a low value at the center of the pellet. Such a situation could occur if the pellets oxidized while cooling. The moisture content of the effluent gas, measured during the cooling of these sintering runs, did decrease as temperature decreased; however, when the partial free energy of O_2 in the furnace atmosphere was calculated from the moisture values, it was found that the furnace atmosphere was oxidizing to the pellets during cooling. The overall average ratio of O:metal for the pellet is the quantity of interest, since the O_2 will be redistributed at operating temperature, but the presence of such a steep gradient complicates the

control of this ratio. Thus, if the situation indicated by the ratio of O:metal of sintering runs 103 through 106 is true, it will require further investigation.

Analytical Characterization (K. E. Spear, J. P. DeLuca)

We performed experiments to (1) establish standard oxide samples for determining O content, and (2) establish the relationship of composition, lattice parameters, and O potential in oxide fuels.

Standard Samples. — We are in the process of preparing $(U,Ce)O_2$ samples for examination after irradiation by means of the electron microprobe. The samples are coprecipitated, centrifuged, washed, centrifuged again, dried, partially reduced in H_2, and then pressed and sintered into 1/4-in.-diam specimens for mounting.

Measurements of Oxygen Potential. — We have customarily defined our O potentials by mixtures of gases, usually CO and CO_2. For a variety of reasons it seems desirable to be able to measure O potentials independently of mixing conditions. To accomplish this we have constructed an O meter. The principle behind the meter is the fact that conduction through CaO-stabilized ZrO_2 is ionic via O ions rather than electronic. Thus, the potential across such a plate that has different O potentials on each side will be given by

$$E = \frac{RT}{4F} \ln \frac{P_{O_2(a)}}{P_{O_2(b)}} \quad , \tag{1.1}$$

where E is the potential, R is the gas constant, T is the temperature of the tube, F is the Faraday constant, and $P_{O_2(a)}$ and $P_{O_2(b)}$ are the O_2 pressures on side (a) and (b) of the plate.

The element itself is constructed of a Ca-stabilized ZrO_2 tube. The furnace gas contacts the inside of the tube and air contacts the outside. A simple wire-wound heater is used to keep the temperature of the tube at the desired level.

The measurements of O potential can be exceedingly accurate if temperature is controlled and measured carefully. Thus, we have successfully measured O potential within 0.1% of the calculated value

for a 10:1 gas mixture of CO and CO_2 at 1100°K: 1.040 v. This corresponds to an O pressure (at this temperature) of 2×10^{-18} atm.

It costs about $20 to construct this meter. If it is to be used for monitoring a glove box, for example, an inexpensive device for measuring voltage will provide all the sensitivity desired. Measurement of precise potentials requires more elaborate equipment, but the element is the same.

Solution of Rare-Earth Fission Products in Fuels (W. H. Hendrix,[6] K. E. Spear). — Rare earths constitute about one-fourth of all fission products. Their behavior in a fuel as a function of burnup can have important consequences such as directly affecting the O potential. Most of the rare earths commonly exhibit an oxidation state of +3. When they are dissolved in the UO_2 fluorite structure, however, the effective oxidation state of the whole can become +4 or even greater.[7] The O potential at which this occurs is not known. The O potential as a function of burnup is likely to be an important parameter in the cladding transport via Cs, as discussed above. We have begun an investigation into the relationship between composition, lattice parameter, and O potential in the systems of a rare earth (RE) and either UO_2, PuO_2, or $(U,Pu)O_2$.

Lattice parameters of the UO_2-$REO_{1.5}$ system can be synthesized by one general relationship. (Note that the O composition of the system lies between the fluorite UO_2 and the rare-earth sesquioxide.) Ferguson and Fogg[8] report a general equation,

$$a_f = 0.3943a_c + 1.2285 \text{ (A)} , \qquad (1.2)$$

in which a_c is the lattice constant of a body-centered cubic (bcc) rare-earth sesquioxide and a_f is the lattice constant of an imaginary rare-earth fluorite phase obtained by extrapolating data for the lattice constant of solutions of the rare-earth oxides in fluorite-type oxides to pure, imaginary rare-earth sesquioxides. This equation is closely obeyed by a large number of oxides with the bcc $D5_3$ structure when they are dissolved in a fluorite structure. Ferguson and Fogg[8] showed that the UO_2-$YO_{1.5}$ system also obeys this equation. Our examination of the work of Lynch[9] shows that, within the experimental error, the UO_2-$LaO_{1.5}$

system also obeys this general relationship. Since La_2O_3 represents, in size, one extreme of the rare-earth sesquioxides while Y_2O_3 is nearly at the other extreme, it is reasonable to assume that Eq. (1.2) is general and will be obeyed for all systems of $REO_{1.5}$ and UO_2, PuO_2, and $(U,Pu)O_2$. In Table 1.12 we tabulate the calculated lattice constants for the imaginary fluorite sesquioxide.

Table 1.12. Calculated[a] Fluorite Lattice Constants of Rare-Earth Sesquioxides

Rare Earth	Lattice Constant (A)
Y[b]	5.398
La	5.724
Ce[c]	5.686
Pr[c]	5.647
Nd	5.594
Pm[c]	5.580
Sm	5.538
Eu	5.514
Gd	5.495
Tb	5.452
Dy	5.436
Ho	5.408
Er	5.381
Tm	5.361
Yb	5.341
Lu	5.329

[a]Calculated from the equation

$$a_0 = 0.3943\ a_c + 1.2285$$

where a_c is the lattice constant of the $D5_3$ sesquioxide.

[b]Yttria is often treated as a rare earth, not only because of its size, but also because of its position in the periodic table.

[c]The sesquioxide lattice parameter is an interpolated value.

Our own work, as well as previous work by a number of investigators, indicates that the solutions of UO_2-$REO_{1.5}$ are easily oxidized, although this has not been determined quantitatively. Anderson et al.[7] indicate that $YO_{1.5}$-UO_2 solid solutions "oxidize vigorously at temperatures of −20 to +20°C." Therefore, at this juncture, it is difficult to fix with any confidence the lattice constant versus composition of $(U,RE)O_{2-x}$ compositions; most of the literature data appear to be badly scattered and not determined as a function of O potential. The data of Aitken and Joseph,[10] however, appear to be good in this regard. Their experiments were performed at a constant O potential ($10^{-5.5}$) over the low "YO_2" portion of the range. Extrapolation of their linear data between $U_{0.81}Y_{0.19}O_2$ and $U_{0.54}Y_{0.46}O_2$ to pure, imaginary YO_2 yields a lattice parameter of 5.212 A, while pure, imaginary fluorite-phase $YO_{1.5}$ has a lattice parameter of 5.398 A. Thus, oxidation of $YO_{1.5}$ in the imaginary fluorite phase to the imaginary YO_2 fluorite phase reduces the lattice parameter by 0.186 A.

We continued to investigate the dissolution of rare-earth oxides in UO_2. Blending and heating dry powders of UO_2 and CeO_2 does not appear to yield equilibrium within reasonable time, even at relatively high O potentials. Mixing 80 mole % UO_2 and 20 mole % CeO_2 and heating 16 hr at 1200°C in a 5:1 mixture of CO_2 and CO resulted in lattice parameters of 5.47018 ± 0.00023 for the UO_2 and 5.4112 ± 0.00014 for the CeO_2. These phases should be completely soluble in each other.

Mixing nitrate solutions of the two materials, precipitating with NH_4OH, and subsequent heating appears, however, to allow us to reach equilibrium. We have used this technique to mix the materials to 5, 10, 20, and 40 mole % CeO_2. The data obtained thus far are tabulated in Table 1.13. These samples were quantitatively precipitated into NH_4OH, filtered, heated in precalibrated frits in H_2 for 16 hr at 400°C, and finally equilibrated in mixtures of CO and CO_2.

Apparatus for Measuring Thermal Conductivity to 10 atm and 1400°K
(P. H. Spindler)

We assembled our radial heat-flow apparatus in preparation for measuring thermal conductivity of an 84% dense bed of vibratorily

Table 1.13. Results of Conversion of Ce-U-O Nitrate Mixtures to Oxide

Sample	Weight of Starting Material, g			Weight of H_2-Reduced Material (g)	Weight of Material Converted in Mixed Atmosphere of CO and CO_2,[c] g		
	Ce[a]	U[b]	Total		Ce	U	O
5	0.1748	5.4757	5.6505	6.6294	0.0406	1.2708	0.1663
10	0.3645	5.4746	5.8391	6.8757	0.1327	1.9936	0.2865
20	0.8055	5.4741	6.2796	7.4666	0.2685	1.8248	0.2970
40	2.1531	5.4802	7.6333	9.1563	0.3833	0.9755	0.2072

[a]Weighed as $(NH_4)_2Ce(NO_3)_6$ from standard sample material.

[b]Weighed as ammonium uranate. The amount of U was determined in a separate experiment.

[c]Since we know the absolute amounts of U and Ce in the H_2-reduced material, we can calculate the absolute amount of U and Ce transferred into the crucible for heating in the mixture of CO and CO_2. In the final product, the weight of U, the weight of Ce, and the weight of O are assumed to total 100%.

compacted ThO_2 microspheres of two sizes. This bed of ThO_2 microspheres was loaded into a sample container, but the container has not been placed in the apparatus. In the meantime, we measured the thermal conductivity of two beds of Al_2O_3 powder at room temperature as a function of Ar overpressure from 0.02 to 1 atm. We intend to measure the ThO_2 bed to check our previous measurements to 1200°K and 2 atm of He and Ar. If adequate checks are obtained, we will extend our measurements of this sample to 10 atm and 1400°K before we install a bed of UO_2 microspheres. The present apparatus can be incorporated into the Pu glove box when it arrives.

Conduction of Infrared Radiation (P. H. Spindler, J. P. Moore)

Defining the thermal conductivity of nuclear oxide fuels at high temperatures is important, for thermal conductivity controls the distribution of fuel temperature, which in turn governs the behavior of the fuel under irradiation. One unanswered question about conduction in UO_2 is whether or not there is a significant component for transmission of infrared radiation at high temperatures. Other investigators have attempted to calculate the infrared component, but we believe that their calculations were based on questionable assumptions. Another difficulty is that measurements of thermal conductivity above 1200°C are inaccurate and thereby invalidate experimental answers to the primary question about UO_2.

During the past year we derived equations for calculating the conduction by infrared radiation and attempted to test these equations by measuring the thermal conductivity of materials with known coefficients of spectral absorption. We selected single-crystal and polycrystalline LiF, since we expected the effect of conduction by infrared radiation in materials to be large within the temperature range in which accurate (about ±2%) data could be obtained. The results of our approach are described below.[11]

Experimental Data. — Previous reports[12–15] indicate that the thermal conductivity of single-crystal and polycrystalline LiF decrease with increasing temperature, but not exactly as expected for three-phonon

processes in an electrical insulator. For this case one expects the lattice thermal resistance to be a linear function of temperature. From 200 to 450°K, our data for thermal resistance, λ^{-1}, fit the linear equation

$$\frac{1}{\lambda} = 0.033\ T - 2.83\ , \qquad (1.3)$$

where λ is in w/cm °K and T is temperature in °K; but above 450°K, the thermal resistivity data deviate negatively from the linear function. At all temperatures above 450°K, the difference between the measured thermal conductivity and the values calculated from this equation is assumed to be due to transmission of infrared radiation.

Close examination[16] of the optical properties of the LiF specimens revealed that the single-crystal specimen was nearly optically thin for a radius of 2.54 cm, whereas the polycrystalline specimen of the same size was optically thick. This means that the single crystal of LiF acted like a window in the wavelength range in which thermal radiation occurs (0.12 to 9.0 μm); that is, photons were passing through the single crystal without significant interaction. A calculation for the single crystal of LiF, assuming limited photon interaction and boundary conditions of blackbody radiation, yielded a nearly linear relationship between thermal resistance and temperature to 1100°K that agreed with the extrapolation of the data for low temperatures. This helped to establish the contribution of the lattice portion of the thermal conductivity to the total thermal conductivity at high temperatures. The data for the thermal conductivity of the optically thick polycrystalline LiF represent the sum of lattice and radiation conduction, and the difference between the actual data for thermal conductivity and the extrapolation of the ratio of thermal resistivity to temperature is the total thermal conductivity that is due to the conduction of infrared radiation. This difference is shown in Fig. 1.2 as a dotted curve. This curve is based on an extrapolation of the linear relationship between thermal resistivity and temperature at low temperatures (which was partly confirmed by the corrected data for single-crystal material that represented the lattice contribution). However, the exact placement of the lattice contribution is still being studied.

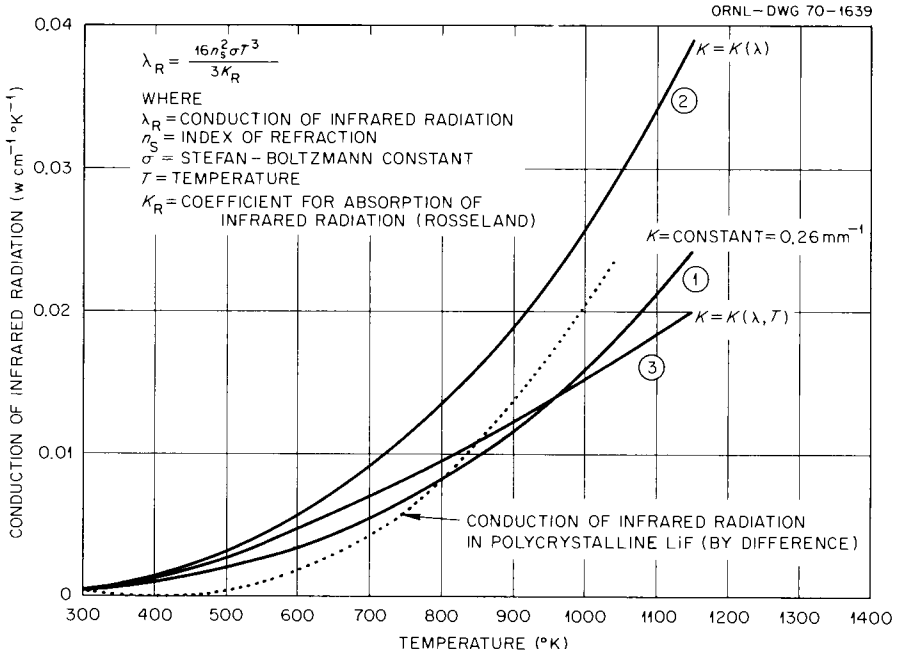

Fig. 1.2. Conduction of Infrared Radiation in Polycrystalline Lithium Fluoride. Rosseland approximation and the Genzel equation applied to experimental data to calculate conduction of radiation. Curve 1: calculated for a constant absorption coefficient of 0.26 min^{-1}. Curve 2: calculated for an absorption coefficient dependent on wavelength. Curve 3: calculated absorption coefficients dependent on wavelength and temperature.

The contribution to the total thermal conductivity that we infer from our experiments to be due to conduction of infrared radiation increases with temperature. Figure 1.2 compares a curve for these values with three curves determined by calculations of the infrared component by means of the procedures described below. The values inferred from our experiments fall within ±0.005 w $cm^{-1} °K^{-1}$ of all three calculated values and offer no firm confirmation of which calculation is best, but all seem to be satisfactory.

Calculation Procedure. – Application of the Rosseland approximation[17] for calculating the contribution made to the total thermal conductivity by the conduction of radiation (see, for example, Flynn[18]), requires that the specimen be optically thick (that is, that the optical thickness of the material be much greater than 1 for all wavelengths). This is only the case when the total thermal radiation emitted at one boundary of the material is completely absorbed by the sample matter. Therefore,

a knowledge of the optical properties of the material used for measurements of thermal conductivity is essential for analysis of the results. The first computer program we developed, which is based on a work of Czerny and Genzel,[19] allows a determination of the depth of transmittance of radiation emitted in the center of a solid cylinder.[20] If we assume that the radiating core emits blackbody radiation, we obtain for the depth that diffuse radiation penetrates into the cylindrical specimen

$$\Pi_b = \frac{8\,hc^2}{\sigma n_s^4 T^4}\left(1+\frac{r}{R}\right)\int_{\lambda=0}^{\infty}\frac{1}{\lambda^5\left[\exp\left(\frac{hc}{n_s kT}\right)-1\right]}\int_{\alpha=0}^{\alpha_0}\exp\left[\frac{-K(\lambda)r\left(+\frac{r}{2R}\right)}{\cos\alpha}\right]\cdot$$

$$\arctan\left(\frac{\cos\alpha}{\sqrt{\left(1+\frac{r}{R}\right)^2-1}}\right)\cos\alpha\,\sin\alpha\,d\alpha\,d\lambda\,, \qquad (1.4)$$

where

Π_b = depth of diffuse radiation,
h = Planck's constant,
c = velocity of light,
σ = Stefan-Boltzmann constant,
T = temperature,
n_s = index of refraction of specimen,
n_c = index of refraction of core,
R = radius of core,
r = radius of specimen,
λ = wavelength,
k = Boltzmann's constant,
α = angle under which the radiation flux hits an area element on the cylinder mantle,

$$\alpha_0 \begin{cases} = \frac{\pi}{2} \text{ for } n_c \geq n_s \\ = \arcsin\left(\frac{n_c}{n_s}\right) \text{ for } n_c < n_s, \end{cases}$$

K = absorption coefficient.

If one knows the temperature and the distribution of spectral energy in the core as well as the wavelength and temperature dependence of the absorption coefficient, K, then this equation can be solved by numerical integration.

In some particular cases it is possible to assume the specimen to be a gray absorber. Then the equation for the depth of transmittance reduces to

$$\Pi_g = \frac{4}{\pi}\left(1 + \frac{r}{R}\right) \int_{\alpha=0}^{\alpha_0} \exp\left[-\frac{K \cdot r\left(1 + \frac{r}{2R}\right)}{\cos\alpha}\right] \arctan\left(\frac{\cos\alpha}{\sqrt{\left(1 + \frac{r}{R}\right)^2 - 1}}\right) \cdot$$

$$\cos\alpha \sin\alpha \, d\alpha \, . \qquad (1.5)$$

If $\pi \approx 0$ for the sample dimensions for all temperatures of interest (equivalent to the optically thick limit), then the Rosseland approximation for calculating the contribution of thermal radiation can be applied. The total radiative thermal conductivity is

$$\lambda_r = \frac{16 \, n_s^2 \, \sigma \, T^3}{3K_R} \quad , \qquad (1.6)$$

where K_R is the Rosseland mean absorption constant, which is defined by

$$\frac{1}{K_R} = \int_0^\infty \frac{1}{K(\lambda, T)} \cdot \frac{dE_{b\lambda}}{dE_b} \, d\lambda \quad , \qquad (1.7)$$

where $E_{b\lambda}$ and E_b are the abbreviations for Planck's radiation law and the Stefan-Boltzmann law, respectively.

For the polycrystalline LiF, $\pi_b \approx 0$ for r = 1.0 at all temperatures investigated; that is, the material was optically thick in the case of our sample dimensions (r = 2.54 cm). In the single crystal, for r = 2.54, the depth of transmittance π_b indicates 4% of the thermal radiation is absorbed at room temperature and about 33% at 1100°K; that is, the Rosseland approximation cannot be used per se, but one has to

consider that 67 to 96% of the total radiation energy is exchanged between the boundaries of the specimen.

The three curves shown in Fig. 1.2 for the portion of total thermal conductivity due to radiation were calculated by means of the Rosseland approximation. Curve 1 represents Eq. (1.6) with an average constant absorption coefficient $K = 0.26\ mm^{-1}$. It is the simple case of gray absorption and shows a cubic dependence of the conduction of infrared radiation with temperature. In curves 2 and 3, the absorption coefficients used for the computation of K_R in Eq. (1.7) are respectively dependent on wavelength alone and on wavelength and temperature. As is shown in Fig. 1.2, both curves are no longer cubic with temperature, T; but Flynn[18] showed that the conduction of infrared radiation, λ_R, for some materials could increase with T^n, where n might be as large as 10. As outlined above, the dotted curve in Fig. 1.2 shows the calculated values of $\lambda_R = \lambda_{total} - \lambda_{phonon}$, for which we used our experimental data for the total thermal conductivity and assumed that the thermal resistivity due to λ^{-1}_{phonon} is the extrapolation of the straight line between 300 and 400°K.

Extension to UO_2

The significance of the radiation component in UO_2 is difficult to assess because of the lack of data for the spectral absorption coefficient at high temperatures. If we use the room-temperature values of Bates[21] and assume that the coefficient does not vary with temperature, the above equations predict a value of 0.022 w $cm^{-1}°K^{-1}$ for the radiation component at 1400°K. This upper limit value would be roughly equivalent to the lattice conduction.

We believe that conduction of infrared radiation is insignificant at all temperatures — even for stoichiometric single-crystal UO_2 — because the absorption coefficient should increase rapidly with increasing temperature. Since UO_2 is a semiconductor, the absorption of infrared radiation would increase above the intrinsic temperature due to electronic transitions.[22] Even below the intrinsic temperature, the absorption coefficient would increase almost exponentially with

temperature due to multiphonon effects.[23] This increase in the absorption coefficient is reflected in the behavior of the emittance of UO_2 with increasing temperature.[24] Because of this, we believe that the effects of temperature on the absorption coefficient negate a significant contribution of infrared radiation to the total thermal conductivity. Proof of this must await measurements of the spectral absorption coefficient of UO_2 above room temperature.

Irradiation Testing of $(U,Pu)O_2$ Fuels

C. M. Cox

The performance characteristics of mixed $(U,Pu)O_2$ fuels are being evaluated in a variety of irradiation tests for potential application in an LMFBR. We are now concentrating on comparative tests of sol-gel fuel fabricated as pellets or as microspheres compacted by the Sphere-Pac technique. The program includes thermal-flux experiments, which permit use of instrumented capsules and the achievement of high levels of burnup in relatively short periods of time, and fast-flux experiments, in which the fission rate distribution and radiation effects on the cladding are more typical of those for operating conditions anticipated in an LMFBR. Mathematical models of fuel behavior are being developed in conjunction with the experimental program.

Uninstrumented Thermal-Flux Irradiation Tests (A. R. Olsen, D. R. Cuneo[25])

A series of uninstrumented capsules is being irradiated in the X-Basket facilities of the ETR. Each capsule contains four test pins arranged in tandem. The initial objective of these tests was to investigate the effects of fabrication form with extended burnup on the release of fission gas, migration of fission products, and fuel swelling. Some capsules are now being irradiated specifically to provide short-cooled irradiated fuel for LMFBR reprocessing studies. The results of the first three capsules irradiated to low burnup in this series were discussed at the Winter Meeting of the American Nuclear Society.[26] The current status of all the tests in this series is given in Table 1.14.

Table 1.14. Uninstrumented Thermal-Flux Tests of $(U,Pu)O_2$ Fuels

Capsule Number	Fuel Form	Fuel Composition	Number of Fuel Pins	Peak Burnup (% FIMA)[a]	Peak Linear Heat Rate (w/cm)	Peak Cladding Inner Surface Temperature (°C)	Status November 1969
43-99	Sphere-Pac	$(^{235}U_{0.80},Pu_{0.20})O_{2.00}$	2	1.5[b]	1640[b]	1000	Examined
43-100	Sphere-Pac	$(^{235}U_{0.80},Pu_{0.20})O_{2.00}$	2	1.4[b]	1470[b]	900	Examined
43-103	Sphere-Pac Pellet	$UO_{2.02}$ (20% ^{235}U) $UO_{2.00}$ (20% ^{235}U)	3 1	5	690	530	Being Examined
43-112	Sphere-Pac	$(^{238}U_{0.85},Pu_{0.15})O_{1.97}$ $UO_{2.02}$ (20% ^{235}U)	3 1	0.7	500	360	Examined
43-113	Sphere-Pac	$(^{238}U_{0.85},Pu_{0.15})O_{1.97}$ $UO_{2.02}$ (20% ^{235}U)	3 1	10[c]	500[c]	380[c]	In-reactor ≅ 8.5% FIMA
43-115	Sphere-Pac	$(^{238}U_{0.85},Pu_{0.15})O_{1.97}$ $UO_{2.02}$ (20% ^{235}U)	3 1	6.5	600	460	Being examined
43-116	Sphere-Pac	$(^{238}U_{0.85},Pu_{0.15})O_{1.97}$	4	1.5[c]	600[c]	460[c]	Being examined
43-117 43-118 43-119	Ref. FTR Pellets	$(^{238}U,Pu)O_{1.98}$	4	1.5[d]	600[c]	460[c]	In preparation

[a] FIMA is fissions per initial actinide metal atom.

[b] Pins failed in reactor from overpowering.

[c] These are target design values.

[d] This is an approximate level. Test will be irradiated for two ETR cycles to produce fuel for reprocessing studies.

Capsule 43-113, the only capsule currently under irradiation, was reinserted after interim neutron radiography for one ETR cycle at the same flux used to achieve the initial calculated burnup of 7.5% fissions per initial heavy metal atom (FIMA). The capsule was then moved to a new position with an unperturbed neutron flux measured to be 10% higher than that of its old position. This step in flux was designed to maintain the peak linear heat rate in the center two fuel pins at about 15 kw/ft for the remainder of the scheduled burnup to 10% FIMA.

During the past quarter we continued the metallographic examination of capsules 43-103 and 43-115. Only one fuel pin from capsule 43-115 has not yet been examined.

Capsule 43-103, which contained three Sphere-Pac UO_2 (20% ^{235}U) pins and one pellet pin of the same composition fuel, was irradiated in a slightly higher flux than was requested. This led to high peak linear heat rates as reported previously.[27] No fuel pins failed, and there were no significant changes in the diameter of the claddings; but the molten fuel in the center of the two centrally located pins penetrated the ThO_2 insulators between the fuel bed and the gas plenum. During subsequent reactor process cycling some fuel was expelled through this central hole into the plenum region. This is shown in Fig. 1.3. The increased cooling provided by the fuel pin end plug reduced this penetration for the lower ThO_2 insulators. This is shown in Fig. 1.4. This figure also shows additional features of interest. The photomacrograph clearly shows columnar grains in the center with the Sphere-Pac fuel retained at the interfaces with the cladding as reported previously.[28] The beta-gamma autoradiograph does not show the distinct line of fission products normally seen near a molten boundary. This confirms the temperature analysis of the restructured fuel, which indicates no melting after restructuring, even at a linear heat rate of 22 kw/ft. The alpha autoradiograph shows a uniform distribution of ^{235}U; the darker regions near the cladding resulted from reduced self-shielding in the lower density fuel. Comparison of the beta-gamma and the alpha autoradiographs with the photomacrograph shows that the ThO_2 densified beyond the depth of U diffusion. Although all of the standard metallographic

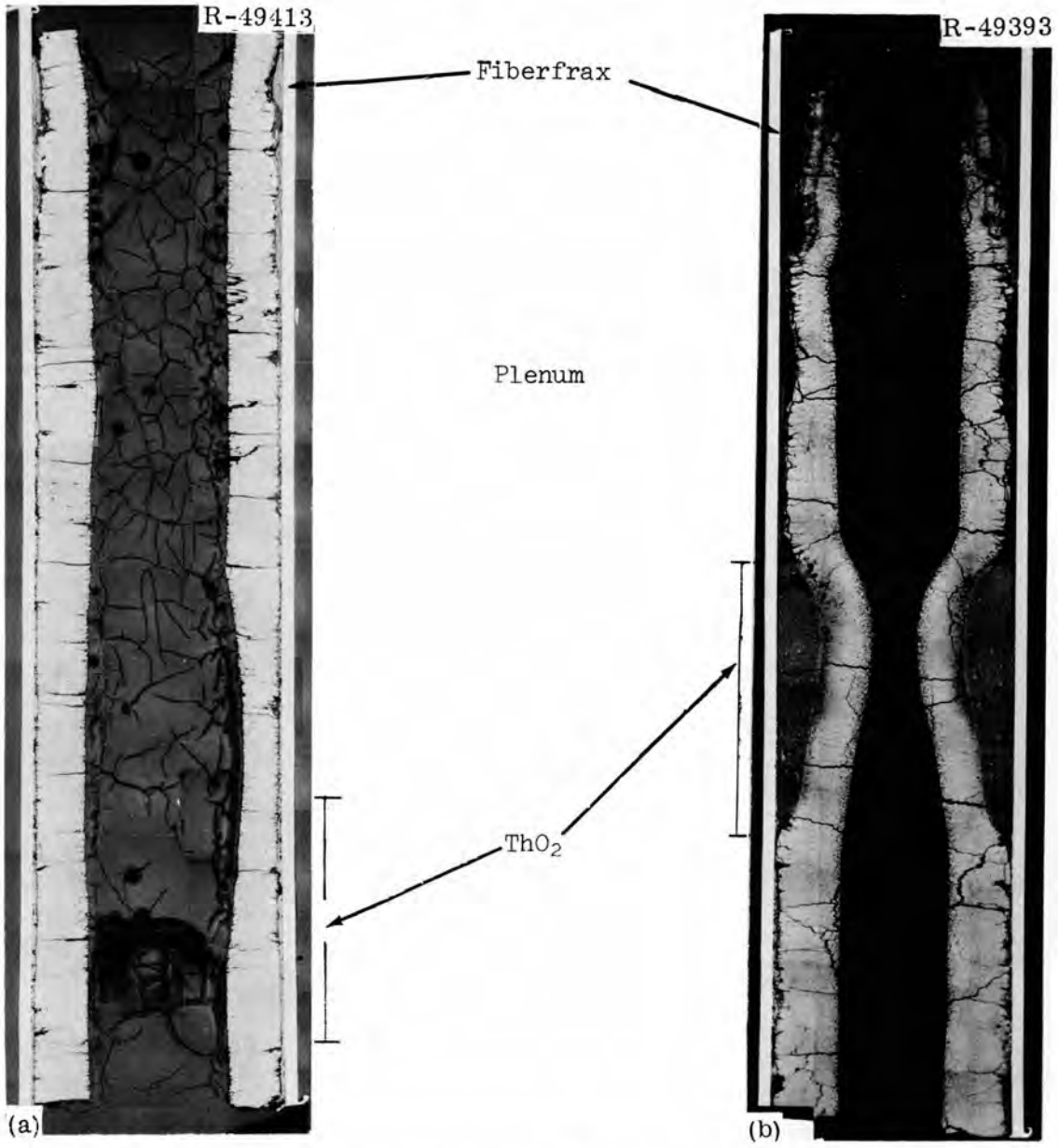

Fig. 1.3. Longitudinal Sections Through the Top Thoria Insulator in Urania Fuel Pins Showing Fuel Penetration into the Plenum Regions at Heat Rates in Excess of 20 kw/ft. (a) Pellet pin 43-103-2. (b) Sphere-Pac pin 43-103-3.

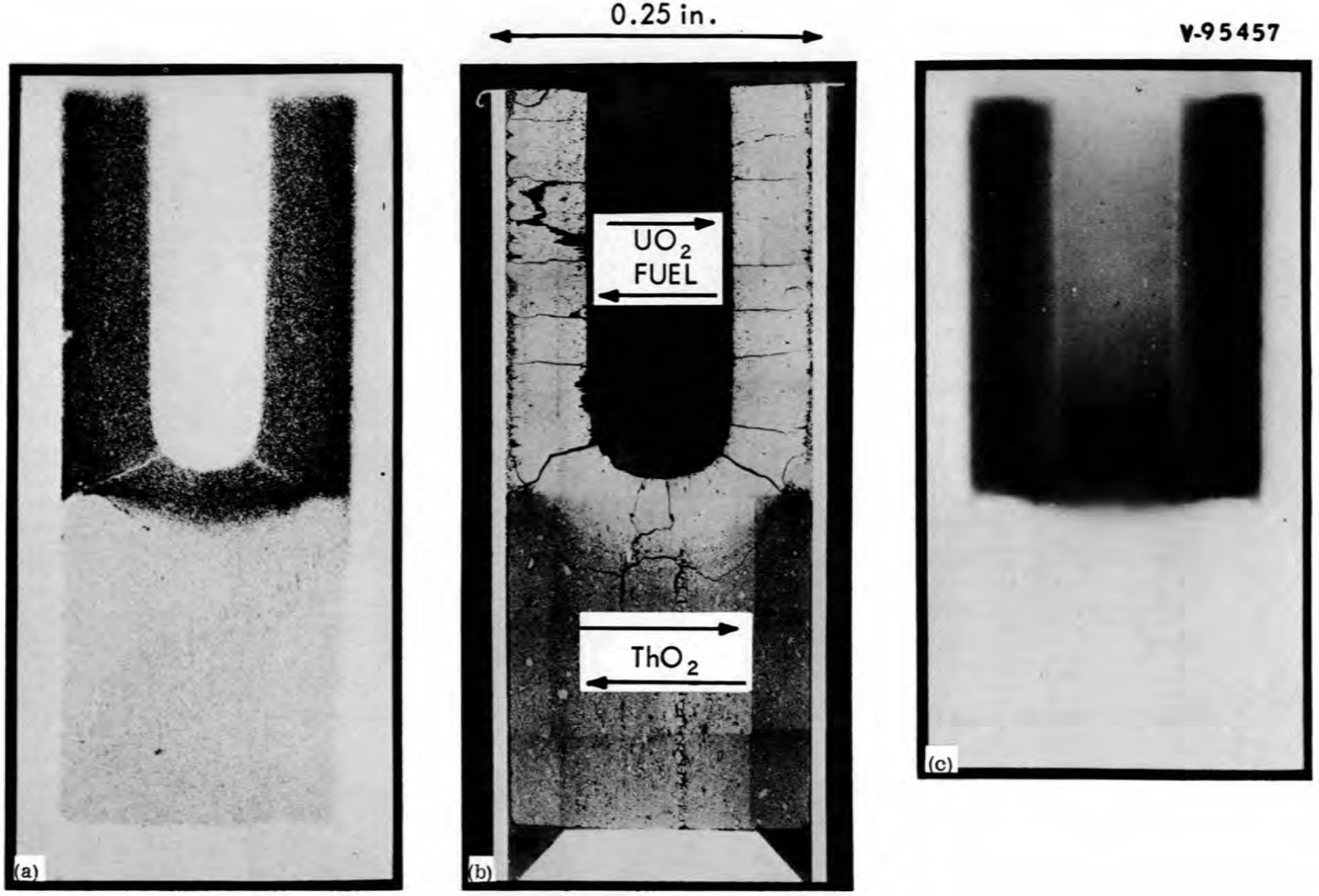

Fig. 1.4. Longitudinal Section Through the Bottom Thoria Insulator in Urania Fuel Pin 43-103-3. Peak linear rate was 22 kw/ft. (a) Alpha autoradiograph. (b) Photomacrograph. (c) Beta-gamma autoradiograph.

examinations of the 43-103 samples are complete, not all of the beta-gamma or alpha autoradiographs have been made, so analysis of the data is incomplete.

Examination of the fuel pins from experiment 43-115 is incomplete. Available data from burnup analyses indicate peak burnup levels between 5 and 6% FIMA for the two center pins. This indicates that the intended time-averaged linear heat rates of 18 to 19 kw/ft were achieved. Figure 1.5 is a transverse cross section of the top pin, 43-115-4, which contained $(U_{0.85},Pu_{0.15})O_{1.97}$ and operated at 14.5 kw/ft linear heat rate to 4.5% FIMA. The fuel restructuring is typical of oxide fuels; the original Sphere-Pac structure remains in the cooler regions. Agreement is excellent between the observed extent of restructuring, such as

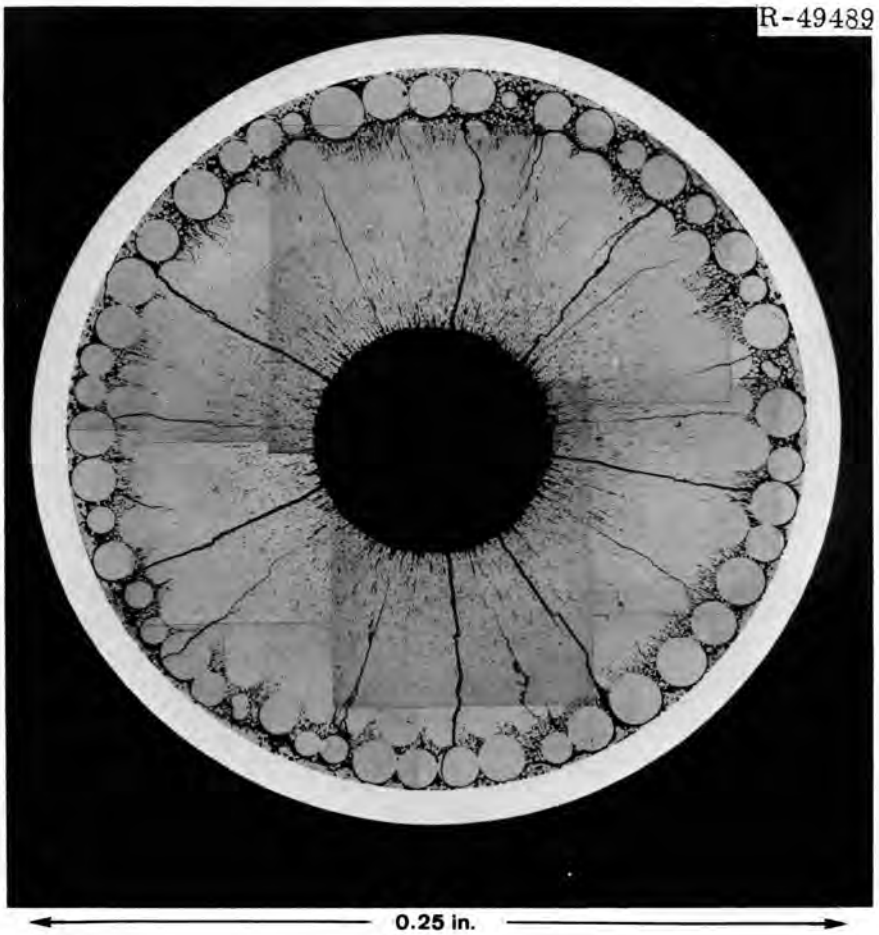

Fig. 1.5. Transverse Section of $(U_{0.85},Pu_{0.15})O_2$ Sphere-Pac Pin 43-115-4. Burnup 4.5% fissions per initial heavy metal atom at a time-averaged linear heat rate of 14 kw/ft.

columnar grain growth, with the predicted restructuring calculated by means of the PRØFIL code[29] with data for thermal conductivity derived from $(U,Pu)O_2$ pellets. This provides further indirect support for the conclusion[30] that the thermal conductance of Sphere-Pac beds in the reactor is comparable to that of pellets of similar density.

The four capsules, 43-116 through 43-119, are being irradiated to provide fuel that will contain fission products with short half-lives for processing studies. No detailed postirradiation examination of these fuel pins is planned. Experiment 43-116 has been processed, and the results are being evaluated. Fuel for capsules 43-117 through 43-119 has been ordered. These pins will use reference Fast Test Reactor fuel and cladding materials.

Instrumented Tests in Oak Ridge Research Reactor (R. B. Fitts, V. A. DeCarlo,[31] K. R. Thoms,[31] D. R. Cuneo[25])

The instrumented irradiations in the Oak Ridge Research Reactor (ORR) are designed to monitor the thermal performance of test fuel pins.[32] The temperatures of the cladding and the fuel center and the rates of heat generation in the fuel pins are continuously measured and recorded. These data are being used to evaluate the thermal characteristics of various fuels in the reactor and the effects of irradiation conditions upon the temperatures and rates of structural change within the operating fuels.

The first test in this series, SG-1, was used to check the design of the test capsule and obtain a preliminary indication of the thermal performance of sol-gel Sphere-Pac fuel. Both objectives were attained. The Sphere-Pac performed generally the same as would have been expected for pellet fuels.

The second test, SG-2, contained Sphere-Pac $(U_{0.80},Pu_{0.20})O_2$ fuel and was operated at gradually increasing rates of heat generation until a temperature of 1500°C was reached at the fuel center. At this temperature, the experiment was removed from the reactor for metallographic examination of the fuel structure. This examination will provide a characterization of the fuel structure at and below 1500°C for use as a temperature indicator in uninstrumented irradiation tests. Samples

for this purpose are awaiting examination. Detailed analysis of the data for operation in the reactor is proceeding.

The third capsule, SG-3, contains one fuel pin of $(U_{0.80},Pu_{0.20})O_2$ Sphere-Pac fuel that had a smear density of 82% of theoretical and a second fuel pin of sol-gel pellet fuel of the same composition and smear density. This experiment will provide a direct comparison of the thermal performance of Sphere-Pac and pellet fuels to central temperatures of about 2000°C and will reveal the relationship between the structure and temperature near 2000°C. This capsule was inserted into the ORR poolside facility on December 7, 1969, and has operated satisfactorily to a maximum central temperature of 1100°C as of December 24, 1969.

Instrumented Tests in Engineering Test Reactor (C. F. Sanders)

Two instrumented capsules are being constructed for irradiation in the ETR to investigate the swelling of Sphere-Pac fuels under conditions of high retention of fission gas. These capsules will operate at a peak linear heat rate of 15.5 kw/ft, which will give an inner cladding temperature of 550°C.

The fuel pins have been fabricated, and the capsule assembly will be completed during January 1970. The capsules will be inserted into the ETR at the beginning of cycle 108 (March 15, 1970).

Transient Tests (E. J. Manthos, D. R. Cuneo[25])

Six fuel pins containing unirradiated $(U_{0.80},Pu_{0.20})O_2$ produced by the sol-gel process were recently subjected to power transients at the Transient Reactor Test Facility (TREAT). No failures occurred even though two Sphere-Pac pins were subjected to a transient that probably melted 50 to 60% of the fuel in the peak power regions.

The tests, described earlier,[33] were conducted with two capsules, each containing three fuel pins in tandem. Each fuel pin had an 8-in.-long fuel column and was clad with 0.254-in.-OD × 0.016-in.-wall thickness type 304 stainless steel tubing. The principal fuel variables were smear density, (81 and 88% of theoretical) and fabrication form (pellets and Sphere-Pac vibratorily compacted spheres). The fuel columns

were partially restrained axially with a spring-loaded extensometer that was capable of measuring up to 3/16-in. increase in fuel length.

The first capsule, TR-1, was initially subjected to a calibration transient to verify the design techniques. The verification was based on an excellent agreement between calculated and measured temperatures in the Na annulus around the fuel pins. The maximum temperature calculated for the center of the fuel was about 1800°C during the calibration transient. The experiments were continued with test transients designed to melt about 25% of the 81% dense fuel in the peak power region of the first capsule and 50% for the second capsule, TR-2. The operating data for these transients are given in Table 1.15. Fabrication data and

Table 1.15. Operating Data for Experiments in Transient Reactor Test Facility

	Capsule		
	TR-1	TR-1	TR-2
TREAT transient	1293	1294	1295
Initial reactor period, Msec	630	204	200
Peak reactor power, Mw	29.8	202	202
Integrated reactor power, Mwsec	88	140	172

preliminary results are listed in Table 1.16 for the test transients. Pins A and B in each capsule operated at approximately equivalent powers; pin C had about 30% less power.

Neutron radiographs made at TREAT after the transient experiments are shown in Figs. 1.6 and 1.7. The radiographs showed no regions of low density within the fuel pellets, but did show that two of the pellet pins had fuel-column separations, apparently at pellet interfaces. Subtracting the measured separations from the total change in the length of the fuel columns indicates that some fuel restructuring and densification occurred in fuel pin TR-1A and also, perhaps, in pin TR-2C. We

Table 1.16. Fabrication Data and Preliminary Results for Fuel Pins for Capsules TR-1 and TR-2

	Fuel Pin					
	TR-1A	TR-1B	TR-1C	TR-2A	TR-2B	TR-2C
Fabrication Data						
Fabrication Form[a]	P	S	P	S	S	P
Ratio U:(U+Pu)	0.801	0.801	0.801	0.801	0.801	0.801
Ratio O:metal	1.983	1.980	1.991	1.980	1.980	1.990
Gas release, cm^3/g (STP) released at 1600°C	0.07	0.14	0.23	0.14	0.14	0.19
Fuel smear density, % of theoretical	0.88	0.82	0.79	0.82	0.81	0.80
Fuel length, in.	8.03	8.00	7.98	8.01	8.00	8.10
Gap between fuel and cladding, in.	0.005		0.005			0.005
Preliminary Results[b]						
Cladding deformation	none	none	none	none	none	none
Change in length of fuel column, in. (±0.020 in.)	+0.090	−0.020	−0.030	−0.060	−0.030	+0.040
Number of fuel-column separations	2	3	0	0	2	1
Total width of fuel-column separations, in. (±0.020 in.)	0.140	0.160−0.250			0.120	0.060
Maximum diameter of central void, in. (±0.020 in.)	0	0.100	0	0.120	0.100	0
Fuel pin failure?	no	no	no	no	no	no

[a] P = Solid pellets; S = Sphere-Pac.

[b] Estimated from neutron radiographs.

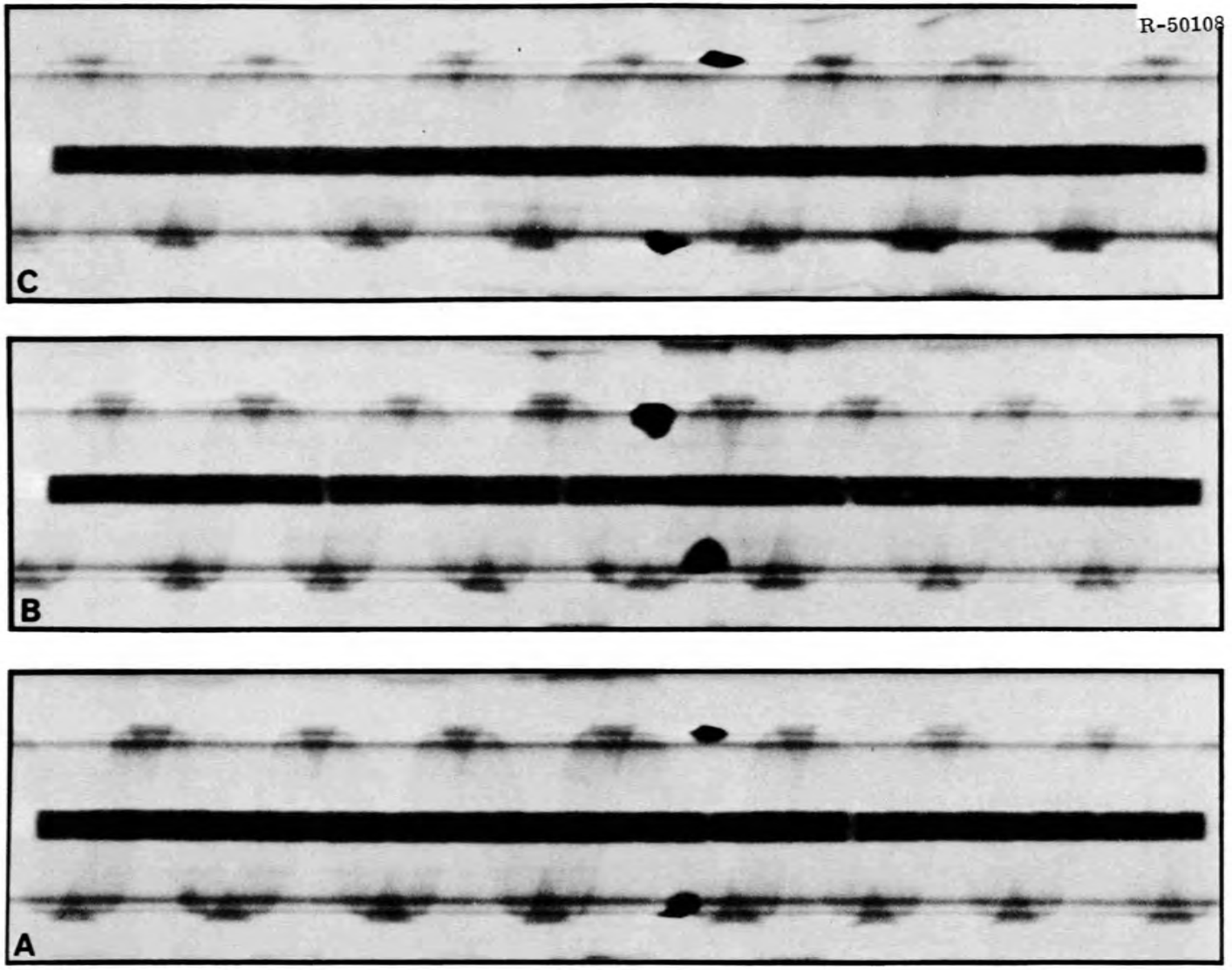

Fig. 1.6. Neutron Radiographs of Capsule TR-1 After Transient 1294.

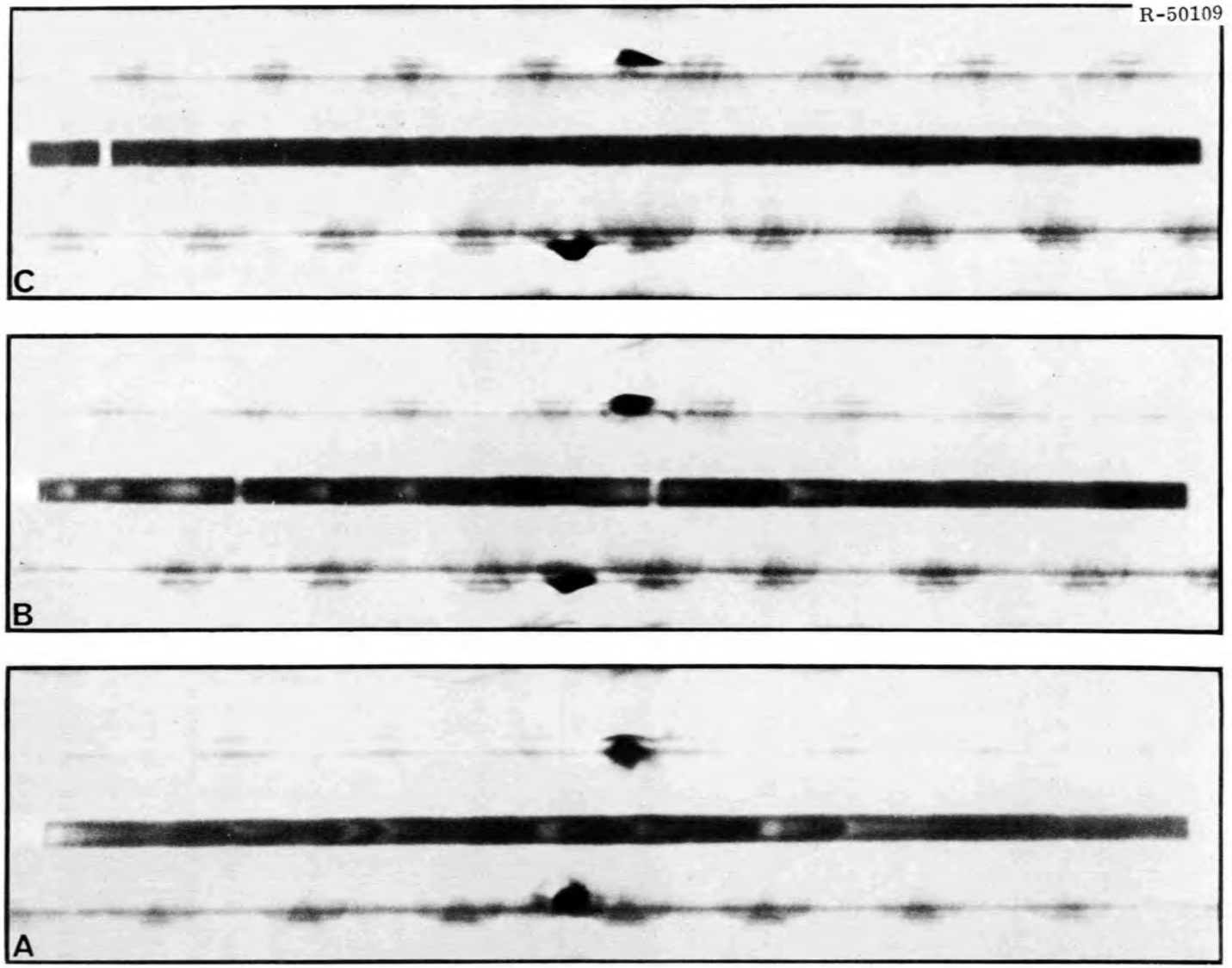

Fig. 1.7. Neutron Radiographs of Capsule TR-2 After Transient 1295.

observed regions of low density, which we interpret as voids, along the axis of Sphere-Pac pin TR-1B at the peak power end of the pin. The absence of voids in pellet pin TR-1A exposed to nearly the same neutron-flux distribution is probably due to the higher fuel density of this pellet pin. Sphere-Pac pins TR-2A and TR-2B were exposed to the most severe transient conditions and were similar in appearance; each contains a number of separated, conical voids. In addition, pin TR-2B had two band-type separations in the fuel column, each about 0.06 in. wide. All of the Sphere-Pac fuel columns apparently shortened due to fuel densification. There is no indication of failure or cladding deformation even though a preliminary analysis of data indicates that 50 to 60% of the fuel probably melted at the peak positions in pins TR-2A and TR-2B.

Postirradiation examinations of the fuel pins were started. These confirmed that none of the fuel pins failed. Gas samples, both from the regions between the inner capsules and their outer containments and from the regions above the Na coolant, showed no fission-product activities. Visual inspection, dimensioning, and gamma scanning are under way.

Fast-Flux Irradiation Tests (A. R. Olsen)

The series I encapsulated tests are continuing their irradiation in the EBR-II subassembly X050. At the time of the scheduled extended shutdown of the EBR-II following run 38, they had been exposed to about 6400 Mwd of EBR-II operation. This is equivalent to a calculated peak burnup of 3.4%.

Subassembly X050 is scheduled to be discharged from the EBR-II at the completion of run 39 in January 1970. At that time, two of the five series I capsules will be sent to ORNL. We obtained approval-in-principle this quarter to reinsert the remaining three capsules and continue their irradiation to a target burnup of 10% FIMA. Continued irradiation of these capsules will yield information on the effects of high burnup on Sphere-Pac fuels about 18 months sooner than the tests in series II, provided a suitable subassembly is available soon.

We obtained approval-in-principle for the series II unencapsulated tests from the AEC in November. The series II tests were described

previously.[34] A design for the fuel pin was developed and is being reviewed by personnel of the EBR-II project. This design involves a 40-in.-long fuel pin 0.250 in. in diameter with a 0.040-in. wire-wrap spacer. The design is compatible with the preliminary drawings for a J-37 (high cladding temperature) subassembly. In addition, we requested that personnel of the EBR-II project modify the design of the subassembly so that the same pin design could be incorporated into a less expensive standard H-37 subassembly or, if required at the higher burnup levels, an E-37 (high risk) subassembly. Details of the studies of fabrication are reported elsewhere in this report.[35]

Mechanism for Transport of Cladding Material into Fuel During Irradiation

J. M. Leitnaker R. B. Fitts
D. R. Cuneo[25] E. L. Long, Jr.
K. E. Spear

Cladding material components have been observed in fuel[31] during postirradiation examination of mixed oxide fuel pins. An example is shown in Fig. 1.8. Iodine transport in a manner similar to the van Arkel-de Boer process[32] has been suggested.[33]

We have already discussed in some detail the likelihood that a mechanism that involves I is not operable in most reactor situations.[34,35] A novel observation of the location of Cs in a white, crystalline deposit in irradiated fuel pins indicates to us that a Cs compound is a likely candidate for cladding transport.

This white, crystalline deposit formed on irradiated $(U,Pu)O_2$ fuel when unmounted sections cut from fuel pins were allowed to stand several days before mounting and polishing.

The fuel was annular pellets of $(U,Pu)O_2$ with 92% of theoretical density and 85% smear density and clad in either stainless steel or Hastelloy X and had been irradiated at 700°C (outside surface of cladding) and 15.5 kw/ft to 6 at. % burnup as a part of the irradiation tests of fuels for gas-cooled fast reactors jointly conducted by Oak Ridge National Laboratory and Gulf General Atomic.[36]

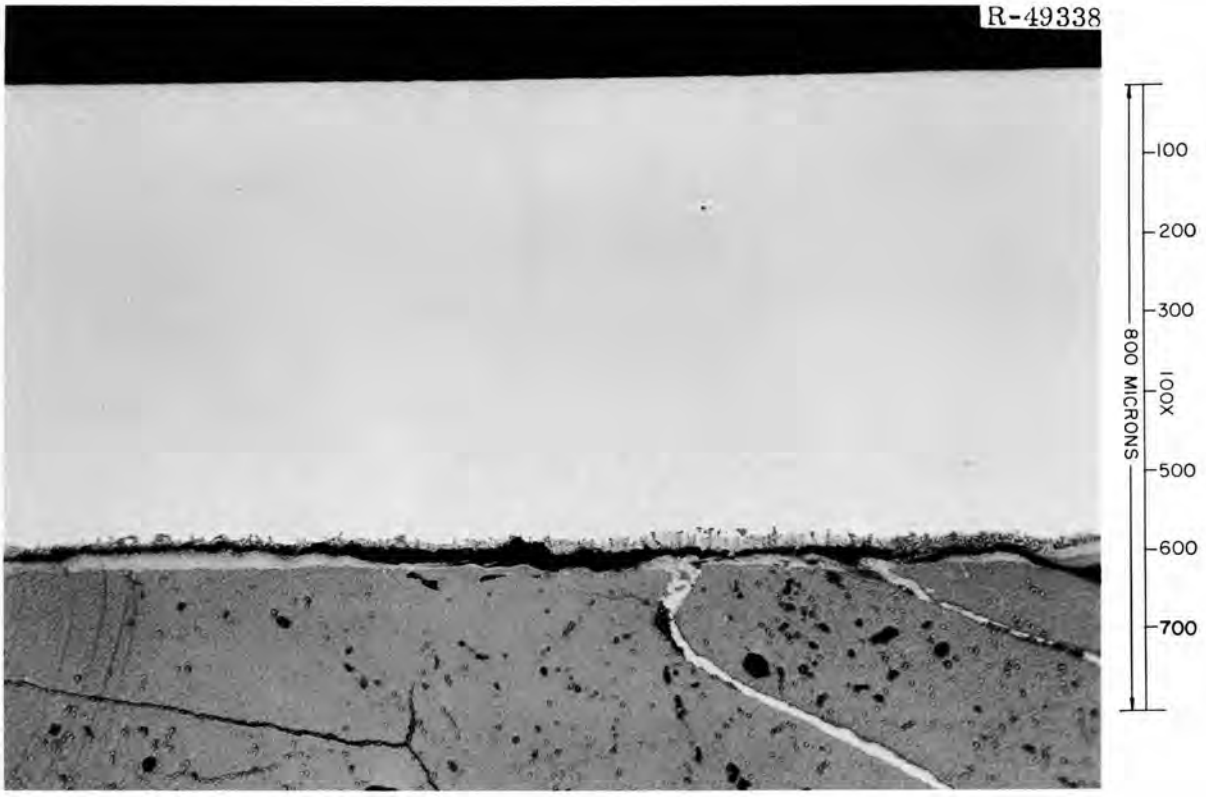

Fig. 1.8. Example of Cladding Material Extending into Fuel. Sample is from GA-17B. Note long river of metal extending into fuel.

Figure 1.9 shows the location of the deposit on one of the more heavily decorated sections. It is most prevalent in sections near the ends of the fuel column and is clearly heaviest in the gap between fuel and cladding.

The deposit had a high concentration of Cs and is tentatively identified as hydrated cesium carbonate. Gamma spectrum analysis of the white material reveals ^{134}Cs and ^{137}Cs activity only. The gamma scan revealed nothing but Cs at a confidence level of 95%. This tentative identification of the white material as hydrated cesium carbonate is consistent with the location, the gamma analysis, and the general behavior of alkali metals and their oxides. The heaviest concentrations of Cs have previously been observed in the colder portion of the fuel pin.

This identification is further supported by the formation of a similar material on an unirradiated sample of sodium uranate. This

Fig. 1.9. Hydrated Cesium Carbonate Growth on Section of Irradiated Fuel.

sample had been mounted, polished with water, and set aside for several weeks in the laboratory atmosphere. Figure 1.10 shows an enlargement of the crystal growth (note the two morphologies of the crystals). X-ray diffraction indicated primarily $Na_2CO_3 \cdot H_2O$ and traces of other phases that we tentatively identified as $Na_6U_7O_{24}$ and $Na_4UO_2(CO_3)_3$. Chemical analysis of the white material revealed about 3% U.

The observation of this Cs compound deposited on irradiated fuel is, as far as we know, unprecedented, either in this laboratory or elsewhere. The reason may be coincidence. Perhaps moisture and appreciable CO_2 in the atmosphere did not previously exist for a sufficient length of time between the cutting of the sample and its polishing. Prompt polishing after cutting could dissolve Cs or its compounds, depending on the polishing medium. Alternatively, washing and handling procedures

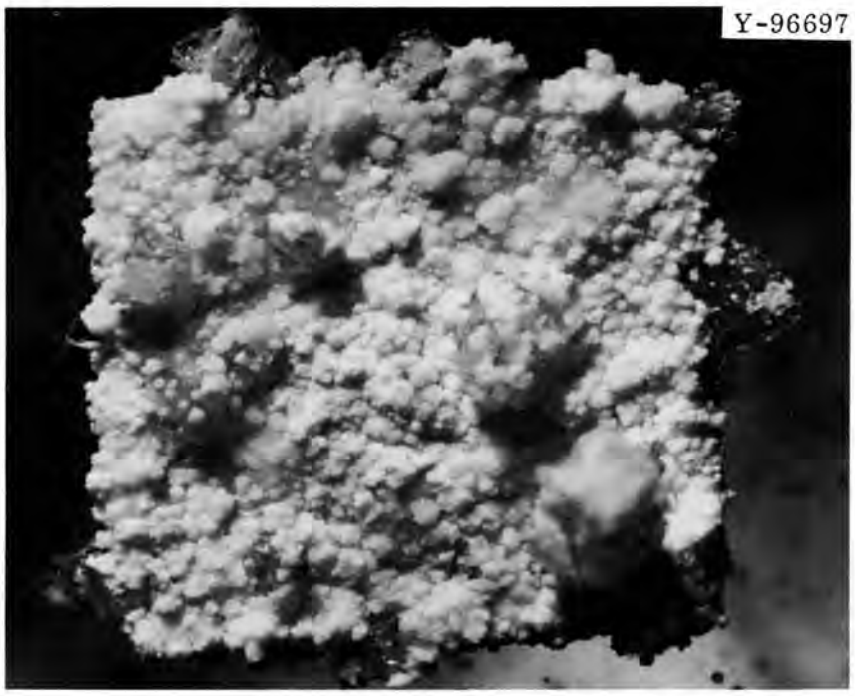

Fig. 1.10. Hydrated Sodium Carbonate on Unirradiated Sodium Uranate.

could be such that on a routine basis a sample would not be seen before such a buildup had been washed off.

These observations suggest a mechanism for the migration of cladding components. We hypothesize that components dissolved from the cold cladding could move via ferrates, nickelates, or chromates of Cs and be deposited on the hot fuel. The concentration of the deposit between the fuel and cladding and in some of the cracks argues for transport by a liquid medium (Cs-CsO, perhaps). These observations also suggest the possibility of an easy way to observe directly the location of alkali metals within a fuel element.

References

1. Chemical Technology Division.
2. W. H. Pechin and R. A. Bradley, "Control of Gas Release and Ratio of Oxygen to Metal," pp. 20–27, this report.
3. A. R. Olsen, "Fast-Flux Irradiation Tests," pp. 48–49, this report.
4. W. H. Pechin, Fuels and Materials Development Program Quart. Progr. Rept. Sept. 30, 1969, ORNL-4480, pp. 11–16.

5. W. H. Pechin, Fuels and Materials Development Program Quart. Progr. Rept. June 30, 1969, ORNL-4440, pp. 12–13.

6. Cooperative training student from Georgia Institute of Technology.

7. J. S. Anderson, I. F. Ferguson, and L.E.J. Roberts, J. Inorg. Nucl. Chem. 1, 340–341 (1955).

8. I. F. Ferguson and P.G.T. Fogg, J. Chem. Soc., 3679 (1957).

9. E. D. Lynch, "Oxidation and Phase Stability in Solid Solution Systems Containing Uranium Oxide," pp. 434–457 in Meeting on Characterization of Uranium Dioxide, Held at Oak Ridge National Laboratory, Oak Ridge, Tenn., December 12–13, 1961, TID-7637.

10. E. A. Aitken and R. A. Joseph, J. Phys. Chem. 70, 1090–1097 (1966).

11. These descriptions are extended abstracts of rough drafts of technical reports prepared by P. H. Spindler, a visiting scientist whose two-year assignment ends January 16, 1970.

12. P. H. Spindler, Fuels and Materials Development Program Quart. Progr. Rept. June 30, 1968, ORNL-4330, pp. 16–17.

13. D. L. McElroy, Fuels and Materials Development Program Quart. Progr. Rept. March 31, 1969, ORNL-4420, pp. 14–19.

14. P. H. Spindler and D. L. McElroy, Fuels and Materials Development Program Quart. Progr. Rept. June 30, 1969, ORNL-4440, p. 14.

15. P. H. Spindler, J. P. Moore, and R. S. Graves, Metals and Ceramics Div. Ann. Progr. Rept. October 1969, ORNL-4470, p. 32.

16. P. H. Spindler, Fuels and Materials Development Program Quart. Progr. Rept. Sept. 30, 1969, ORNL-4480, pp. 20–21.

17. S. Rosseland, Astrophisik Auf Atom-Theoretischer Grundlage, Springer, Berlin, Germany, 1931.

18. D. R. Flynn, "Thermal Conductivity of Ceramics," pp. 63–123 in Symposium on Mechanical and Thermal Properties of Ceramics, Gaithersburg, Maryland, April 1–2, 1968, Nat. Bur. Std. Spec. Publ. 303, ed. by J. P. Wachtman, Jr., National Bureau of Standards, Washington, D.C., 1969.

19. M. Czerny and L. Genzel, Glastechn. Ber. 25, 134 (1952).

20. P. H. Spindler, Calculation of Depth of Transmittance, in preparation.

21. J. L. Bates, Visible and Infrared Absorption Spectra of Uranium Dioxide, HW-79033 (September 1963).

22. J. A. Christensen, Thermal Conductivity of Nearly Stoichiometric UO_2-Temperature and Composition Effects, WCAP-2531 (1963).

23. J. T. Houghton and S. D. Smith, Infra-Red Physics, Oxford University Press, London, 1966.

24. P. C. Held and D. R. Wilder, J. Am. Ceram. Soc. 52(4), 182 (1969).

25. On loan from Reactor Chemistry Division.

26. A. R. Olsen, C. M. Cox, and R. B. Fitts, Trans. Am. Nucl. Soc. 12(2), 605–606 (November 1969).

27. A. R. Olsen, R. B. Fitts, and J. Komatsu, Fuels and Materials Development Program Quart. Progr. Rept. Sept. 30, 1968, ORNL-4350, pp. 22–25.

28. A. R. Olsen, R. B. Fitts, and D. R. Cuneo, Fuels and Materials Development Program Quart. Progr. Rept. June 30, 1969, ORNL-4440, pp. 23–26.

29. C. M. Cox and F. J. Homan, PRØFIL – A One Dimensional FØRTRAN IV Program for Computing Steady-State Temperature Distribution in Cylindrical Ceramic Fuels, ORNL-TM-2443 (March 1969) and ORNL-TM-2443 Addendum (August 1969).

30. R. B. Fitts, Fuels and Materials Development Program Quart. Progr. Rept. Dec. 30, 1968, ORNL-4390, pp. 25–27.

31. Reactor Division.

32. R. B. Fitts and V. A. DeCarlo, Fuels and Materials Development Program Quart. Progr. Rept. June 30, 1968, ORNL-4330, pp. 20–23.

33. C. M. Cox and R. E. Adams, Fuels and Materials Development Program Quart. Progr. Rept. March 31, 1969, ORNL-4420, pp. 30–31.

34. A. R. Olsen, Fuels and Materials Development Program Quart. Progr. Rept. Sept. 30, 1969, ORNL-4480, pp. 29–32.

35. R. B. Pratt and M. K. Preston, "Series II Unencapsulated Fuel Pins for Irradiation in the Experimental Breeder Reactor-II," pp. 17–20, this report.

36. R. B. Fitts, D. R. Cuneo, E. L. Long, Jr., and A. R. Olsen, "Post-irradiation Examination of Capsule 04," p. 8 in GCR Program Semiann. Progr. Rept. Sept. 30, 1969, in press.

2. DEVELOPMENT OF HIGH-PERFORMANCE LMFBR FUELS

P. Patriarca J. L. Scott

The goals of this program are to investigate the properties and behavior of those U- and Pu-based ceramic fuels that we term conductors — such as the mononitrides, carbonitrides, and monocarbides — and to compare their potential as liquid-metal fast breeder reactor (LMFBR) fuel with that of $(U,Pu)O_2$, which by comparison is an insulator. Since the thermal conductivity of the ceramic conductors is about ten times that of $(U,Pu)O_2$, it is theoretically possible to operate a conductor at ten times the power density with the same temperature at the center of the fuel. In practice, heat-transfer limitations, thermal stresses in the cladding, and high rates of swelling at high temperatures limit the power density that can be achieved with thermal conducting fuels to about two or three times that of $(U,Pu)O_2$ — still a challenging improvement. Additionally, the margins for transient overpower in the ceramic conductors are much higher than those for $(U,Pu)O_2$.

We seek to provide the information necessary for evaluating the true potential of nitrides, carbonitrides, and carbides in comparison to each other and to mixed oxides. We need to define the structures, composition, and quality control required to achieve 150,000 Mwd/metric ton at peak linear heat ratings of 30 to 50 kw/ft. We must also demonstrate the possibility of a low-cost fuel cycle for manufacturing fuel with the needed properties. And since austenitic stainless steel is a poor conductor of heat, we seek to establish the physical and thermodynamic criteria for the new cladding material that will probably be required to exploit the conducting fuels.

Our work is oriented primarily toward demonstrating the irradiation performance of (U,Pu)N at high burnups and high heat ratings. Therefore, much of our effort is devoted to fabricating and characterizing fuel for irradiation testing. The myriad preliminary tasks required to begin irradiation testing of new types of capsules in the Engineering Test Reactor (ETR) and Oak Ridge Research Reactor (ORR) comprise another large portion of our work. These tasks include physics analysis, design of

capsules, procurement of components, and development of a facility for capsule assembly. Somewhat less emphasis is placed on studies of thermodynamics and compatibility. We have reduced our emphasis on studies of V alloys because of their questionable compatibility with Na that contains more than 10 ppm O. Type 316 stainless steel will be used in near-term irradiation tests. Finally, some effort is being expended to develop economical methods of fabricating high-performance fuels. Since carbothermic reduction of oxide followed by nitriding appears attractive, we are generating basic kinetic data that will allow us to evaluate the process.

Synthesis, Fabrication, and Characterization of Nitride Fuels

V. J. Tennery

The purpose of this portion of our program is to develop methods for preparing (U,Pu)N powders of high purity, to characterize them, and to fabricate pellets of variable but controlled density for use in irradiation test capsules.

Synthesis and Fabrication of Mixed Nitrides (E. S. Bomar)

Fabrication by Hot Pressing. — We previously reported[1] difficulty in separating hot-pressed pellets from the Mo and W material used to line the graphite die. During this period we prepared and examined several metallographic samples of hot-pressed pellets. Figure 2.1 shows several features we observed, including the behavior of the refractory liner in contact with mixed nitride. A very fine grain size (ASTM 10) was retained under the hot-pressing conditions. The mixed nitride was quite plastic and extruded past the W end shim into the clearance between the graphite punch and the Mo liner of the graphite die. There was no evidence of reaction at the interface between the mixed nitride and the W shim. The Mo liner was grossly altered, however, especially at the surface in contact with the nitride powder; there were also changes in the microstructure of the nitride fuel at this interface. Therefore, Mo is of questionable value as a liner material due both to bonding problems

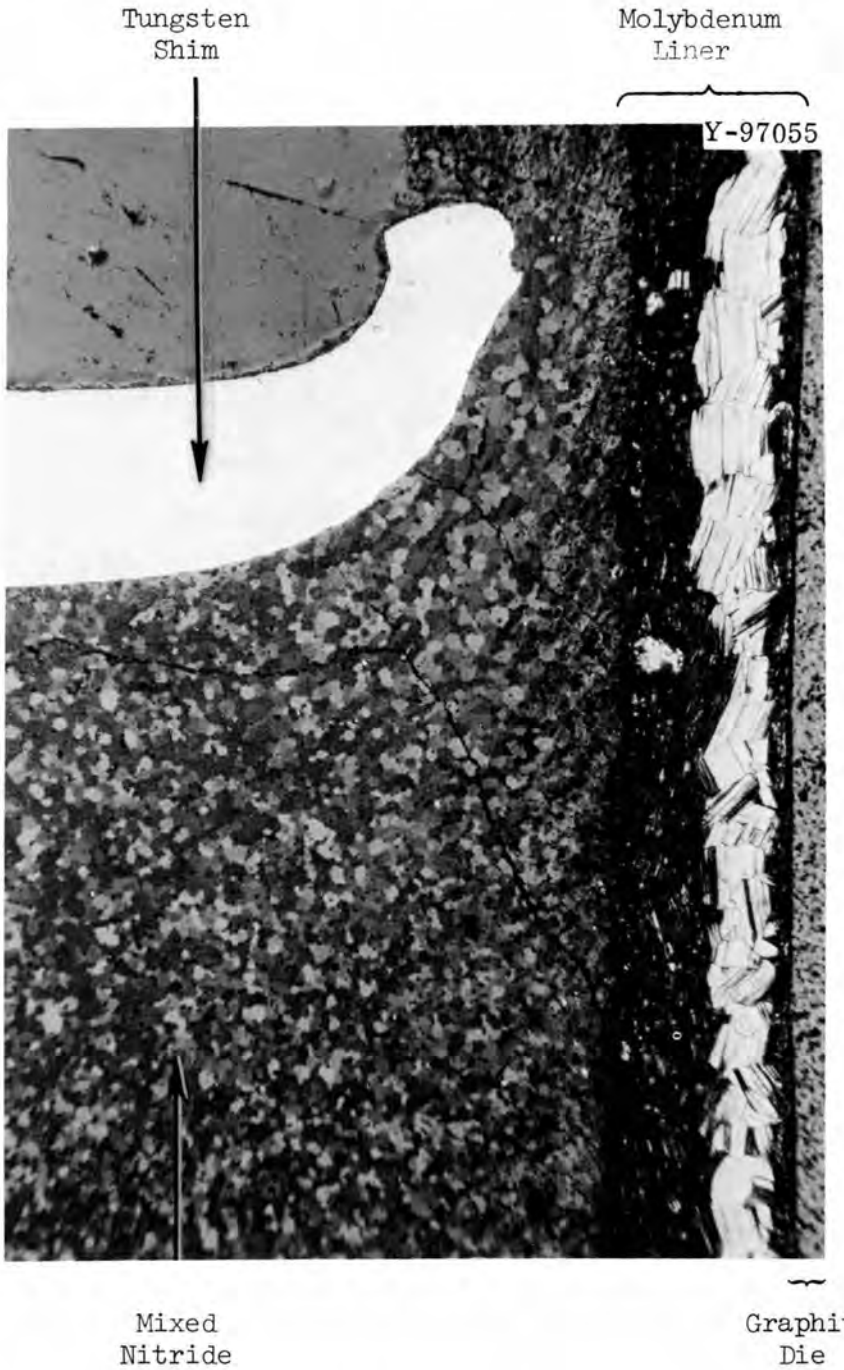

Fig. 2.1. Mechanical Mixture of −325 Mesh UN Plus 20% PuN Hot Pressed for 30 min at 6 tsi and 1650°C in an Atmosphere of Nitrogen and Argon. The grain size of the nitride fuel is ASTM 10. 200×. Etchant: 50 parts lactic acid, 40 parts nitric acid, and 2 parts hydrofluoric acid.

and reaction with the nitride. There was a shallower penetration of the Mo on the side in contact with the graphite die.

Fabrication by Sintering. — We are experimenting with mechanical mixtures of UN and PuN to determine if there are conditions under which pellets of acceptable density can be obtained. There is an advantage in using mechanical mixtures of UN and PuN powders to fabricate pellets of the mixed nitrides for an LMFBR since the major component, UN, can be fabricated without the complication of the presence of Pu. Experience at Battelle Memorial Institute in Columbus, Ohio, has shown,[2] however, that compacts that contain mechanical mixtures of fine UN and PuN sinter poorly and, further, that those that contain coarse powders actually swell instead of densifying during heat treatment at 1900°C.

Both the UN and PuN powders used in our work were prepared from metal by a hydride-dehydride process, followed by nitriding of the resulting powder with gaseous N_2. A quantity of the mixed nitride was also prepared from prealloyed metal.

A summary of the sintering behavior observed during our first experiments with both the mechanical mixtures and the prealloyed nitride is given in Table 2.1. Pellets cold pressed from a mixture of UN and PuN, as synthesized, densened only slightly to about 65% of theoretical density after they were sintered for 3 1/2 hr at 2100°C, and additional heating at 2100°C caused no further increase in density. The pellets lost 1 to 3% of their weight during the first 3 1/2 to 4 hr of sintering but less than 1% during a second 4 hr of heating.

Grinding[3] the mixture of UN and PuN for 10 min did not change the sintering behavior at 2100 or 2200°C nor did it reduce the loss of weight.

A holding period at 1700°C was added to the sintering cycle to determine if sufficient solid solution would occur between the UN and PuN to lower the Pu vapor pressure and thus reduce the loss of material by evaporation. This had no effect on the mixture ground for 10 min; however, grinding the PuN fraction for 30 min before mixing with the UN plus a hold at 1700°C eliminated loss of weight and yielded a product 75% of theoretical density during subsequent heating at 2100°C. Holding for 1 hr at 1700°C did not prevent loss of weight during sintering at 2200°C.

Table 2.1. Sintered Density and Weight Loss of $(U_{0.80},Pu_{0.20})N$ Pellets as a Function of Initial Powder Condition and Subsequent Heat Treatment

Sample	Initial Condition[a] of Powder	First Heat Treatment[b]				Second Heat Treatment			
		Temperature (°C)	Time (hr)	Weight Loss (%)	Density[c] (% theoretical)	Temperature (°C)	Time (hr)	Weight Loss (%)	Density[c] (% theoretical)
		Mechanical Mixtures of UN and PuN							
35	Mixture of −325 mesh UN and PuN blended by tumbling	2100	3.5	2.7	65	2100	4	0.7	66
43	Mixture of −325 mesh UN and PuN ground[d] for 10 min	2100	4	1.3	66	2100	4	0.3	70
51	Mixture of −325 mesh UN and PuN ground for 10 min	1700[e] 2100	2 3.5	2.9	66				
62	Mixture of −325 mesh UN and PuN ground for 10 min	1700 2200	1 4	4.0	67				
55	PuN fraction ground for 30 min, mixed with as-synthesized UN (−325 mesh)	1700 2100	2 3.5	0.0	72	1700 2200	1 4	2.3	73
65	PuN fraction ground for 30 min, mixed with as-synthesized UN (−325 mesh)	1700 2200	1 4	3.5	63				
53	Made from powder prepared by crushing sample 42 (same as 35) and grinding for 5 min	1700 2100	2 3.5	0.4	84	2200	4	0.7	87[f]
54	UN (−325 mesh) as synthesized with no PuN additive	1700 2100	2 3.5	0.0	87	2200	4	0.1	90
		(U,Pu)N Prepared from Prealloyed U and Pu							
57	(U,Pu)N as synthesized	2100	4	0.0	81	2200	4	1.0	82[g]
59	(U,Pu)N ground for 15 min	2200	4	0.0	91	2200	4	0.0	90
72–75	(U,Pu)N ground for 30 min	2200	4.5	0.1–3.0	84–80				

[a] Each powder was pressed in a 1/4-in.-diam die at 40 tsi before sintering. The die was lubricated with stearic acid.

[b] Each sample was heated to 1400°C under vacuum. At this temperature, the furnace was backfilled with N_2 to a pressure of 24 in. of Hg absolute. The sequence was reversed for cooling.

[c] Density was determined from micrometer measurement and weights. This was supplemented by point count of the metallographic microstructure of two samples as noted.

[d] A "Shatter Box," Model 8500, Spex Industries, Inc., was used for grinding all samples in table.

[e] A holding period at 1700°C was added to determine the effect of partial formation of solid solution on subsequent treatment at a higher temperature.

[f] A void volume of 10% was indicated by point count.

[g] A void volume of 18% was indicated by point count.

The most striking results were obtained by recycling mixed nitride powder previously pressed and sintered. A sintered pellet was crushed, ground for 5 min, pressed again, and sintered for 3 1/2 hr at 2100°C. The product was 84% of theoretical density. When the pellet was reheated to 2200°C, its measured density was 87% of theoretical. Figure 2.2 shows the microstructure of this pellet. A point count gave a void content of 10%. There was no evidence of second-phase material in the microstructures after either polishing or etching; the results of characterization of this material by x-ray diffraction are given elsewhere in this report.[4] The grain size of the product was ASTM 8.

Pellets of (U,Pu)N prepared from prealloyed U and Pu metals and given no further treatment after synthesis were sintered without weight loss for 4 hr at 2100°C to a measured density of 81% of theoretical. The density of the pellet was not increased by additional heating for 4 hr at 2200°C. Figure 2.3 shows the comparative microstructures for polished and etched surfaces. Point count gave a void volume of 18%. Again, no evidence of second-phase material was found in either microstructure, and the grain size was ASTM 8.

Grinding the (U,Pu)N powder for 15 or 30 min before pressing and sintering produced an unexpected behavior. Powder ground for 15 min was sintered at 2200°C to a measured density of 91% of theoretical while a series of pellets made from powder ground for 30 min was sintered to an average density of 82% of theoretical.

Metallographic examination of the 91% dense material disclosed a metallic phase at the grain boundaries of the interior of the pellet and a metal-free band of nitride near the surface of the pellet as is shown in Fig. 2.4. Fine grains (ASTM 9) formed a skin over the pellet surface with a wider and denser band of coarse grains (about ASTM 7) beneath. Neither of these layers contained free metal. If we assume the presence of free metal in the starting (U,Pu)N powder to be due to incomplete conversion of the U and Pu to the nitride, the structure can be explained as follows. Metal was lost rapidly from the surface layer before substantial sintering and grain growth took place, leaving a fine grain structure. The free metal aided sintering in both the layer under the surface and in the interior of the pellet. This enhanced sintering

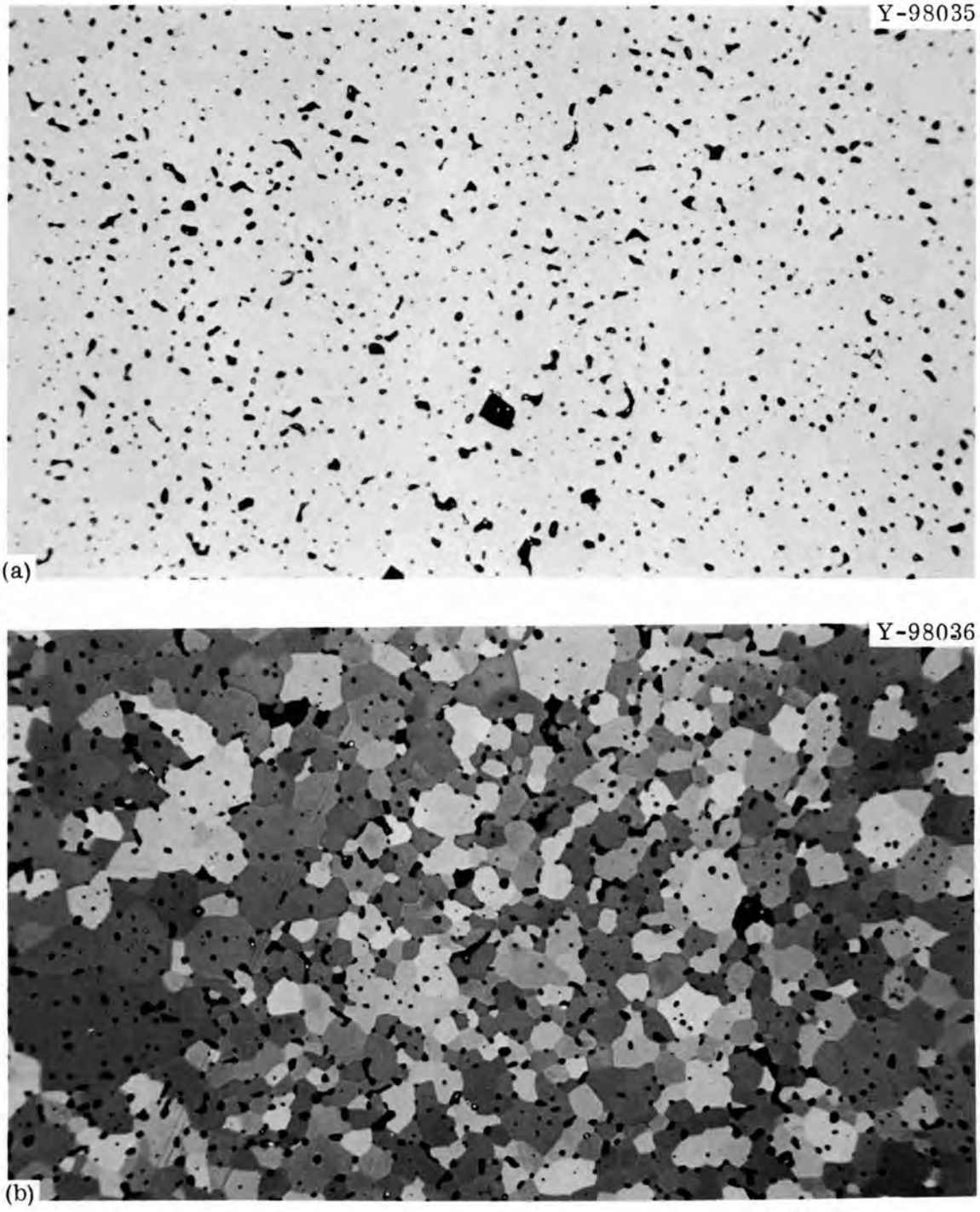

Fig. 2.2. Polished Microstructure of $(U_{0.80},Pu_{0.20})N$ Pellet Formed From Powder Made by Crushing and Grinding Previously Sintered Mixture of UN and PuN. Pellet sintered at 1700°C for 2 hr plus 3 1/2 hr at 2100°C. 200×. (a) Unetched point count gave a void content of 10%. (b) Etched with 50 parts lactic acid, 40 parts nitric acid, and 2 parts hydrofluoric acid. Grain size is ASTM 8.

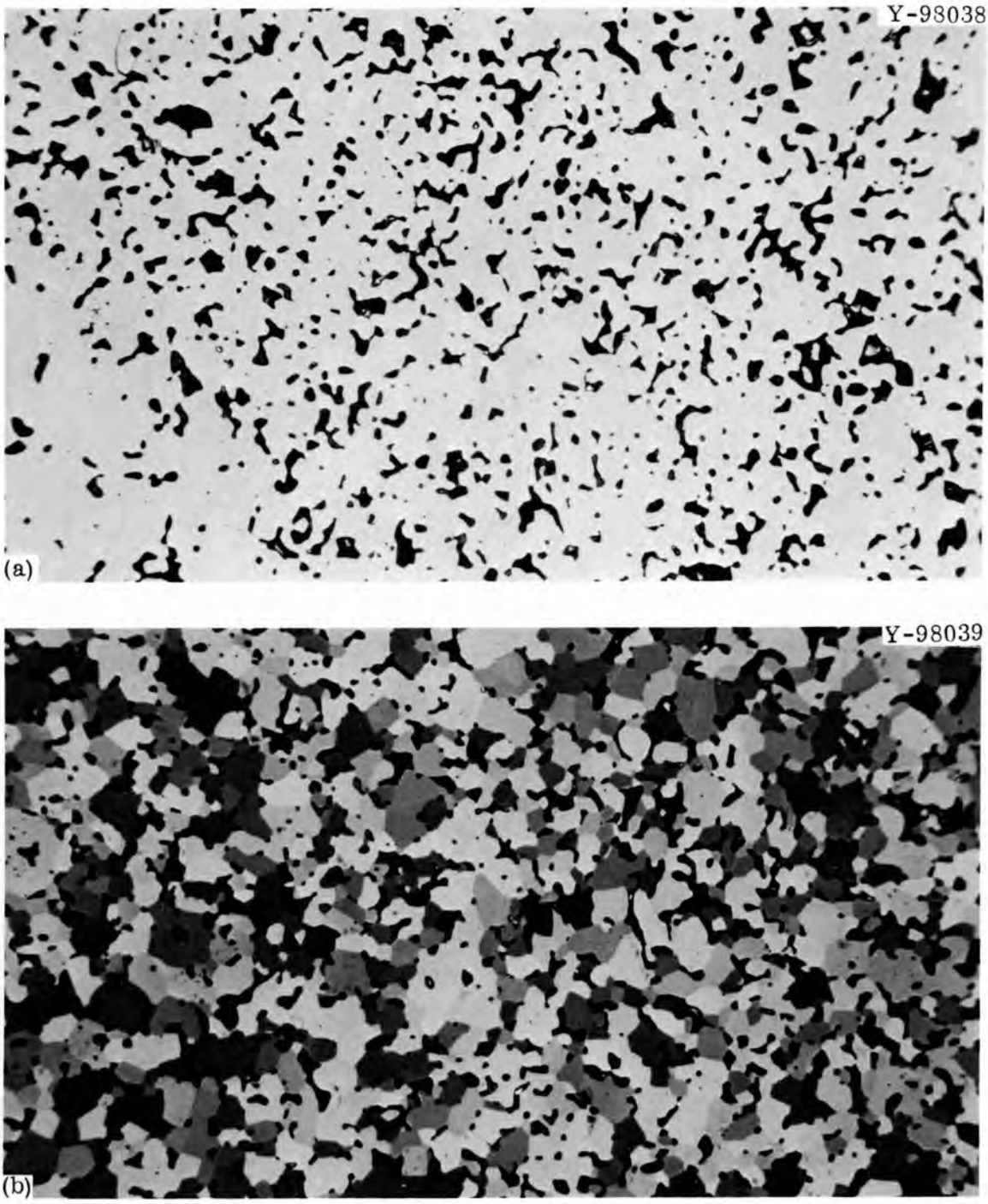

Fig. 2.3. Polished Microstructure of $(U_{0.80},Pu_{0.20})N$ Pellet Formed From Powder Made From Prealloyed Uranium and Plutonium Metals. Pellet sintered at 2100°C for 4 hr. 200×. (a) Unetched point count gave a void content of 18%. (b) Etched with 50 parts lactic acid, 40 parts nitric acid, and 2 parts hydrofluoric acid. Grain size is ASTM 8.

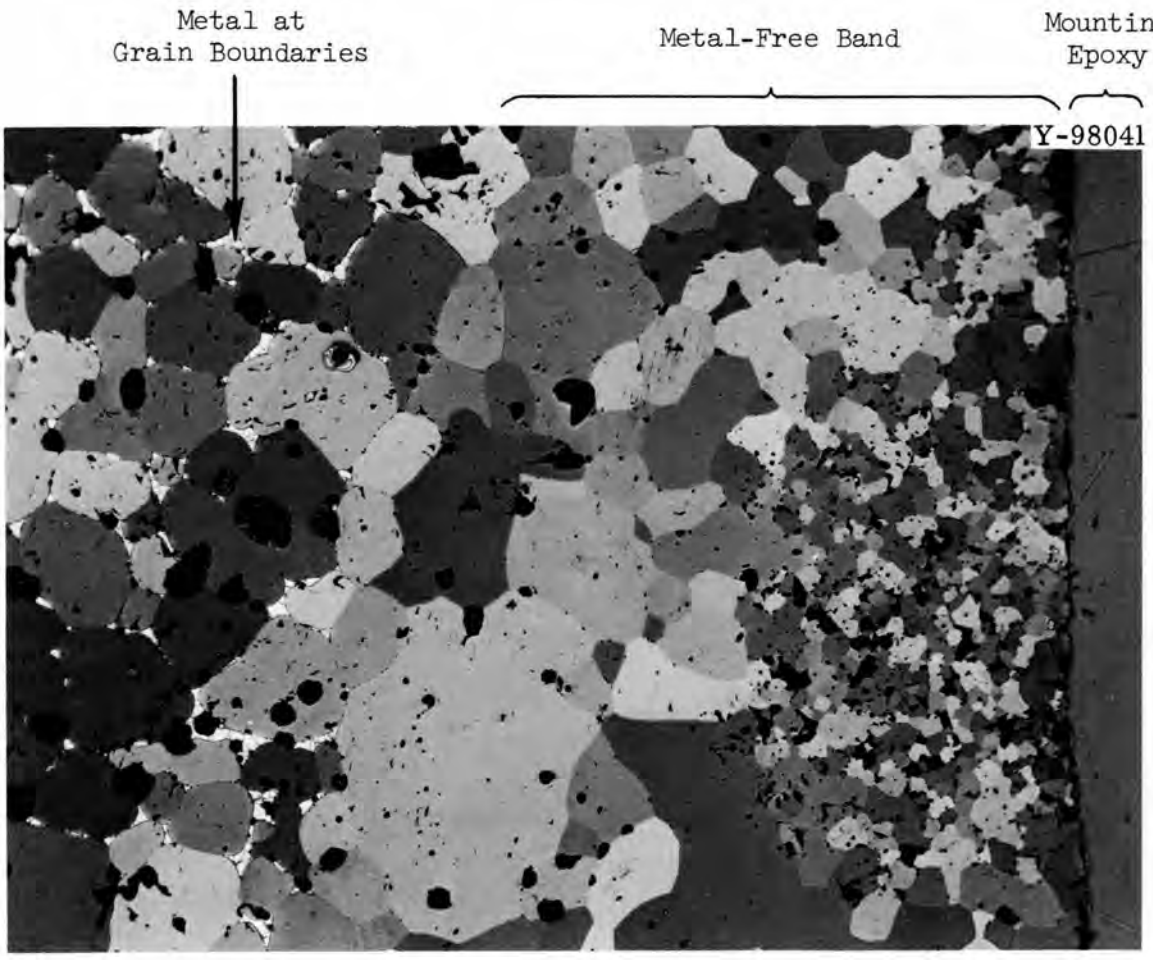

Fig. 2.4. Etched Microstructure of Cross Section of $(U_{0.80},Pu_{0.20})N$ Pellet Made From the Same Powder Used for Pellet Shown in Fig. 2.3. Powder for this pellet was ground for 15 min before sintering at 2200°C for 4 hr. White intergranular phase is thought to be metal. 100×. Etchant: 50 parts lactic acid, 40 parts nitric acid, and 2 parts hydrofluoric acid.

coarsened the grain structure, but as time passed N_2, diffused from the furnace atmosphere, gradually converted all the free metal to nitride in a band beneath the surface of the pellet. The loss of metal by evaporation would have to be balanced by the addition of N_2, since there was no change in weight during sintering. An unresolved anomaly remains with regard to free metal, however, since the pellets pictured in Figs. 2.3 and 2.4 were prepared from the same (U,Pu)N powder and, further, since both pellets were in the furnace at the same time during heating at 2200°C.

We have not yet seen the metallographic structure of the pellets made from powder ground for 30 min, but we infer from the experimental

results that the beneficial effect of grinding is offset at longer grinding times by a negative contribution, possibly the pickup of impurities from the grinding mill.

To date, the results of experimental work in which a number of variables were systematically changed show that an identical mixed nitride product can be made from either mechanical mixtures of UN and PuN or prealloyed Pu and U metal. The x-ray data given in the next section show that identical lattice spacings were obtained for (U,Pu)N prepared by either method. It is clear that preparation of metal-free (U,Pu)N powders from prealloyed metal is more difficult than preparation of either pure PuN or UN from their respective metals.

Characterization of Nitride Fuels (V. J. Tennery)

X-Ray Diffraction Studies of Uranium-Plutonium Nitrides. — A study is under way of the x-ray lattice parameter of $(U_{0.80},Pu_{0.20})N$ and PuN as a function of the state of the starting material and the thermal history of the specimens. The x-ray facility can now handle samples containing Pu, and the quality of the atmospheres in the glove boxes in this suite is sufficient to allow the handling of finely powdered Debye-Scherrer samples without measurable oxidation during the preparation procedures. The Ar atmospheres in the glove boxes typically contain 2 to 3 ppm O and 2 to 5 ppm moisture.

The PuN was synthesized by first reacting the Pu with H_2 at room temperature. The reaction was usually rapid enough not to require subsequent heating to complete the hydriding reaction. The plutonium hydride was then slowly heated in H_2 to 500°C to determine if additional reaction with H_2 was occurring. Rarely was any reaction observed in this temperature range. The plutonium hydride was decomposed at about 500°C and N_2 (as a N_2–1% H_2 mixture) was introduced slowly to the powdered Pu metal. The reaction with N_2 was initially quite rapid at a given temperature, and then the rate of reaction decreased. An increase in the temperature led to another period of rapid reaction that subsequently slowed down. This procedure was continued until a temperature of 800 to 900°C and a N_2 pressure of −15 in. Hg was achieved. The material was held under

these conditions until no further reaction with N_2 was measurable. The material was then cooled to room temperature.

Debye-Scherrer x-ray patterns of the powders produced by this process were made and analyzed. The precision lattice parameter was determined by means of a precision parameter extrapolation program of Vogel and Kempter[5] as modified by J. M. Leitnaker.[6] The lattice parameter a_o = 4.9101 ± 0.002 A for PuN agrees reasonably well with the values of this parameter cataloged previously by Spear and Leitnaker[7] but is slightly higher than the values given for "pure" PuN. This is probably due to self-damage in the PuN due to the fissioning of the Pu. These effects are being studied in detail. Only the diffraction lines of PuN were observed. The PuN powder contained about 1600 ppm O as determined by inert-gas fusion. X-ray patterns of various specimens of $(U_{0.80},Pu_{0.20})N$ were made and are being analyzed. The x-ray patterns of mechanical mixtures of UN and PuN powders that were heat treated indicate that homogeneous solid solution can be achieved in these mixtures without the necessity of heating to temperatures high enough to volatize significant quantities of Pu. The lattice parameter of a specimen consisting of a mechanical mixture of UN and PuN was heated in vacuum first to 1400°C and then to 2000°C in 1 atm N_2 and held 6 hr. The specimen did not lose significant weight, and the lattice parameter was found to be 4.8906 ± 0.0005 A. The back-reflection lines of this specimen were very sharp. This value is somewhat below the Vegard law relationship behavior discussed by Anselin.[8]

The precision lattice parameter of specimen 53, shown in Fig. 2.2, was measured to be 4.89049 ± 0.0002 A, which is essentially the same as that found for the mechanically mixed (U,Pu)N specimen discussed previously. We made (U,Pu)N powder from an alloy of molar composition U–20% Pu and determined the phase composition and lattice parameter of the synthesized powder and the lattice parameter of a pellet fabricated and sintered from this powder. The lattice parameter of the powder synthesized from the alloy was 4.89158 ± 0.00028 A; the lattice parameter of the sintered powder was 4.89040 ± 0.00035 A. Thus the (U,Pu)N sintered from the powder derived from the alloy had a lattice parameter identical

to that observed in the two specimens derived from the mechanical mixtures of UN and PuN powders. The powder derived from the alloy was well crystallized, and the α_2 lines were resolved at Bragg angles as low as about 90°. No phases other than the mononitride were indicated by the diffraction lines. Later fabrication work on this powder showed that it contained a small amount of free metal. It should be noted that these x-ray diffraction techniques are perhaps not sensitive to free metal in nitride powders derived from the hydride-nitride process. We suspect that the free metal exists as a kernel in some of the nitride particles derived from the alloy and are thus screened from the x rays due to the high absorption coefficients of U and Pu for CuKα x-radiation. We are now correlating these results with the processing variables involved in synthesizing the powders from the alloy. We are also trying to establish an explanation of the apparent reduction of the lattice parameter of (U,Pu)N powder derived from alloys when it is sintered at high temperatures.

We are now trying to determine if the phase separation of UN_x-PuN, reported by Anselin[8] to occur during nitriding of U-Pu alloys, occurs in our material. We are also determining the experimental conditions required for obtaining homogeneous solid solutions of $(U_{0.80},Pu_{0.20})N$ from mechanical mixtures of very fine powders of UN and PuN.

Synthesis, Fabrication, and Thermodynamic Properties of Carbonitride Fuels

J. M. Leitnaker

Manufacture of (U,Pu)(C,N) From $(U,Pu)O_2$ (T. B. Lindemer)

The processes we developed for converting UO_2 to UCN are now being applied to Pu-bearing fuels. The conversion equipment to be used for this work is a fluidized bed furnace that is also being used to apply C coatings to PuO_2 microspheres. Three runs on this equipment were made with UO_2-C sol-gel shards to determine the operating characteristics of the system. We found that the product of these runs had an ultimate content of 1.2 to 1.7 wt % O_2, and a total C content that decreased with

time of conversion. We know from previous work by Leitnaker, Notz, and Beatty[9] on this process that the O content should be a few hundred parts per million. These results strongly indicated that the fluidizing gas was contaminated with O_2 and that the original plumbing on the system was suspect. We have, therefore, replaced the original plastic gas lines with stainless steel tubing and have also installed a gettering system to remove O_2 and water from the Ar and N_2. Several items of auxiliary equipment were designed and built for O_2-free containment and transfer of the oxide-carbon feed and of the carbonitride product. An O_2 meter is also being installed to monitor the O_2 potential in the system. This instrument is capable of indicating O_2 pressures from 0.2 to 10^{-38} atm O_2.

A second box is being converted for use in preparing shards, since this work will require several small batches of sol-gel material that have widely varying ratios of metal:C and, eventually, of U:Pu. The external utilities to this box were installed, but a few minor items must still be installed inside the box. A dryer was designed and built to dry the material and to adjust the ratio of O:metal of the oxide.

Work in the immediate future will be concerned primarily with completion of modifications and construction of equipment. Considerable precautions will be taken to validate the capability of all the equipment to maintain an environment that has a low O potential. This is essential to control the ratio of C:N and the O content of the product.

Sufficient amounts of sol-gel $(U,Pu)O_2$-C material were obtained to begin the conversion studies when the equipment is ready.

Compatibility of Mixed-Nitride and Carbonitride Fuels with LMFBR Cladding Alloys

J. M. Leitnaker

Our approach to compatibility in high-performance fuel systems is to characterize interactions that can occur between the fuel and cladding material. A basic understanding of these reactions may point to methods for tailoring the fuel so that the reactions cannot occur and perhaps to methods for hindering these reaction kinetics.

Research this quarter on the U-V-N phase behavior was performed to obtain a basic understanding of the chemical and thermodynamic properties of interactions of V alloys with nitride fuels. Tailoring nitride fuels with additions of V or V_2N is also discussed. Work was begun on the U-Pu-Cr-N system in order to evaluate and understand potential problems that may occur with nitride fuels clad with stainless steel.

Ternary U-V-N System (K. E. Spear)

The possible use of V alloys with nitride reactor fuels has generated interest in the phase behavior of the U-V-N system. In addition to compatibility interests, V or its nitride, V_2N, can be added to nitride fuels in order to maintain low N_2 pressures in the system. The phase behavior reported here is also important for understanding this buffering action.

Last quarter we presented some of the conclusions that resulted from preliminary experimental results and discussed the effects of O contamination on the samples.[10] We previously reported the discovery and crystallographic properties of UVN_2 (ref. 11). Here, we give more of the experimental details, list the experimental data, and show the ternary phase diagram deduced from these data.

Ternary samples containing U, V, and N were heated under constant pressure and temperature for varying times and then cooled to below red heat in 3 to 5 min. Temperatures of 1400 to 2000°C and N_2 pressures of 50 to 600 torr were used. X-ray diffraction patterns of powder samples were used to identify the phases present in the ternary samples.

Samples were heated in vacuum in a W crucible by an induction furnace equipped with an eddy-current concentrator. This system can be used for pressures to about 600 torr. We purified the N_2 gas we used by passing it over Nb–1% Zr chips at 800°C and measured pressures with a Hg manometer. We measured temperatures with a calibrated optical pyrometer.

Three different types of starting materials were used, but all samples were −325 mesh (less than 44 μm in diameter) powders compacted into 1/4-in.-diam pellets before heating. The most commonly used samples were mixtures of UN and VN, a few were mixtures of UN and V, and some

were a nitrided U-V alloy. The molar ratio of U:V for each sample was determined from the masses of the U and V in the starting materials.

Two ternary samples (5 and 63) were analyzed spectrographically. Sample 5 contained 2000 ppm Fe, which was probably introduced during the grinding of the sample in a hardened steel mortar. The sum of the rest of the impurities in this sample was less than 650 ppm, and the sum of all the metallic impurities in sample 63 was less than 700 ppm.

The data and results for the ternary U-V-N samples are given in Table 2.2 in order of increasing ratio of U:V, and the phase diagram deduced from these results is shown in Fig. 2.5. This phase diagram is a projection of the results obtained over the temperature and pressure ranges studied rather than being the usual ternary diagram for constant temperature and pressure. However, we did not obtain any results that indicated a change in the positions of the tie lines with temperature. The UVN_2 phase appears to be stable at least between 1400 and 1800°C.

Diffraction patterns for almost all samples showed UO_2. Except for some interactions with U_2N_3, which we have discussed elsewhere,[12] we do not believe the oxide had any significant effect on the U-V-N phase results. The number of phases observed indicate that we did not achieve equilibrium in most of our samples. For an experiment performed under constant temperature and pressure on a three-component system, three phases can normally exist in equilibrium. Since the N_2 gas accounts for one phase, two solid phases would normally be observed in an equilibrium condition. However, even though many samples contained three solid nitride phases, changes in the phases present and in the intensities of the x-ray diffraction patterns of the phases with successive heatings of the same sample indicated which tie lines had to exist.

Tailoring Nitride Fuels with Vanadium or V_2N (K. E. Spear)

The presence of V metal or V_2N in nitride nuclear fuels creates a buffer or sink that minimizes the N_2 overpressure that may occur during reactor operating conditions. Vanadium compounds appear to be ideal for tailoring nuclear fuels because of the small atomic dimensions and small neutron-absorption cross section of the metal. The need for a tailored

Table 2.2. History and Results of X-Ray Diffraction for Ternary U-V-N Samples

Sample	Starting Material[a]	Molar Ratio U:V	Annealing Conditions			X-Ray Diffraction Pattern[b]					
			Temperature (°C)	N_2 Pressure (torr)	Time (hr)	V_2N	VN	UVN_2	UN	U_2N_3	UO_2
1	A	0.126	1450	590	16		s	ms		s	vw
2	A	0.236	1450	580	17		m	ms		s	w
3	A	0.258	1600	400	6		m	s		m	m
41	B	0.279	1800	200	2		ms	s			vw
42	C	0.279	1600	c	4	m			s		vw
43	D	0.279	d	c	d	m			s		
5	A	0.490	1600	400	6		w	s		s	w
61	A	0.501	1795	203	5		w	s	m		w
62	C	0.501	1700	407	6			s	vw		w
63	C	0.501	1550	c	1	m		m	s		w
71	E	0.54	1410	590	50			ms		s	vw
72	C	0.54	1600	195	19			s		w	w
73	C	0.54	1600	90	66			s			mw
81	F	0.93	1400	c	3				s		w
82	C	0.93	1600	c	2				s		
91	A	1.03	1790	203	5			s	ms	m	w
92	C	1.03	1700	406	4			s	m	mw	w
93	C	1.03	1550	c	1	mw		m	vs		w
10	A	1.19	1450	590	16			w		s	
111	A	1.95	1790	207	2			ms	s		w
112	C	1.95	1690	407	4			s	s	ms	mw
12	A	6.04	1450	590	16				m	s	
13	B	7.04	2000	202	2				s		
141	G	7.3	1450	570	68					s	
142	C	7.3	1600	195	16				s	s	
143	C	7.3	1600	100	64			w	s	m	m
15	A	10.5	1450	650	16					s	

[a] A = mixture of UN and VN; B = nitrided alloy of U and V; C = residue of sample immediately above it in the table; D = a portion of the residue from sample 41; E = mixture of residues of samples 1 and 10; F = mixture of UN and V; G = mixture of residues of samples 12 and 15.

[b] Relative intensities of phases are indicated by s = strong, m = medium, w = weak, and v = very.

[c] Heated in vacuum of 2×10^{-5} torr or less.

[d] The temperature was varied between 1600 and 2000°C for 20 min.

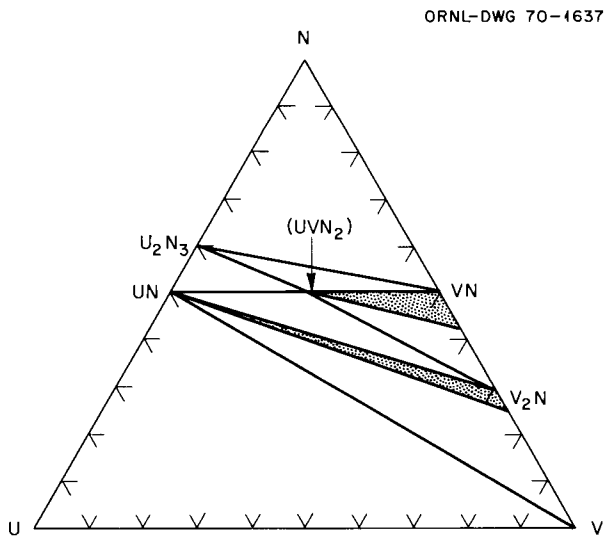

Fig. 2.5. Equilibrium Tie Lines Between the Solid Phases in the U-V-N System at 1400 to 1800°C. Shaded areas and lines are two-phase regions.

nitride fuel arises from the excess N that results from either reaction of the fuel with residual O in the pin or nuclear fissioning.[13] This excess N in the form of U_2N_3 can react with cladding. In order to maintain the N_2 pressure below that for the UN-U_2N_3 system, the fuel may be tailored with V, V_2N, or O_2 (ref. 12).

The buffering action is explained as follows. For a ternary system, such as the U-V-N system, the pressure at constant temperature is fixed when three condensed phases and the gas phase are in equilibrium. The relative amount of each phase is not important insofar as fixing the pressure is concerned. For example, if we assume we start with a UN-V mixture and add N, V_2N is formed (see Fig. 2.2) and the overall composition of the condensed phases moves into the UN-V-V_2N three-phase region. As long as the overall composition remains in this three-phase region, the N_2 pressure at constant temperature will remain fixed, independent of the relative amounts of UN, V, and V_2N present. As more N is added, the overall composition moves into the UN-V_2N-UVN_2 three-phase region, and the N_2 pressure at constant temperature is again fixed but at a value larger than that over the UN-V-V_2N region. The ability of the system to absorb N without a corresponding increase in the N_2 pressure is what is meant by buffering the fuel system.

Given below are the approximate N_2 pressures (in atmospheres) for the constant-pressure, three-phase regions in the U-V-N system at 1400°C.

Constant-Pressure Three-Phase Regions	Nitrogen Pressure (atm)
U-UN-V	10^{-9}
UN-V_2N-V	10^{-5}
UN-UVN_2-V_2N	0.08–10^{-5}
UVN_2-VN-V_2N	0.08
UN-U_2N_3-UVN_2	1.6
U_2N_3-VN-UVN_2	> 1.6

These pressures were calculated from binary nitride data for the U-N and V-N systems. For example, the pressure over the UN-V-V_2N region is fixed by the reaction

$$V_2N(s) = 2V(s) + 1/2\ N_2(g)\ .$$

If we assume little solubility of UN in the V phases, the activities of V_2N and V are the same in the ternary U-V-N and binary V-N systems, and thus the N_2 pressure for the ternary three-phase system is the same as that for the binary two-phase system. No binary system two-phase region bounds the ternary UN-V_2N-UVN_2 region. Therefore, we cannot calculate the pressure in the ternary region from binary data; we can only calculate limits on this pressure at constant temperature. This is also true for the U_2N_3-UVN_2-VN three-phase region. The V-N system pressures were from Brauer and Schnell,[14] the U-UN pressure was from Inouye and Leitnaker,[15] and the UN-U_2N_3 pressure was from Katsura and Sano.[16]

Pure Cr metal can be nitrided to Cr_2N at 1400°C by a N_2 pressure of 0.05 atm or greater according to the data of Schwerdtfeger.[17] The N_2 pressure in the UN-V_2N-UVN_2 three-phase region at this temperature is constant at some value between 0.08 and 10^{-5} atm. Therefore, if the activity of Cr is maintained at a value of 0.62 or less, it cannot be nitrided by the UN-V_2N-UVN_2 system, even if the pressure generated by this system is the calculated upper limit of 0.08 atm.

The U-Pu-Cr-N System (J. P. DeLuca, K. E. Spear)

A mixed-nitride fuel pellet clad in type 316 stainless steel is a potential advanced fuel for LMFBR's. In order to determine what constituents of the fuel-cladding system can cause compatibility problems and subsequently to determine their solutions, one needs to have a minimum amount of thermodynamic and phase data for the system.

We hope to follow a three-step procedure in evaluating and solving these compatibility problems. The first step is to investigate the phase behavior in (U,M)N systems where M will be Cr, Fe, Ni, V, or Mo. We added V and Mo because both are possible backup cladding materials. Vanadium can also be used to buffer the fuel, and Mo is a major fission product and thus should be investigated in any fuel-cladding system. As a second step, the results for the (U,M)N systems will be used to guide the experiments involving Pu instead of U and the different metal components. This substitution takes advantage of the thermodynamic similarity between U and Pu nitrides and will allow the fewest experiments with Pu to produce a maximum amount of information.

The third step of our three-step procedure will be to investigate the phase relations between the metal components, N_2, and alloys of U and Pu.

U-Cr-N System. — Work has begun on the U-Cr-N system. We nitrided Cr metal and analyzed it by x-ray diffraction techniques to be Cr_2N. This material will be used as the starting material for the U-Cr-N system and also for the Pu-Cr-N system.

We mixed UN and Cr_2N to a U:Cr ratio of 1 and heated this mixture at 1600°C under 400 torr N_2 for 4 1/2 hr. The x-ray diffraction pattern of the powder product is tentatively thought to be caused by a ternary (U,Cr)N compound. The diffraction lines are not caused by UN, U_2N_3, Cr_2N, CrN, or UO_2. The existence of a ternary compound, $U_{1.9}Cr_{1.1}N_{2+x}(x < 1)$, was recently reported by Holleck.[18]

Pu-Cr-N System. — The induction heating furnace was modified and assembled in glove box 9 in the Interim Plutonium Facility. The glove box was closed and connected to the central Ar system. The induction furnace is capable of heating a sample (less than 100 g) to 2500°C in a

vacuum (1×10^{-6} torr) or any noncorrosive atmosphere at a pressure below 760 torr.

The furnace consists of a 12-turn induction coil on the outside of a 4-in.-diam quartz tube. A current concentrator is located inside the quartz tube. The upper end of the furnace is sealed by a Cu plate and rubber gasket. The bottom leads directly to the Venco Model 8031 6-in.-diam vacuum system. The tube and end plate are held in place by atmospheric pressure when the system is under vacuum.

A small amount of PuN was obtained for use in this study.

Thermodynamic Investigations of High-Performance Fuel Systems

J. M. Leitnaker

The goal of our thermodynamics program for high-performance fuels, the carbides, nitrides, and carbonitrides, is to be able to predict the limiting equilibrium behavior of fuel and cladding in fast-reactor environments. Our experiments, though limited to measurements out of reactor, are of value for defining and understanding the factors that affect fuel performance.

Thermodynamic Properties of UVC_2 (K. E. Spear, T. B. Lindemer)

We confirmed the existence of the ternary UVC_2 compound in phase studies of the U-V-C system[19] and determined the thermodynamic properties of this phase.[20] At 298°K, the heat of formation (ΔH_f°) of UVC_2 is -48.6 ± 3.0 kcal/mole, the entropy of formation (ΔS_f°) and the entropy are 0.5 ± 2.0 and 22.2 ± 2.0 cal $mole^{-1}$ $°K^{-1}$, respectively. We estimated the uncertainties in these quantities.

The determination of thermodynamic data from phase equilibria results is not unprecedented, as is exemplified by the recent calculations by Holleck and Kleykamp.[21] They calculated the limits of the free energies of formation of many ternary and quaternary carbides that contain U and/or Pu from data existing in phase diagrams. The UVC_2 ternary compound was one of these phases, but they used the estimated diagram of Gorle *et al.*,[22] which shows two incorrect tie lines, the UVC_2-V_2C and

UVC_2-C lines. They also did not know about the peritectoid decomposition of the ternary UVC_2 phase at 1900 ± 100°C.

One check on the accuracy of the thermodynamic data we obtained for UVC_2 is a comparison of $\Delta S^\circ_{f,298}$ (UVC_2) with similar values for other carbides. Using data from Storms[23] and Kubaschewski et al.,[24] we found that the $\Delta S^\circ_{f,298}$ values of M_xC compounds all lie between −3.5 and +3.5 eu (M = Ca, B, Al, Ti, Zr, Hf, Si, V, Nb, Ta, Cr, Mo, W, Mn, Fe, Th, or U). The UVC_2 value we determined is +0.25 eu per mole of C as compared with 0.9 eu for UC and −1.7 eu for $VC_{0.88}$, also in terms of 1 mole of C. Thus, the UVC_2 value compares well with those for other metal carbides, including those for the binary compounds in the U-V-C system.

Thermodynamic Properties of UVN_2 (K. E. Spear)

We discovered the ternary compound UVN_2, determined its crystal structure,[11] and have recently completed a study of the phase relationships in the ternary U-V-N system.[25] These phase data can be used to estimate the heat of formation and entropy for the UVN_2 phase.

The phase diagram for the U-V-N system[25] shows that the two solid-state reactions,

$$UN + VN = UVN_2 \ , \qquad (2.1)$$

and

$$UVN_2 + 1.17\ V = UN + 2.17\ VN_{0.46} \ , \qquad (2.2)$$

proceed from left to right and thus have negative free energies of reaction. The composition $VN_{0.46}$ is taken for the phase V_2N because thermodynamic information is available for the former composition. As a first approximation for solid state reactions, it is reasonable to assume that the enthalpies (ΔH) of reaction are negative. We calculated limits of −121.5 and −135.7 kcal/mole on the enthalpy of formation ($\Delta H^\circ_{f,298}$) of UVN_2 by means of this approximation and $\Delta H^\circ_{f,298}$ data for the binary phases. In terms of kilocalories per mole, these data are −69.6 for UN (ref. 15), −51.9 for VN (ref. 26), and −30.4 for $VN_{0.46}$ (ref. 27).

The entropy of UVN_2 at 298°K(S°_{298}) can be reasonably approximated by assuming that the entropy change for reaction (2.1) is zero. It follows, then, that the entropy of UVN_2 is equal to the sum of the entropies of UN and VN. The value for UVN_2 is calculated to be 23.9 ± 3.0 eu (the uncertainty was estimated). The S°_{298} value for UN was taken from Inouye and Leitnaker,[15] and the value for VN was from Shomate and Kelley.[28]

Thermodynamics of PuN (J. P. DeLuca)

As a part of our study of the compatibility of mixed nitride fuels we are building a system for measuring of N_2 pressures over nitrides and carbonitrides that contain Pu to define the factors that affect fuel performance and the behavior of the fuel toward cladding materials. The general characteristics of the system were described previously.[29]

Our work this quarter was concerned with the assembly of the apparatus. All parts necessary for the vacuum system for the glove box were received. Detailed sketches were made to assist craftsmen in completing all necessary services to the system. The saturable core reactor was assembled. The control panels for the vacuum system and the recording microbalance were assembled. The vacuum system is 75% assembled, and the services (electricity, air, water, Ar) are 40% complete.

Thermophysical Properties

D. L. McElroy

Measurement of the Physical Properties of (U,Pu)N Alloys (S. C. Weaver, T. G. Kollie)

We began a study of the thermal conductivity of (U,Pu)N alloys, since this property largely determines the distribution of temperatures in the fuel and its irradiation behavior. Irradiation effects, such as swelling, release of fission gas, and distribution of fission products, depend on the distribution of temperatures in the fuel. We plan to study the effects of fuel density, impurity content (C and O), and U:Pu ratio in these alloys.

We are preparing to install equipment in two glove boxes. One glove box will contain apparatuses for determining comparative and absolute longitudinal heat flow. The second glove box will contain equipment for measuring electrical resistivity, since these alloys are conductors. Parts for these items were delivered, and initial assembly will be started early in 1970.

In the meantime, measurements of the electrical resistivity of UN are proceeding. A novel innovation was recently made in this test. The PDP-8 computer-recorder system was connected, with appropriate amplifiers and switching, to the four-probe electrical resistivity sample. This system reverses the current flow in the specimen, records the needed voltage readings, and computes and prints the electrical resistivity and the thermocouple electromotive force every 2 min. This frees the operator for other tasks and has increased our capability for recording data by about one thousandfold. We still need to find a means to ensure less movement of the thermocouple wires on the sample. The present system is applicable to the glove-box equipment.

We measured the electrical resistivity of UN from 295 to 1675°K, using the combination of the computer and resistivity rig. Before we connected the computer into the circuitry, we measured resistivity from 294 to 975°K by means of the six-dial potentiometer, which has an accuracy of 0.01 μv. Over this temperature range, the computer data agree with the potentiometer data to within ±0.1 μohm-cm, or about ±0.06%. With the addition of these data, the resistivity of UN has now been measured from 4.2 to 1675°K. We may have to use N overpressures to obtain resistivity data at higher temperatures.

Some of our recent data are tabulated in Table 2.3. The temperatures reported probably are not accurate; we are not satisfied with the calibration reported by the manufacturer for the W vs W–26% Re thermocouple wires. We plan a calibration test so that we may obtain temperature measurements with greater accuracy. This will be important in obtaining good data for the Seebeck coefficient. The slope of the curve for resistivity versus temperature between 295 and 800°K decreases to a constant at about 800°K. Between 800 and 1400°K, the resistivity

Table 2.3. Electrical Resistivity of Uranium Nitride Between 300 and 1675°K

Temperature (°K)	Electrical Resistivity, μohm-cm[a]			
	ORNL Data (by Computer)	ORNL Data (by Potentiometer)	CANEL Data[b]	Linear Extrapolation Above 1400°K
300	149.2	149.2	147.9	
400	154.1	154.1	154.1	
600	161.0	161.0	161.0	
800	166.7	166.7	166.7	
1000	172.1		172.3	
1200	177.6		178.3	
1300	180.3		181.5	
1350	181.6		183.9	
1400	183.0		185.4	
1500	187.1		185.6	185.7
1600	192.5		190.0	188.4
1675	196.9			190.4

[a]These values were obtained by using a porosity correction factor of $1 - P/1 + 0.5\ P$, where P is the volume fraction porosity.

[b]B. A. Hayes and M. A. De Crescente, Thermal Conductivity and Electrical Resistivity of Uranium Mononitride, PWAC-481 (October 1965).

increases linearly with temperature at a rate of 0.027 μohm-cm/°K. Above 1400°K, the slope of the curve begins to increase significantly so that at 1675°K the curve lies 6.5 μohm-cm, or 3.4%, above a linear extrapolation of the curve from 1400°K. Although we know the thermocouple calibration may not be accurate, an error correction of 150°K at 1675°K is needed to bring the data back to the linear curve. More measurements are to be made on this sample.

Irradiation Testing of Nitride Fuels for LMFBR Applications

T. N. Washburn

The objective of this program is to establish the irradiation performance of the U-Pu nitrides and carbonitrides. The nitrides and carbonitrides have a thermal conductivity about 5 times higher, a theoretical

density 30% higher, and a metal content in the compound 7% higher than the oxides. These properties make the nitride and carbonitride strong contenders as advanced fuel for a LMFBR.

Thermal-Flux Tests (C. F. Sanders)

The thermal-flux irradiation of the mixed nitride fuel will consist of two types of tests — an uninstrumented series in the Engineering Test Reactor (ETR) at Idaho, and an instrumented series in the Oak Ridge Research Reactor (ORR). The initial test in both series will use the design specifications listed in Table 2.4. The first series of capsules in the ETR should be inserted during the spring of 1970, and the first series of capsules in the ORR should be inserted during the summer of 1970.

The detailed design of the ETR capsules is completed, and the hardware is being fabricated.

Table 2.4. Design Specifications for Mixed Nitride Capsules

	Mixed Nitride Capsules[a]		
	N-1	N-2	N-3
Fuel composition	$(U_{0.80},Pu_{0.20})N$	$(U_{0.80},Pu_{0.20})N$	$(U_{0.80},Pu_{0.20})N$
Fuel diameter, in.	0.245	0.245	0.245
Fuel length, in.	3	3	3
Fuel density, % theoretical	> 90	> 90	> 90
Cladding material	type 316 stainless steel	type 316 stainless steel	type 316 stainless steel
Cladding diameter, in.	0.3	0.3	0.3
Cladding wall thickness, in.	0.0175	0.0175	0.0175
Bond between fuel and cladding	NaK-19	NaK-19	Na
Gap between fuel and cladding, in.	0.010	0.010	0.010
Capsule material	type 304 stainless steel	type 304 stainless steel	type 304 stainless steel

Table 2.4. (continued)

	Mixed Nitride Capsules[a]		
	N-1	N-2	N-3
Capsule diameter, in.	0.501	0.501	0.501
Capsule wall thickness, in.	0.025	0.025	0.025
Instrumentation	none	none	cladding thermocouples
Heat rating, kw/ft	30	30	30
Maximum burnup, % FIMA[b]	3	10	10
Temperature at fuel center, °C	925	925	910
Temperature at fuel surface, °C	610	610	600
Temperature at inner surface of cladding, °C	585	585	585
Temperature at outer surface of cladding, °C	495	495	492
Pins per capsule	3	3	1
Capsules per test	1	1	4

[a]N-1 and N-2 will be irradiated in the Engineering Test Reactor, and N-3 will be irradiated in the Oak Ridge Research Reactor.

[b]FIMA is fissions per initial actinide metal atom.

References

1. E. S. Bomar, Fuels and Materials Development Program Quart. Progr. Rept. Sept. 30, 1969, ORNL-4480, pp. 37–41.
2. D. L. Keller, Annual Report, Progress on Development of Materials and Technology for Advanced Reactors During July 1968 Through June 1969, BMI-1868, pp. A-1–A-13.
3. A "Shatter Box" Grinder, Model 8500, Spex Industries, Inc., was used in this work.
4. V. J. Tennery, "Characterization of Nitride Fuels," pp. 66–68, this report.
5. R. E. Vogel and C. P. Kempter, Acta Cryst. 14(11), 1130–1134 (1961).
6. J. M. Leitnaker, "The Ideality of the UC-UN Solid Solution," pp. 317–330 in Thermodynamics of Nuclear Materials, 1967, International Atomic Energy Agency, Vienna, 1968.

7. K. E. Spear and J. M. Leitnaker, Review and Analysis of Phase Behavior and Thermodynamic Properties of the Plutonium-Nitrogen System, ORNL-TM-2106 (March 1968).

8. F. Anselin, J. Nucl. Mater. 10(4), 301–320 (1963).

9. J. M. Leitnaker and R. L. Beatty, Metals and Ceramics Division, and K. J. Notz, Chemical Technology Division, personal communication.

10. K. E. Spear, Fuels and Materials Development Program Quart. Progr. Rept. Sept. 30, 1969, ORNL-4480, pp. 45–46.

11. K. E. Spear and J. M. Leitnaker, Fuels and Materials Development Program Quart. Progr. Rept. March 31, 1969, ORNL-4420, pp. 58–65.

12. J. M. Leitnaker, R. L. Beatty, and K. E. Spear, Trans. Am. Nucl. Soc. 12(1), 86–87 (1969).

13. K. E. Spear and J. M. Leitnaker, Trans. Am. Nucl. Soc. 12(2), 593–594 (1969).

14. G. Brauer and W.-D. Schnell, J. Less-Common Metals 6, 326–332 (1964).

15. H. Inouye and J. M. Leitnaker, J. Am. Ceram. Soc. 51(1), 6–9 (1968).

16. M. Katsura and T. Sano, J. Nucl. Sci. Technol. 4(6), 283–288 (1967).

17. K. Schwerdtfeger, Trans. Met. Soc. AIME 239, 1432–1438 (1967).

18. H. Holleck, Ternary Uranium-Transition Metal-Nitrides, KFK-1011 (July 1969).

19. K. E. Spear and T. B. Lindemer, Fuels and Materials Development Program Quart. Progr. Rept. Sept. 30, 1969, ORNL-4480, pp. 46–50.

20. K. E. Spear and T. B. Lindemer, Fuels and Materials Development Program Quart. Progr. Rept. Sept. 30, 1969, ORNL-4480, pp. 51–52.

21. H. Holleck and H. Kleykamp, J. Nucl. Mater. 32, 1–19 (1969).

22. F. Gorle et al., "Preparation Processes and Stabilization of Uranium Monocarbide," pp. 481–496 in Thermodynamics of Nuclear Materials, 1967, International Atomic Energy Agency, Vienna, 1968.

23. E. K. Storms, The Refractory Carbides, Academic Press, New York, 1967.

24. O. Kubaschewski et al., Metallurgical Thermochemistry, 4th Ed., Pergamon Press, Ltd., London, 1967.

25. K. E. Spear, "Ternary U-V-N System," pp. 70–71, this report.

26. Alla D. Mah, Heats and Free Energies of Formation of Vanadium Nitride and Vanadium Carbide, RI-6177 (1963).

27. E. G. King, Quarterly Metallurgical Progress Report Number 43, for Period April 1 Through June 30, 1969, USBM-RC-1399, pp. 11–16.

28. C. H. Shomate and K. K. Kelley, J. Am. Chem. Soc. 71, 314–315 (1949).

29. J. P. DeLuca, Fuels and Materials Development Program Quart. Progr. Rept. Sept. 30, 1969, ORNL-4480, p. 52.

3. EFFECT OF POWER CYCLING ON LMFBR FUEL-CLADDING BEHAVIOR

O. Sisman

This program investigates the effects of power cycling and transients on fuel behavior and the interaction of fuel and cladding for a liquid-metal fast breeder reactor (LMFBR), first for mixed oxide fuel and stainless steel cladding and later for other fuels and claddings. The objectives of this study are to compare the mechanical interactions of fuel (flat-ended pellets, dished pellets, and particulate fuel) and cladding during thermal-cycling conditions typical of those to be expected in an LMFBR. Fuel relocation is periodically monitored by neutron radiography. Relocation and cracking of the fuel, reactions between fuel and cladding, and the migration of Pu and fission products will be studied by postirradiation examination.

Power Cycling of Mixed Oxide Fuel with Stainless Steel Cladding to Moderate Burnup

J. G. Morgan

We are designing a series of reactor experiments for studies of the effects of power cycling and power transients on the behavior of oxide fuel and the interactions of fuel and cladding. This quarter, we made the calculations necessary to establish the geometry of the capsules in preparation for the preliminary design for the first experiment. Complete details of this work will be reported next quarter.

4. LMFBR FUEL ELEMENT DESIGN AND MODEL DEVELOPMENT

P. Patriarca A. L. Lotts C. M. Cox

The objective of this program is to develop analytical methods to predict and evaluate the performance of liquid-metal-cooled fast breeder reactor (LMFBR) fuel pins and fuel elements. This work is closely coordinated with the related programs for development of fuel and cladding. It provides methods for designing and systematically evaluating irradiation tests, evaluating the influences of materials properties on the performance of fuel elements, and identifying specific areas in which experimental research needs to be intensified.

The program is divided into three areas: model integration, fuel performance, and cladding performance. The fuel and cladding performance tasks are oriented toward mathematical description of the various phenomena of the fuel and cladding under irradiation such as swelling, gas formation, and mechanical, thermal, and chemical behavior. These individual models are incorporated into a large, central computer program that simulates the performance of an operating fuel pin.

Model Integration

Analysis of Fuel Pin with FMØDEL Computer Code (F. J. Homan, W. E. Stillman,[1] B. R. Dewey[1])

The models that describe the behavior of fuel and cladding under irradiation that are now used in the FMØDEL code were described previously.[2] The code was used in its present form to study some of the design and performance parameters of fuel pins designed for a LMFBR. Some results are discussed below.

The performance of a typical LMFBR fuel pin[3] was examined in detail by means of the FMØDEL code. The pin was divided into nine axial regions, each with a characteristic coolant temperature, coolant pressure, linear heat rate, and neutron flux. These data are summarized in Fig. 4.1. We calculated a temperature distribution for each axial region and applied an empirical restructuring model to determine the

ORNL-DWG 69-11681R

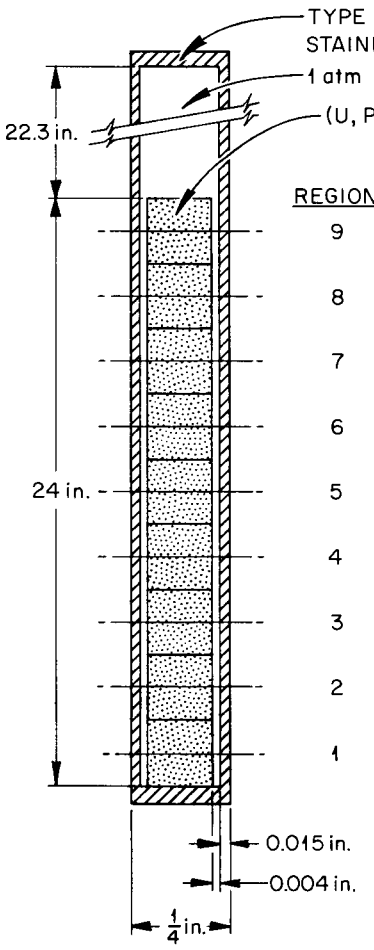

REGION	COOLANT TEMPERATURE (°C)	COOLANT PRESSURE (psig)	LINEAR HEAT RATE (kw/ft)	TOTAL NEUTRON FLUX (neutrons/cm^{-2} sec^{-1}) x 10^{15}
9	614.0	36.7	12.40	6.74
8	592.0	44.1	13.36	7.26
7	570.0	51.4	14.73	8.05
6	549.0	58.8	15.54	8.51
5	528.0	66.1	16.02	8.75
4	506.0	73.5	16.09	8.75
3	484.0	80.8	15.44	8.43
2	462.0	88.1	14.32	7.79
1	440.0	95.5	13.36	7.26

$$\frac{\phi_{t\,>0.1\ \mathrm{Mev}}}{\%\mathrm{FIMA}} \simeq 2.24 \times 10^{22}$$

Fig. 4.1. Simulation of Typical LMFBR Fuel Pin.

size of the central void and location of the regions of columnar and equiaxed grains. The results of these calculations are summarized in Figs. 4.2 and 4.3. Our analysis of the interaction between fuel and cladding in this pin began with a determination of the kinetics of gap closure. For this we assumed for comparison two entirely different fuel characteristics. First, we assumed that the fuel in the cool outer region, adjacent to the cladding, had strength sufficient to contain the expansion of the hot, plastic fuel in the central regions of the pin without rupture or cracking. We calculated the stress-strain distribution for both fuel and cladding in accordance with the technique described previously.[2] We compared the outside diameter of the fuel and the inside diameter of the cladding periodically during the lifetime of

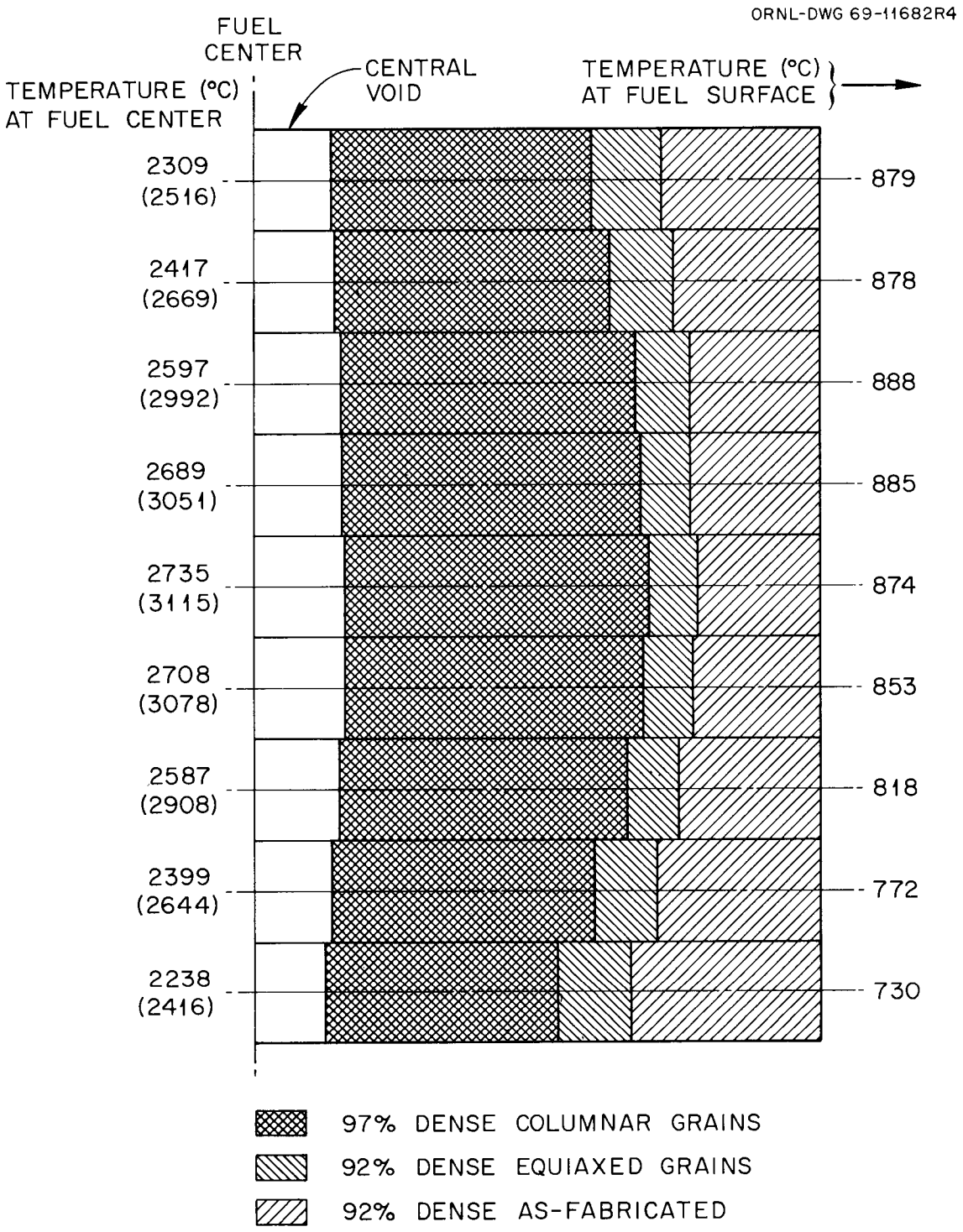

Fig. 4.2. Calculated Fuel Temperature Distribution and Fuel Restructuring on Initial Startup. Values in parentheses follow if fuel restructuring is neglected.

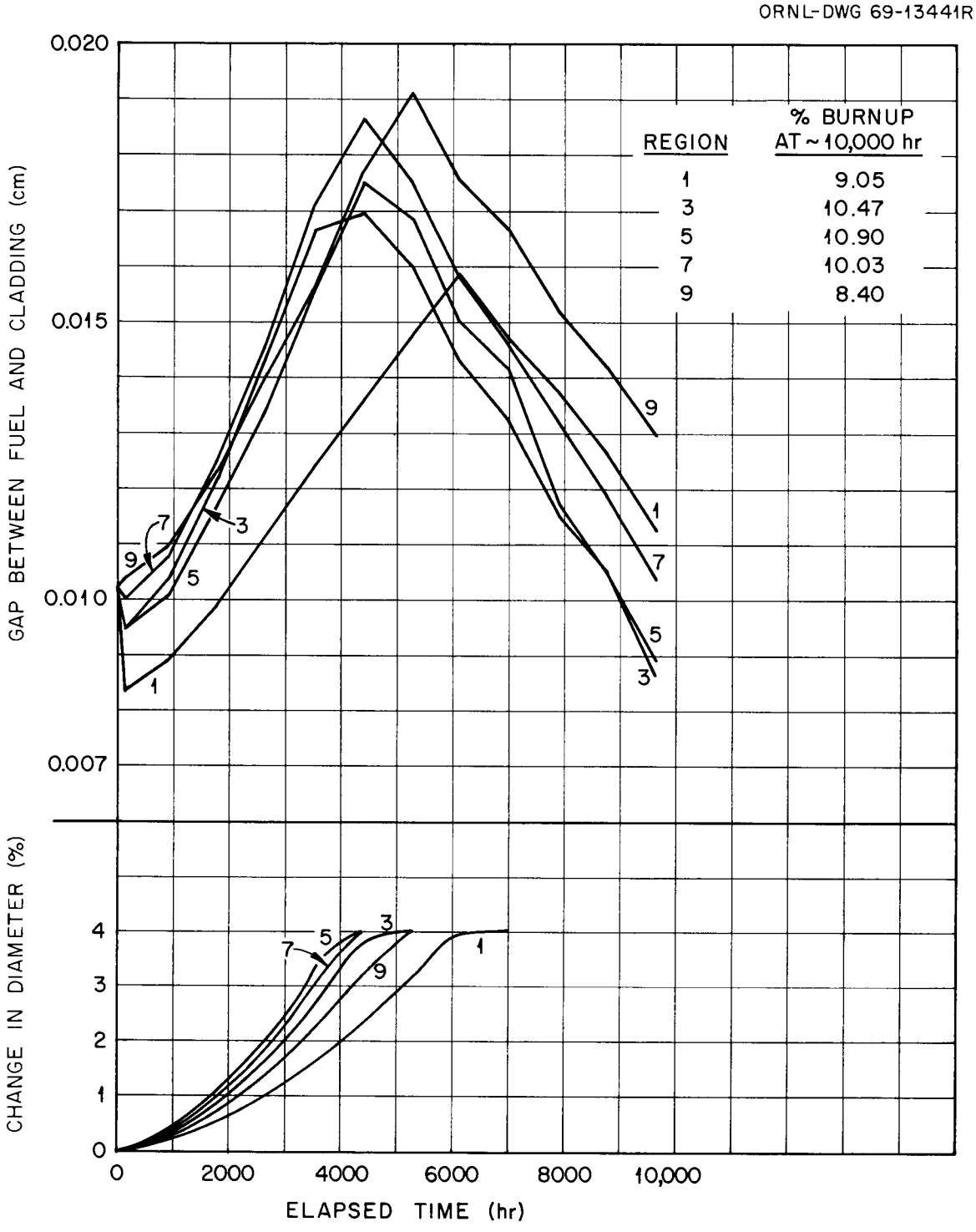

Fig. 4.3. Gap Between Fuel and Cladding and Percent Change in Diameter as Functions of Elapsed Time.

the fuel pin to see when the initial 0.004-in. gap had closed. Both fuel swelling due to accumulation of fission products and swelling of the cladding due to formation of voids were considered. The results of the calculations are summarized in Fig. 4.3, where it can be seen that the gap still existed in all nine axial regions at the end of life (about 10% burnup). The initial decrease in the gap is due to differential thermal expansion. This is followed by an increase in gap dimension due to rapid swelling of the cladding at the high neutron flux, while fission products are accommodated in fabricated porosity. The particular model[2] used to predict swelling of the cladding assumes a saturation at 12% increase in volume; then the gap begins to close again as the buildup of fission products swells the fuel. The model for swelling of the cladding is a very preliminary, empirical model that requires considerable extrapolation from existing data. The predicted diametral expansion of the cladding is due primarily to the formation of voids with a slight contribution from thermal expansion and mechanical deformation due to fission gases accumulated in the gas plenum.

The second assumption was that the cool, outer region of the fuel has no strength to contain the hot plastic center. This would perhaps represent a Sphere-Pac fuel. According to this assumption, all thermal expansion and swelling of the fuel must be accommodated by movement into the gap between fuel and cladding. Figure 4.4 summarizes the kinetics of gap closure for the center axial region and two end regions for the assumption of a weak fuel. Comparing Figs. 4.3 and 4.4 reveals that the initial differential thermal expansion is much more pronounced when a weak fuel is assumed. The period of rapid increase in the size of the gap is present in both figures, and in both cases a gap remains in each axial region at the end of life, although this gap is much smaller in the case of weak fuel.

It is obvious from these results that two major factors in the mechanical interactions of fuel and cladding are the rate at which the cladding swells due to formation of voids, and the strength of the fuel adjacent to the cladding. This observation is supported by the calculations summarized in Fig. 4.5. Here the assumptions of strong and weak fuel are compared for the central axial region at two different levels

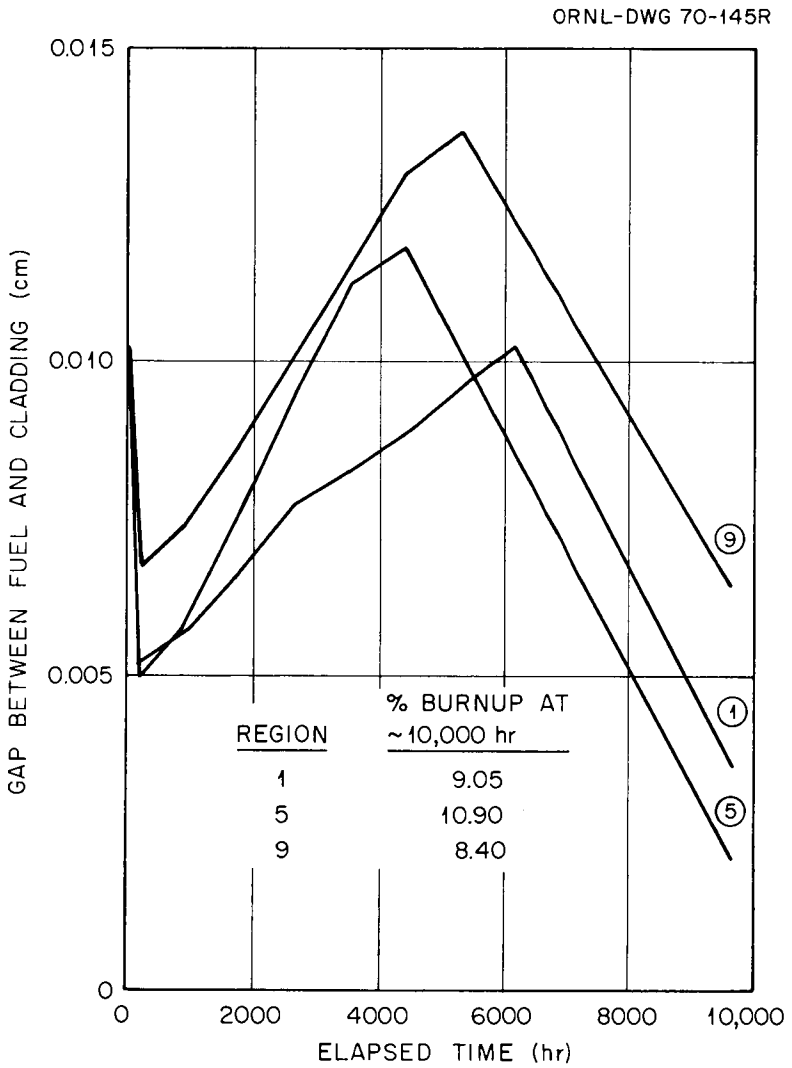

Fig. 4.4. Gap Between Fuel and Cladding as a Function of Elapsed Time for a Weak Fuel.

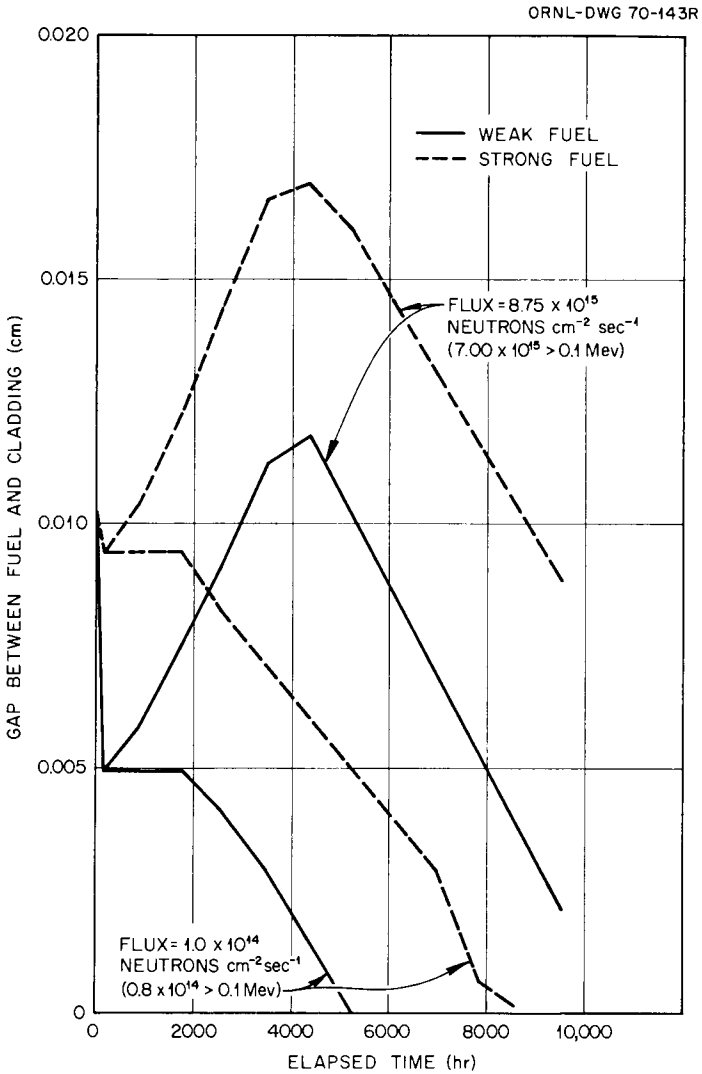

Fig. 4.5. Dependence of Gap Closure on Neutron Flux and Fuel Strength.

of neutron flux. The higher flux level is the one used in our typical pin (see Fig. 4.1), and the lower level is one chosen for convenience, which produces very little swelling of the cladding. It can be seen that in the absence of significant swelling of the cladding, the gap between fuel and cladding closes by the end of life. In an operating fuel element, the gap may close more rapidly due to cracking of the pellets or transport of vaporized fuel.

A design variable of considerable importance with respect to the economy and performance of a fuel pin is the thickness of the cladding. By using the temperature and pressure characteristics associated with axial region 4 (from Fig. 4.1), we analyzed the stress-strain distributions in claddings 0.015, 0.012, and 0.0092 in. thick. These calculations are summarized in Fig. 4.6. The internal pressure was assumed to increase linearly from 50 to 1000 psi in 10,000 hr. The external pressure remained constant at 75 psi, and the temperature gradient was assumed to be 1250°C/cm. The steady-state creep law used is described below.[4] Figure 4.6 shows the similarity in initial stress distribution for all cladding thicknesses studied, but the thinner cladding exhibits less initial plastic deformation and more relaxation of thermal compressive stresses. There was plastic strain at the inner and outer surfaces of the 0.015- and 0.012-in.-thick cladding, with the thicker cladding exhibiting the greater amount of strain. There was plastic deformation in all three cladding thicknesses as a result of creep, but the increase over the initial plastic deformation was very slight for the 0.015-in.-thick cladding. For the 0.0092-in.-thick cladding, all the plastic deformation was due to creep. These results certainly agree with qualitative expectations. It remains to be debated what kind of trade-offs can be made between the decreased creep strength inherent in the thinner cladding and the increased neutron economy.

Fuel Performance

Improved Analytical Models (W. J. Lackey)

The objective of this work is to develop improved analytical models to describe in-reactor swelling and release of fission gas from $(U,Pu)O_2$.

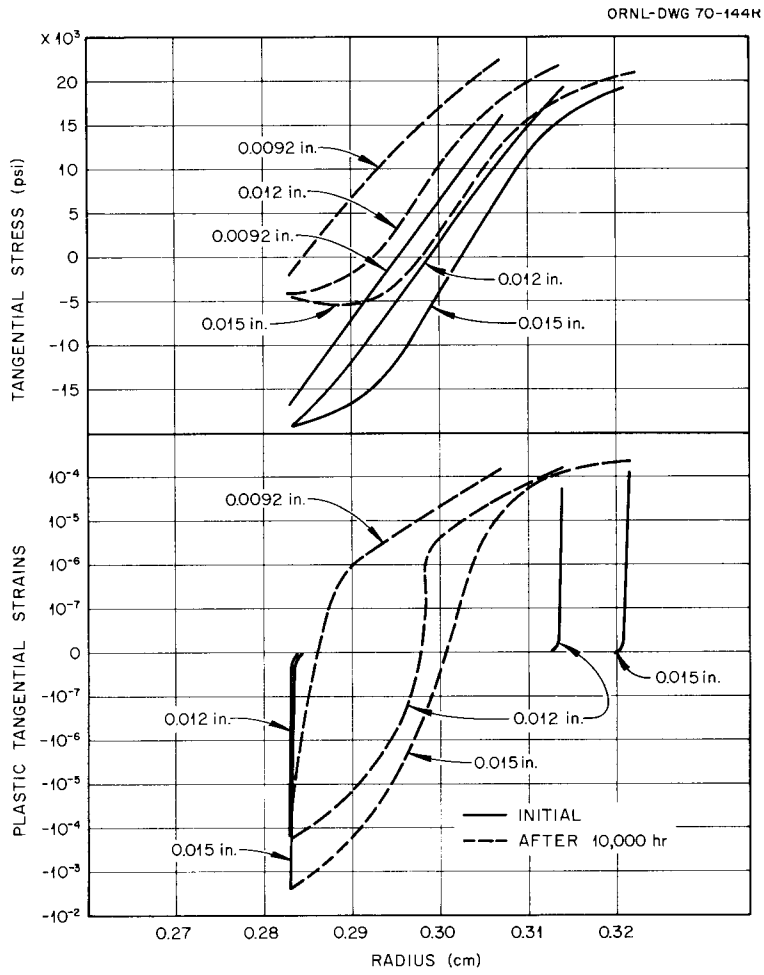

Fig. 4.6. Influence of Cladding Thickness on Stress-Strain Distribution.

As these models are developed they will be incorporated into the FMØDEL code. The effects of the following factors will be accounted for in the models for fuel swelling and release of fission gas.

1. formation of bubbles of fission gas,
2. coalescence of bubbles of fission gas that results in a reduction of the gas pressure and thus an increase in bubble volume for a given quantity of fission gas,
3. formation of metallic and nonmetallic inclusions,
4. expansion of the mixed oxide lattice caused by "forced solubility" of normally insoluble fission products (x-ray measurements[5,6] show this to be a minor factor for the majority, if not all, of the fuel; it may be more important for the cooler fuel located near the cladding),

5. lattice expansion caused by a decrease in the ratio of Pu:U as a result of preferential fissioning of Pu [as an example, a change in PuO_2 content from 20 to 10% (10% fissions per intial actinide metal atom, FIMA, with no breeding) would result in a volume change of about 0.33% or about 10% of the total fuel swelling expected for 10% FIMA],
6. counteraction of fuel swelling[5,7–9] by contraction of the lattice as a result of solution of Zr, Y, and rare earths (the magnitude of the volume change for this effect should be between 0.13 and 0.61% for 10% FIMA),
7. a change in the ratio of O:metal from 1.98 to 2.00, which causes a contraction of the $(U_{0.8},Pu_{0.2})O_2$ lattice and results in a volume decrease of about 0.25% (such a change in the ratio of O:metal could result from the thermal-gradient effect or from fissioning of Pu and U), and
8. an increase in density during restructuring of the fuel, which could cause swelling or possibly counteract swelling.

Since the behavior of bubbles of fission gas is of primary importance in both fuel swelling and release of fission gas, current work has been directed toward improving our knowledge of the formation and coalescence of these bubbles. Replica electron microscopy of irradiated $(U,Pu)O_2$ is being conducted with particular emphasis on the radial distribution of bubble sizes. Bubbles of fission gas 0.25 to 1.5 μm in diameter were observed in the region of columnar grains in a $(U_{0.85},Pu_{0.15})O_2$ fuel pin irradiated at a linear heat rate of 13.6 kw/ft to 0.7% FIMA. A previous analysis[10] indicates that the fuel temperature at a radius corresponding to the location of the bubbles was 1850° C. The occurrence of the bubbles in the columnar grains is somewhat surprising since it is generally assumed that essentially all fission gas is released from this region.

Recent attempts to prepare replicas by the conventional cellulose acetate technique were unsuccessful in that the alpha activity of the replicas was above that permitted in the electron microscope laboratory. We expect that a technique developed by Padden[11] will allow cleaner

replicas to be made since, contrary to the cellulose acetate technique, hydrofluoric and sulfuric acids can be used for decontamination.

Cladding Performance

Physical Properties of Type 316 Stainless Steel (R. W. Swindeman, W. H. Bridges)

We systematically compiled the physical properties of type 316 stainless steel available from the literature. Compilation of the mechanical properties is in progress. This catalog of information will enable us to easily evaluate the spread of data values for a given property and will serve as the foundation for further data compilations. In addition, we hope that this collection of information will assist in determining the systematic variation of properties with fabrication and irradiation history and in determining the influence of this variation on the performance of fuel elements.

In any performance analysis, it would be highly desirable to use data for the in-reactor properties of test specimens with a history identical to that of the material from which the actual cladding was fabricated. But there are very few such data yet available. Therefore, we are using data from unirradiated tubing in our models to test the working of our mechanical analysis. We have completed an evaluation of tensile and creep data for "low strength" type 316 stainless steel. Typical of this material are two heats of type 316 stainless steel studied by Garofalo[12,13] and that investigated by the British. Some of the unpublished British data for the temperature range 600 to 700°C were used to formulate the following creep equation, which is based on the Garofalo parameter:

$$\dot{\epsilon} = 1.3 \times 10^{15} \exp(-83{,}000/RT) \left| \sinh \frac{\sigma}{15800} \right|^{3.9} , \qquad (4.1)$$

where

$\dot{\epsilon}$ = creep rate, hr^{-1},

σ = stress, psi,

R = gas constant, and

T = temperature, °K.

Curves plotted by use of Eq. (4.1) for 600, 650, and 700°C are shown in Fig. 4.7, and the data published by Garofalo are included for comparison. Other data plotted in Fig. 4.7 correspond to the results of four thermal- and load-cycling creep tests that we performed. The implication is that, in the absence of irradiation, solution-annealed material is reasonably insensitive to mechanical history. All of our data were from short tests of less than 1000 hr; we are now performing longer tests to evaluate any influence of time hardening. We are also studying the behavior of "high strength" type 316 stainless steel such as the 20% cold-worked tubing being produced for Fast Flux Test Facility and LMFBR fuel pins.

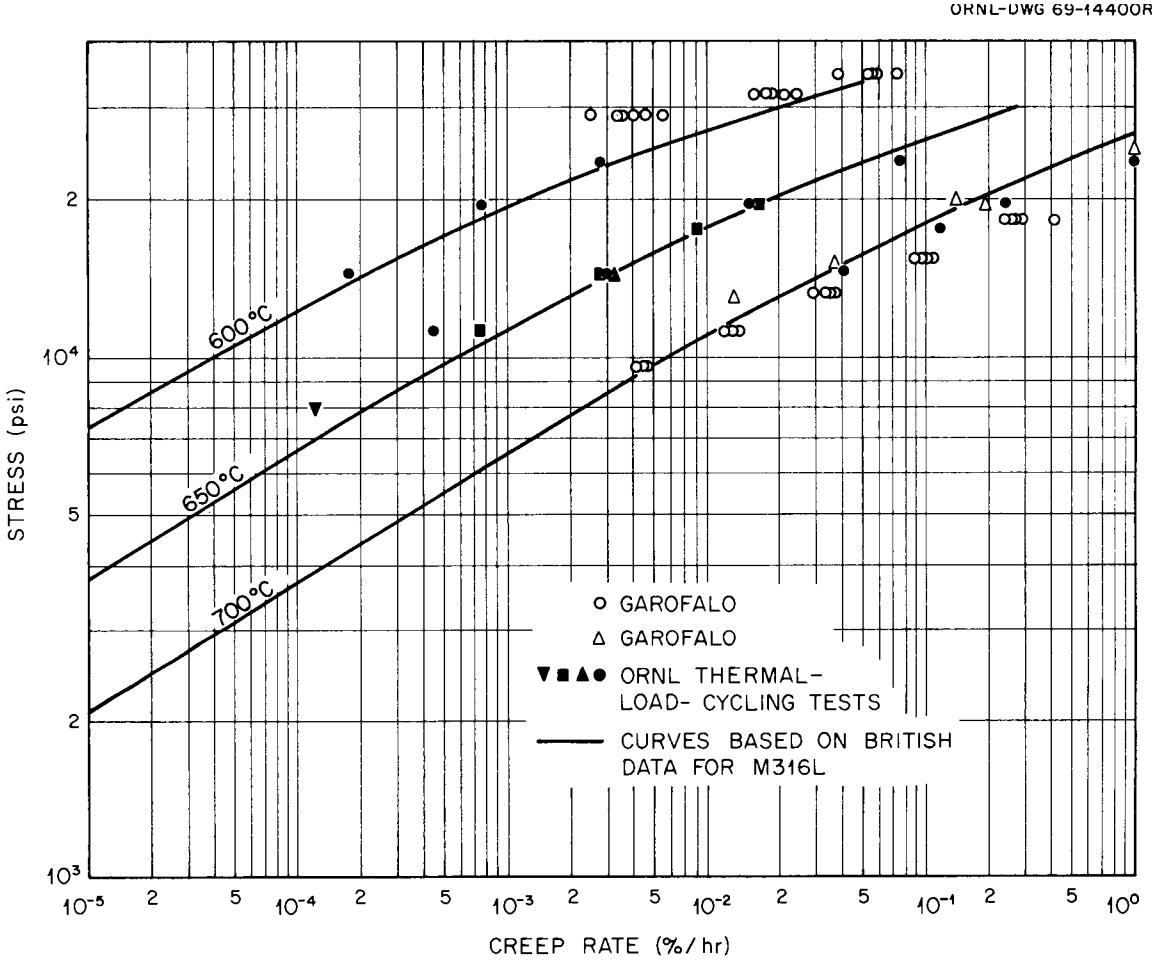

Fig. 4.7. Creep Rate Versus Stress for "Low Strength" Type 316 Stainless Steel. [Refs. F. Garofalo et al., Trans. Met. Soc. AIME 221, 310 (1961); Trans. Am. Soc. Metals 54, 430 (1961).]

References

1. Consultant from The University of Tennessee.
2. C. M. Cox and F. J. Homan, Fuels and Materials Development Program Quart. Progr. Rept. Sept. 30, 1969, ORNL-4480, pp. 59–61.
3. K. P. Cohen and G. L. O'Neill, Safety and Economic Characteristics of a 1000 Mwe Fast Sodium-Cooled Reactor Design, GEAP-4939 (December 1965).
4. R. W. Swindeman and W. H. Bridges, "Physical Properties of Type 316 Stainless Steel," pp. 94–95, this report.
5. B. F. Rubin and K. J. Perry, The Irradiation of Urania-Plutonia Fuel to 125,000 Mwd/tonne in a Thermal Flux, GEAP-5761 (March 1969).
6. M. L. Bleiberg et al., Effects of High Burnup on Oxide Ceramic Fuels, WAPD-T-1455 (March 1962).
7. E. J. McIver, The Unit Cell Size of Solid Solutions of Uranium Dioxide and Fission Product Oxides, AERE-M-1612 (April 1966).
8. R. J. Beals and J. H. Handwerk, J. Am. Ceram. Soc. 48(5), 271–274 (1965).
9. Franz Schmitz, Structures and Properties of $(U,Pu)O_2$ Containing Non-Active Fission Products – A Simulation of Irradiated Nuclear Fuel, CEA-R-3795; English translation: BNWL-TR-43 (April 1969).
10. A. R. Olsen, Oak Ridge National Laboratory, personal communication, December 1969.
11. Thomas R. Padden, Polyvinyl Chloride Replica Technique for High Burnup Reactor Fuels, WAPD-T-1595 (August 1963).
12. F. Garofalo et al., Trans. Met. Soc. AIME 221, 310 (1961).
13. F. Garofalo et al., Trans. Am. Soc. Metals 54, 430 (1961).

CLADDING AND OTHER STRUCTURAL MATERIALS

5. MECHANICAL PROPERTIES OF ALLOYS IN REACTOR ENVIRONMENTS AND DEVELOPMENT OF LMFBR CLADDING AND STRUCTURAL MATERIALS

J. R. Weir, Jr. H. E. McCoy, Jr.

This program is concerned with the effects of irradiation on the mechanical properties of various metals of potential use in nuclear reactors. The materials of primary concern are types 304 and 316 stainless steel, both materials of interest for liquid-metal fast breeder reactors (LMFBR). These alloys are being exposed to high neutron fluences, and the resulting changes in density, microstructure, and mechanical properties are being measured. Other materials under study include Incoloy 800 and V. Some attention is also being given to the use of particle accelerators to simulate neutron damage.

Austenitic Stainless Steels

Status of Irradiation Experiments (E. E. Bloom, A. F. Zulliger,[1] J. W. Woods)

Experiments are being conducted in the High Flux Isotope Reactor (HFIR), the Oak Ridge Research Reactor (ORR), and the Experimental Breeder Reactor-II (EBR-II) to investigate the effects of neutron irradiation on the mechanical properties, microstructure, and swelling characteristics of austenitic stainless steels.

The first experiment, conducted in a peripheral target position of the HFIR, was removed and is being evaluated. The primary purpose of this experiment was to measure the nuclear heating rate in the peripheral target positions. The experiment consisted of 15 holders, 8 of which contained SiC temperature monitors and 7 of which contained specimens for tests of mechanical properties. Figure 5.1 is an illustration of these two types of holders. The desired irradiation temperature is obtained by adjusting the width of the He gas gap. For design purposes in this initial experiment, we used the nuclear heating rates determined from

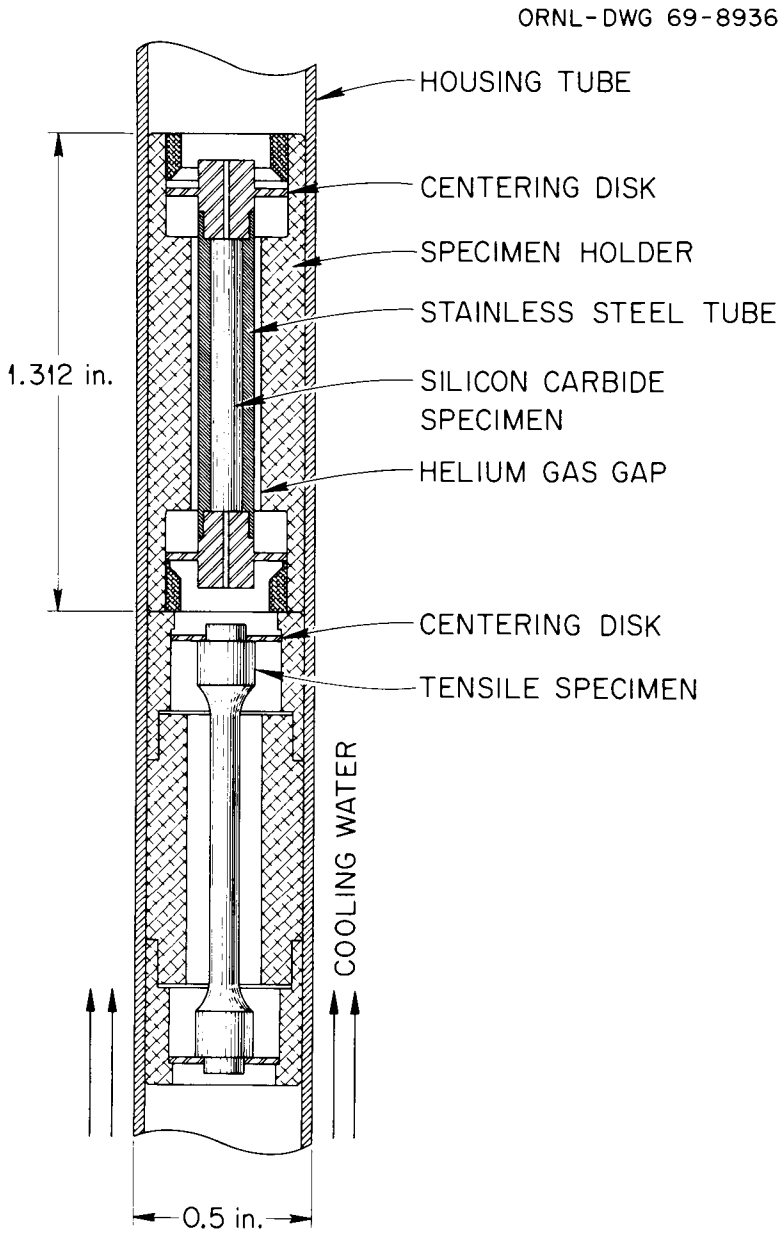

Fig. 5.1. Two Types of Holders Used in Experiments in the High Flux Isotope Reactor.

previous[2] irradiation experiments on graphite that were conducted within the target region. The SiC monitors were spaced alternately along the length of the experiment, and each was designed to operate at 400°C during reactor operation. The experiment remained in the reactor for one complete cycle (about 21 days). The fast-neutron fluence at the reactor midplane was calculated to be 2.9×10^{21} neutrons/cm^2 (> 0.1 Mev); the fluence at the end positions of the experiment was only about half of that. The irradiation temperature of the SiC is determined on the basis of the temperature at which the increase in volume induced by irradiation begins to recover during isochronal annealing after irradiation.[3]

Four SiC monitors from this first experiment have been evaluated. Figure 5.2 is a plot of the length of a SiC monitor as a function of the temperature at which it was annealed after irradiation. At annealing temperatures below the irradiation temperature there was no recovery from the damage, while at each annealing temperature above the irradiation temperature a portion of the damage recovered. The irradiation temperature was determined by the intersection of two straight lines through the data, as illustrated in Fig. 5.2.

In analyzing the data for change in the length of these monitors, we ignored the data from annealing temperatures of 350, 400, and 450°C since we did not know whether these data belonged to the low- or high-temperature curves. A straight line with zero slope was fit to the low-temperature data (i.e., annealing temperatures less than 350°C). The intersection of that line with a least-square line through the high-temperature data gave irradiation temperatures between 420 and 430°C for each of the monitors. It thus appears that the nuclear heating rate in the peripheral target position is slightly higher than our initial estimate. Using the adjusted heating-rate values, we designed and constructed five experiments containing 75 test specimens that are now being irradiated in the HFIR.

Subassembly X0-34 was removed from a row 2 position of the EBR-II after accumulating 11,035 Mwd. Three capsules of this subassembly were removed and are being evaluated. These capsules were replaced by three new ones, and the reconstituted subassembly (X0-34-A) was replaced into a row 2 position.

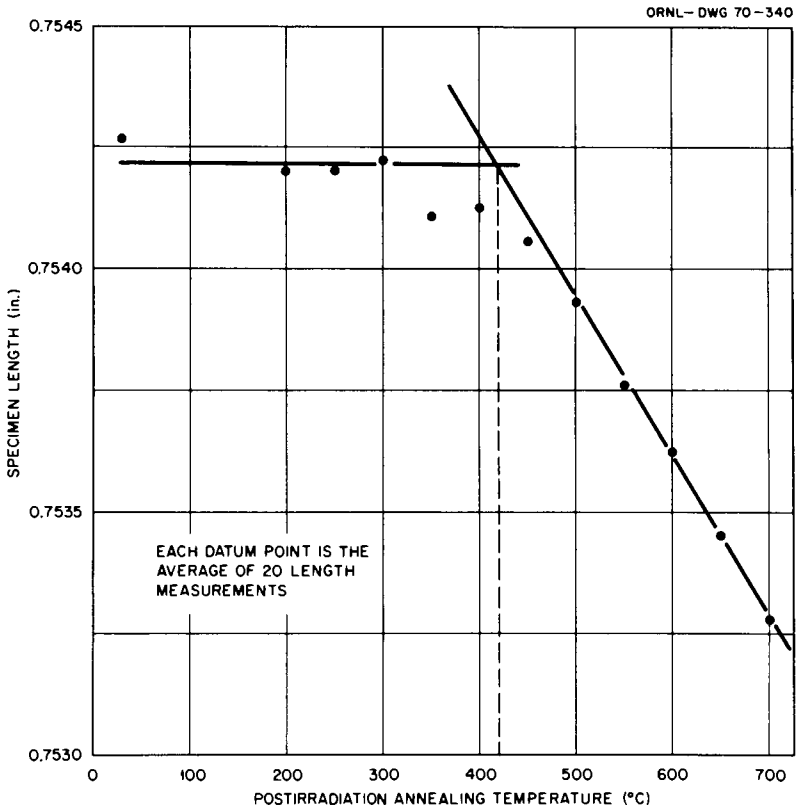

Fig. 5.2. Length Change of SiC During Postirradiation Annealing. The irradiation temperature was estimated from the intersection of the two lines to be 420°C.

Subassembly XO-35 remains in a row 7 position in the EBR-II, where it has accumulated an exposure of 13,184 Mwd.

The Effect of Helium on the Formation of Voids in Irradiated Stainless Steel (E. E. Bloom, J. O. Stiegler)

When stainless steel is subjected to neutron irradiation at 350 to 650°C, voids form and, as a result, density decreases.[4–9] The voids, as observed in the electron microscope, are present in concentrations as high as 10^{16} voids/cm^3 and in sizes ranging from the smallest observable (> 25 A in diameter) to those with a maximum diameter of several hundred angstroms. The mean diameter of the voids increases and their concentration decreases as the irradiation temperature is increased in this range.

The mechanism responsible for the nucleation of the voids has been the subject of considerable discussion and speculation. Cawthorne and

Fulton[4] initially offered the suggestion that He atoms produced by (n,α) reactions in some unspecified way formed nuclei on which vacancies produced by the irradiation subsequently precipitated to form the voids. Experimental evidence that He does influence void formation was obtained by Nelson and Mazey,[10] who showed by means of ion bombardment experiments that void concentrations and swelling were significantly greater in materials that had been injected with uniform distributions of He before bombardment than in materials free of He.

On the other hand, Claudson and coworkers[11] concluded from examination of the dependence of the decrease in density on fluence in type 304 stainless steel that the most plausible mechanism for formation of voids was nucleation in displacement cascades generated by neutrons. Harkness and Li[7] developed a model based on classical concepts of nucleation and growth that was designed to explain the effects of temperature and fluence on swelling. They argued that agreement between their model and experimental data justified the approach.

We have attempted to resolve these differences and to define more clearly the role of He in the formation of voids by repeating the Nelson and Mazey experiment but using neutron irradiation instead of ion bombardment. This approach avoids the problems of surface effects, differences in recoil spectra, and the dependence of damage rate on position that are inherent in experiments involving ion bombardment.

Sheet specimens of annealed type 304 stainless steel were irradiated in the EBR-II in contact with the liquid-Na reactor coolant. The composition of the alloy was Fe—18.15% Cr—9.60% Ni—0.046% C—1.77% Mn—0.62% Si—0.25% Cu—0.33% Mo—0.03% Co—0.023% P—0.010% S. A uniform concentration of 20×10^{-6} atom fraction He was injected into one set of specimens before irradiation by bombarding them with α-particles of variable energy.[12] A second set of unbombarded specimens was irradiated in the same position in the reactor experiment. The irradiation temperature, fast-neutron flux, and neutron energy spectrum were identical for the two sets of specimens. The irradiation temperature was about 390°C, and the fast-neutron fluence was 8.5×10^{21} neutrons/cm^2 (> 0.1 Mev).

After irradiation, the specimens were examined by transmission electron microscopy. The sizes of the voids were determined from

photomicrographs at 200,000× magnification; the concentrations of the voids were determined by measuring the foil thickness by stereo microscopy.

The microstructures of specimens irradiated with and without He are given in Fig. 5.3(a) and (b), respectively. Voids were smaller and more numerous in the specimen injected with He. In it the voids were all less than about 75 A in diameter, while in the material into which no He had been injected before irradiation the voids ranged from the smallest we are able to detect (about 40 A in diameter) up to a maximum of 130 A in diameter. The concentration of voids in the specimen injected with He before irradiation was about 5.2×10^{15} voids/cm^3, which is significantly greater than the concentration in the other specimen, 2.4×10^{15} voids/cm^3. We emphasize that these concentrations are based upon only those voids larger than 40 A in diameter, since we are unable to detect those that are smaller. We suspect that the error in the measurement of void concentration is greater in the specimen injected with He, in which all the voids are less than 75 A in diameter, and that the disparity in concentrations is even greater than is stated above.

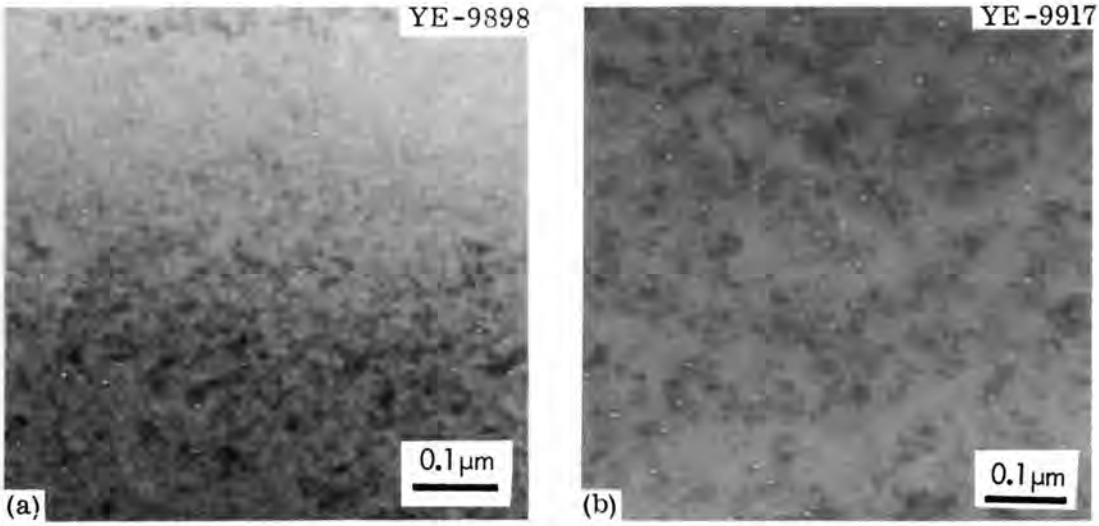

Fig. 5.3. Transmission Electron Photomicrographs Showing Voids in Type 304 Stainless Steel Specimens Irradiated at 390°C to a Fluence of 8.5×10^{21} neutrons/cm^2 (> 0.1 Mev). (a) Specimen injected with 20×10^{-6} atom fraction He before irradiation. (b) Control specimen containing no helium injected before irradiation. NOTE: Since the foil shown in (a) is much thinner than that shown in (b), these photomicrographs do not give a true impression of differences in void concentration. The void density in (a) was 5.2×10^{15} voids/cm^3; that for (b) was 2.4×10^{15} voids/cm^3.

Decreases in density of 0.06 and 0.10% for the specimens with and without injection of He before irradiation, respectively, were calculated from the concentrations of voids detected and the experimentally determined size distributions. In this case, although the concentration of voids was greatly increased by the injection of He before irradiation, the density was not greatly altered.

Similar differences in the scale of the dislocation-loop structure were also noted. The loops were smaller and more numerous in the specimen injected with He before irradiation. The structure was so complex that we were unable to make even qualitative estimates of loop sizes or concentrations.

The appearance of the damage structure in the vicinity of grain boundaries also differed between the two specimens. In the specimen injected with He, the loops persisted nearly to the boundary; the zone denuded of voids was less than 200 A wide. In the specimen not injected with He, a zone almost 1000 A wide adjacent to the boundaries was denuded of both voids and loops, although some loops were present at the boundary. Similar observations of a zone near a grain boundary that is denuded of loops and of enhanced formation of loops at the boundary were reported previously.[8]

We also examined the structure of a specimen that had been injected with 20×10^{-6} atom fraction He but not irradiated. Within our limits of detection, we found no evidence of damage as a result of the α-particle bombardment under either diffraction or absorption conditions.

The significant result of our work is that we demonstrate that He is a very effective agent for nucleating voids during neutron irradiation. The differences between our samples are not as striking as those obtained by Nelson and Mazey[10] in their studies of ion bombardment, possibly because in both of our specimens He was generated by (n,α) reactions during neutron irradiation. In fact, for the fluence used here [8.5×10^{21} neutrons/cm^2 (> 0.1 Mev)] about 2×10^{-6} atom fraction He would be generated (as calculated from concentrations of He measured after irradiation of stainless steel in EBR-II and reported by Hutchins et al.[13]).

The smaller voids in the specimen that initially contained He may be due to a high nucleation rate and a consequently high concentration of voids early in the irradiation. As a result of a high density of sinks, the vacancy supersaturation and the rate of void growth would be reduced. The differences in the denuded zones at grain boundaries also may be interpreted in this light. In the material injected with He, suitable nuclei exist uniformly distributed in the material at the beginning of the neutron irradiation. In the specimen not injected with He, nucleation could not occur until sufficient He had been generated by the irradiation. If the He were mobile, zones adjacent to sinks, such as grain boundaries, would be depleted of He and, therefore, of voids. There is the possibility, however, that the voids and loops form on a finer scale in the material injected with He as a result of damage that occurs during the injection process. The absence of detectable damage cannot be interpreted as a total absence of damage.

Nevertheless, it is clear from this work that He is an effective agent for nucleating voids. In our material that was not injected with He, the irradiation created about 70 He atoms for every void. In practice, therefore, He is generated during neutron irradiation in quantities large enough to be significant. Models[7] that ignore the effects of He on the nucleation of voids cannot explain these results and, in our opinion, are of dubious value.

The objections of Claudson et al.[11] to a mechanism for the nucleation of voids that involves He rest on some implied assumptions in their analysis: (1) that the vacancy supersaturation during irradiation remains constant and (2) that the He is immobile during irradiation. We believe that these assumptions are not correct and that the dependence of swelling on fluence cannot be taken at this time as firm evidence against He produced by transmutation playing an important part in the nucleation of voids. Our results suggest quite the opposite.

Distribution and Shape of Voids in Irradiated Metals[14] (J. O. Stiegler, K. Farrell, E. E. Bloom, F. W. Wiffen)

Out of the extensive work during the past few years on the development of voids in metals during neutron irradiation, a number of

generalizations have evolved that in our view are not fully justified. The hypotheses in question are that (1) the voids are homogeneously distributed and (2) have regular polyhedral shapes (octahedral in face-centered cubic metals). Neither of these generalizations seems to have been critically examined. In fact, no experimental tests for randomness appear to have been applied, although some clearly nonrandom distributions have been observed, and examples of irregularly shaped voids have been generally ignored. These points are of more than academic interest, for they involve the nucleation and growth of voids, the understanding of which is basic to our ability to predict radiation performance. We believe that a fuller discussion of the "anomalous" observations is in order and, indeed, that these features have an important bearing on understanding the physical processes involved. In this report we summarize observations made at this Laboratory on a variety of materials that support this view and then consider the implications of these observations in relation to mechanisms for the nucleation and growth of voids.

Inhomogeneous distributions of voids were first reported[15] in high-purity Al. The irregularities took several forms. Most conspicuous were the walls of voids pictured in Fig. 5.4. In this case the wall was composed of relatively large voids that defined an irregular surface surrounded by about 0.5-μm-thick zones free of voids. Voids not associated with walls were generally smaller than those on the walls. It was suggested[15] that the walls delineated former grain boundaries and that nucleation of voids was associated with unidentified clusters of impurities that had formed at the boundary but were left behind when it moved away. Regions adjacent to some precipitate particles contained higher than average concentrations of voids that were smaller than average in size. In general, the size of the voids in a specimen of this material was inversely proportional to their concentration. In addition to these gross irregularities, fine-scale variations in the concentrations of voids were observed that lay outside the scope of statistical fluctuations as evidenced by the simple test for randomness described by Minter and Foreman.[16]

Even more dramatic variations were observed[17] in some high-purity Fe irradiated in a partially recrystallized state. Large patches of

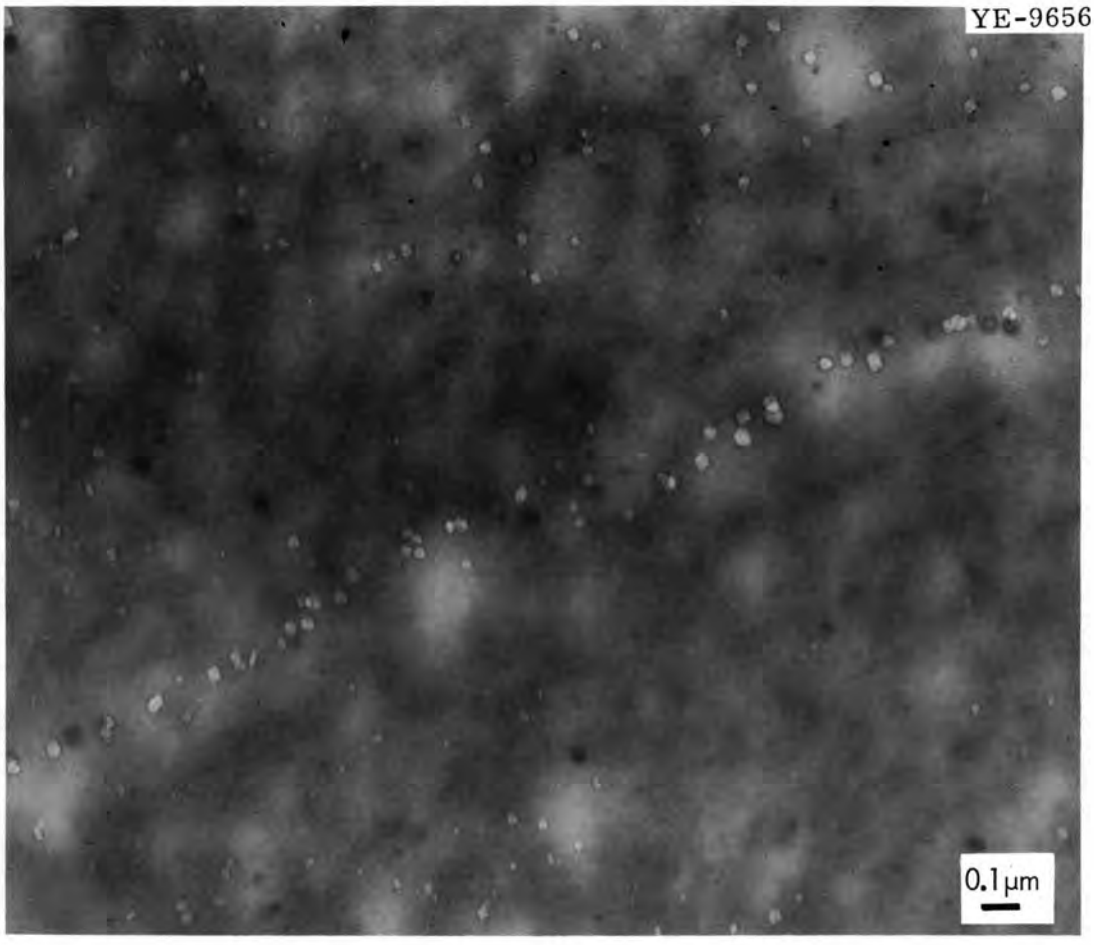

Fig. 5.4. Wall of Voids Formed in 99.9999% Pure Aluminum Irradiated in the High Flux Isotope Reactor to a Fluence of 3.5×10^{20} neutrons/cm^2 (> 0.8 Mev) at 50°C.

voids were surrounded by material free of voids, as can be seen in Fig. 5.5. In addition, lines or perhaps again walls of voids were detected. Recovered and recrystallized regions of the specimen were also greatly different: voids were both larger and more numerous in the recrystallized area.

In some commercial-purity Al, shells of voids like those in Fig. 5.6 were commonly observed.[18] We believe these to be analogous to the displacement damage halos noted in other materials irradiated at lower homologous temperatures. Measurements of the radii of the spheres of voids show that they are compatible with recoil distances for α-particles in Al.

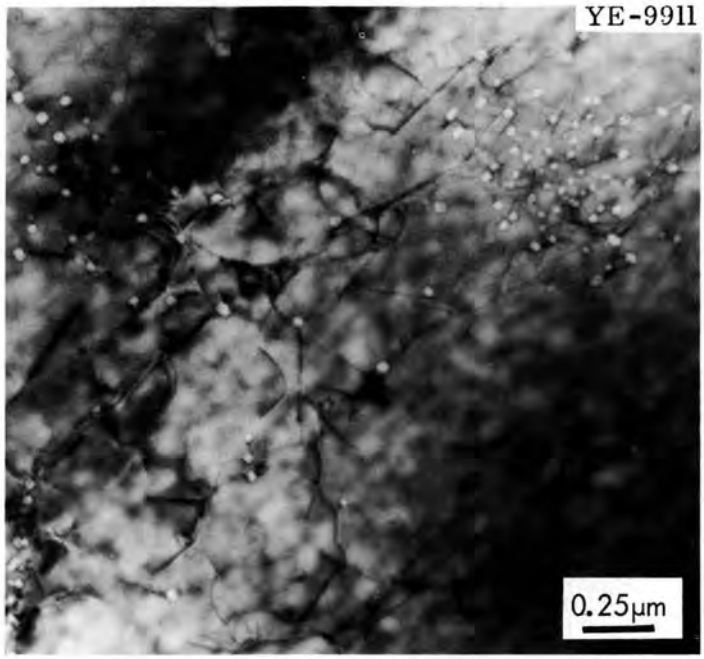

Fig. 5.5. Patch of Voids in High-Purity Iron Irradiated in the High Flux Isotope Reactor to a Fluence of 1.5×10^{21} neutrons/cm^2 (> 0.1 Mev) at 415°C.

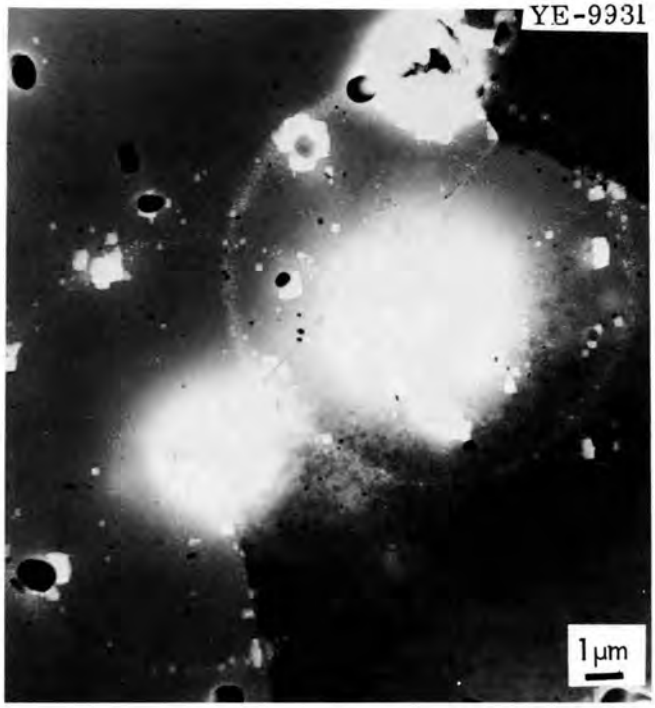

Fig. 5.6. Section Through Shells of Voids Formed Around Precipitate Particles in Commercial-Purity Aluminum (99%) Irradiated in the High Flux Isotope Reactor to a Fluence of 1×10^{22} neutrons/cm^2 (> 0.8 Mev) at 50°C.

In 270-grade Ni, both voids and dislocation loops tended to group in clusters, which again were shown to lie outside the range of statistical fluctuations.[19]

Very striking fluctuations in the sizes and concentrations of voids (see Fig. 5.7) were observed[20] over microscopic distances near a grain boundary in unalloyed V. A relatively low concentration of large voids existed within 0.6 μm of the boundary. Adjacent to this was a layer about 0.2 μm wide that contained a much higher concentration of smaller voids. Voids of intermediate size and concentration existed throughout the remainder of the grain.

Fig. 5.7. Variation in Void Structure Near a Grain Boundary of Commercial-Purity Vanadium Irradiated in the Experimental Breeder Reactor-II to a Fluence of About 1.7×10^{22} neutrons/cm^2 (> 0.1 Mev) at About 600°C.

Heterogeneous distributions were also reported for stainless steel specimens exposed to relatively low fluences.[21] In this case, however, the voids appeared to be associated with grown-in dislocation lines, as can be seen in Fig. 5.8. Such an association was not evident in any of

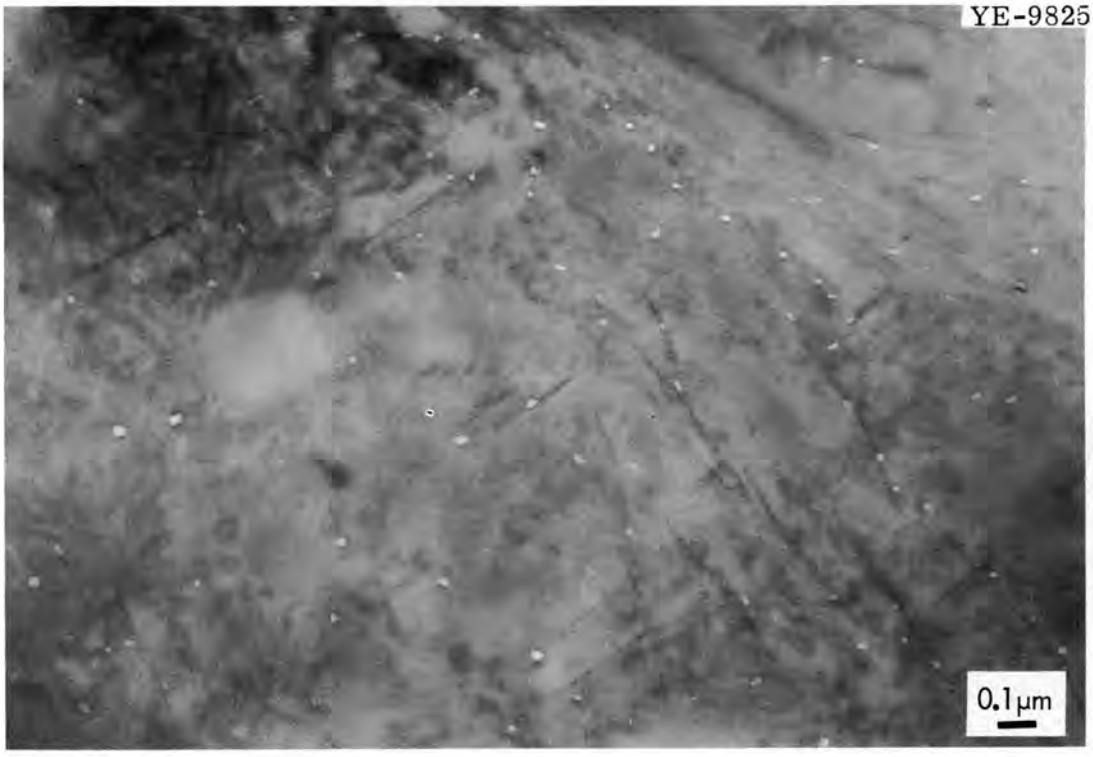

Fig. 5.8. Voids Associated with Grown-In Dislocations in Type 304 Stainless Steel Irradiated in the Experimental Breeder Reactor-II to a Fluence of 4×10^{21} neutrons/cm^2 (> 0.1 Mev) at 460°C.

the other materials examined. In other specimens, linear arrays of voids were observed (Fig. 5.9), but the high density of dislocation loops induced by radiation made it impossible to determine whether the voids were associated with dislocations. In addition, long strings of voids, such as those shown in Fig. 5.10, were observed but could not be associated with any structural irregularity.

We have attempted here to illustrate both the variety of forms that the heterogeneous distributions take and the range of materials in which they occur. In fact, all materials examined at this Laboratory have, under appropriate conditions, been shown to contain inhomogeneous distributions of voids.

Although the voids are polyhedral in all these systems, they are neither regular nor all of the same shape in a given specimen. Figure 5.11, for example, shows a variety of shapes within a small area of a stainless steel specimen. An even more striking example of shape variations in high-purity Fe was reported by Kulcinski et al.[22]

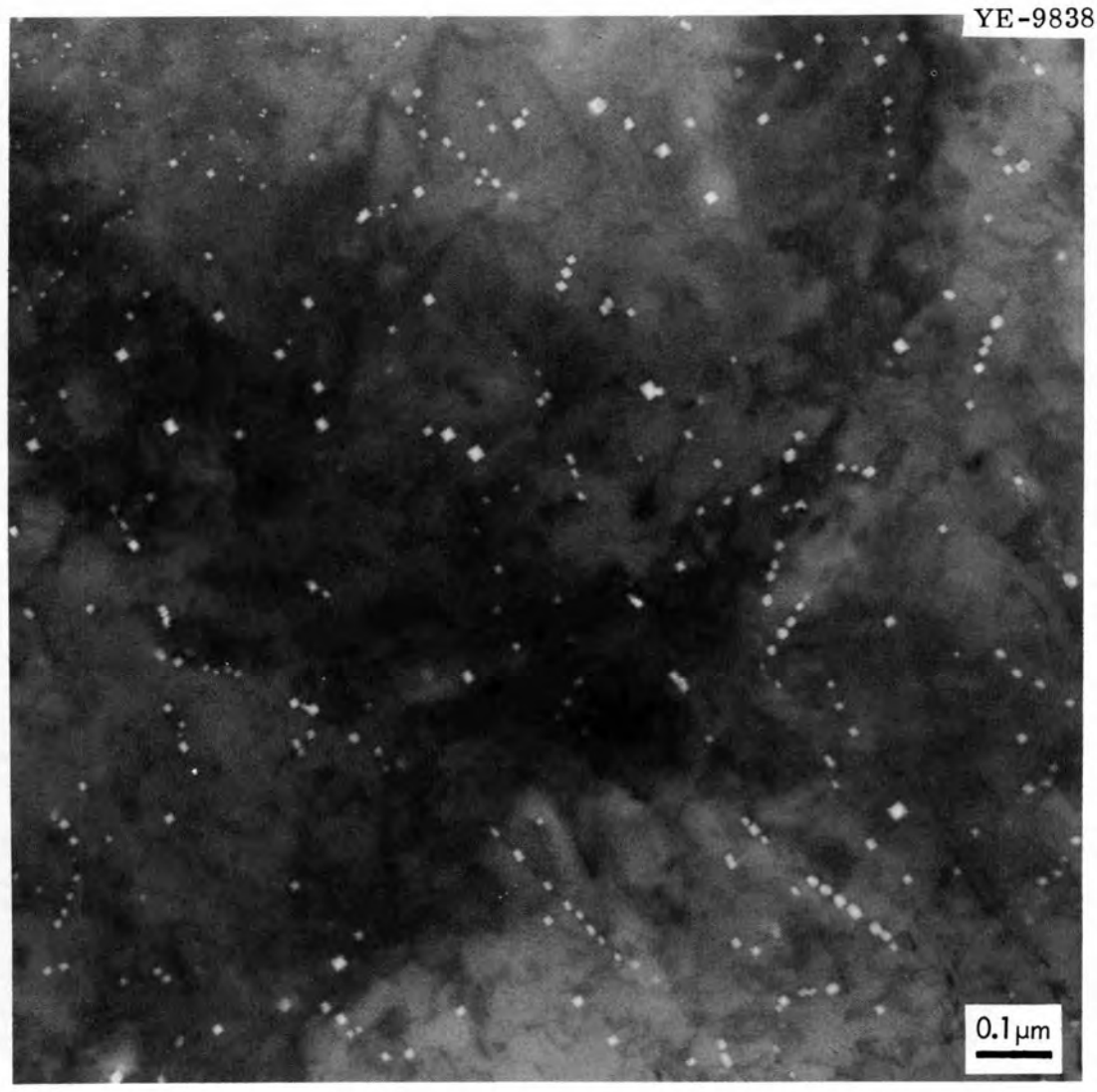

Fig. 5.9. Nonrandom Distribution of Voids in Type 304 Stainless Steel Modified by the Addition of 0.2% Ti Irradiated in the Oak Ridge Research Reactor to a Fluence of 1.4×10^{21} neutrons/cm^2 (> 0.1 Mev) and 1.8×10^{21} neutrons/cm^2 (Thermal) at 550°C.

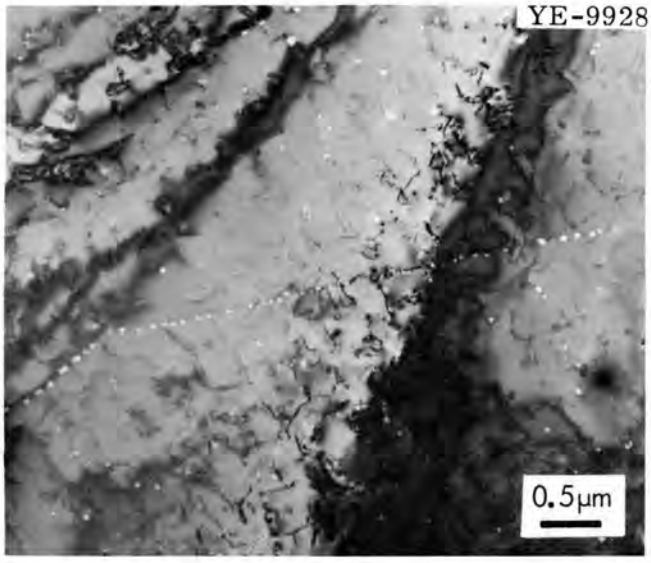

Fig. 5.10. Linear Array of Voids in Type 304 Stainless Steel Modified by the Addition of 0.2% Ti Irradiated in the Oak Ridge Research Reactor to a Fluence of 1.4×10^{21} neutrons/cm^2 (> 0.1 Mev) and 1.8×10^{21} neutrons/cm^2 (Thermal) at 550°C.

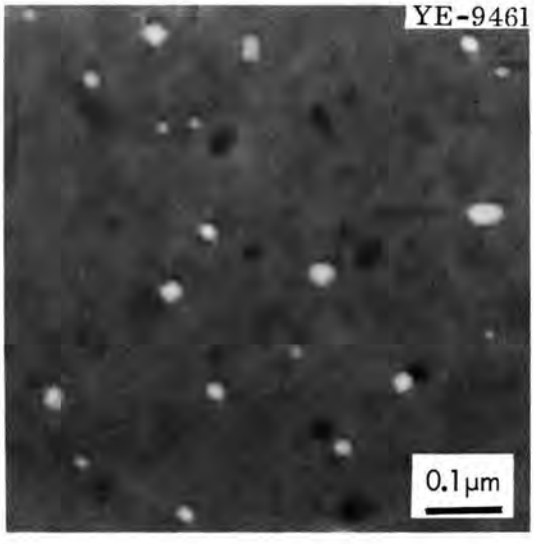

Fig. 5.11. Variation in Shape of Voids in Type 304 Stainless Steel Irradiated in the Experimental Breeder Reactor-II to a Fluence of 9×10^{21} neutrons/cm^2 (> 0.1 Mev) at 470°C.

In Ni, the shape of the voids appeared to vary with the irradiation temperature.[20] At low temperatures, most voids were octahedral, but significant numbers were not consistent with this shape. Figure 5.12 shows voids near a twin boundary that clearly do not have their sides parallel to {111} planes, which would be required if they were octahedra. At

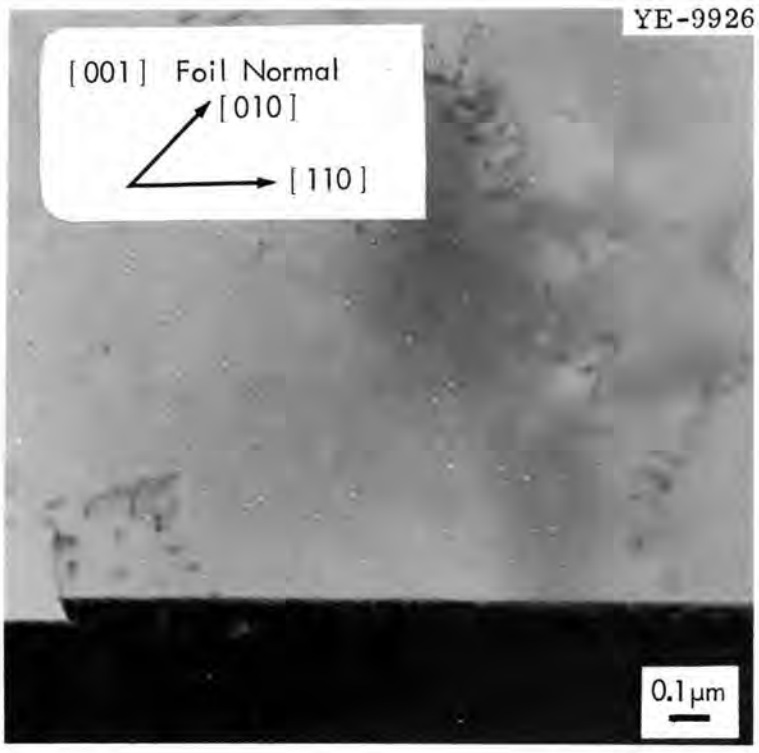

Fig. 5.12. Voids in 270-Grade Nickel with Shapes Other than Octahedra. The specimen was irradiated in the Experimental Breeder Reactor-II to a fluence of 1.4×10^{20} neutrons/cm^2 (> 0.1 Mev) at 410°C.

higher irradiation temperatures, many of the voids were shaped like elongated rods, as shown in Fig. 5.13.

Nonequiaxed voids were also observed[23] in high-purity Al irradiated at higher temperatures; the ribbon, plate, and rod shapes shown in Fig. 5.14 could be identified clearly. In addition, a strong association was noted between voids and precipitate particles. Generally the particles were located near the ends of elongated voids.

Although the dislocation loops have been less extensively studied, they show corresponding variations in concentration and shape. Clustering of loops in Ni was noted earlier, and inhomogeneous distributions of loops were reported[15] in Al. Amorphous, or amoeboid-shaped, loops are common in stainless steels irradiated to low fluences,[22] as is illustrated in Fig. 5.15.

In contrast to the behavior in high-purity Al, voids were not formed in commercial-purity material until very high fluences were reached.[15]

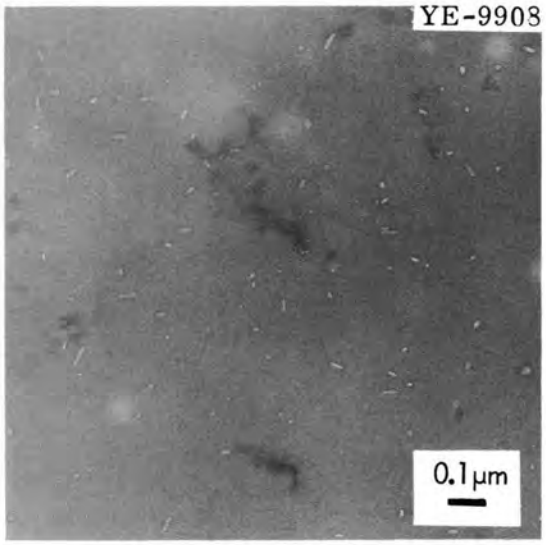

Fig. 5.13. Elongated Voids in 270-Grade Nickel Irradiated in the Experimental Breeder Reactor-II to a Fluence of 1.4×10^{20} neutrons/cm^2 (> 0.1 Mev) at 524°C.

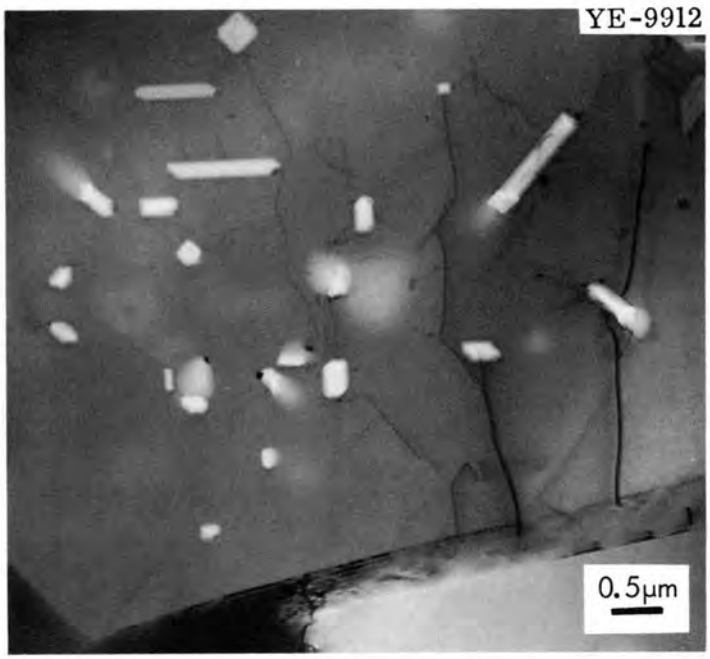

Fig. 5.14. Variety of Void Shapes Formed in 99.9999% Pure Aluminum Irradiated in the Oak Ridge Research Reactor to a Fluence of 4×10^{20} neutrons/cm^2 (> 0.1 Mev) at 150°C.

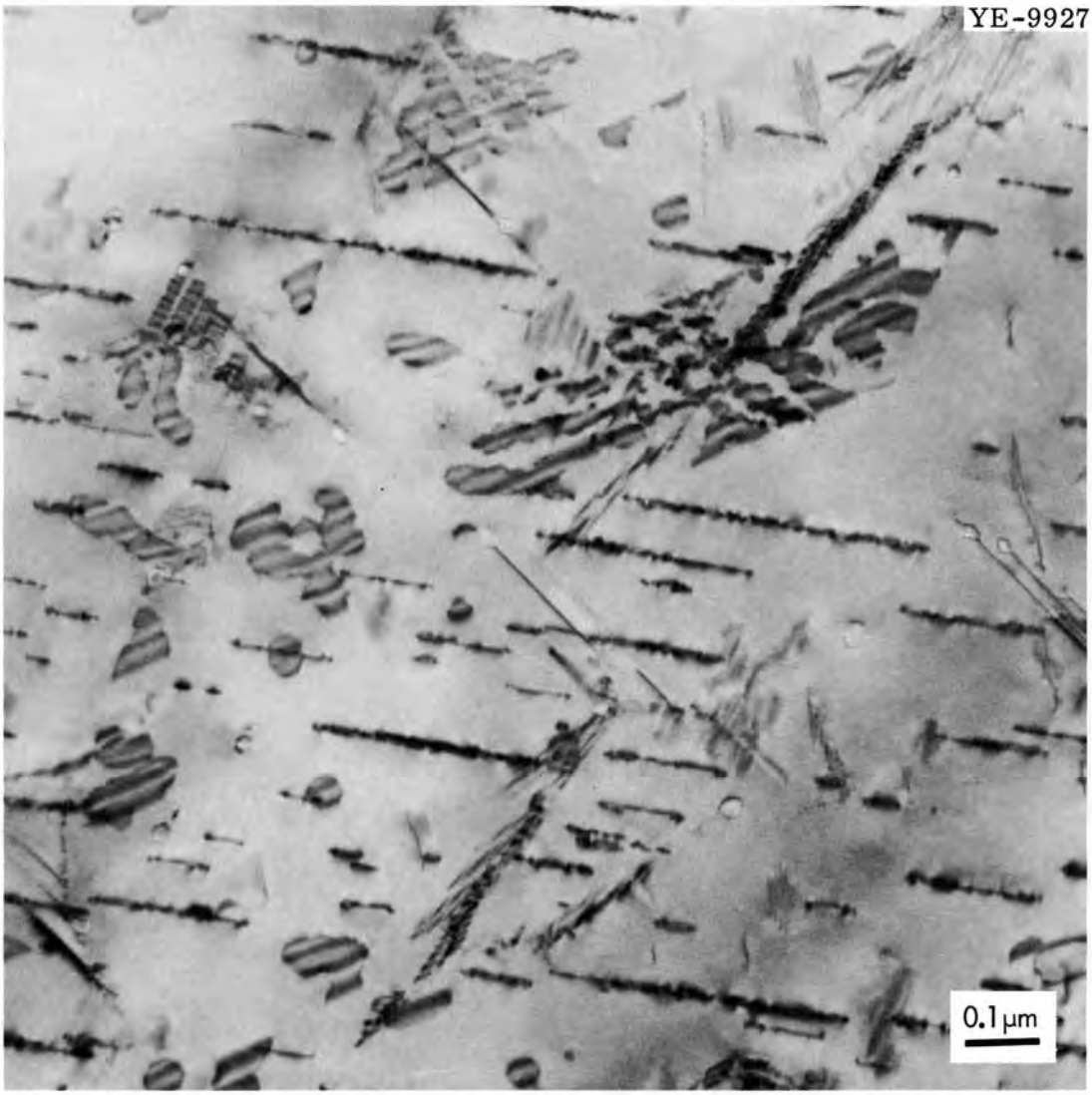

Fig. 5.15. Structure of Dislocation Loops in Type 304 Stainless Steel Irradiated in the Experimental Breeder Reactor-II to a Fluence of 2.8×10^{21} neutrons/cm^2 (> 0.1 Mev) at 462°C.

At lower levels, the damage consisted of dislocation loops that were very heterogeneously distributed. In the example shown in Fig. 5.16 the loops are clustered near the grain boundary and grown-in dislocation lines. Similar effects have also been reported for Cu (ref. 24) and Ni (ref. 21).

From a practical standpoint, the heterogeneous aspects of the damage may play a disproportionately large role in determining the physical and mechanical properties of irradiated materials. For example, in commercial-purity Al, layers of large voids were observed[15] adjacent to grain boundaries, as can be seen in Fig. 5.17. This material is much like a sheet

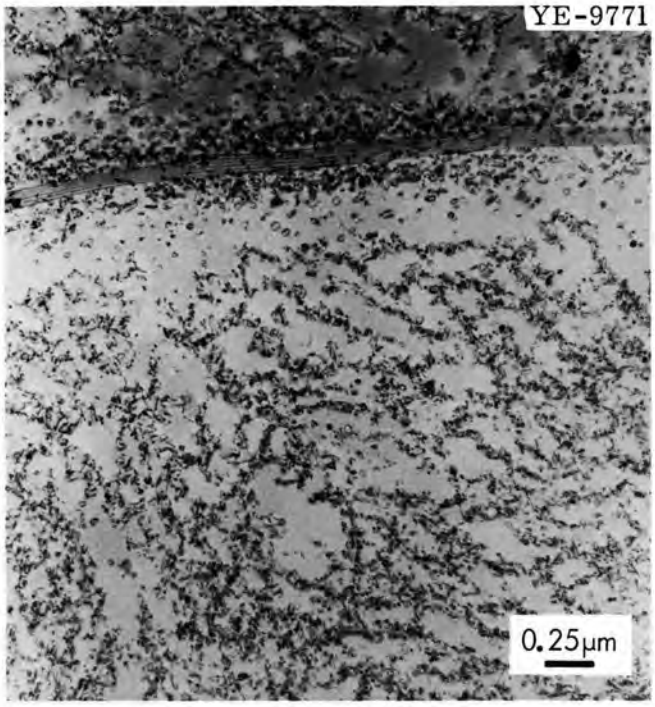

Fig. 5.16. Concentration of Dislocation Loops Produced by Irradiation Near a Grain Boundary and Grown-In Dislocations in Commercial-Purity Aluminum Irradiated in the High Flux Isotope Reactor to a Fluence of 1×10^{21} neutrons/cm^2 (> 0.8 Mev) at 50°C.

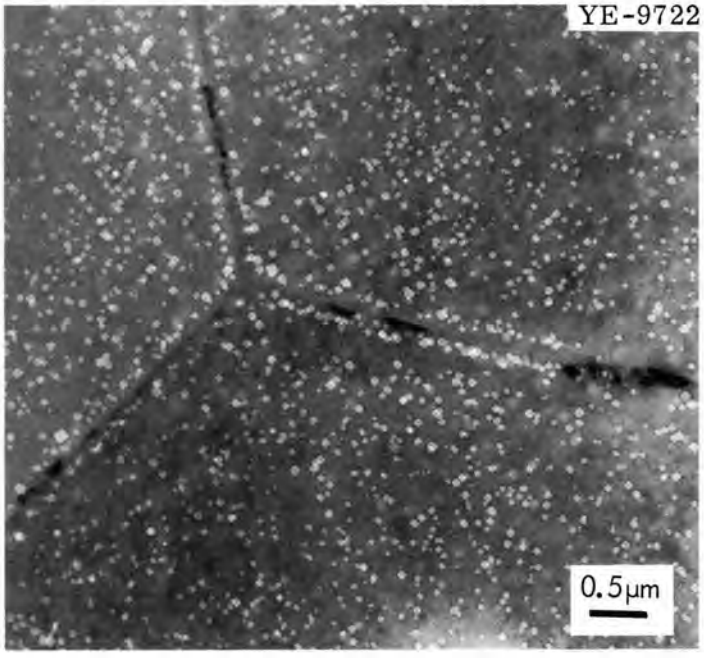

Fig. 5.17. Layers of Voids Adjacent to Grain Boundaries Formed in Commercial-Purity Aluminum Irradiated in the Oak Ridge Research Reactor to a Fluence of 1.5×10^{22} neutrons/cm^2 (> 1 Mev) at 45°C.

of postage stamps; the individual grains, like the stamps, are perforated near their boundaries. It is not at all difficult to imagine that the mechanical integrity of this material may be limited more by the large voids near the grain boundaries than by the "average" voids within the grains.

These observations indicate that the mechanisms of nucleation and growth of voids are more complicated than those proposed in simple models and that models that require a homogeneous distribution of voids cannot be generally applicable. In particular, the heterogeneous distributions of voids suggest that structural or chemical imperfections influence the nucleation of voids. The examples that most clearly demonstrate this were taken from materials irradiated in recovered or partially recrystallized states or, in the case of high-purity Al, from specimens that were allowed to recrystallize at room temperature. Under these conditions, the distribution of impurities would be determined by the prior working conditions and might well be inhomogeneous.

The irregular void shapes may be explained in terms of a heterogeneous mechanism of nucleation in which the nucleating agent influences the subsequent growth of the void. In quenching experiments, elongated cigar-shaped voids were observed[25,26] and shown to be associated with precipitate particles. In ORNL work, particles were clearly identified with voids only in the case of high-purity Al. The irregular shapes and the elongated voids in Ni suggest that submicroscopic particles may be involved. If a void were growing simply by the condensation of vacancies at a nonwetting particle, we should expect roughly equiaxed growth. The elongated growth from one side of a particle suggests the possibility that the nucleating agent is a small gas bubble attached to the particle. Interfaces between particles and the matrix have been observed to be preferred sites for the nucleation of bubbles of He gas produced by transmutation during high-temperature irradiation.[27] In addition, when sintered Al powder was bombarded with α-particles at 150°C, He bubbles formed at the Al_2O_3 particles.[28]

We believe that our warning against generalizing from limited information applies to these observations as well. We have shown in several

systems that voids are heterogeneously distributed. All of these observations were made on materials irradiated to relatively low fluences in which the irregularities are easily identified. At higher fluences, the distributions appear superficially to be homogeneous, but no critical tests have been conducted to prove this.

It is possible that more than one nucleation process forms the void structures observed. At low fluences a heterogeneous mechanism, possibly involving resident impurities, may predominate. We cannot be very specific about mechanisms at any higher fluence except to comment that neither homogeneous nor spike nucleation is likely to be dominant. The time required for steady-state concentrations of point defects to build up at these temperatures ought to be short compared with irradiation times. Therefore, if homogeneous nucleation occurs, it should be evident after very short irradiation times — when the most heterogeneous distributions of voids are observed. Spike nucleation ought to occur at a linear rate, starting with the beginning of the irradiation. Observations on stainless steel[22] showed that at an irradiation temperature of 470°C the nucleation rate increases with increasing fluence (at least up to 2×10^{22} neutrons/cm^2). The dominant mechanism in this material at higher fluences, therefore, is one that becomes increasingly probable as the fluence increases — that is, it is not simple spike nucleation.

The possibility that gases generated by neutron irradiation are involved in the nucleation of voids cannot be discounted at this point. There is evidence that the presence of He does increase void concentrations,[10,20] but we do not know what mechanisms are involved or whether or not this is the principal cause for the nucleation of voids.

Changes in Density and Microstructure Induced by Irradiation in Cold-Worked Type 304 Stainless Steel (E. E. Bloom, J. O. Stiegler)

Table 5.1 lists the results of measurements of the immersion density of specimens of type 304 stainless steel irradiated in two conditions: (1) 10% cold work and (2) 10% cold work plus 24 hr at 482°C plus 100 hr at 700°C. These specimens were irradiated in a specimen holder[29] that extended from 4.5 to 6.75 in. above the midplane in a row 2 position of EBR-II. The specimens were irradiated at ambient Na temperature, estimated

Table 5.1. Density Change Induced by Irradiation in 10% Cold-Worked Type 304 Stainless Steel

Specimen Number	Treatment Before Irradiation	Irradiated Density[a] (g/cm^3)	Density[b] Change (%)
B0914	1 hr at 1038°C + 10% cold work + 24 hr at 482°C + 100 hr at 700°C	7.8245	−0.62
B0920	1 hr at 1038°C + 10% cold work	7.8787	+0.06
B0921	1 hr at 1038°C + 10% cold work	7.8816	+0.10

[a]Average of five measurements.

[b]Based on the unirradiated density of 7.8737 that was determined for specimens of this heat in the annealed condition.

to be 400°C, for an exposure of 11,035 Mwd or a fast-neutron fluence of 2.8×10^{22} neutrons/cm^2 (> 0.1 Mev). As can be seen from the data listed in Table 5.1, a specimen that was cold worked 10% and then aged at 482 and 700°C decreased 0.62% in density. This decrease is in reasonable agreement with what would be expected from annealed type 304 stainless steel irradiated under similar conditions. In comparison, two specimens irradiated in the 10% cold-worked condition both increased slightly in density (within the accuracy of the measurement technique).

A specimen irradiated in the 10% cold-worked condition is being examined by transmission electron microscopy. A typical microstructure is shown in Fig. 5.18. For comparison, a specimen of annealed type 304 stainless steel (cladding for EBR-II driver fuel) irradiated at about the same temperature to 1.2×10^{22} neutrons/cm^2 (> 0.1 Mev) is shown in Fig. 5.19. The distribution of void sizes appears to be about the same in each case. The concentration of voids in the specimen irradiated in the 10% cold-worked condition was about 2.1×10^{14} voids/cm^3 or about one-twentieth what would be expected[30] in annealed type 304 stainless steel irradiated at the same conditions. Specimens cold worked 10% and then aged 24 hr at 482°C and 100 hr at 700°C have not been examined by

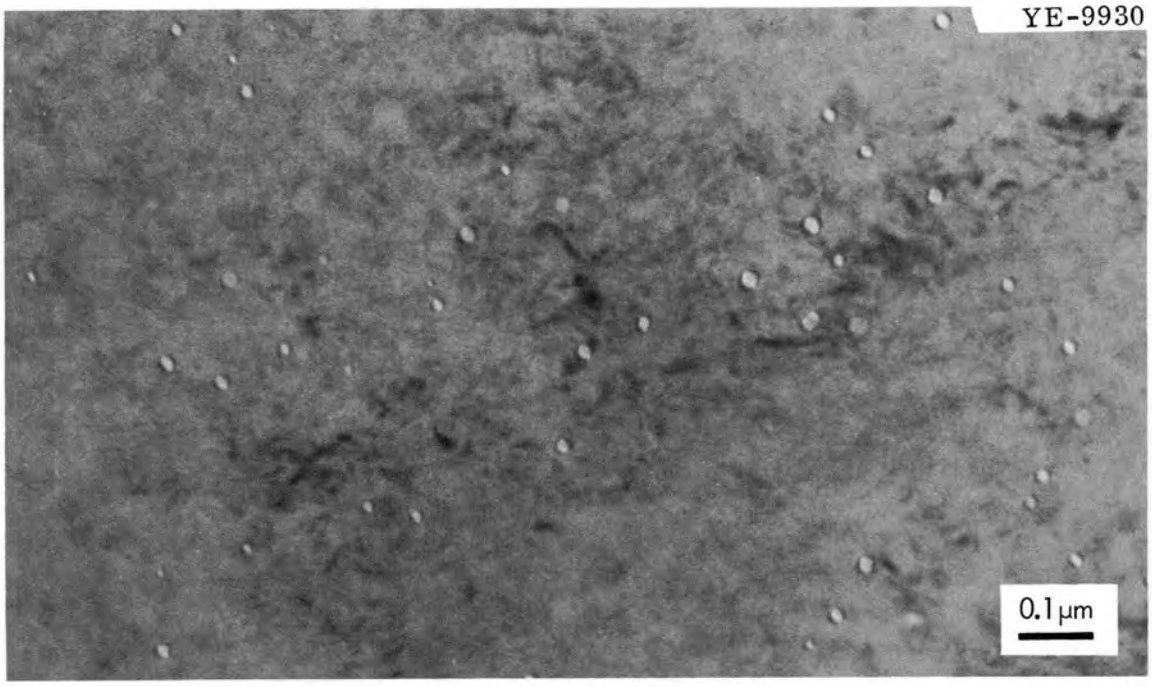

Fig. 5.18. Microstructure of Type 304 Stainless Steel Cold Worked 10% Before Irradiation at 400°C to 2.8×10^{22} neutrons/cm^2 (> 0.1 Mev).

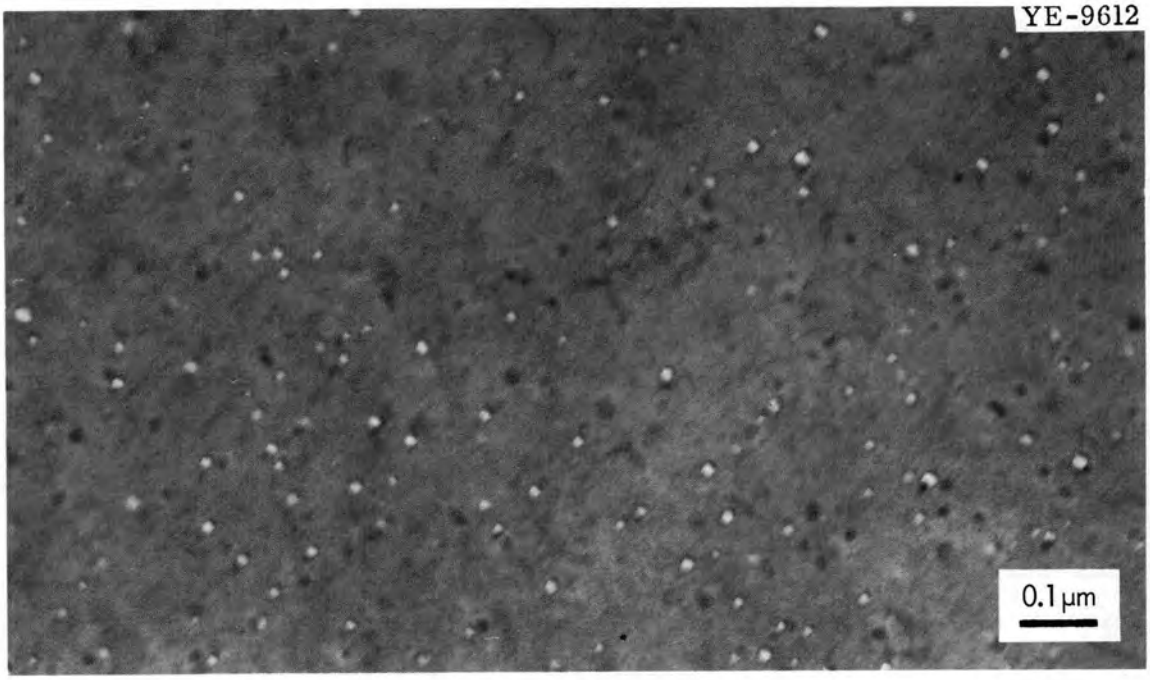

Fig. 5.19. Microstructure of Annealed Type 304 Stainless Steel Irradiated at 400°C to 1.2×10^{22} neutrons/cm^2 (> 0.1 Mev).

transmission electron microscopy. It is possible, however, that this heat treatment caused sufficient recovery of the dislocation structure that the material swelled as if it were in the annealed condition.

These results indicate that for these irradiation conditions cold work reduces the amount of swelling primarily through decreasing the concentration of voids. The use of cold work as a technique for controlling the amount of swelling in LMFBR components will depend upon the dependency of the swelling in cold-worked and annealed materials upon fluence and temperature. Since material cold worked 10% and annealed at 482 and 700°C before irradiation swelled essentially the same as annealed material, the use of cold-worked material at irradiation temperatures above 700°C would certainly be questionable.

Effects of Irradiation on the Mechanical Properties of Type 316 Stainless Steel (E. E. Bloom, J. O. Stiegler)

The effects of irradiation at temperatures between 350 and 750°C on the mechanical properties of type 316 stainless steel are being investigated. Experimental variables include preirradiation heat treatment, irradiation temperature, and fast- and thermal-neutron fluence. Mechanical properties being evaluated include tensile and creep-rupture properties. The composition of the heat of material being investigated was reported previously.[31]

Figure 5.20 shows the available data on the effects of irradiation in the ORR at 550 and 650°C to 1.8×10^{21} neutrons/cm^2 (thermal) and 1.4×10^{21} neutrons/cm^2 (> 1 Mev) on the creep-rupture properties of this heat of type 316 stainless steel when tested at the irradiation temperature. The specimens were annealed 1 hr at 1050°C either before irradiation or before testing.

Results for specimens irradiated and tested at 550°C are limited but do suggest that the reduction in ductility is very sensitive to the strain rate. In a tensile test the total elongation was reduced from 40.6% to 21.8%, whereas in creep-rupture tests at 40,000 psi the total elongation was reduced from 7.3% to 1.0% as a result of the irradiation.

Data obtained during the last reporting period suggest that at 650°C the plot of the stress-rupture life changes in slope at a stress

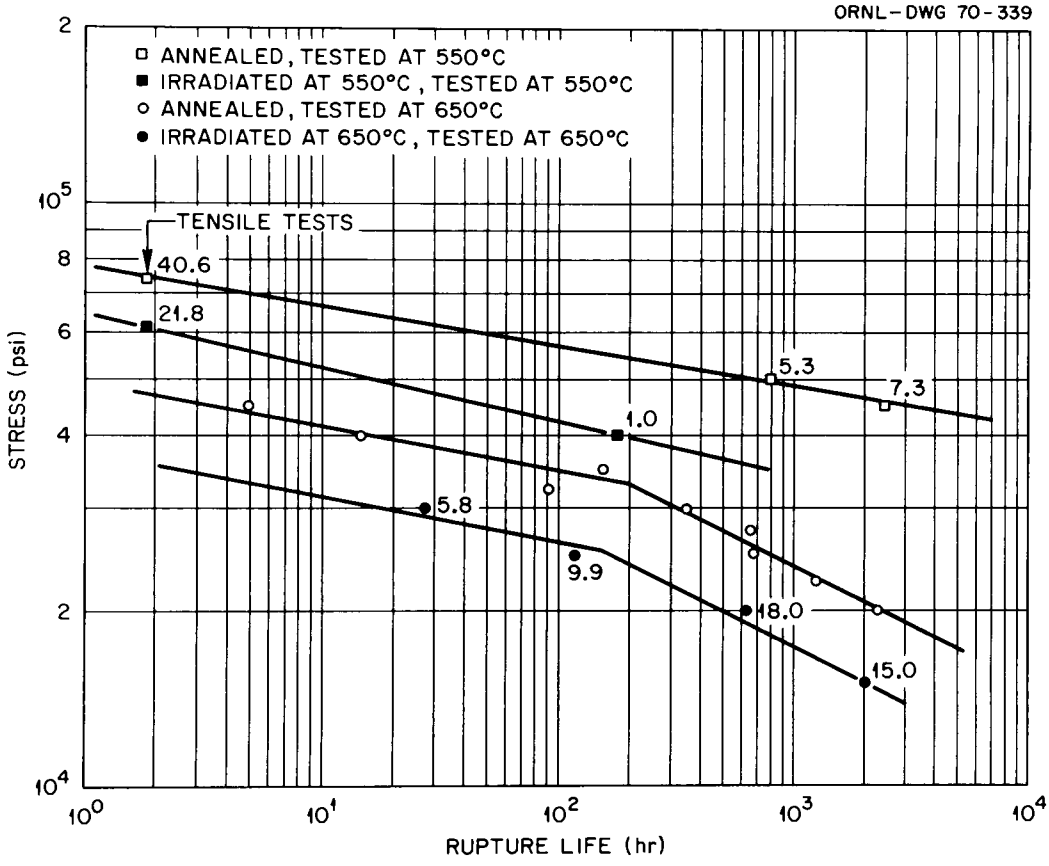

Fig. 5.20. Effect of Irradiation on the Rupture Life of Type 316 Stainless Steel at 550 and 650°C. Numbers in parentheses indicate the fracture strain.

of 30,000 to 35,000 psi. At stresses below 30,000 to 35,000 psi, irradiation and thermal aging combine to reduce rupture life by four-fifths, and, at higher stress levels, by about an order of magnitude. The ductility of specimens irradiated at 650°C in the annealed condition was reduced from between 40 and 60% to between 10 and 20% for rupture lives longer than 600 hr.

The results of tensile tests on specimens that had received various levels of cold work before irradiation at 550 and 650°C are listed in Table 5.2.

The yield strength of specimens irradiated at 550°C was significantly higher than that of thermal controls aged 4000 hr at 550°C; this difference suggests that some displacement damage occurred. At 650°C, the yield strengths of irradiated and thermal control specimens were the same.

Table 5.2. Tensile Properties[a] of Type 316 Stainless Steel at 550 and 650°C

Condition	Stress, psi				Elongation, %			
	Yield		Ultimate		Uniform		Total	
	Unirradiated[b]	Irradiated[c]	Unirradiated[b]	Irradiated[c]	Unirradiated	Irradiated	Unirradiated	Irradiated
	× 10^3	× 10^3	× 10^3	× 10^3				
Properties at 550°C								
Annealed at 1050°C	18.9	24.6	71.5	66.2	37.2	19.3	40.6	20.8
5% Cold Work		35.4		64.0		16.0		19.7
10% Cold Work		50.8		62.8		3.3		4.0
20% Cold Work		63.6		80.3		7.7		8.2
Properties at 650°C								
Annealed at 1050°C	27.5	26.5	54.6	40.8	17.7	8.0	39.9	10.4
5% Cold Work	35.7		54.3		15.7		41.4	
10% Cold Work	38.9	37.7	54.6	46.4	13.3	3.7	34.2	4.0
20% Cold Work	46.6	44.8	57.7	51.8	9.5	2.4	34.2	2.5

[a] Tested at 0.002 min^{-1}.

[b] Specimens aged 4000 hr at the test temperature before testing.

[c] Irradiated at the test temperature to 1.8×10^{21} neutrons/cm^2 (thermal) and 1.4×10^{21} neutrons/cm^2 (> 1 Mev).

Cold working before irradiation increased the postirradiation yield stress after irradiation and decreased the uniform and total elongations after irradiation for specimens irradiated at either 550 or 650°C.

Titanium-Modified Types 304 and 304L Stainless Steel

Effect of Planetary Swaging and Annealing Temperature on the Biaxial Stress-Rupture of Titanium-Modified Type 304L Stainless Steel Tubing (R. T. King)

The biaxial stress-rupture properties of the first batch of tubing of type 304L stainless steel modified with 0.2% Ti were reported earlier.[32,33] This report describes the testing of the second batch of tubing produced from Allvac Metals Company heat 3756, in which the effects of planetary swaging and drawing are compared and the effect of final annealing temperature is investigated.

All tubing of the second batch was produced by mandrel drawing with intermediate anneals in H_2 for 40 min at 1200°C except for the final 6.5% cold-working pass, which was planetary swaging for one-half the batch of tubing and mandrel drawing for the remainder of the batch.

The tubing was then ultrasonically inspected for longitudinal and transverse discontinuities that produced stronger signal responses than standard 0.002-in.-deep × 0.030-in.-long spark-machined reference discontinuities, and for variations in wall thickness. The tubing tested in this series exhibited virtually no discontinuities of any size at the sensitivity settings of the instruments employed.

The 4-in.-long specimens were prepared in the usual manner.[32] All of the drawn tubing specimens were then annealed for 1 hr at 925°C in H_2, but planetary-swaged specimens were annealed for either 1 hr at 925°C or 1 hr at 1038°C in H_2. The specimens were then tested at nominal temperatures of 550 and 650°C; the tubes failed at points where their maximum temperatures were within ±5°C of the nominal temperature, but a 7°C/in. temperature gradient existed along the remainder of the specimens. Testing pressures were calculated from the minimum measured wall thickness to produce tangential hoop stresses that would cause rupture times ranging from a tenth to several hundred hours.

The two important variables under examination in this work are fabrication technique and final annealing temperature. The rupture times of planetary-swaged and drawn tubing, both annealed at 925°C, are compared in Fig. 5.21 for tests at 550 and 650°C. Although there is a slight amount of scatter in the test results for 550°C (part of which was caused by failures of the weldments for end caps), the rupture times for planetary-swaged and drawn tubes are essentially identical for any given applied stress at 550 and 650°C. In Fig. 5.22, a similar plot comparing planetary-swaged tubing annealed at either 925 or 1038°C indicates that both annealing treatments produce nearly identical rupture times.

Ductility was measured two ways: first, the total circumferential strain at the point of failure was measured by wrapping tape around the failed region, stripping it off, and measuring its length; secondly, the uniform strain about 0.25 in. from the failed region was measured with a

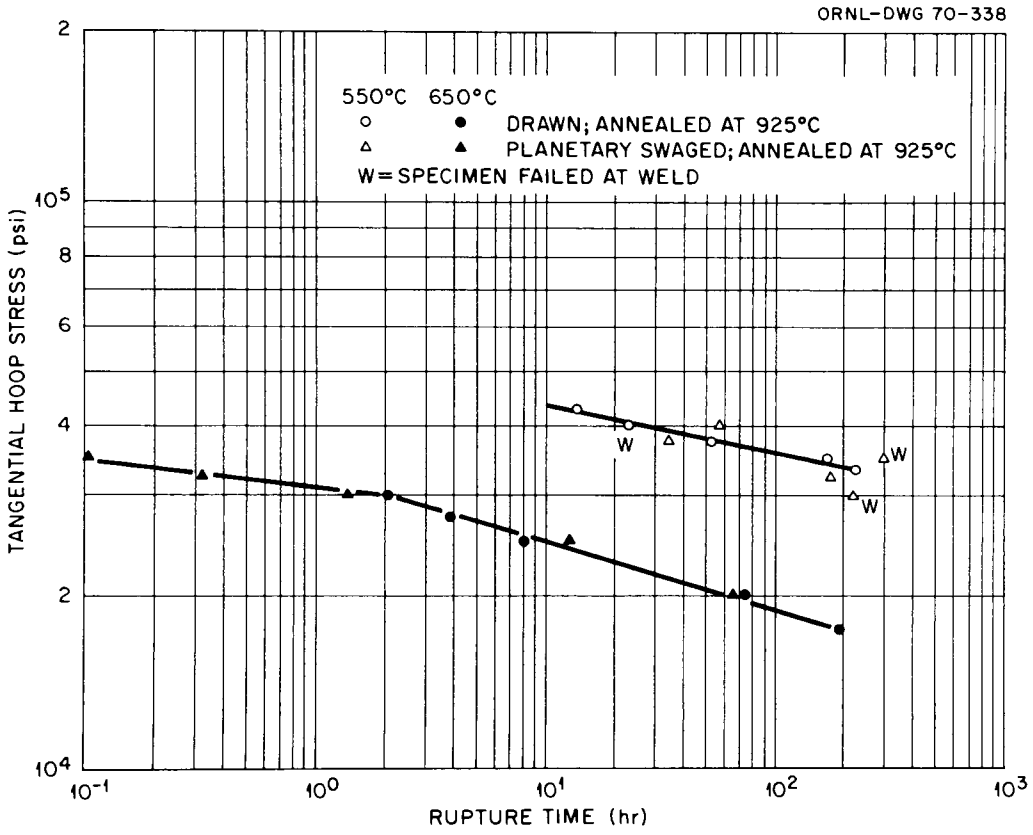

Fig. 5.21. Effect of Planetary Swaging on the Stress-Rupture Behavior of 0.2% Ti-Modified Type 304L Stainless Steel Tubing at 550 and 650°C.

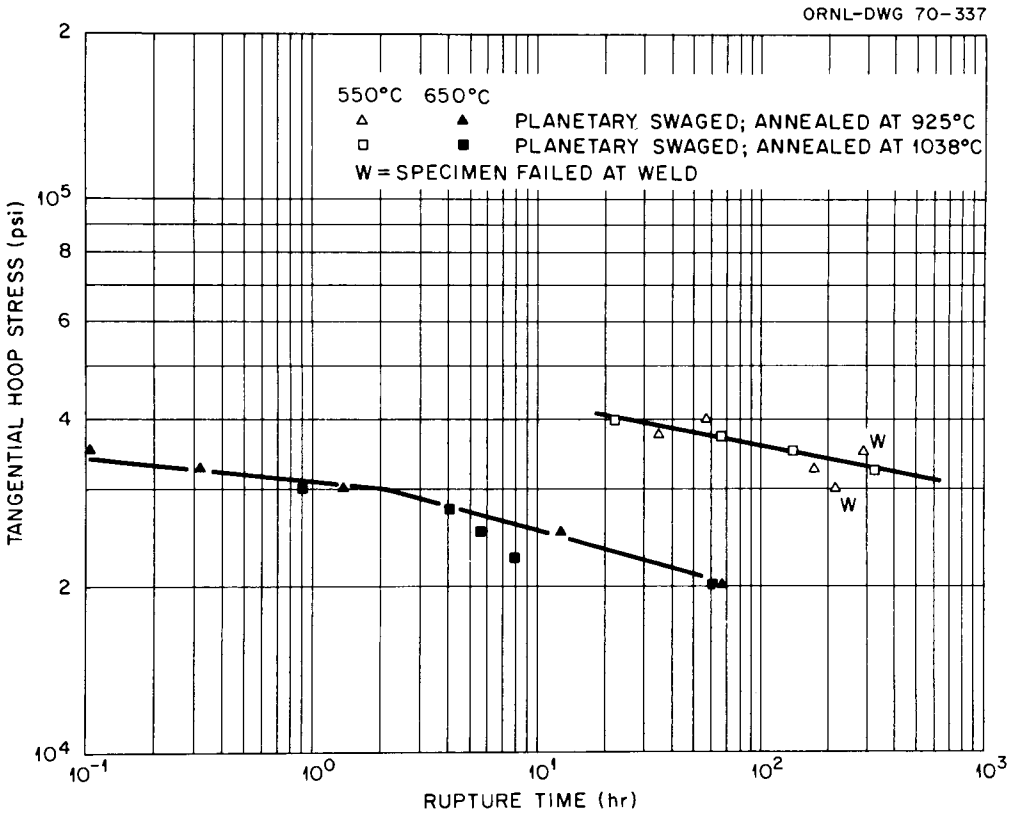

Fig. 5.22. Effect of Annealing Temperature on the Stress-Rupture Behavior of 0.2% Ti-Modified Type 304L Stainless Steel Tubing at 550 and 650°C.

knife-edge micrometer. The total measurements of circumferential strain are only reproducible to ±4% strain, whereas those of the uniform strain are reproducible to about ±2% strain. A circular cross section was assumed to be elliptical for the latter measurements, and the circumferences, C, were calculated from

$$C = 2\pi \left(\frac{a^2 + b^2}{2} \right)^{\frac{1}{2}} ,$$

where a and b are the major and minor axes of the ellipse.

The total circumferential strains of all tubing tested at 550 and 650°C are plotted versus rupture time in Figs. 5.23 and 5.24, respectively. Although the data are represented by a single scatter band at each temperature, there is a strong tendency for the drawn tubing to exhibit lower ductility than the planetary-swaged tubing. The statistical significance of this observation is not clear for this small number

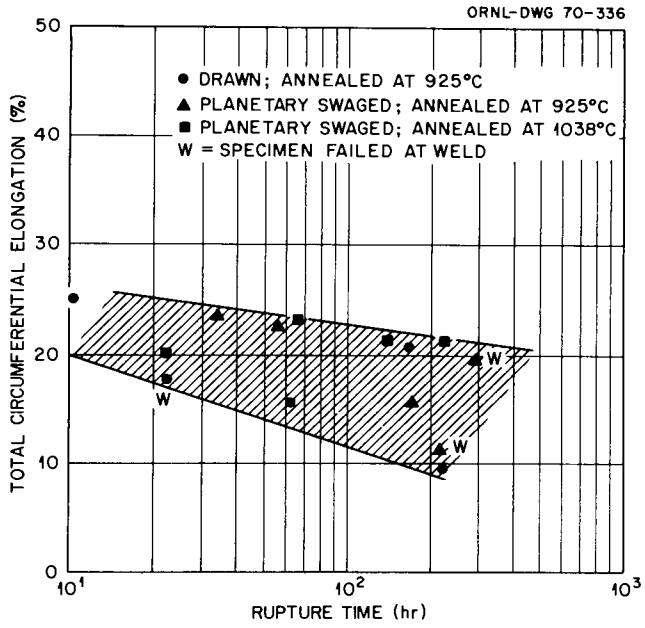

Fig. 5.23. Ductility of 0.2% Ti-Modified Type 304L Stainless Steel Tubing at 550°C.

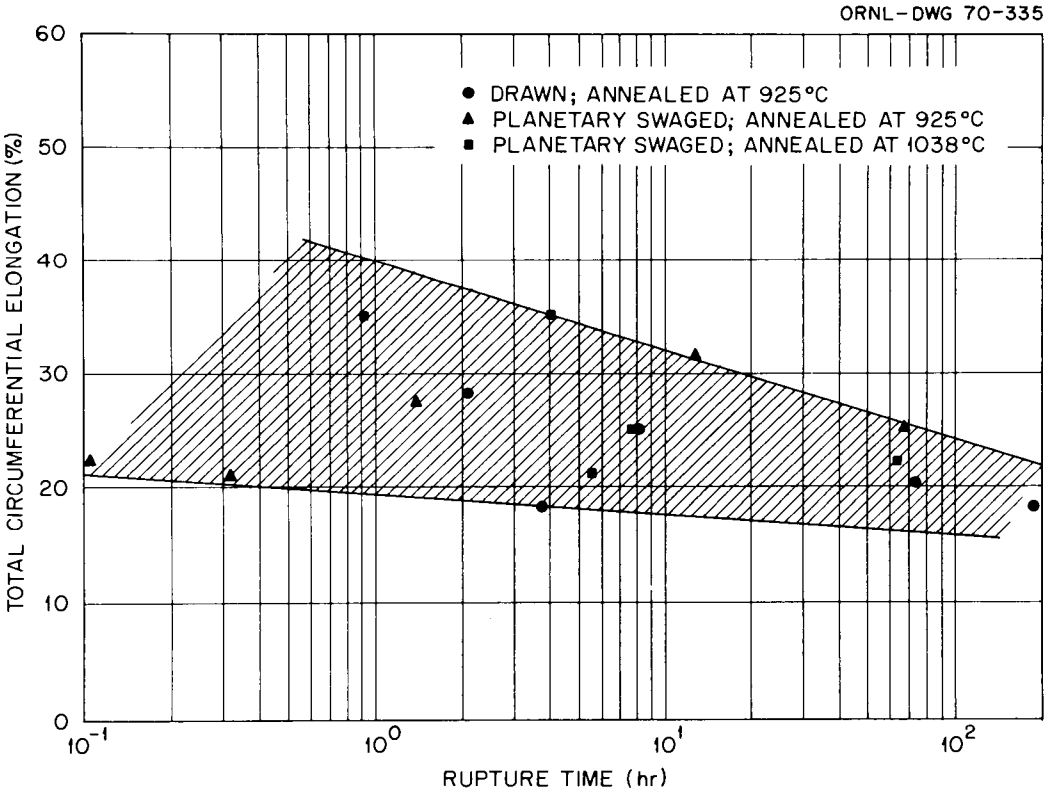

Fig. 5.24. Ductility of 0.2% Ti-Modified Type 304L Stainless Steel Tubing at 650°C.

of tests, however. At both temperatures the total elongations are sensitive to strain rate, tending toward lower average rupture strains with increasing testing times. It is quite significant that the lowest elongations for these defect-free tubes (as determined by ultrasonic inspection) at 550 and 650°C were 9.5 and 18.5%, respectively. Earlier work[32] (at 600 and 700°C test temperatures) indicated that annealed tubing containing ultrasonically detectable discontinuities may fail after only 1.4% strain. In fact, only one of the defect-free specimens that failed normally (not at a weld) at 550°C had less than 15% ductility.

The uniform strains measured at 550 and 650°C are shown in Figs. 5.25 and 5.26, respectively. As was true for the total strains, the uniform strains tend to decrease slightly with increasing rupture time. Furthermore, there is a strong tendency for planetary-swaged tubes to have higher uniform strains than drawn tubes at 550°C, although the effect of

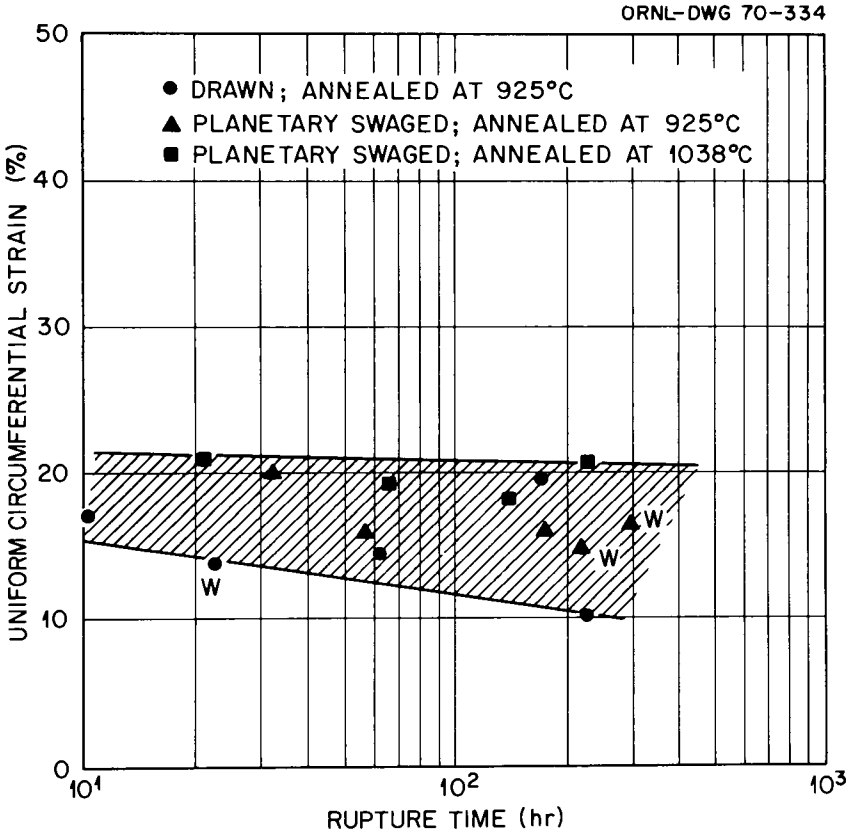

Fig. 5.25. Uniform Circumferential Strain of 0.2% Ti-Modified Type 304L Stainless Steel Tubing at 550°C.

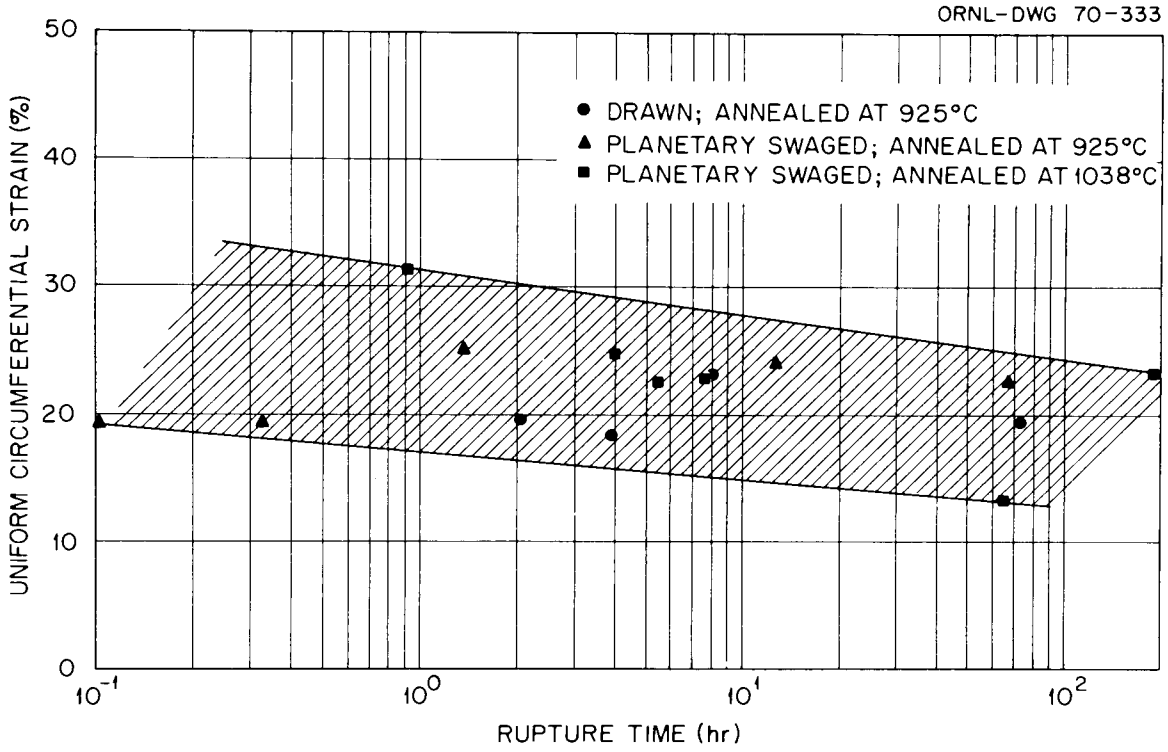

Fig. 5.26. Uniform Circumferential Strain of 0.2% Ti-Modified Type 304L Stainless Steel Tubing at 650°C.

this fabrication variable on uniform strain is not as noticeable at the 650°C test temperature. No significant differences in uniform-strain behavior can be discerned between planetary-swaged tubes annealed at 925°C and those annealed at 1038°C at either test temperature, nor were any highly significant differences observed in total-elongation characteristics.

It is not possible to conclude from this work whether the slight differences between the strain behavior of planetary-swaged and drawn tubing specimens are due to the texture differences reported by Reimann and Nilsson,[34] to possible microstructural differences, or to differences in surface irregularities or flaws.

It is highly significant that the minimum uniform strains measured at 550 and 650°C were 10 and 13.5%, respectively, since the useful ductility of a tube for some reactor designs may be defined in terms of uniform strain. The ratios of uniform strain to total circumferential strain (R) for all tests at 550 and 650°C are plotted versus the

tangential hoop stress in Figs. 5.27 and 5.28, respectively. Ratios greater than one occur occassionally, but they simply reflect measuring errors, since the uniform strain cannot exceed the total strain. At 550°C (Fig. 5.27), almost all of the strain that occurs in low-stress tests is uniform, while at higher stresses there is a tendency for more localized deformation to occur during the latter portion of a test. At 650°C (Fig. 5.28), no such trend is observed; however, the lowest value of R observed was R = 0.48, and in the majority of the tests uniform straining accounted for more than three-quarters of the total strain. There were no strongly noticeable effects of either fabrication variable upon the ratio of uniform to total circumferential strain.

Because very little strain normally occurs during the first stage of creep in cold-worked austenitic stainless steel and since very little nonuniform straining occurred, a good approximation to the second-stage

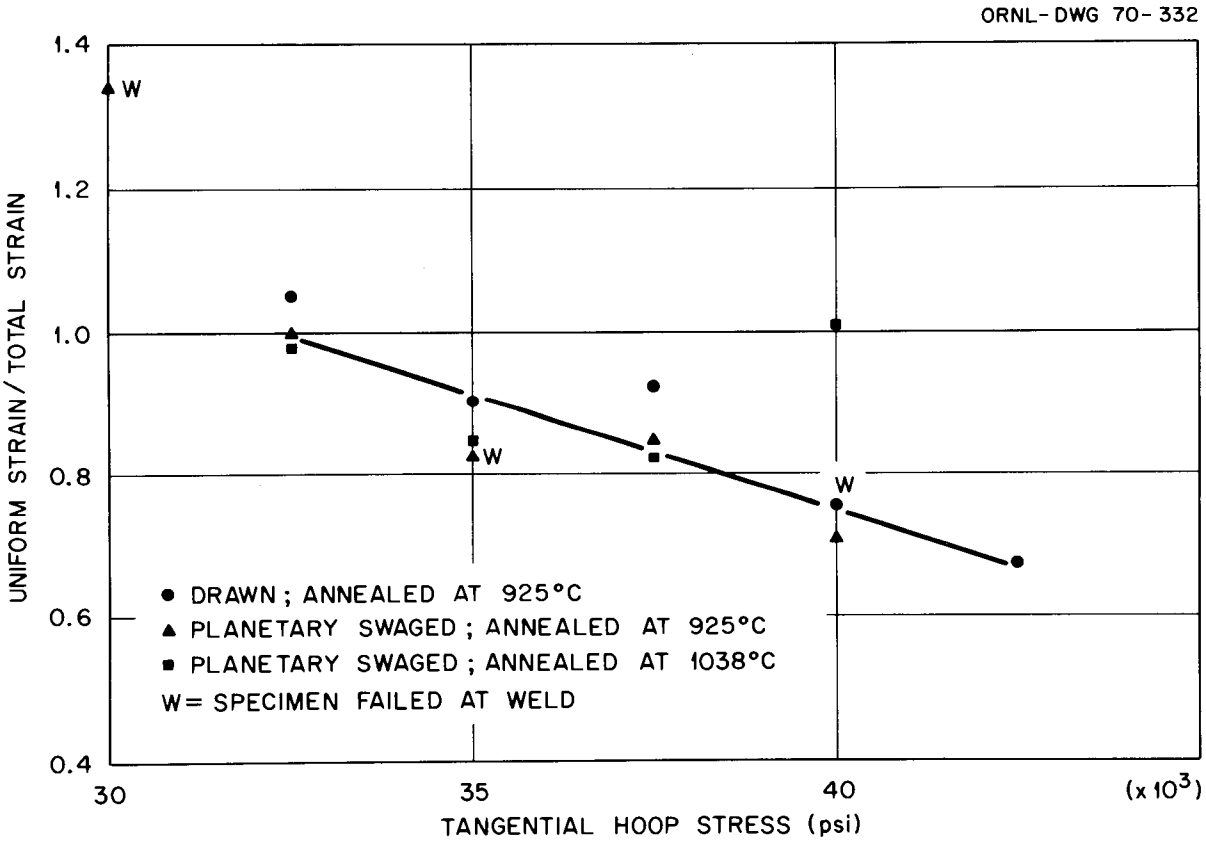

Fig. 5.27. Ratio of Uniform Strain to Total Circumferential Strain of 0.2% Ti-Modified Type 304L Stainless Steel Tubing at 550°C.

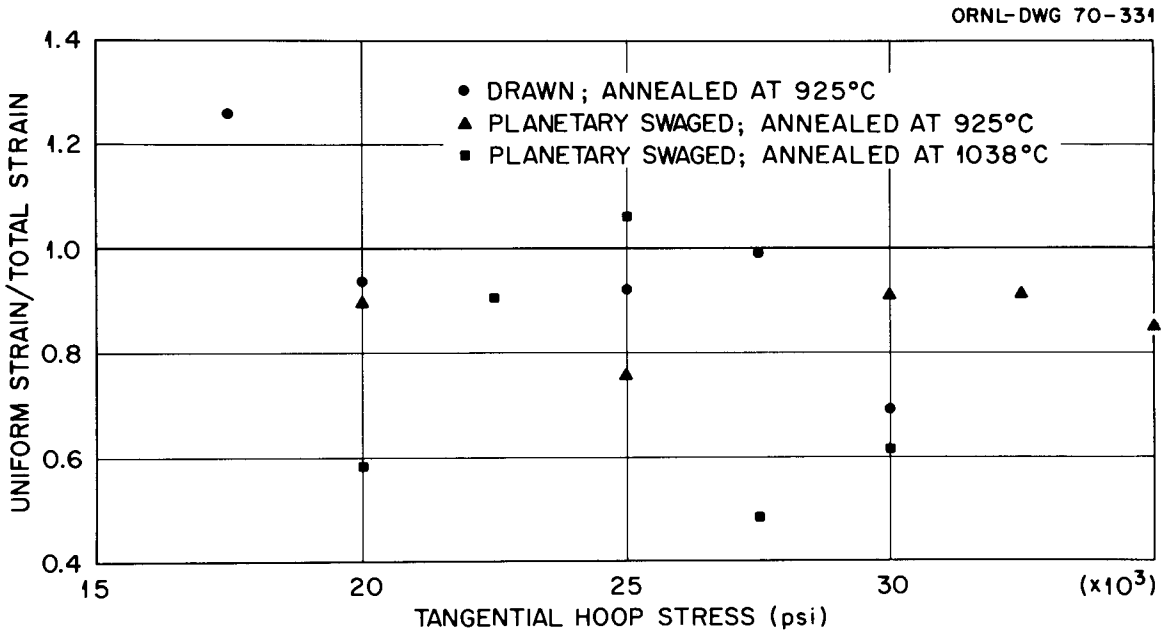

Fig. 5.28. Ratio of Uniform Strain to Total Circumferential Strain of 0.2% Ti-Modified Type 304L Stainless Steel Tubing at 650°C.

creep rate may be obtained by dividing the uniform strain by the rupture time. These results are plotted in Fig. 5.29 for tests performed at both 550 and 650°C. Test data[35] from uniaxial stress-rupture of rod specimens of the same heat of material, annealed at 925°C and tested at 650°C, are also plotted in Fig. 5.29. From this graph it is apparent that drawn tubing exhibits a somewhat lower creep rate than planetary-swaged tubing at 550°C, but that no such correlation can be made at 650°C. The creep rates of planetary-swaged tubing annealed at 925 and 1038°C are the same within the limits of experimental error. Furthermore, the coincidence of the uniaxial and biaxial stress-rupture data suggests that the principal strain rate in each case is determined by the maximum principal stress.

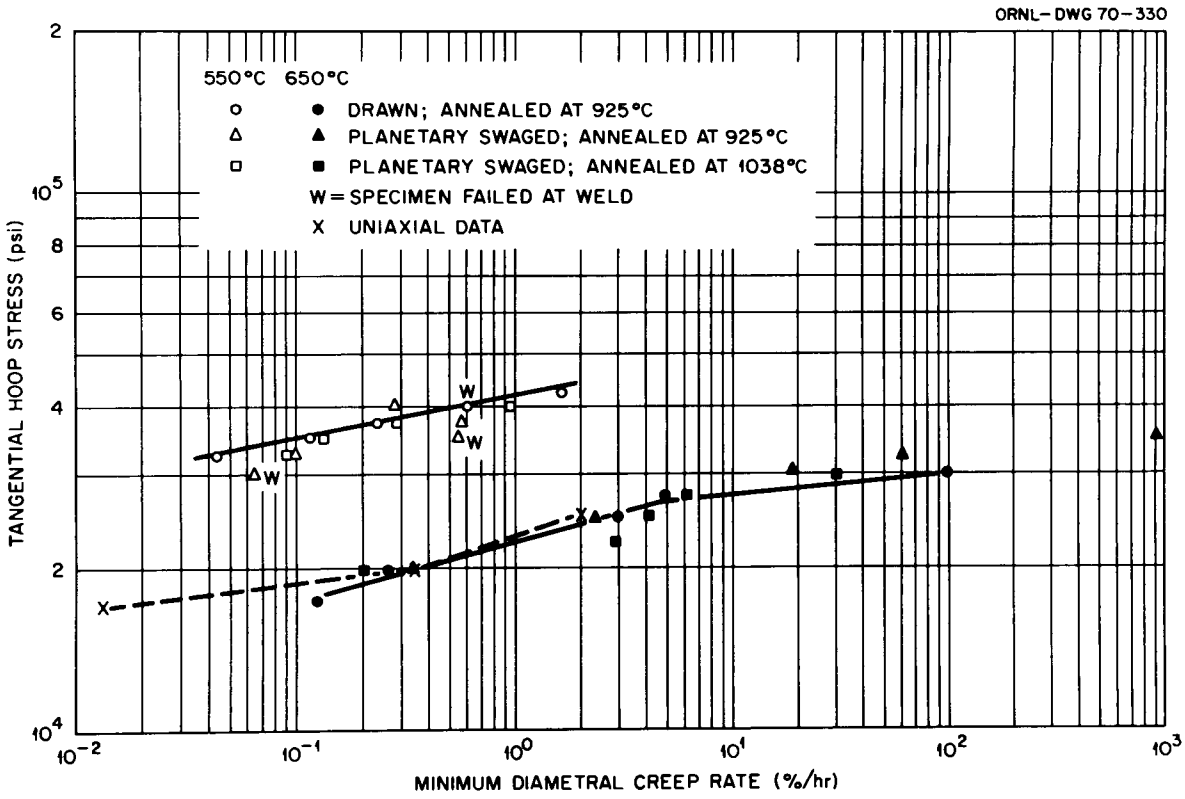

Fig. 5.29. Minimum Creep Rate (Diametral) of 0.2% Ti-Modified Type 304L Stainless Steel Tubing at 550 and 650°C.

References

1. General Engineering Division.
2. A. F. Zulliger and C. R. Kennedy, Oak Ridge National Laboratory, personal communication.
3. W. H. Martin and A. M. Price, Determination of Irradiation Temperature in Graphite Irradiation Experiments Performed in the Dounreay Fast Reactor, UKAEA TRG Report 1117(C), 1966.
4. C. Cawthorne and E. J. Fulton, "The Influence of Irradiation Temperature on the Defect Structures in Stainless Steel," pp. 446–460 in The Nature of Small Defect Clusters, Vol. II, AERE-R-5269 (1966).
5. C. Cawthorne and E. J. Fulton, Nature (London) 216, 515 (1967).
6. J. J. Holmes et al., Acta Met. 16, 955 (1968).
7. S. D. Harkness and Che-Yu Li, "A Model for Void Formation in Metals Irradiated in a Fast-Neutron Environment," pp. 189–214 in Radiation Damage in Reactor Materials, Vol. II, International Atomic Energy Agency, Vienna, 1969.
8. J. O. Stiegler and E. E. Bloom, J. Nucl. Mater. 33, 173 (1969).

9. T. Lauritzen, A. Withop, and U. E. Wolff, Nucl. Eng. Des. 9, 265 (1969).

10. R. S. Nelson and D. J. Mazey, "Void Formation in Stainless Steel During Charged-Particle Irradiation at Elevated Temperatures," pp. 157–163 in Radiation Damage in Reactor Materials, Vol. II, International Atomic Energy Agency, Vienna, 1969.

11. T. T. Claudson et al., "Fast-Reactor Radiation-Induced Changes in Cladding and Structural Materials," pp. 165–181 in Radiation Damage in Reactor Materials, Vol. II, International Atomic Energy Agency, Vienna, 1969.

12. R. T. King, "Cyclotron Simulation of Neutron-Transmutation Produced Gases in Reactor Cladding and Structural Materials," paper presented at International Conference on the Use of Cyclotrons in Chemistry, Metallurgy, and Biology, St. Catherine's College, Oxford, England, September 22–23, 1969. To be published in the proceedings.

13. B. A. Hutchins, J. E. Turner, H. Busboom, and F. A. Comprelli, Trans. Amer. Nucl. Soc. 12, 587 (1969).

14. Portions of this comprehensive study were supported by the Division of Research.

15. J. O. Stiegler, K. Farrell, C.K.H. DuBose, and R. T. King, "High-Fluence Neutron-Irradiation Damage in Aluminum," pp. 215–232 in Radiation Damage in Reactor Materials, Vol. II, International Atomic Energy Agency, Vienna, 1969.

16. F. J. Minter and E.J.E. Foreman, J. Mater. Sci. 4, 218 (1969).

17. K. Farrell and J. T. Houston, "Non-Randomly Distributed Irradiation Voids in Iron," submitted for publication.

18. K. Farrell and J. T. Houston, Oak Ridge National Laboratory, unpublished data.

19. E. E. Bloom and J. O. Stiegler, Trans. Amer. Nucl. Soc. 12, 116 (1969).

20. F. W. Wiffen and J. O. Stiegler, Oak Ridge National Laboratory, unpublished data.

21. E. E. Bloom and J. O. Stiegler, Fuels and Materials Development Program Quart. Progr. Rept. Sept. 30, 1969, ORNL-4480, p. 89.

22. G. L. Kulcinski et al., Radiat. Eff. 2, 57 (1969).

23. K. Farrell and R. T. King, "Supervoids in Irradiated Aluminum," submitted for publication.

24. G. P. Scheidler et al., "The Effect of Irradiation Temperature on the Formation of Clusters in Neutron Irradiated Copper," pp. 405–418 in The Nature of Small Defect Clusters, Vol. II, AERE-R-5269 (1966).

25. K. H. Westmacott et al., Metal Sci. J. 2, 177 (1968).

26. I. A. Johnson et al., "The Heterogeneous Nucleation of Tetrahedra in Quenched Gold," pp. 140–153 in International Conference on Vacancies and Interstitials in Metals, Jülich, September 23–28, 1968, Vol. I, KFA-Jül-Conf-2, Kernforschungsanlage, Jülich, Germany.

27. J. O. Stiegler and J. R. Weir, Jr., "Effects of Irradiation on Ductility," p. 311 in Ductility, American Society for Metals, Metals Park, Ohio, 1968.

28. E. Ruedl, "Direct Observation of Radiation Damage in Al-Al_2O_3 Alloys," pp. 171–183 in Radiation Damage in Reactor Materials, Vol. I, International Atomic Energy Agency, Vienna, 1969.

29. E. E. Bloom, Fuels and Materials Development Program Quart. Progr. Rept. Dec. 31, 1968, ORNL-4390, pp. 134–137.

30. E. E. Bloom and J. O. Stiegler, Fuels and Materials Development Program Quart. Progr. Rept. Sept. 30, 1969, ORNL-4480, pp. 76–85.

31. E. E. Bloom, Fuels and Materials Development Program Quart. Progr. Rept. Sept. 30, 1969, ORNL-4480, pp. 70–72.

32. R. T. King, Fuels and Materials Development Program Quart. Progr. Rept. Dec. 31, 1968, ORNL-4390, pp. 213–222.

33. R. T. King, Fuels and Materials Development Program Quart. Progr. Rept. June 30, 1969, ORNL-4440, pp. 190–191.

34. T. M. Nilsson, Fuels and Materials Development Program Quart. Progr. Rept. June 30, 1969, ORNL-4440, pp. 181–190.

35. E. E. Bloom, Oak Ridge National Laboratory, private communication.

6. FABRICATION DEVELOPMENT FOR LMFBR STAINLESS STEEL TUBING

W. O. Harms W. R. Martin

The tubing fabrication program involves development of fabrication techniques for the manufacture of high-quality type 316 and modified type 304 stainless steel tubing in sizes of interest to the liquid-metal fast breeder reactor (LMFBR) program.

The general scope includes using fabrication techniques that may be transferred to commercial vendors and sufficient nondestructive and destructive testing of the intermediate and final products to assure and demonstrate the quality. The initial studies used Ti-modified type 304 stainless steel, and recently work was begun on type 316 stainless steel.

Effect of Fabrication Variables During Mandrel-Plug Drawing on the Quality and Properties of Type 316 Stainless Steel

A. C. Schaffhauser H. E. McCoy, Jr.

Procedure for Producing Ultrafine Grain Size in Stainless Steel Tubing (G. A. Reimann)

Our earlier studies on the effect of annealing temperature and cold work on the grain size of the finished tubing were reported,[1] and the continuation of this work is reported here.

We altered certain fabrication variables to study the effect on the quality, properties, and structure of type 316 stainless steel tubing. During the course of this work, we developed a fabrication process easily adaptable to commercial manufacturing techniques that produced a very fine grain size and a fine, randomly distributed carbide precipitate.

Type 316 stainless steel is the current choice for tubing for cladding LMFBR fuel elements, and the fine-grained structure could minimize the deleterious effects of the reactor environment on the properties of this cladding. The fine grain size will improve preirradiation ductility,[2] and the larger area of grain boundaries coupled with particles of precipitated carbide could provide more sinks for vacancies and thereby diminish swelling due to the formation of voids.

Two heats of type 316 stainless steel (Allegheny-Ludlum Steel Corporation heat 65808 and Crucible Steel heat 065219) were drawn to tubing 0.250 in. in outside diameter by 0.016 in. in wall thickness for easier comparison with tubing drawn earlier. Some of the data reported previously are included here for more direct comparison of results.

The tubing was drawn to the specified final size according to the schedules listed in Table 6.1, beginning with 1.505-in.-OD × 0.134-in.-wall-thickness stock from Allegheny-Ludlum Steel Corporation heat 65808. The "BA1" and "1A2" designations were given by Allegheny-Ludlum Steel Corporation to identify individual tubes from this heat, and we added the suffixes to identify portions of these tubes subjected to a particular drawing schedule or heat treatment.

Schedule 1, used for drawing the BA1-1 tubes, closely resembles commercial drawing practice. The anneals for 15 min at 950°C produced a grain size equal to about ASTM 6, and the anneal at 925°C produced a grain size between 7 and 8 at the temper point. The fine-grained tubing with the fine carbide precipitate was produced by the same schedule of dies and mandrels but a lower annealing temperature between passes.

Figure 6.1 shows a curve for C solubility for austenitic stainless steel plotted as a function of temperature and C content. At conditions above those indicated by the curve, precipitated C dissolves; at conditions below those indicated by the curve, dissolved C precipitates. Heat 65808 (0.06% C) had to be heated above 900°C to ensure solution of the carbide. Once C is in solution, the tubing must be cooled to room temperature within 1 1/2 to 2 min to avoid reprecipitation of carbide. Maintaining the recrystallized structure at 700 to 800°C after solution of the carbides will result in substantial precipitation at the grain boundaries. On the other hand, if the structure with carbide in solution is cold worked before heating to 700 to 800°C, carbide will be precipitated at the slip lines as well as at the grain boundaries.

Cold drawing austenitic stainless steel 40 to 45%, reductions normally encountered in commercial practice, allows complete recrystallization below the temperature at which the carbide goes into solution. Thus, tube drawing may be completed without requiring anneals at temperatures sufficient to cause solution of precipitated carbides.

Table 6.1. Schedules for Drawing Tubing from Allegheny-Ludlum Steel Corporation Heat 65808

Schedule Number	Pass Number	Anneal			Die (in.)	Mandrel (in.)	Reduction, %	
		Number	Time (hr)	Temperature (°C)			Per Pass	Total
1	1				1.145	0.950	42.8	
		1	1/4	1050				
	2				0.895	0.750	41.5	
		2	1/4	1050				
	3				0.682	0.570	41.3	
		3	1/4	950				
	4				0.535	0.450	40.3	
		4	1/4	950				
	5				0.410	0.344	40.5	
		5	1/4	950				
	6				0.325	0.275	39.5	
		6	1/4	950				
	7				0.267	0.230	38.5	
		7	1/4	925				
	8				0.250	0.218[a]	19.5	
2	1				1.145	0.950	42.8	
	2				1.025	0.850	19.5	54.0
		1	100	775				
	3				0.705	0.540	42.8	
		2	1	775				
	4				0.560	0.450	40.8	
		3	1	775				
	5				0.440	0.360	42.3	
		4	1	775				
	6				0.338	0.275	39.7	
		5	1	775				
	7				0.292	0.250	40.9	
	8				0.267	0.230	19.1	52.3
		6	1	775				
	9				6.250	0.218[a]	19.5	

[a]Plug drawn.

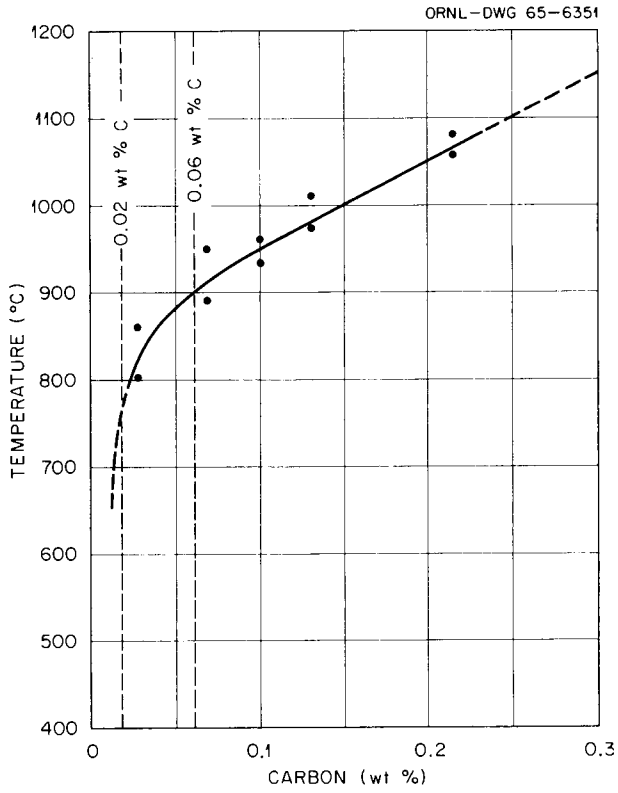

Fig. 6.1. Solubility of Carbon at Different Temperatures in Steel Containing 18% Cr, 8% Ni.

Tubes designated 1A2-A were drawn according to schedule 1, except that the temperature for anneals 2 through 7 was reduced to 775°C. The C was in solution after the first anneals, and subsequent annealing at 775°C precipitated carbide on the slip lines as well as the boundaries, and the low temperatures resulted in a fine grain size. Complete recrystallization did not occur during the first anneal at low temperature but did occur during subsequent anneals. We emphasize that the fine grain sizes obtained resulted from repetitive cold working and annealing at low temperature. Previous work[1] at higher annealing temperatures demonstrated that a finer recrystallized grain size can be obtained by cold working a fine-grained structure than by working a coarse-grained structure, assuming the same level of cold work and annealing temperature.

Figure 6.2(a) shows the structure of 1A2-A tubes after the seventh anneal and before the 20% finishing pass. Since conventional optical metallographic techniques were not adequate for resolving this structure, we used transmission electron microscopy. The fine carbide precipitate

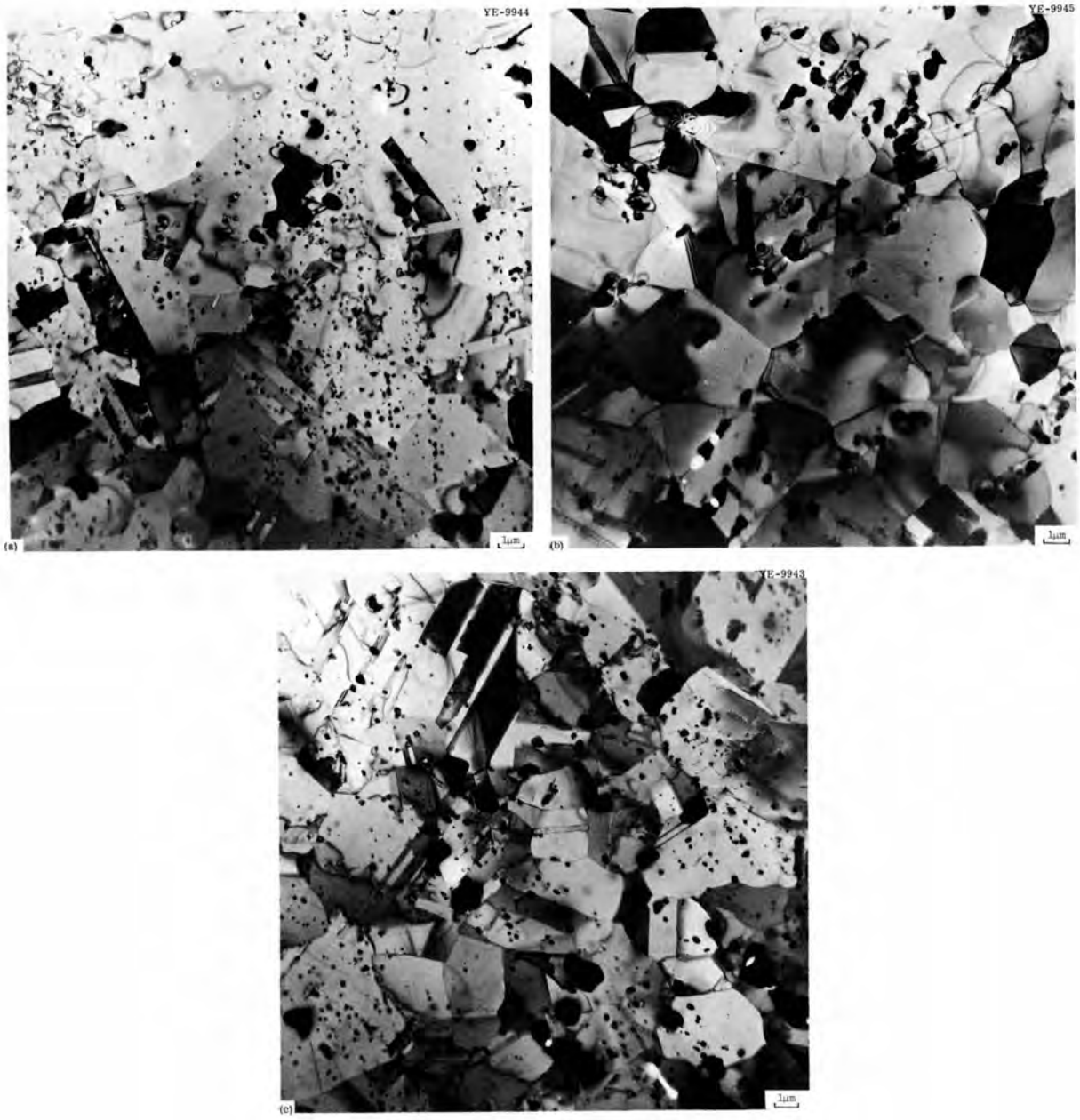

Fig. 6.2. Ultrafine Grain Structure in Type 316 Stainless Steel (0.06% C).

is evident, and the average diameter of the grains is between 3 and 4 μm (ASTM 13).

Figure 6.2(b) shows the structure obtained from 1A2-B tubes by the same schedule as given to 1A2-A, except that immediately after the solution anneal at 1050°C, the tubing was maintained at 775°C for 100 hr to ensure that carbide would precipitate as a heavy deposit at the grain boundaries. Subsequent anneals at low temperature precipitated little additional carbide, and the original deposit, while scattered somewhat, remained as large particles. The larger grain size in this instance suggests that the better dispersion of fine particles in the 1A2-A tubing is helpful in restricting grain growth.

The structure from tube 1A2-C is shown in Fig. 6.2(c). This tubing was produced by schedule 2. The essential differences in this drawing schedule are (1) more cold work before the first and last anneals, and (2) a 100-hr precipitation anneal at 775°C after the first cold-working stage. The carbide precipitated on a larger number of slip lines as well as on a much larger area of grain boundaries that resulted from the finer grain size. The smallest grain size (2 to 2.5 μm, or smaller than ASTM 14) resulted from this schedule, but we attribute this mainly to the higher level of cold work before the final anneal. A better distribution of carbide precipitate was produced in 1A2-A tubing, and it is evident that the 100-hr anneal is unnecessary and should be eliminated.

Samples of type 316 stainless steel tubing from Crucible Steel heat 065219 (0.04% C) were drawn according to a tooling schedule similar to schedule 1 as applied to the 1A2-A tubing except that the last three anneals were reduced to 760°C, which was sufficient to cause complete recrystallization. The microstructure obtained from the final anneal at 760°C is shown in Fig. 6.3. As we anticipated from the lower C content reported, the amount of precipitate was less, and, as a possible consequence of this, the grain size was larger. According to the solubility curve in Fig. 6.1, about 0.02% C will remain in solution at 760 to 780°C; therefore, the C available to precipitate in heat 065219 is about half that in heat 65808. Subjecting the final structure to 100 hr at 760°C produced no discernible changes in grain size, but fewer small carbide

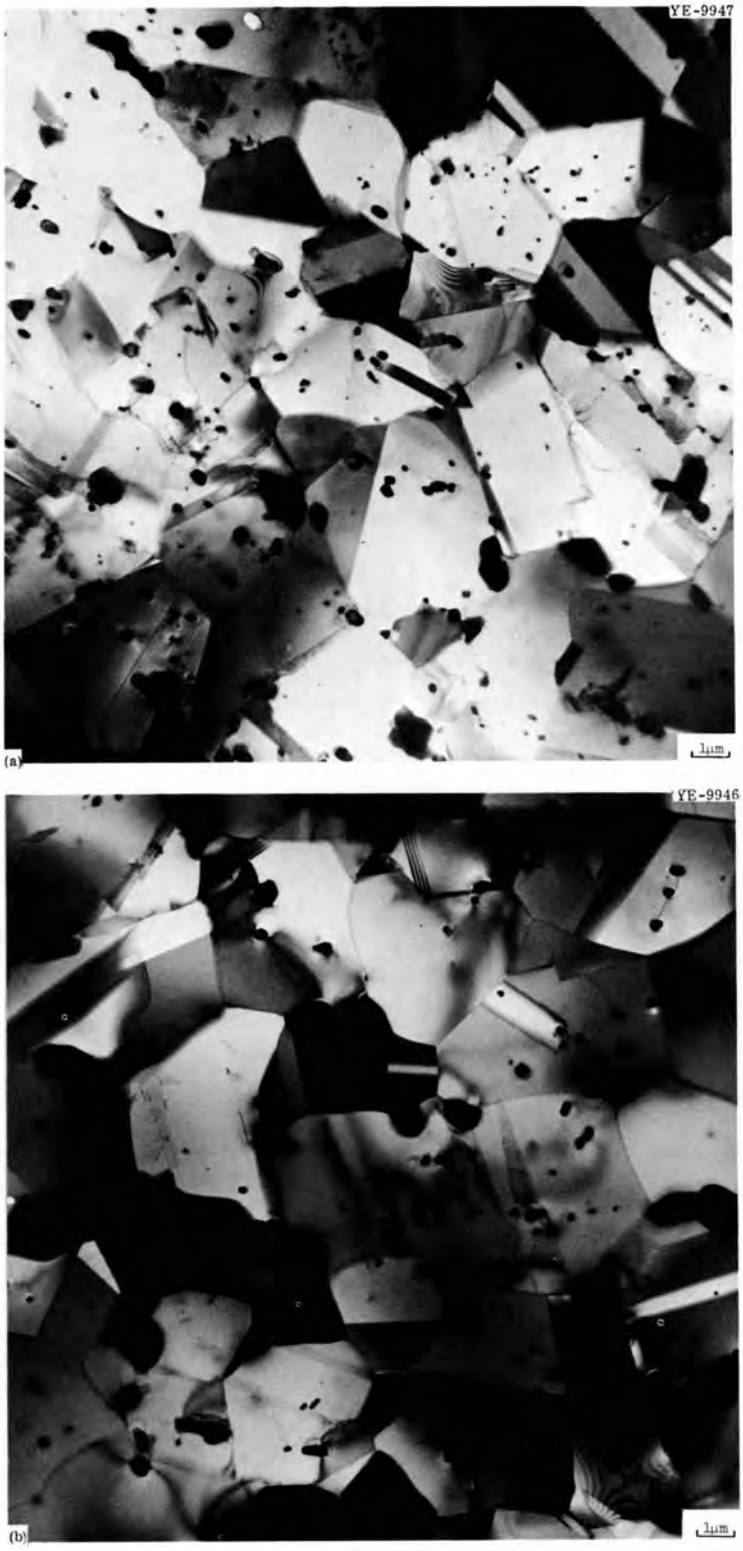

Fig. 6.3. Ultrafine Grain Structure in Type 316 Stainless Steel (0.04% C). (a) Annealed 1 hr at 760°C. (b) Annealed 100 hr at 760°C.

particles were present. This suggests a tendency of the carbides to agglomerate when the structure is heated for long periods. No conclusions should be drawn regarding structural stability for reactor applications until the stress and irradiation variables are added to temperature.

It is evident that type 316 stainless steel tubing with an ultrafine grain size and a fine carbide precipitate can be produced with little difficulty by a procedure that can be incorporated easily into commercial practice. We have not yet received any data that could either refute or verify our assumption of improved postirradiation properties. Samples are being prepared for tests at 550 to 650°C, and other samples are undergoing irradiation in the Experimental Breeder Reactor-II (EBR-II).

Nondestructive testing disclosed a somewhat higher level of detectable flaws in the fine-grained tubing than in tubing from the same heat of material drawn in the conventional manner; however, when judged against the specification limit, the acceptance rate was nearly the same. The fine-grained tubes also exhibited greater eccentricity, but this was related more to the eccentricity of the starting stock than to a difference in processing.

Samples of the fine-grained tubing were subjected to hydrostatic burst tests at room temperature; the results are compared in Table 6.2 with those for commercial tubing.

The 1A2 series of tubes appear considerably stronger and harder than the commercial tubing, and ductility decreases correspondingly. The properties at room temperature appear related mostly to grain size. Stress relieving tube 1A2-C at 700°C reduced the strength to that of BA1-1, but the ductility was considerably improved. It is also evident that the prior fine grain size still exerts some influence on the properties after the anneal at 925°C, but after annealing at 1050°C the effect of prior grain size is essentially eliminated.

Stress-Rupture Properties of Cold-Worked Type 316 Stainless Steel Tubing with Ultrafine Grain Size (R. T. King)

It has been suggested[3] that very fine grain size and a dense distribution of carbide precipitate may make stainless steel tubing resistant to void formation and swelling in a fast-neutron fluence. This report

Table 6.2. Results of Tube-Burst Tests

Tubing Identification	Diamond-Pyramid Hardness[a]	Average Burst Pressure (psi)	Average Hoop Stress (psi)	Average Elongation (%)
		20% Cold Work		
303407[b]	310	22,080	172,300	2.2
BA1-1	283	19,930	158,700	3.1
1A2-A	322	23,000	181,200	2.3
1A2-B	318	23,310	178,000	2.5
1A2-C	329	23,160	184,400	2.3
		Stress Relieved 1 hr at 700°C		
1A2-C		20,090	159,300	4.5
		Annealed 15 min at 925°C		
BA1-1		11,300	87,900	37.5
1A2-C		12,640	100,400	27.6
20276[c]		11,280	84,400	41.8
		Annealed 15 min at 1050°C		
1A2-A		10,280	83,100	36.9

[a]Vickers hardness, 500-g load.

[b]Drawn to size from 0.375-in.-OD × 0.035-in.-wall-thickness commercial stock.

[c]Drawn to Fast Flux Test Facility specification and annealed by Superior Tube Company. Annealing conditions unknown.

describes early results obtained for the 1A2-C tubing drawn[3] from Allegheny-Ludlum Steel Corporation heat 65808 of type 316 stainless steel. The final tubing was 0.250 in. in outside diameter by 0.016 in. in wall thickness and had a grain size finer than ASTM 14 and a dense distribution of carbide precipitate produced during fabrication at ORNL. The tubing was tested in the 20% cold-worked condition.

The tubing was ultrasonically inspected for variations in wall thickness and for longitudinal and transverse discontinuities that produced a signal response greater than that of a standard 0.002-in.-deep by 0.030-in.-long reference notch produced by electro-discharge machining. The tubing tested in this series exhibited no such discontinuities and was, in fact, essentially free from any signal response except an occasional transverse indication, which may have been caused by bubbles in the sound-transmitting fluid.

Specimens 4 in. long were prepared in the usual manner and fitted with end caps.[4] The specimens were tested in a horizontal tube-burst facility that included a five-zone furnace with a hot zone controllable to ±1°C of the nominal test temperature over the specimen length. The specimens were pressurized with a He–1% O_2 environment; the test pressures were calculated to yield desired initial hoop stresses on the basis of the minimum measured wall thickness for each individual specimen.

Test Results and Discussions. – Six specimens were ruptured at 650°C; others are under test at lower stresses at 650 and at 550°C. The rupture lives of these specimens are plotted in Fig. 6.4 versus tangential data obtained at Atomics International[5] on 0.275-in.-OD × 0.010-in.-wall-thickness tubing from the same heat of material in the 10 to 15% cold-worked condition. Quite clearly, the fine-grained tubing with a dense dispersion of carbide precipitate had shorter rupture life at all stresses investigated than the material with ASTM 7 grain size studied at Atomics International. We were interested in comparing biaxial stress state rupture times with uniaxial data. Atomics International has found that the rupture times of type 316 stainless steel are best related by a maximum principal stress criterion in uniaxial, 1:1 biaxial, and 2:1 biaxial tests. Data obtained by uniaxial creep tests on 20% prestrained specimens from a similar heat of type 316 stainless steel[6] are also plotted in Fig. 6.4; these data support the Atomics International hypothesis.

The drastic difference between the slopes of the stress-rupture curves for 1A2-C tubing and for the standard tubing may be related to differences in the amounts of C in solution at the start of the stress-rupture tests. Bloom and Morris[6] found the strain-rate activation energy

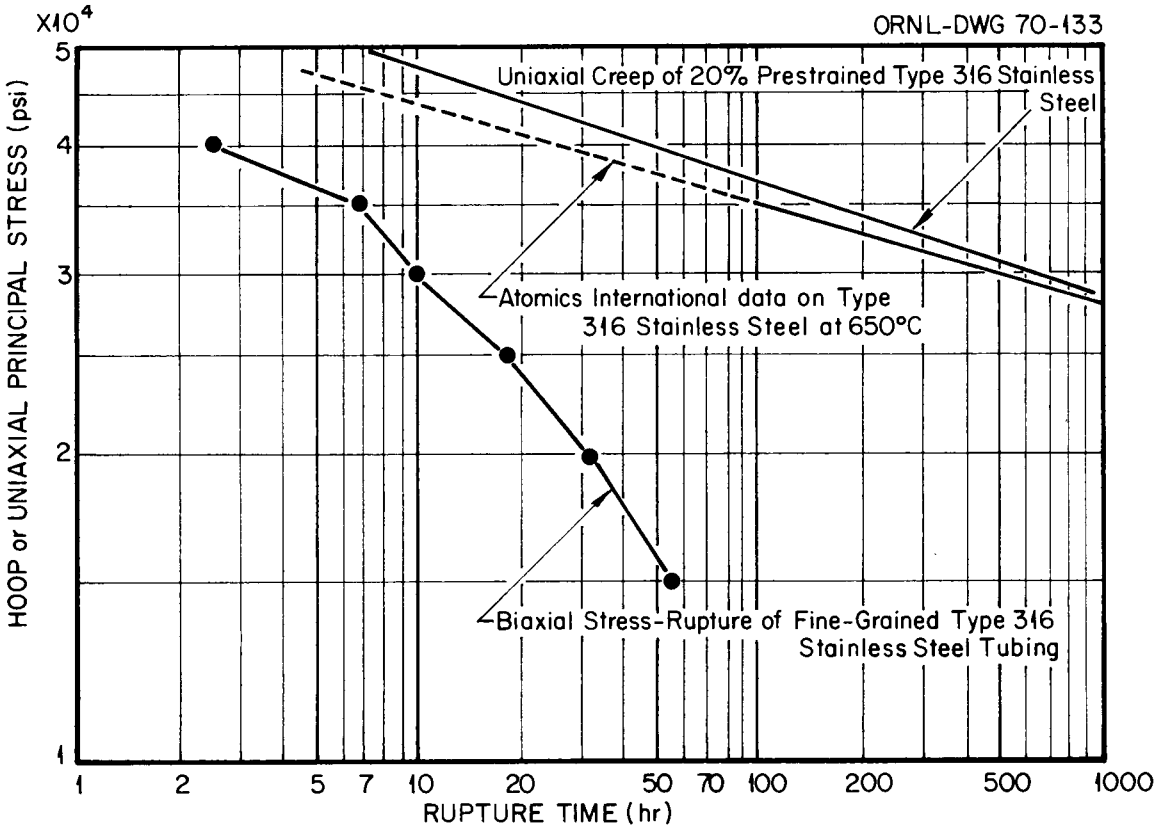

Fig. 6.4. Stress-Rupture Behavior of 20% Cold-Worked Fine-Grained Type 316 Stainless Steel Tubing at 650°C. (Ref. J. J. Gill and D. F. Athins, Atomics International, personal communication, January 1970.)

for creep in type 316 stainless steel to be nearly that for C diffusion. When C is available in solid solution, dynamic segregation of C or precipitation of C as carbides on dislocations during testing may be important in reducing the mobility of dislocations or pinning dislocations. The results obtained by Bloom and Morris and by workers at Atomics International would thus be affected by this mechanism. However, nearly all of the C in the 1A2-C material has been precipitated in the form of fine carbides, where it can only interact with dislocations through a dispersion-hardening mechanism. This explanation is obviously only tentative: it ignores the usual effects of grain size, sliding and cracking of grain boundaries, and final rupture strain.

Total and uniform circumferential elongations measured[7] for a limited number of specimens from the 1A2-C batch of type 316 stainless steel

tubing are shown in Fig. 6.5. Both the total and uniform strains are in the range of 13 to 25%, which is considerably higher than that observed[7] for cold-worked 0.2% Ti-modified type 304L stainless steel tubing of the same dimensions. These ductility values are also higher than the 5 to 7% strain values reported for the tubing tested at Atomics International.[5] The fact that uniform straining accounts for much of the total strain observed is important, since only uniform strain may be useful in some reactor applications. Furthermore, the data show a definite trend toward increasing uniform and total elongation with increasing rupture time over the range of stresses investigated.

This series of tests on type 316 stainless steel tubing will be extended to cover fine-grained material in the recrystallized and recovered conditions and to material produced by normal commercial techniques at ORNL.

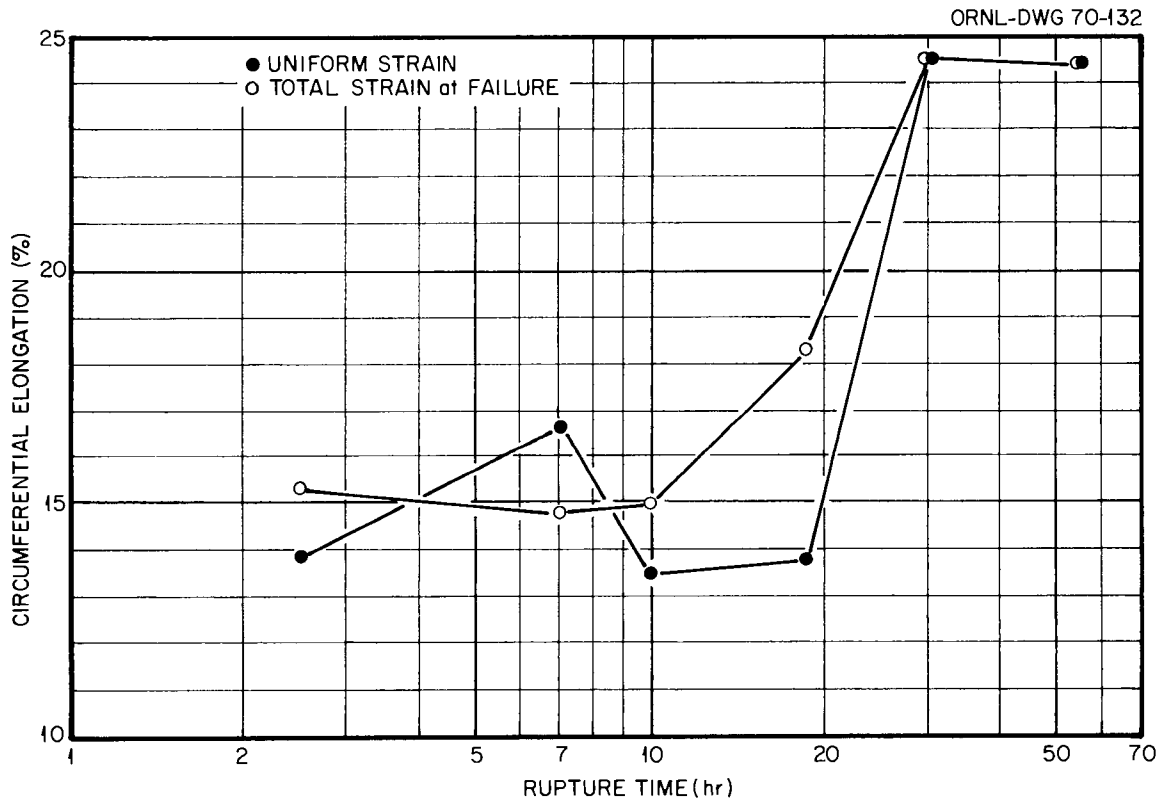

Fig. 6.5. Ductility of 20% Cold-Worked Fine-Grained Type 316 Stainless Steel Tubing at 650°C.

Origin and Significance of Natural Defects Generated During Fabrication
(G. A. Reimann)

The influence of defects on the burst characteristics of type 316 stainless steel tubing at room temperature were discussed previously.[1] We noted a pronounced adverse effect on properties only if the defect was in the thinner wall of tubing that met the specification for eccentricity but was known to contain defects that approached the specification limit for defects. Defects that exceeded the limit but were in the thicker wall of the tube often resulted in no adverse effect on strength and ductility. This is mentioned here only to emphasize that the allowable eccentricity can obscure the influence of flaws on mechanical properties. Absolute concentricity, while unattainable, remains one of the manufacturing goals for high-precision seamless tubing. Any flaw is of more consequence as concentricity is approached since its effect cannot be masked by a thicker wall.

One of the objects of this work is to detect and characterize the defects in tubing in order to determine their origin and assist in eliminating them. Four sources of defects have been identified: flaws in the starting material that are below the limit of detection, mechanical damage during and between processing steps, adhering particulate matter, and inclusions.

The sequence shown in Fig. 6.6 illustrates how internal defects may be formed in a tube shell that has an initial machined surface with a roughness, in terms of the average deviation from the mean (root-mean-square), of 125×10^{-6} in. After tube reducing, the concentric grooves caused by machining are more widely spaced and are somewhat shallower, although the angle of the lighting gives the impression that they are deeper. Folding and smearing of peaks was slight after tube reducing but substantial after the first draw, as determined by examination of the longitudinal cross section. Lubricant trapped in the fissures by enfolding cannot be removed completely by solvents and carbonaceous residues form during annealing and remain trapped in these fissures. By the fifth draw, some vestiges of machining flaws are aligned nearly parallel to the tube axis, in the worst possible orientation if good tangential ductility is desired.

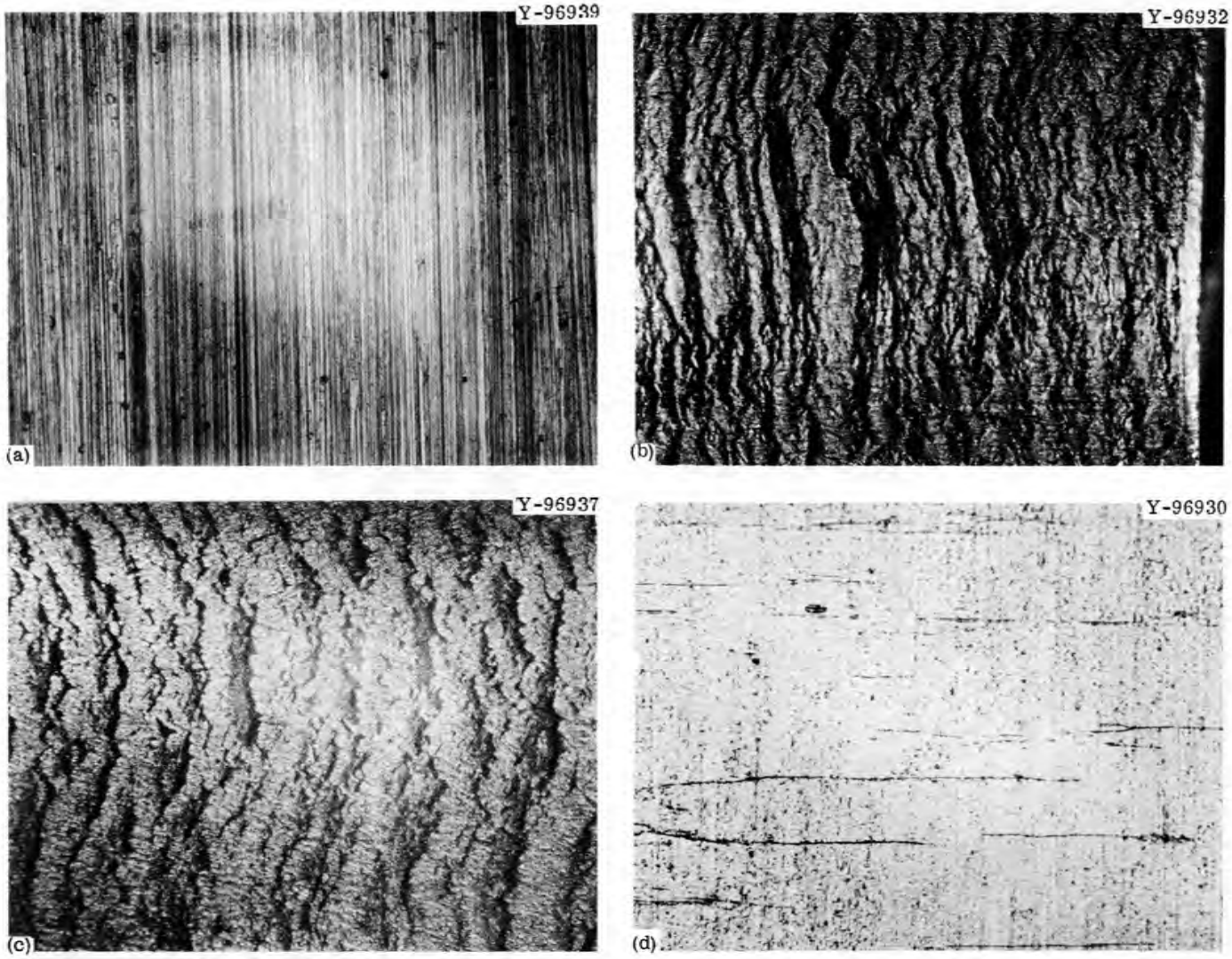

Fig. 6.6. Evolution of Machined Surface into Defects. (a) After machining. 20×. (b) After tube reducing. 20×. (c) After first draw. 20×. (d) After fifth draw. 250×. Reduced 22%.

Figure 6.6 illustrates how an apparently minor characteristic of the starting product can have an adverse effect on the final product. The 63×10^{-6} in. surface finish specified for Fast Flux Test Facility tube shells appears to be insufficient to ensure the production of quality tubing. The difference between a 63×10^{-6} and a 125×10^{-6} in. machined finish cannot be detected by ultrasonic inspection. A new nondestructive testing technique needs to be developed for this purpose.

Defects that appear to have developed during the drawing process are shown in Fig. 6.7. This figure is subdivided into (1) defects that were discovered in the finished size during the course of ultrasonic inspection and (2) those defects that were undetected by nondestructive testing but that become evident in the strained metal adjacent to the rupture caused by burst testing. Flaws were detected nondestructively by measuring and comparing the signal response they produce with that from an artificial reference notch 0.001 in. deep, 0.0025 in. wide, and 0.030 in. long. The larger flaw shown in Fig. 6.7(a), a crack 0.004 in. long that extends 0.001 in. beneath the surface of the tube, produced a substantial response and was located visually once the general area of the defect was indicated. We believe that it resulted from mechanical damage to the tube during handling. In the example shown in Fig. 6.7(b), a smaller flaw (arrow) produced an "indication," or a questionable response. Notice also the small particle of foreign material (circle) imbedded into the surface of the tube. When this tube was sectioned, a flaw that extended 0.001 in. below the surface of the tube was discovered. It is quite possible that this defect would not adversely affect tangential ductility if it were located on the thick side of the wall in a tube.

A substantial number of minor flaws, or incipient flaws, remain undetected because they are below the threshold for ultrasonic inspection. Those that become visible in the strained metal adjacent to the point of rupture (arrows) after burst testing were not apparent in transverse cross sections examined at 500× before burst testing. Defects of this nature were found most often in finished tubing that contained more than 10% cold work, and they appear to become more numerous as the annealing temperature between passes is reduced. These defects appear

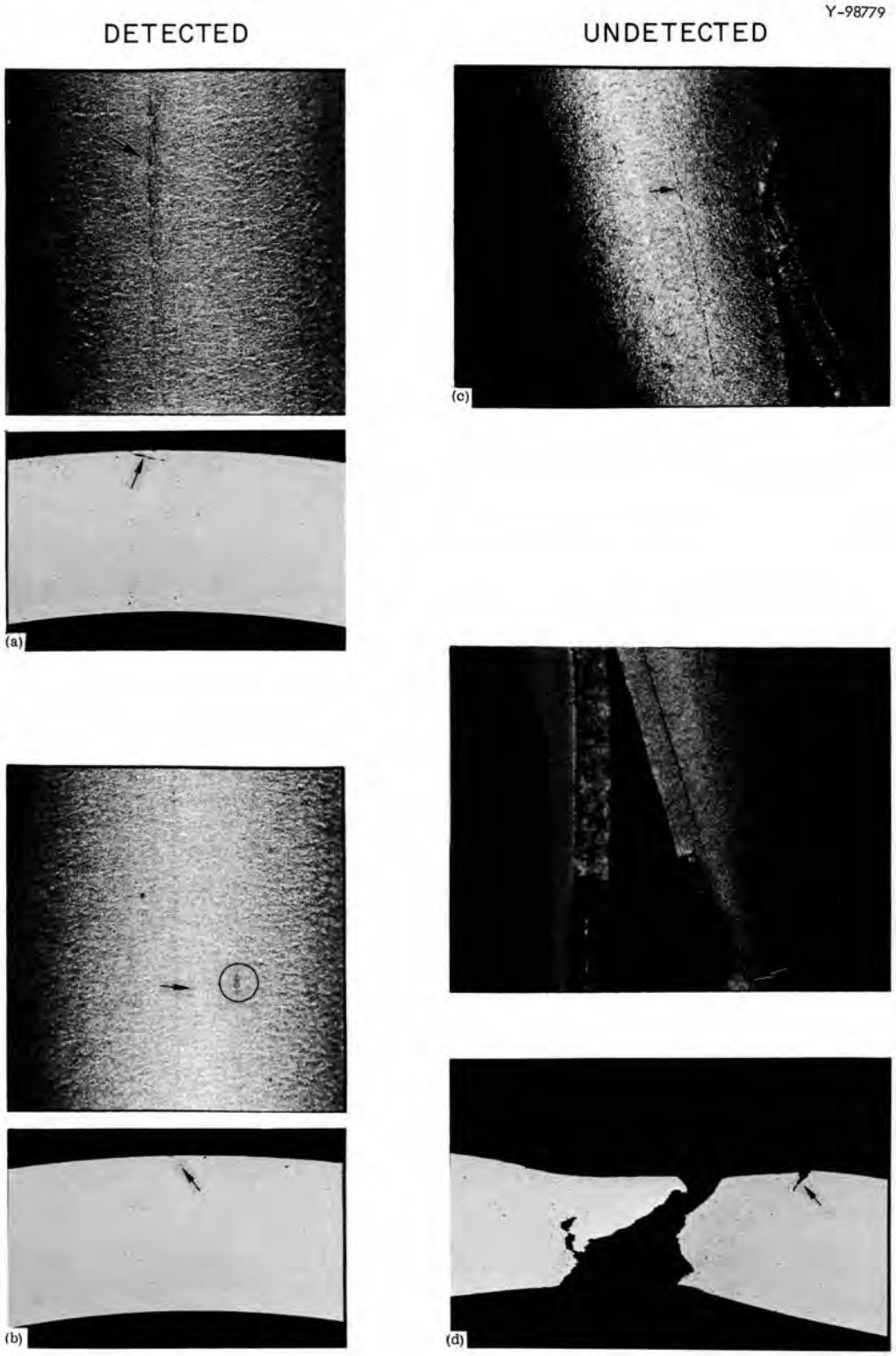

Fig. 6.7. Defects in Tubing Ultrasonically Inspected. (a) Flaw that exceeds reference standard. (b) Flaw slightly smaller than reference standard. (c) and (d) Flaws below limit of detection.

to be less harmful in annealed tubing. In any case, tangential ductility is related to the number and size of these subthreshold flaws, which in turn are partially related to the number of inclusions in the heat.

Thus, we conclude that variations within the limits of acceptable melting practice can markedly affect performance of the finished product.

Generation and Evaluation of Artificial Defects (K. V. Cook)

We have begun a study of artificial defects in tubing. Primary objectives of the program are (1) to establish fabrication procedures for artificially producing flaws that resemble natural defects; (2) to determine the effect of simulated defects at known orientations and locations on mechanical properties, ultrasonic response patterns, and tube drawing schedules; (3) to determine if more realistic calibration standards for nondestructive testing can be produced; and (4) to determine the required inspection sensitivities for evaluating tubing before the final fabrication operation to assure that the tubing will be free of defects.

We simulate defects by first electro-discharge machining notches and then altering the dimensions of the notches to more nearly resemble natural flaws by further processing of the tubing. For example, we notched the inner and outer surfaces of two tubes of type 316 stainless steel by electro-discharge machining to 0.0015 in. deep by 0.0025 in. wide by 0.030 in. long, the dimensions normally used for calibration notches for eddy-current and ultrasonic examination. The two tubes were 0.250 and 0.325 in. in outside diameter and 0.015 and 0.0375 in. in wall thickness, respectively. The notches were so placed in the tubes that specimens containing the flaws may later be sectioned for tube-burst tests. Both tubes were then drawn to a nominal outside diameter of 0.228 in. and wall thickness of 0.015 in.

The 0.250-in.-OD tube was reduced in one pass with no reduction in wall thickness. The tube with the 0.325 in. diameter was drawn in three passes with a reduction both in diameter and wall thickness.

Notch widths and depths were measured with the aid of a microscope after each pass. The notches in the 0.250-in.-OD tube changed significantly only in width, but the notches in the 0.325-in.-OD tube changed

significantly in width, depth, and length. These data were used to plot the curves in Figs. 6.8 and 6.9 that relate the change in the depth and width of the notches to the change in the dimensions of the tube. Even though the curves are only approximations because of the limited data, they show very interesting trends. Figure 6.8 indicates that the percentage of change in depth can be approximated by a straight line relationship to the percentage of change in wall thickness. Figure 6.9 shows that the change in notch width per pass is an exponential function of the change in outside diameter. From these preliminary data it appears that we should be able to calculate the necessary starting depth of notch to obtain the desired, predicted notch in the final tube.

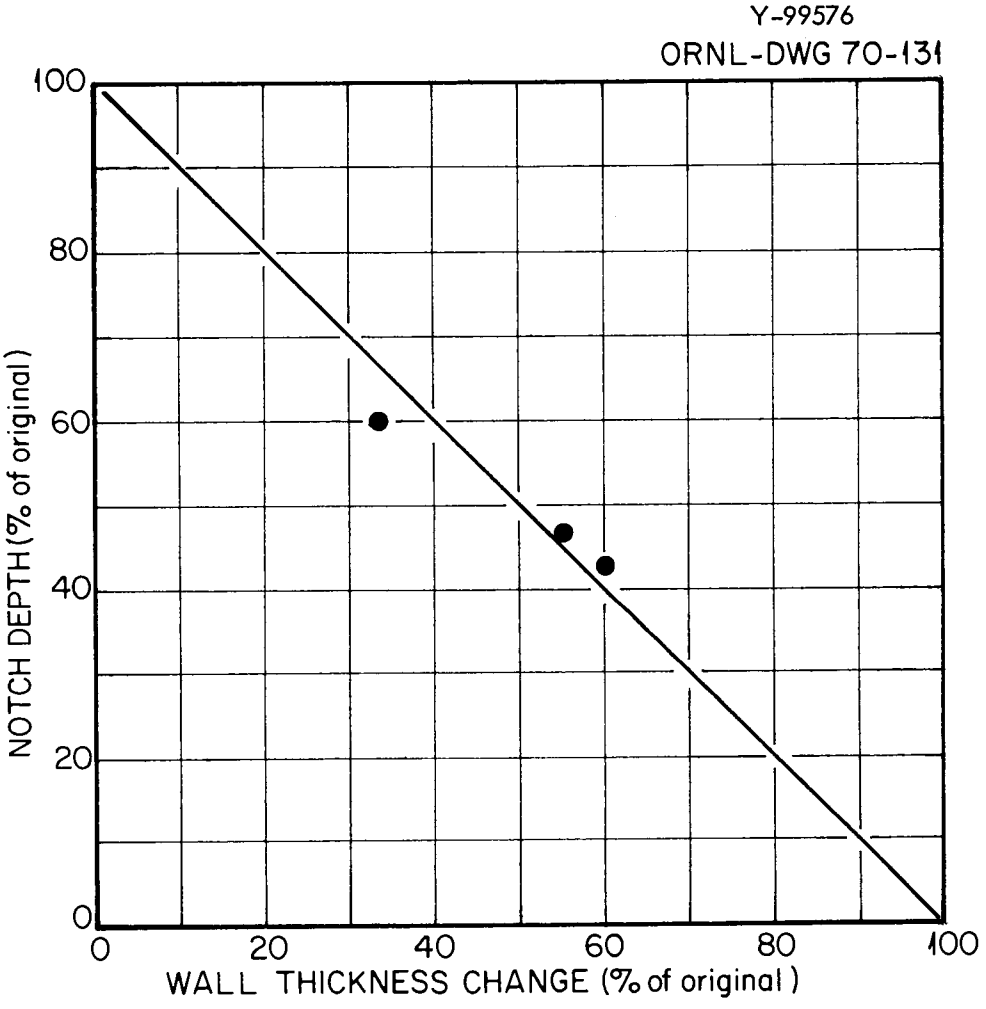

Fig. 6.8. Depth of Simulated Defect as a Function of Change in the Wall Thickness of Tubing.

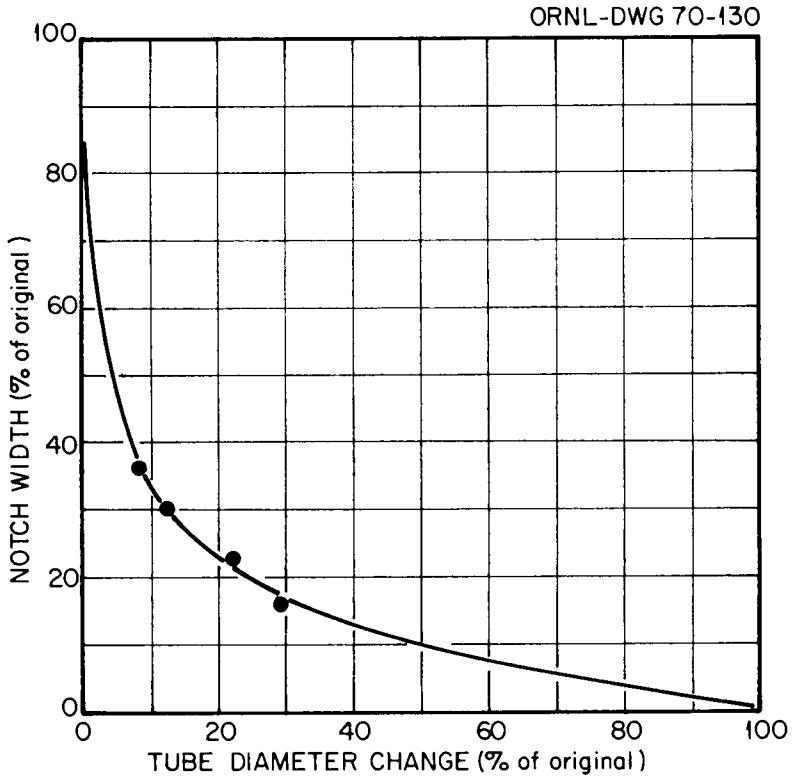

Fig. 6.9. Width of Simulated Defect as a Function of Change in the Outside Diameter of Tubing.

References

1. G. A. Reimann, Fuels and Materials Development Program Quart. Progr. Rept. June 30, 1969, ORNL-4440, pp. 176–180.

2. W. R. Martin and J. R. Weir, Jr., Influence of Grain Size on the Irradiation Embrittlement of Stainless Steels at Elevated Temperatures, ORNL-TM-1043 (March 1965).

3. G. A. Reimann, "Procedure for Producing Ultrafine Grain Size in Stainless Steel Tubing," pp. 134–141, this report.

4. R. T. King, Fuels and Materials Development Program Quart. Progr. Rept. June 30, 1969, ORNL-4440, pp. 190–191.

5. J. J. Gill and D. F. Athins, Atomics International, personal communication, January 1970.

6. E. E. Bloom and J. G. Morris, Fuels and Materials Development Program Quart. Progr. Rept. June 30, 1969, ORNL-4440, pp. 117–123.

7. R. T. King, "Effect of Planetary Swaging and Annealing Temperature on the Biaxial Stress-Rupture Properties of 0.2% Ti-Modified Type 304L Stainless Steel Tubing," pp. 123–131, this report.

7. WELDING DEVELOPMENT FOR LMFBR VESSELS AND COMPONENTS

J. R. Weir, Jr. G. M. Slaughter

We are evaluating the behavior of weldments in austenitic stainless steel at 370 to 650°C as a function of both the welding process and the variables within a process for application to liquid-metal fast breeder reactor (LMFBR) vessels and components. The solidification substructure (the finest structural detail that can be resolved by an optical microscope) markedly influences the mechanical properties of a weldment at elevated temperatures. Since the size and type of substructure in a weldment are significantly influenced by factors that the welder can control, our approach is to determine the effects of different welding processes and of the variables within each process (current, voltage, travel speed, etc.) upon mechanical properties.

The research for this program is closely interrelated with that for Shielded Metal-Arc Welding for LMFBR Components.[1] For example, the mechanical-properties and metallographic studies on the two programs directly complement each other, and occasional cross referencing of information is useful.

Study of Submerged-Arc Process

Preparation of Weldment Specimens (G. M. Goodwin, D. G. Harman, Nancy C. Cole)

We procured two 48 × 96 × 1-in. plates of type 304 stainless steel that conform to standards set by the Division of Reactor Development and Technology (RDT). These plates were machined into 6 × 32 × 1-in. strips, and one edge of each strip was prepared for welding. We also purchased RDT-qualified 5/32-in.-diam type 308 stainless steel wire to supplement an available supply of wire that conforms to standards of the American Society for Testing and Materials (ASTM) that was upgraded to meet RDT standards.

A submerged-arc weld was deposited in 1-in. plate under the following conditions:

Base plate:	Type 304 stainless steel, Republic Steel Company, heat 67430, 1 in. thick
Filler wire:	Type 308 stainless steel, Arcos Corporation, heat 1021T308, 5/32 in. in diameter
Flux:	Arcos S-4, Lot 8M1F
Backing strip:	Type 304L stainless steel, Crucible Steel Company, heat E158489, 3/16 × 2 in.
Joint design:	"Vee" groove, 80° included angle
Current, amp, ac:	600
Voltage, v:	35–37
Travel speed, in./min:	18

We are machining all-weld-metal specimens to investigate the effect of heat treatment after welding on the creep-rupture properties of typical austenitic stainless steel weld metal.

Bead-on-plate welds were made on 1-in.-thick stainless steel plate under each of the sets of conditions listed in Table 7.1. These represent the range of conditions practically attainable with our equipment and 5/32-in.-diam wire. Note that energy input can be varied by a factor of about 20 without changing the equipment setup. Cross sections of selected beads produced at 600 amp and 34 v are shown in Fig. 7.1. Note that the depth of penetration achieved is essentially insensitive to travel speed within the range 3 to 30 in./min. The amount of filler metal deposited per pass and the heat input, however, vary by a factor of 10. Specimen 11 represents the conditions used to produce the submerged-arc welds for the Fast Flux Test Facility (FFTF) weldment irradiation program.[1] As is evident from these photomacrographs, the predominant direction of growth varies markedly, from roughly vertical in specimen 21 to roughly 45° from vertical in specimen 61. The latter growth pattern results in a discontinuity at the center line that can in certain situations promote cracking. We would expect these differences in predominant growth orientation to be reflected in the directionality of mechanical property values; that is, a transverse all-weld-metal specimen from weld 21 should show different properties than a similar specimen from weld 61.

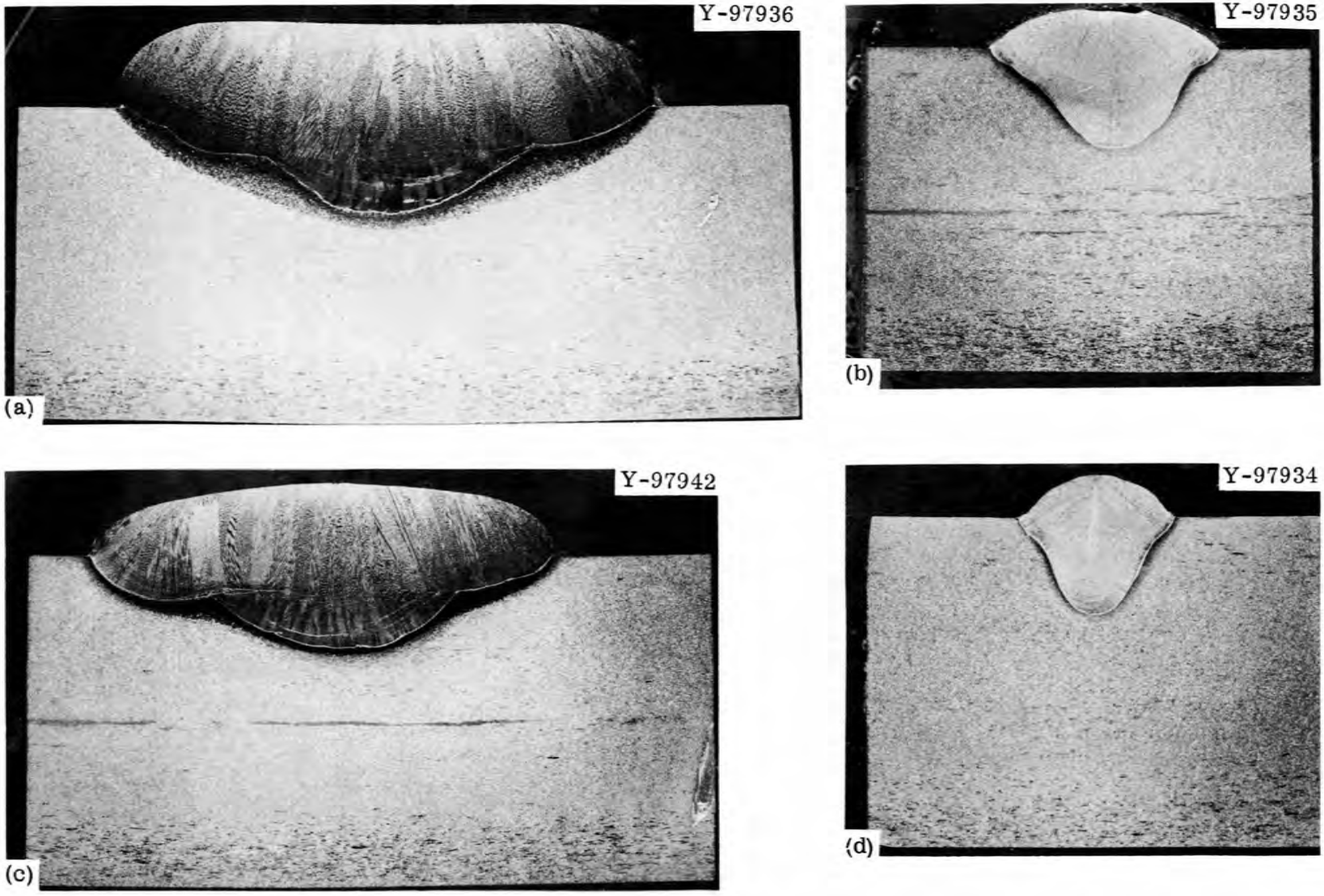

Fig. 7.1. Bead-On-Plate Submerged-Arc Welds Produced at 600 amp and 34 v. (a) Weld 21, 3 in./min, (b) weld 11, 18 in./min; (c) weld 31, 6 in./min; (d) weld 61, 60 in./min. 2X.

Table 7.1. Welding Conditions for Bead-On-Plate Submerged-Arc Test Welds

Weld Identification Number	Current (amp)	Voltage (v)	Travel Speed (in./min)	Energy Input (kJ/in.)
11	600	34	18	68
21	600	34	3	408
31	600	34	6	204
51	600	34	60	20
61	600	34	30	41
71	600	34	24	51
81	600	34	12	102
12	600	60	18	120
42	600	60	24	90
52	600	60	20	108
62	600	60	12	180
72	600	60	6	360
13	900	47	12	211
23	900	47	6	423
33	900	47	18	141
43	900	47	24	106
53	900	47	60	42
14	900	60	12	270
24	900	60	18	180
34	900	60	30	108
44	900	60	60	54
25	1200	60	24	180
35	1200	60	30	144
55	1200	60	60	72
65	1200	60	18	240

Other factors also complicate the situation, however. Figure 7.2 shows the solidification substructure at the fusion line in each of the welds shown in Fig. 7.1. Note that the substructure texture (i.e., fineness or coarseness) varies markedly as measured by the average width of the cellular dendrites. Since approximately the same amount of segregate is redistributed during the solidification process in each of the welds, it is generally accepted that the finer substructure (that of weld 61 in this case) results in a higher degree of segregation and steeper concentration gradients. This is borne out by the etching

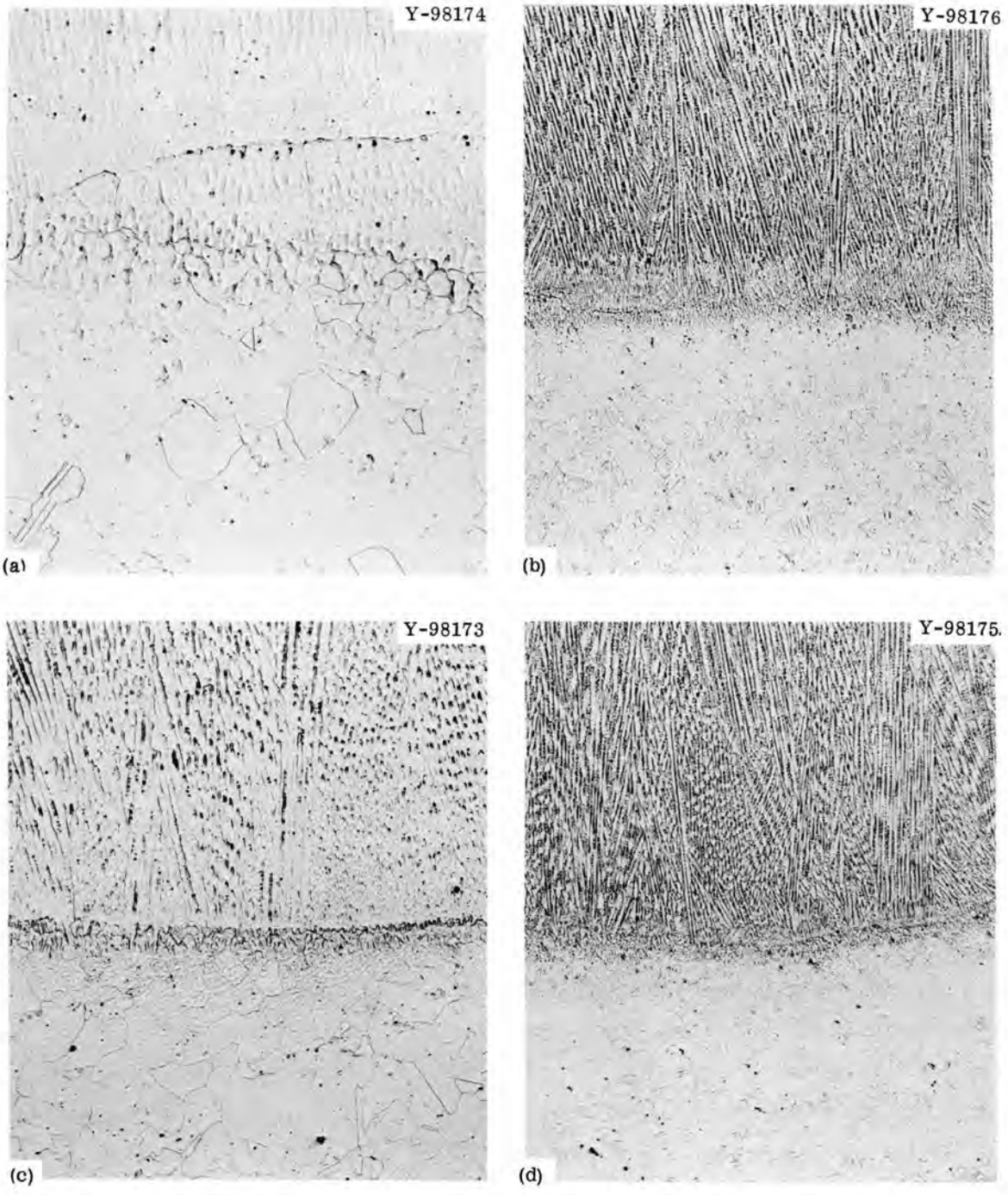

Fig. 7.2. Bead-On-Plate Submerged-Arc Welds Produced at 600 amp and 34 v. (a) Weld 21, 3 in./min; (b) weld 11, 18 in./min; (c) weld 31, 6 in./min; (d) weld 61, 30 in./min. 100×. Reduced 20%.

behavior of the specimen shown in Fig. 7.2. Note that the weld produced at 30 in./min shows a fine substructure that is sharply etched, while, on the other extreme, the weld produced at 3 in./min shows a coarse substructure that is poorly revealed even after extended etching.

Another complicating factor in this case is the degree of dilution; note that the ratio of added filler metal to melted base metal, as evidenced by the relative areas above and below the top surface of the plate, varies markedly. Weld 21 has a ratio of filler metal to base metal of greater than 1:1 while in weld 61 the ratio is nearer 1:3 or 1:4.

Selected welds made at 900 and 1200 amp are shown in Fig. 7.3. Note that it is possible to produce welds at very high levels of current and voltage (weld 55) that still approximate the energy input used in the FFTF irradiation weldments (weld 11, shown in Fig. 7.1). Extremely high energy inputs are also attainable, as in weld 23. The average substructure size also varies markedly.

Multipass weldments are being produced in 1-in.-thick plate using selected conditions from this bead-on-plate study. We will evaluate the mechanical properties of these weldments at elevated temperatures and attempt to correlate the properties obtained with the observed microstructure. We have also examined several of the fractured weld specimens. In all cases, the fracture path tends to coincide with the substructure boundaries. Figure 7.4 shows the longitudinal cross section of a fractured creep specimen. The main fracture, as well as the secondary cracks, follows the substructure. Also evident is the influence of the crystallographic orientation on crack formation. The grain located along the specimen surface does not show the same propensity toward secondary cracking as does the adjacent grain located toward the interior of the specimen.

We are also using the scanning electron microscope to examine several of the fracture surfaces. Again, we find strong evidence that the substructure affects the appearance of the fracture. Typically, we find the fracture surface of a ruptured specimen to consist of several areas of interphase fracture connected by areas of ductile shear.

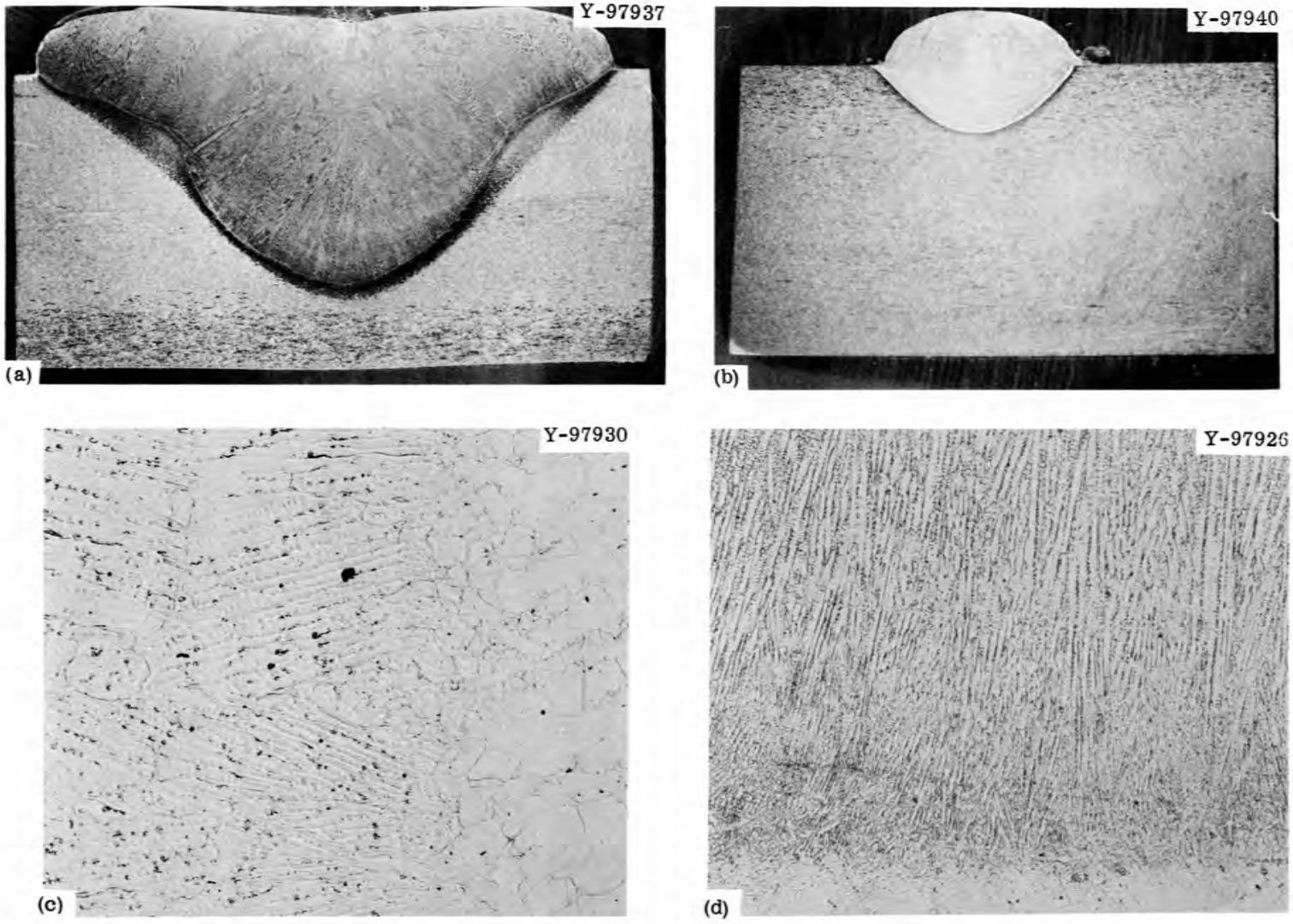

Fig. 7.3. Bead-On-Plate Submerged-Arc Welds. (a) Weld 23, 900 amp, 47 v, 6 in./min, 2X; (b) weld 23, 100X; (c) weld 55, 1200 amp, 60 v, 60 in./min, 2X; (d) weld 55, 100X. Reduced 15%.

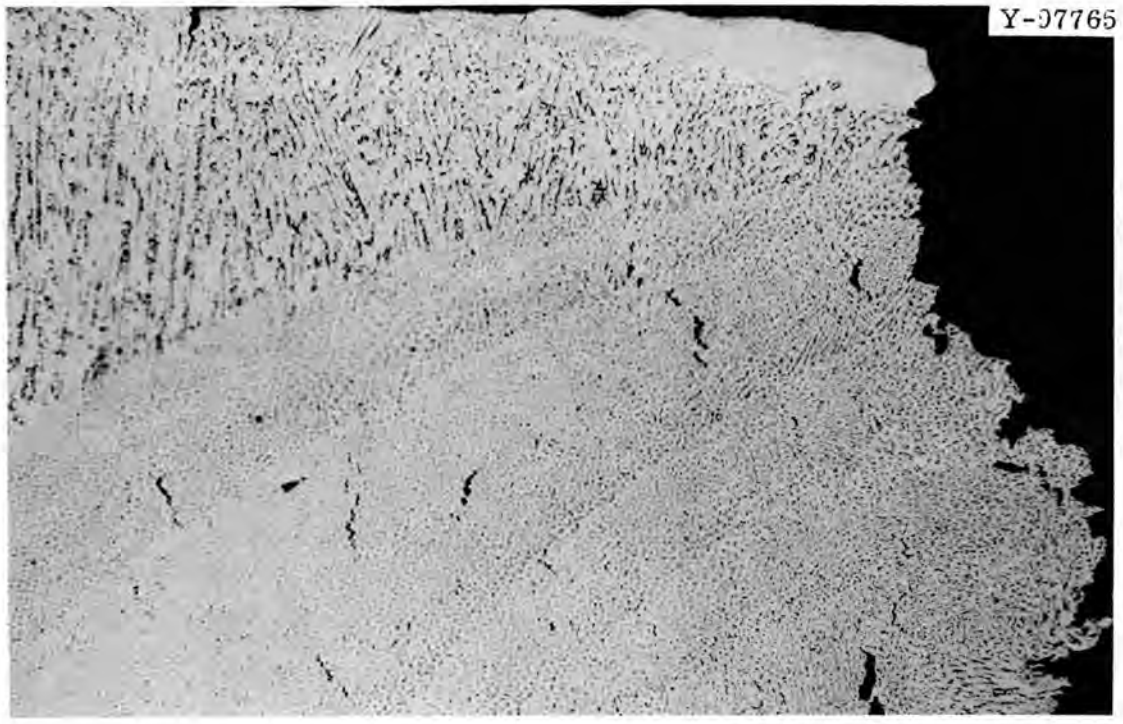

Fig. 7.4. Longitudinal View of Failed Creep Specimen. Specimen was from weld 2 and was creep tested in air at 650°C and 25,000 psi. The grain shown in the lower portion shows many cracks, and the cracks tend to follow the substructure boundaries. 100×.

The relative amounts of each type of fracture apparently depend upon material and testing variables.

Figure 7.5 shows an area of the fracture surface of weld 1 after creep-rupture testing at 25,000 psi. The scanning electron photomicrograph in Fig. 7.5(a) shows the area at 100× to be adjacent to the surface of the gage section. An area of interphase fracture is bounded on the lower left and upper right by ductile shear fracture. Also evident are several secondary cracks on the surface of the gage section (top) that are normal to the stress axis. This area is shown at successively higher magnifications in Figs. 7.5(b) through 7.5(d).

Scanning electron photomicrographs of a shear fracture area of this same fracture surface are shown in Fig. 7.6. Many of the second-phase particles that initiate the dimple features are evident. We have not analyzed these particles but expect them to be primary carbides, which are prevalent in type 304 stainless steel. Additional studies of fracture surfaces are under way that will facilitate a more complete

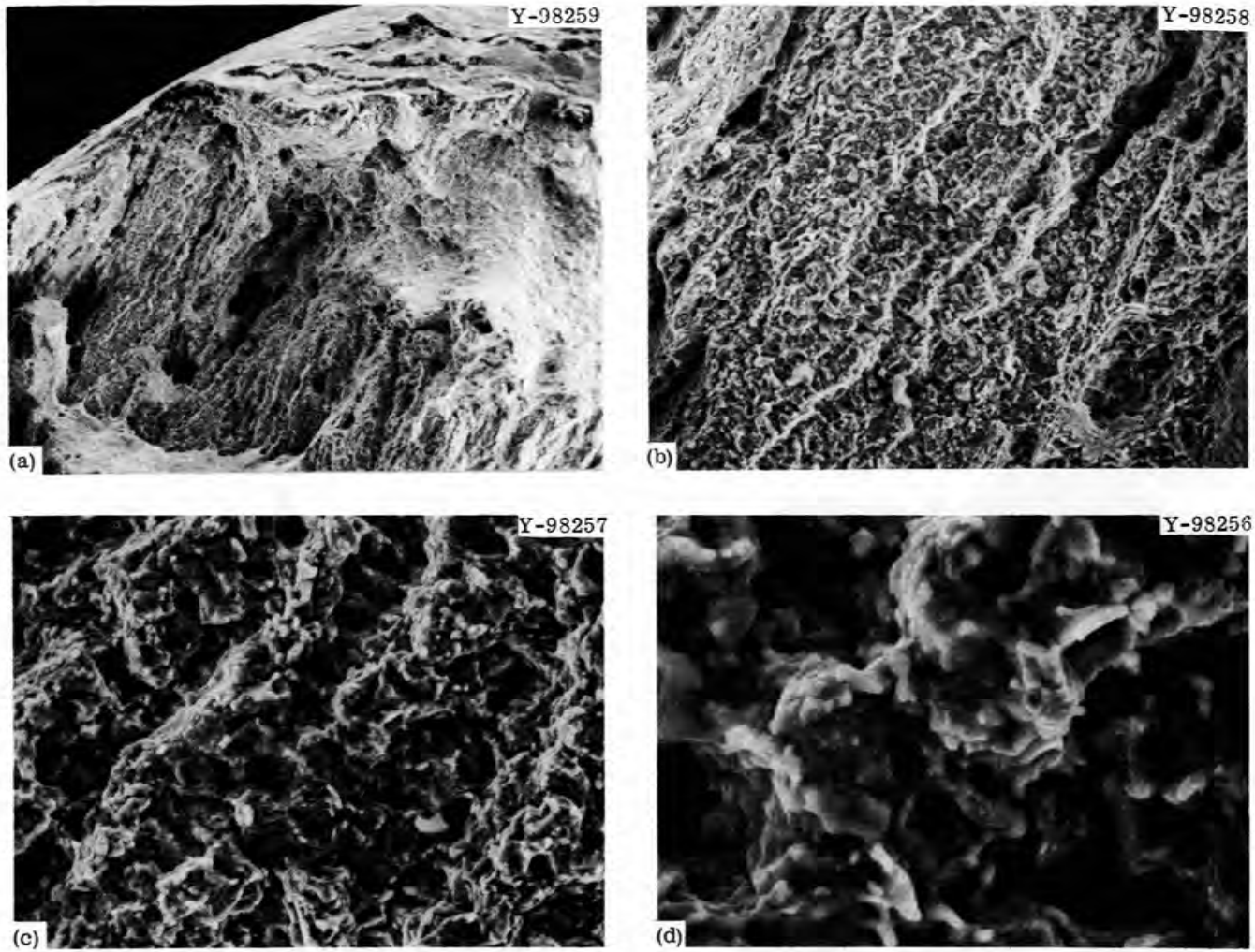

Fig. 7.5. Fractographic Analysis by Means of Scanning Electron Microscopy. Creep specimen from weld 1 failed after 27 hr at 25,000 psi with a total elongation of 22.5%. (a) Fracture surface at edge of specimen showing interphase fracture bounded upper right and lower left by shear. Secondary surface cracks along gage length are shown at top. 100×. (b) Central portion of (a) at 300×. (c) 1000×. (d) 3000×. Fractographs by R. K. Bennett, Technology Division, Y-12 Plant, Oak Ridge, Tennessee, operated by Union Carbide Corporation for the U.S. Atomic Energy Commission. Reduced 19%.

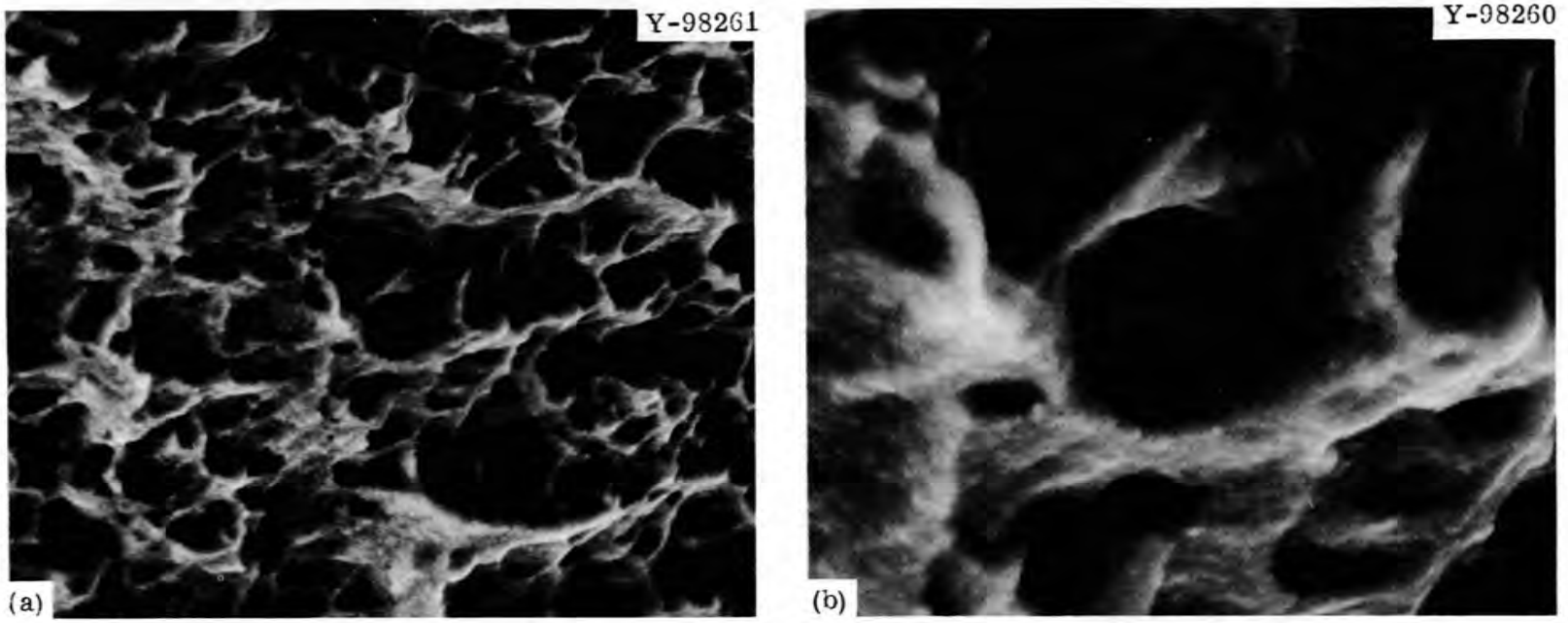

Fig. 7.6. Shear Portion of Fracture Surface. Scanning electron fractographs shows an area of the same specimens as that shown in Fig. 7.5. The elongated dimples are typical of shear fracture. (a) Overall view of shear; 3000X. (b) Higher magnification showing hard particles (probably primary carbides) responsible for dimple initiation; 10,000X. Fractographs by R. K. Bennett, Technology Division, Y-12 Plant, Oak Ridge, Tennessee, operated by Union Carbide Corporation for the U.S. Atomic Energy Commission.

understanding of the fracture process for these welds and possibly indicate means of improving the long-time creep ductility.

Creep-rupture tests of several additional welds are under way and will be discussed in subsequent reports.

We have obtained an additional 48 × 96 × 1-in. type 304H stainless steel plate and will in the near future prepare about 15 linear feet of submerged-arc weld for use in a program sponsored by RDT at the U.S. Naval Research Laboratory. The welds will be prepared under typical industrial conditions and will be evaluated primarily on the basis of the test for dynamic tear.

References

1. W. O. Harms and G. M. Slaughter, "Shielded Metal-Arc Welding for LMFBR Components," pp. 164–172, this report.

8. SHIELDED METAL-ARC WELDING FOR LMFBR COMPONENTS

W. O. Harms G. M. Slaughter

The objective of this new program is to evaluate the shielded metal-arc (stick electrode) welding process for fabricating and repairing certain stainless steel components for liquid-metal fast breeder reactors (LMFBR). We very slightly modified the flux coatings of electrodes and are determining the influence of minor elements on the mechanical properties of the weld metal at elevated temperature. Flux coatings traditionally have been evaluated and selected by the relative ease with which weld metal can be deposited, and bead contour, arc stability, and deposition efficiency are usually prime considerations. The effect of the coating on the properties at elevated temperatures has not been seriously considered.

As part of this effort, we are also providing weld specimens to Battelle Memorial Institute Pacific Northwest Laboratory (BNWL) for a program of irradiations for the Fast Flux Test Facility (FFTF).

Preparation of Weldment Samples for Irradiation and Control

Procurement and Machining of Samples for FFTF Irradiation Program (G. M. Goodwin)

A 16-in.-long submerged-arc weld was made in 1-in.-thick plate under carefully controlled conditions and shipped to BNWL. Samples for the FFTF irradiation program were machined from it.

Approximately 15 ft^2 of 2-in.-thick type 304L stainless steel plate was procured for use in preparing prototypical weldments for evaluation in the second phase of the FFTF weldment irradiation program. We plan to produce about 300 all-weld-metal specimens for tests to determine the effect of irradiation on weldments that approximate as closely as possible those in the actual FFTF vessel and components.

Effect of Variations in Flux Coatings

Preparation and Creep-Rupture Testing of Weldments (N. C. Binkley, G. M. Goodwin, D. G. Harman)

Fourteen shielded metal-arc weldments made with type 308 stainless steel electrodes that contained controlled minor differences in coating type or composition were prepared, and the weld deposits were analyzed chemically.[1] Table 8.1 is a simplified reference guide to the type of electrode coating and chemical analysis of the weld deposit.

Table 8.1. Coating Type and Chemical Analysis of Weld Deposit for Type 308 Stainless Steel Shielded Metal-Arc Welds

Weldment Reference Number	Coating Type	Weld Deposit Chemical Analysis
1	Lime	Standard
2	Lime-TiO_2	Standard
3	TiO_2	Standard
4	Lime-TiO_2	Low Si
5	Lime-TiO_2	High Si
6	Lime-TiO_2	Low P
7	Lime-TiO_2	High P
8	Lime-TiO_2	Low S
9	Lime-TiO_2	High S
10	Lime-TiO_2	Low C
11	Lime-TiO_2	High C
12	Lime-TiO_2	Low B
13	Lime-TiO_2	High B
14	Lime-TiO_2	Medium P

The same heat of stainless steel core wire was used in all 14 batches of electrodes. Batches 1 to 3 produced virtually the same weld deposit (designated as the "standard") and varied only in the general type of flux coating applied. These three types of coatings are all in widespread usage today; however, the lime-TiO_2 coating (batch 2) is used extensively by one manufacturer in the fabrication of large stainless steel vessels. Therefore, it was used as the basic coating for controlled additions of minor elements to the weld deposits (batches 4 to 14). Extensive study

and comparison of all three types of coatings are under way to determine the influence of subtle or unrecorded changes in the nature of the weld deposit.

Welds 1, 2, and 3 were examined by optical metallography. The electrodes gave essentially the same deposit microstructures (Fig. 8.1). They were indistinguishable in regard to ferrite content and morphology, as measured by the quantitative television microscope. Furthermore, we have attempted to characterize the behavior of each of the 14 batches of electrodes as to arc stability, mode of metal transfer across the arc, bead shape, and weld penetration. Four weld beads from each batch of electrodes were deposited on 10-in.-long × 2-in.-wide × 1-in.-thick stainless steel coupons. Thus, we could examine four bead profiles in one metallographic cross section, as shown in Fig. 8.2. The results of the evaluation of electrode performance were averaged and are shown in Table 8.2.

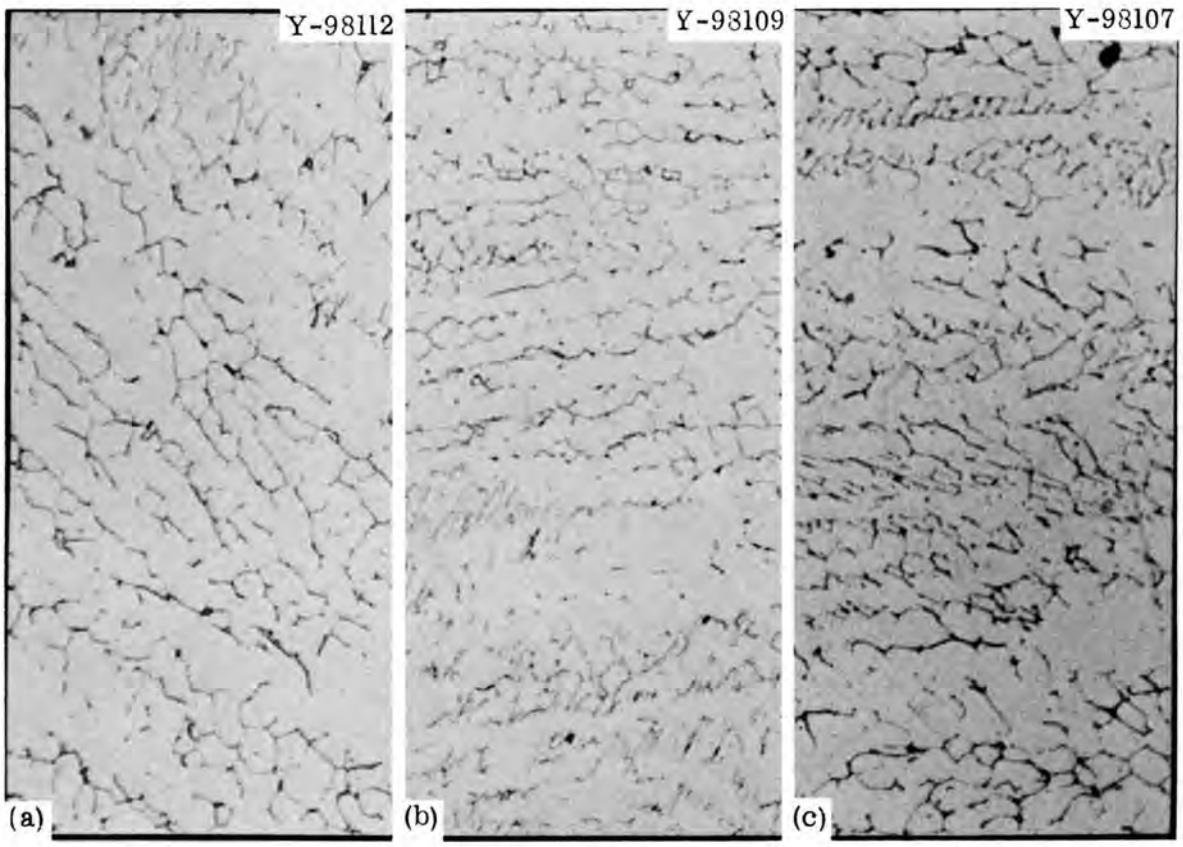

Fig. 8.1. Microstructures of (a) Weld 1 (Lime-Coated Electrodes), (b) Weld 2 (Lime-Titania-Coated Electrodes), and (c) Weld 3 (Titania-Coated Electrodes). 500×. Etchant: H_2O, KOH, K_3FeCn_6.

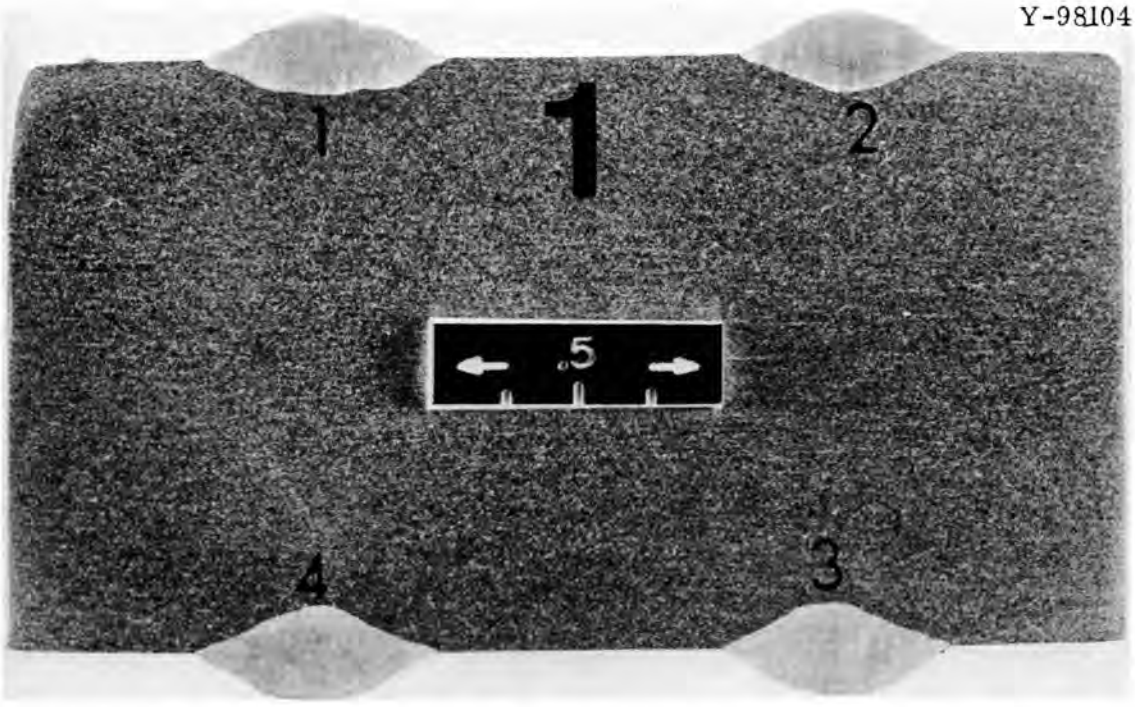

Fig. 8.2. Cross Section of Coupon Used for Evaluations of Electrode Performance.

Table 8.2. Electrode Performance Characterization of Type 308 Stainless Steel Coated Electrodes

Electrode Reference Number	Coating Description	Bead Characteristics				Transfer Rate (drops/sec)
		Width (in.)	Depth (in.)	Area ($in.^2$)	Penetration (in.)	
1	Lime	0.403	0.153	0.350	0.0734	2.7
2	Lime-TiO_2	0.360	0.161	0.344	0.0732	2.7
3	TiO_2	0.387	0.160	0.362	0.0718	2.8
4	Low Si	0.385	0.175	0.393	0.0828	2.6
5	High Si	0.366	0.174	0.366	0.0770	2.6
6	Low P	0.372	0.170	0.369	0.0773	2.5
7	High P	0.357	0.166	0.359	0.0779	2.9
8	Low S	0.358	0.165	0.367	0.0772	2.1
9	High S	0.372	0.168	0.376	0.0783	2.5
10	Low C	0.372	0.175	0.390	0.0831	2.7
11	High C	0.367	0.176	0.367	0.0797	2.2
12	Low B	0.388	0.165	0.366	0.0807	3.3
13	High B	0.375	0.163	0.366	0.0698	2.7
14	Medium P	0.362	0.167	0.355	0.0763	2.5

Such characteristics as bead shape, ease of deposit, slag entrapment, and deposition efficiency are highly dependent upon the arc characteristics and mode of metal transfer. Using a high-speed, low-inertia chart recorder, we recorded the arc voltage and arc current as functions of time. All electrode batches appeared to have very similar arc characteristics, with the "drop" mode of transfer being quite evident. This corresponded to a trace of frequent and regular short circuits caused by a molten drop of transferring metal completely bridging the arc. On the trace, these short circuits appeared as sharp rises in current with corresponding decreases in voltage. The average frequency of these occurrences was determined and is recorded in Table 8.2 as "drops/sec."

Although the results shown in Table 8.2 show modest differences from one electrode batch to another, it appears that the data are sufficiently random so that the performance and appearance of welds from the different batches are essentially indistinguishable. Note that this study of bead-on-plate welds provides data that do not agree with characteristics of type 308 stainless steel welding electrodes commonly reported in the literature and commercial advertisements. For example, it is reported in the literature[2] that lime-coated electrodes give a "flutter drop-type" transfer, while the TiO_2-coated electrodes give a "spray type" transfer. We found virtually no difference between the modes of transfer for the two types of coating. Moreover, one commercial manufacturer claims to have an electrode of type 308 stainless steel with a high Si content that promises to give consistently more penetration than the standard electrode. The high-Si electrode used in our study gave only average penetration, while the low-Si electrode actually gave more penetration than average. In addition, the welder who made all welds included in this study reported that he noticed little, if any, difference in the performances of the different batches.

Our studies of mechanical properties were concentrated on creep-rupture tests at 595 and 650°C. We use a specimen of the size and configuration necessary to produce engineering design data. We are using newly constructed lever-arm creep testing machines that were carefully calibrated to maintain constant load throughout the tests. A continuous

record of specimen extension during the test is obtained along with measurements of the specimens both before and after test.

A sketch of our test specimen is shown in Fig. 8.3. The specimen is 4 1/4 in. long overall and has a 1/4-in.-diam × 2-in.-long gage section. Three of these specimens, oriented longitudinally to the weld axis, were machined from the cross section of the weld as shown schematically in Fig. 8.4. Each specimen blank is identified as to its cross-sectional position and its location along the weld axis.

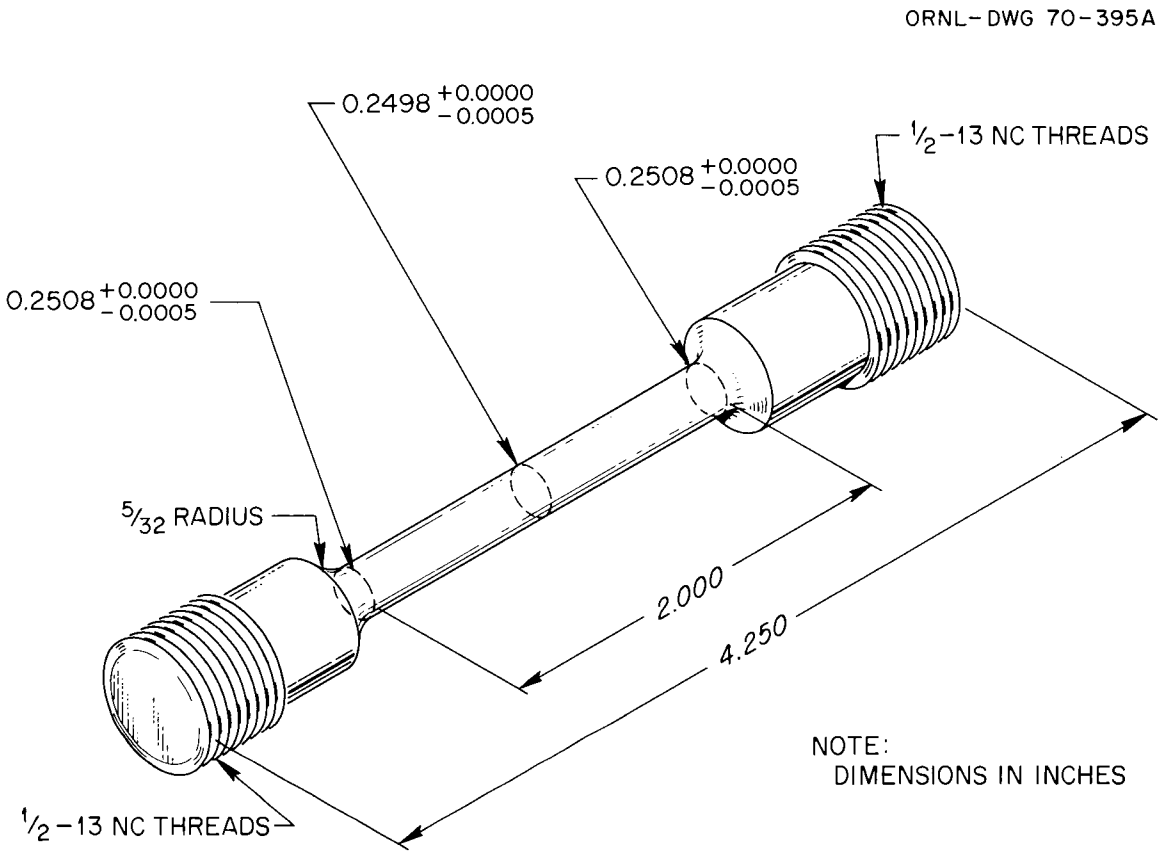

Fig. 8.3. Test Specimen for Weld Evaluation.

Several creep-rupture tests were completed on specimens from welds 1 to 4. The specimens were tested in air in the as-welded condition at 650°C. Stress levels of 25,000, 20,000, and 18,000 psi were used to provide a range of rupture times from 10 to 1000 hr. These test results

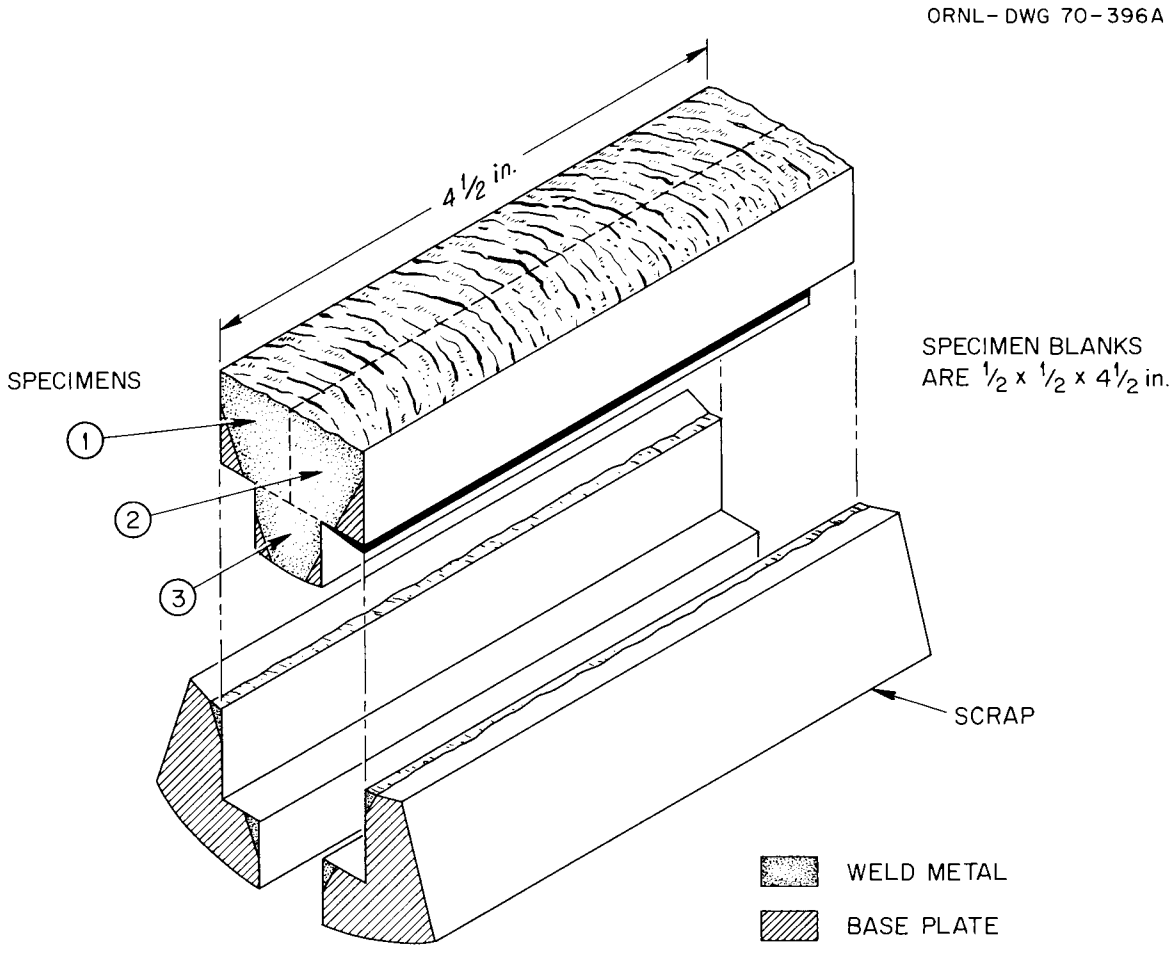

Fig. 8.4. Method of Sectioning Welds to Obtain Test Specimens. A 4 1/2-in.-long section of weld yields three longitudinal specimens. Each specimen is labeled to denote its cross-sectional location and distance along the weld.

are listed in Table 8.3. In general, the welds made with TiO_2 electrode coatings (welds 2, 3, and 4) showed similar rupture times, while weld 1 (lime-coated electrode) showed comparatively shorter rupture times. This is shown graphically in Fig. 8.5. This figure shows that the straight-line extrapolation of the two lines drawn through the data points would yield significantly different stress values at longer rupture times.

Figure 8.6 shows the creep elongation values from Table 8.2 plotted as a function of the rupture time. All four welds lost ductility for the longer tests. Less than 1% total creep elongation would be expected for all four welds for tests longer than 1000 hr. The "standard" weld-metal compositions (welds 1 and 3) show the same relationship between

Table 8.3. Results of Creep-Rupture Tests of Welds 1 to 4

Stress (psi)	Rupture Time, hr				Total Elongation, %			
	Weld 1	Weld 2	Weld 3	Weld 4	Weld 1	Weld 2	Weld 3	Weld 4
$\times 10^3$								
18	212	575	655	592	8.7	0.14	0.85	3.2
20	135	363	322	127	11.5	3.5	1.1	15.7
25	27	44	26	40	22.5	10.2	23.0	26.7

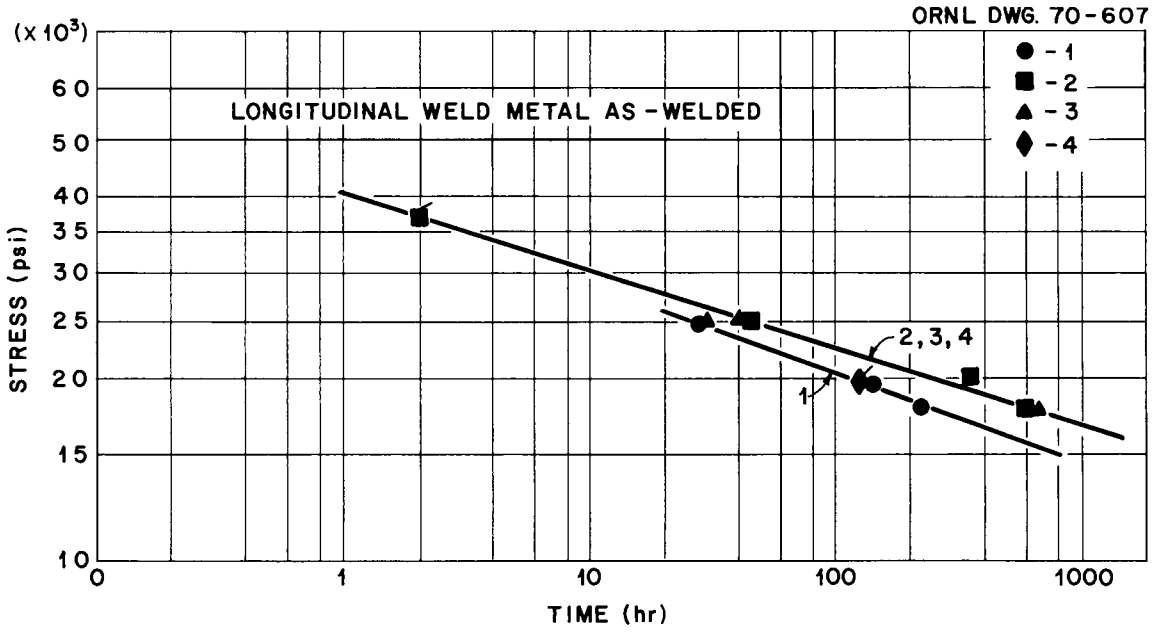

Fig. 8.5. Stress-Rupture Properties of Welds 1 to 4. All-weld-metal specimens were located longitudinally to the welding direction and were creep tested in air at 650°C. The weaker weld 1 was made with a lime-coated electrode. The flagged datum point denotes ultimate tensile strength versus total test time for a 0.002 min^{-1} tensile test.

rupture time and ductility, while weld 2 shows significantly lower ductility at comparable rupture times. The reason for this is not yet known. Weld 4 shows slightly higher ductility. A preliminary conclusion is that the lower Si content of weld 4 (see Table 8.1) enhanced the creep ductility. In this regard, it will be interesting to observe the results from weld 5, which has a higher Si content.

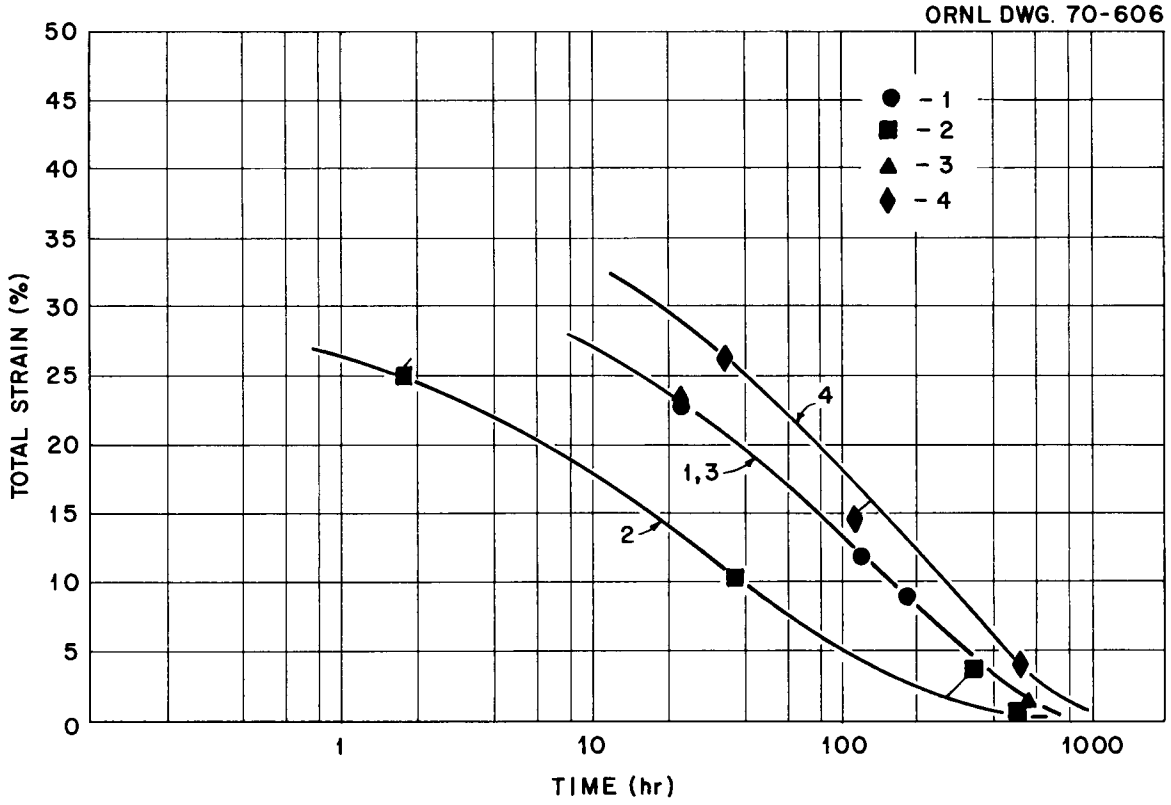

Fig. 8.6. Creep Ductility Versus Rupture Time for Welds 1 to 4. Data are from the same tests as shown in Fig. 8.5. Welds 1 and 3 were made with electrodes coated with lime and titania (> 20% TiO_2), respectively, while the less ductile weld 2 was made with a lime-titania (< 20% TiO_2) electrode. Weld 4, which was somewhat more ductile, differed from weld 2 only in having lower silicon content (0.29% as opposed to 0.47%).

References

1. N. C. Binkley, G. M. Goodwin, and D. G. Harman, Fuels and Materials Development Program Quart. Progr. Rept. Sept. 30, 1969, ORNL-4480, pp. 111–113.

2. R. P. Sullivan, Metals Eng. Quart. 7(4), 16–41 (November 1967).

9. NONDESTRUCTIVE TESTING TECHNIQUES FOR LMFBR

W. O. Harms R. W. McClung

We are developing new methods, techniques, and equipment for nondestructively evaluating materials or components related to the liquid-metal fast breeder reactor (LMFBR). Among the methods studied are electromagnetic induction, ultrasonics, and penetrating radiation. Special emphasis is being given to developing techniques for measuring the degree of cold work in stainless steel tubing with a small diameter.

Development of Advanced Nondestructive Testing

Development of Eddy-Current Instrument (C. V. Dodd)

We are continuing the development of an eddy-current instrument to measure both the size of defects and their depth below the surface. Construction of the modular phase-sensitive eddy-current instrument, whose modules will be used in the new instrument, is continuing, and it is scheduled for delivery on January 2. We have constructed a scaled-up experiment consisting of a large driver coil with two pickup coils encircling a column of Hg. Various simulated defects can be placed in the Hg and moved about to selected locations. We shall use these to measure the phase and amplitude response that would be related to different depths in a solid rod.

Ultrasonic Schlieren Techniques for Evaluation of Welds (H. L. Whaley, Jr., K. V. Cook)

A number of welded samples of stainless steel [butt welds in 1-in.-thick (2.54 cm) plate] were fabricated to our specifications. These have intentional defects similar to those in the welds in the Al samples described in the last report[1] and will be examined similarly with the schlieren system. We will correlate these results with those obtained by independent ultrasonic techniques applicable to the testing of welds.

Measurement of Cold Work in Stainless Steel Tubing

Design and Construction of Impedance Bridge (C. V. Dodd, W. A. Simpson)

We are investigating methods for nondestructively measuring the degree of cold work in stainless steel tubing that has a small diameter. We emphasize the use of electromagnetic induction for detecting the changes in magnetic permeability produced by cold work.

Because of the excellent response of the eddy-current bridge system to cold-rolled flat sheets,[2] we designed a prototype system that uses encircling coils for tubes. As part of the design study, we used a computer program that we recently developed that is a mathematical model for an impedance bridge and allows studies of variations in the components of the circuit.[3] The system finally selected was determined to be the best of a number that we analyzed on the computer. The design calculations indicate that we can measure the relative permeability in the tubes to within ±50 ppm. Our work thus far indicates that a change from 19 to 21% cold work produces an increase in permeability of 150 ppm. We used our computer program to determine how much variance we could allow in the several properties of the impedance bridge and still achieve this accuracy. The results are shown below:

Property	Maximum Drift (%)
Bridge Voltage	
Magnitude	0.01
Frequency	0.01
Bridge Resistors	
Matched drift	0.01
Differential drift	0.0001
Coil Inductance	
Matched drift	0.01
Differential drift	0.0001
Coil Resistance	
Matched drift	0.1
Differential drift	0.01
Amplifier Gain	0.01

Not only must the parameters of the bridge be carefully controlled; our measurement of the AC voltage output from the bridge must be within ±0.01%. All of these tolerances are within those of standard commercial components. The calculations also include an allowable variation of ±0.002 in. in the diameter of the tubing. We are now constructing the necessary coils and amplifiers for the designed impedance bridge. This technique continues to demonstrate the capability of making rapid, accurate measurements of cold work.

References

1. H. L. Whaley, Jr., and K. V. Cook, Fuels and Materials Development Program Quart. Progr. Rept. Sept. 30, 1969, ORNL-4480, pp. 114–115.
2. C. V. Dodd and W. A. Simpson, Fuels and Materials Development Program Quart. Progr. Rept. Sept. 30, 1969, ORNL-4480, pp. 115–117.
3. C. V. Dodd, W. G. Spoeri, W. E. Deeds, and W. A. Simpson, "Design of Coil Systems for Detection of Defects," pp. 308–309, this report.

10. SODIUM CORROSION STUDIES

W. O. Harms J. H. DeVan A. P. Litman

The purpose of this program is to investigate the chemical and metallurgical effects produced in structural materials during exposure to molten Na. The program is designed to guide the selection of container materials for Na-cooled fast breeder reactor (LMFBR) systems and provide guidelines for specifying insulating materials for use with stainless steel components in the Fast-Flux Test Reactor (FTR).

Comparative Corrosion Tests on Refractory Alloys

J. H. DeVan

Although V alloys are highly resistant to dissolution by Na, they are quite reactive with nonmetallic impurities in Na, particularly with C, N, and O. Accordingly, we are investigating the mechanisms by which V alloys are attacked in Na at impurity levels typical of service conditions in a reactor. Our program is concerned with four basic aspects of the oxidation process for V alloys in Na: (1) the partitioning of O between V alloys and Na; (2) the effects of alloying additions of Cr and Zr on the diffusion coefficient of O in V; (3) the effects of Cr and Zr in V on the oxide formed and on the dissolution of the alloys in Na; and (4) the solubility of V in Na as affected by the presence of O in either metal. We are also examining the kinetics of the transfer of C, N, and O between V alloys and types 304 and 321 stainless steel in a Na circuit.

Effect of Oxygen on the Compatibility of Vanadium and Vanadium Alloys with Sodium (R. L. Klueh)

We have completed a series of static capsule tests[1] to compare the uptake of O from Na by various V alloys. Two specimens, the alloy being tested along with an unalloyed V specimen, were exposed in a type 304 stainless steel capsule to Na with 2000 ppm O (added as Na_2O) for 100, 200, 300, and 600 hr. The alloys tested were V–5% Cr, V–10% Cr, V–15% Cr, V–20% Ti, V–15% Cr–5% Ti, Vanstar 7 (V–9% Cr–3% Fe–1.3% Zr–0.05% C),

Vanstar 8 (V–8% Cr–10% Ta–1.3% Zr–0.05% C), and Vanstar 9 (V–6% Fe–5% Nb–1.3% Zr–0.05% C).

All specimens gained weight and had black or dark-brown scales of varying thicknesses. Table 10.1 lists the weight gains for each specimen. Although quantitative conclusions must await chemical analyses of the specimens, some tentative conclusions can be made on the basis of the weight changes. If we relate the weight changes in these tests to O pickup, it appears that the addition of Cr to V strongly affects the O partitioning behavior of the resultant alloy. The V–5% Cr alloy gained less weight than unalloyed V, and the V–10% Cr and V–15% Cr alloys gained still less than V–5% Cr. Note that V–15% Cr gained less weight at longer test times than at shorter times. This suggests that O redistribution is occurring between the alloy and the companion pure V specimen in the capsule. The same appears to be true with the lower Cr alloys. In contrast, the V–20% Ti and V–15% Cr–5% Ti alloys continued to increase in weight with increasing test times.

Vanstar 7 gained much less weight than either Vanstar 8 or Vanstar 9. Since the ratio of Cr atoms to other atoms in Vanstar 7 and 8 is roughly the same, it appears that the cause of the increased weight change of Vanstar 8 and 9 is due to Ta and Nb, respectively.

The specimens are now being analyzed for changes in O concentration during test and will then be examined metallographically.

The Oxidation Kinetics of Vanadium and Vanadium Alloys (R. L. Klueh)

Recently we reviewed published data on the effect of O in Na on V and V alloys.[2] We found that the hardened zone characteristically observed in V-Ti and V-Al alloys can be ascribed to an internal oxidation process. Oxygen dissolution into these alloys first causes internal precipitation of TiO_2 or Al_2O_3. Precipitation proceeds along a front that moves perpendicularly to the exposed surface, and the rate of movement is limited by O diffusion to the front. The O content of the nearly pure V matrix behind the front depends on the chemical potential of O in the Na. If the O concentration in the Na is below that at which an oxide scale forms on the alloy (such as a Zr hot-trapped system), the front moves in accordance with the classical internal oxidation model of Wagner.[3] If

Table 10.1. Weight Change of Vanadium and Vanadium Alloys Exposed to Sodium Containing 2000 ppm O at 600°C

Alloy	Time (hr)	Specimen Weight Gain, mg	
		Vanadium	Alloy
V–5% Cr	100	7.1	4.9
	200	7.6	3.7
	300	6.5	3.8
	600	6.4	3.1
V–10% Cr	100	7.4	3.9
	200	8.1	3.3
	300	7.5	2.4
	600	9.1	3.2
V–15% Cr	100	9.1	2.4
	200	9.1	1.7
	300	10.3	1.3
	600	9.8	0.8
V–20% Ti	100	8.8	3.7
	200	7.7	3.4
	300	7.1	3.3
	600	6.8	4.3
V–15% Cr–5% Ti	100	8.7	0.9
	200	9.2	1.0
	300	5.9	1.2
	600	7.1	1.8
Vanstar 7 (V–9% Cr–3% Fe–1.3% Zr–0.05% C)	100	8.7	0.8
	200	11.0	1.4
	300	7.6	1.1
	400	10.5	1.7
Vanstar 8 (V–8% Cr–10% Ta–1.3% Zr–0.05% C)	100	7.2	4.8
	200	6.6	3.1
	300	6.9	3.2
	400	5.9	3.3
Vanstar 9 (V–6% Fe–5% Nb–1.3% Zr–0.05% C)	100	9.1	5.5
	200	7.4	4.7
	300	5.9	3.7
	400	7.9	3.8

an external scale forms, such as is usually the case in cold-trapped systems, motion of the front can be predicted by the model of Rapp and Colson.[4]

Our analysis of the experimental data on V-Ti and V-Al alloys in terms of these internal oxidation models indicates that such alloys offer no apparent advantages in resistance to corrosion in Na over that of unalloyed V. Although internal oxidation increases the time required for O to affect the interior of the cladding, the attendant precipitation hardening debilitates the alloy as a load-carrying member. Furthermore, the rate of advance of the internal oxidation front is extremely fast relative to the exposure time that would be required for use as a cladding.

Above concentrations of about 10 ppm O in Na, all V alloys tested to date exhibit a nonprotective corrosion scale. Therefore, aside from the problem of O uptake by the alloy, one must consider the problem of scaling, particularly in the event of an O excursion during reactor operation. This problem can be counteracted by developing alloys that will form protective, nonscaling oxides either in service or by an oxidation pretreatment. Such protection might be provided in the internal oxidation type of alloys if conditions could be established so that the flux of the alloying element toward the surface exceeded the flux of O into the alloy. Alternately, one would seek to produce binary oxides with V alloys that exhibit improved coherency. We plan to investigate each of these approaches with respect to the alloy compositions listed in Table 10.1. However, our evaluation will utilize low-pressure O_2 as the O source rather than the O in the Na.

Interstitial Contamination of Vanadium and Its Alloys (R. L. Wagner)

We are studying the interaction of V alloys with low-pressure gases to characterize the effects of alloying additions on the rate and nature of interstitial contamination (with O, N, and C) and to determine the influence of this contamination on their creep properties.

We exposed 0.005-in.-thick specimens of V and of seven V-base alloys to low-pressure O_2 according to the schedule shown in Table 10.2. Oxidation rates of the specimens were determined from weight changes and

Table 10.2. Oxygen Contamination of Vanadium Alloys[a]

Material	Oxygen Contamination Rate, ppm/hr			
	500°C 5×10^{-6} torr 211 hr	600°C 5×10^{-6} torr 235 hr	700°C 5×10^{-6} torr 214 hr	600°C 5×10^{-7} torr 570 hr
Vanadium	88.5	93	105	6.9
V–5% Cr	83.5	79	93.5	6.9
V–10% Cr	73.5	69	74.3	4.4
V–15% Cr	57	59	75.2	5.7
V–15% Cr–5% Ti	36	77	105	7.9
Vanstar 7	41	46	47.7	2.6
Vanstar 8	50	40	53.8	2.2
Vanstar 9	41	44	43.7	3.2

[a]Data based on 0.005-in.-thick specimens.

from chemical analyses based on both vacuum-fusion or neutron-activation techniques. These analytical methods agreed with 20%.

The results shown in Table 10.2 indicate that the O pressure has a much larger effect on the contamination rate than does temperature between 500 and 700°C. Increasing pressure by a factor of 10 at 600°C increases the rate by a factor between 10 and 20. The alloy V–15% Cr–5% Ti appears to be most sensitive to temperature change, and the Vanstar alloys appear to be the least sensitive to temperature change. Furthermore, the Vanstar alloys appear to be more resistant to contamination by O than the other alloys.

On the basis of previous data,[5] we had predicted that the contamination rate of V at 5×10^{-7} torr of O_2 and 600°C would be about 5 ppm/hr. This prediction assumed that the contamination rates would be proportional to the O pressure and inversely proportional to the specimen thickness. Our present data (Table 10.2) show a rate of about 7 ppm/hr and appear to validate the latter assumptions. However, a similar calculation predicts a contamination rate of about 50 ppm/hr at 5×10^{-6} torr O_2 compared to a measured rate of about 100 ppm/hr. The poorer agreement at the higher pressure might be due to the fact that predictions were based on 500-hr data, while the present runs were only about 200 hr. If true, this indicates that the contamination rates decrease with the reaction time.

Mass Transfer of Interstitial Impurities Between Vanadium Alloys and Type 300 Series Stainless Steels (D. H. Jansen)

We are studying the mass transport of interstitial impurities from types 304L and 321 stainless steel to V alloys in liquid Na. Of particular interest are the effects of interstitial impurities (C, N, and O) on the room-temperature and elevated-temperature (700°C) mechanical properties of the ferritic and V materials.

One series of tests is being conducted in bimetallic thermal-convection loops that provide a heated V section and a cooled stainless steel section. Loop 2 in this series, which was described in our last report,[6] has now completed 2200 hr of a scheduled 3000-hr run. A third loop, which is under construction, is designed to provide four times more surface area of V than our two previous loops.

In addition to these loop tests, we are conducting a series of static tests in which tensile specimens of 0.040-in.-thick V sheet are being exposed to Na in stainless steel vessels. Four tests in type 321 stainless steel containers were begun during the past quarter and are described in Table 10.3.

Interactions of Sodium with Nonmetallic Materials

A. P. Litman

Compatibility of Stainless Steel and Insulation for LMFBR Systems (C. D. Bopp[7])

The service temperatures of Na-cooled fast breeder reactors are considerably above those of present-generation power reactors. Among the potential problems associated with higher operating temperatures are the possible interaction of thermal insulation with reactor construction materials and the oxidation of the construction materials in the event of a Na leak. Accordingly, we are studying the reaction of commercial insulating materials with austenitic stainless steels between 370 and 760°C. A related study deals with the effect of Na on the oxidation of stainless steels, both insulated and uninsulated.

Table 10.3. Operating Conditions[a] for Static Tests of Vanadium and Type 321 Stainless Steel in Sodium

Test Temperature (°C)	Surface Area of V and V-Alloy Specimens, in.^{2}				
	Pure V[b]	Commercial V[c]	V–5% Cr[d]	V–10% Cr[e]	V–15% Cr[f]
800	8.0	5.3			
700	2.7	2.7	8.0		
700	2.7	2.7		8.0	
700		2.7			10.7

[a] All tests scheduled for 500 hr; ratio of type 321 stainless steel to V-base alloys = 4.0.

[b] Pure V: 80 ppm O, 2 ppm N, 30 ppm C.

[c] Commercial V: 1400 ppm O, 550 ppm N, 320 ppm C.

[d] V–5% Cr: 180 ppm O, 60 ppm N, 80 ppm C.

[e] V–10% Cr: 77 ppm O, 550 ppm N, 140 ppm C.

[f] V–15% Cr: 17 ppm O, 10 ppm N, 60 ppm C.

Oxidation of Insulated Stainless Steel. — We are testing the compatibility of couples of stainless steel and insulation at 760°C in an atmosphere of 99% N_2, 1% O_2, and 100 ppm (by weight) moisture. This environment is approximately the same as will be used in the Fast Flux Test Facility Closed Loop Cells,[8] although the moisture content exceeds the maximum of 0.1 ppm specified for the cell atmosphere. To achieve the 0.1 ppm value would require extensive drying of our gas mixture; and, since scaling generally increases with the moisture content, the higher moisture level should make our results conservative. (According to a recent theory,[9] moisture increases scaling by catalyzing the formation of volatile oxidation products.)

We have exposed types 304, 304L, 304H, 316, and 316L stainless steel to the N_2 mixture and observed that all of these steels form a highly protective scale within a few hours after the temperature of 760°C is reached; thereafter, the oxidation rate falls below the sensitivity of the measurements.[10] We expect to continue these tests until the exposure reaches about 2000 hr.

Effect of Sodium on the Oxidation of Stainless Steel. — We have also begun experiments to determine the effect of a Na leak on the oxidation behavior of austenitic stainless steels at liquid-metal-cooled fast breeder reactor service temperatures. The experiments will provide data on oxidation for two environments: (1) an atmosphere of 99% N_2, 1% O_2, and 100 ppm (by weight) moisture, and (2) moist air. The test variables under study include the effect of moisture in the atmosphere, the temperature of the Na, and the size of the leak. The test apparatus being used for these studies was described previously.[11]

The first of our experiments with a Na leak was conducted on a 1/4-in.-diam × 0.035-in.-wall-thickness type 304L stainless steel tube. A 0.060-in.-diam hole was drilled through the wall of the tube to serve as the leak, and the hole was surrounded by silica-alumina blanket-type insulation.[12] The external atmosphere consisted of 99% N_2 + 1% O_2 (see above), and the test temperature was 760°C.

The experiment began with the ejection of 2.5 g of Na through the hole into the insulation. An additional 2.5 g of Na was evaporated through the leak during the first few minutes after ejection, while the

temperature of the hole was controlled by heat of reaction and boiling of the initial Na and during a subsequent 10-hr period, while the tempeature was maintained at 760°C and flow of Ar cover gas was maintained through the leak. Examination of the hole after 10 hr showed that the diameter of the leak had increased about 50% and that corrosion products coated the outside of the tube to a distance of a few inches from the leak and the inside of the tube to a distance of about 1/4 in. from the leak. Also, areas of the outside of the tube were coated with yellow sodium peroxide. Zirconium foil, which was placed inside the tube to getter the Na, remained bright. The insulating material used in this test was penetrated to a depth of about 1/2 in. by the Na. The insulating material exposed to Na was converted to a brittle, black, charcoal-like substance. Although we obtained a crystalline x-ray diffraction pattern of the substance, we could not identify it on the basis of standard patterns.

Our second test of a simulated leak was conducted under conditions identical to those of test 1, except that the diameter of the leak was 0.004 in. The leak became plugged by sodium oxide immediately after 2.5 g of Na was ejected. The inside of the tube was pressurized with Ar to 250 psig; but the hole remained closed, and the test was discontinued after 2 hr. The corrosion resulting from this test was less than that in test 1, since there was little enlargement of the leak, no corrosion inside the tube, and no yellow sodium peroxide on the outside of the tube. However, the penetration of the insulation by Na was nearly the same as in test 1.

In our third test, we changed the form of the insulation surrounding the leak and also the shape and location of the leak. The test alloy, temperature, and external environment remained the same as in the first two tests.

The location of the leak in our first two tests was above the level of the Na until the Na was ejected. However, in our third test, the leak was at the bottom of the 1/4-in.-diam tube that served as our test specimen. Thus the Na came into contact with the leak as soon as it was admitted into the tube. The leak was formed by repeated bending of the tube and was in the shape of a small crack, shown in Fig. 10.1(a).

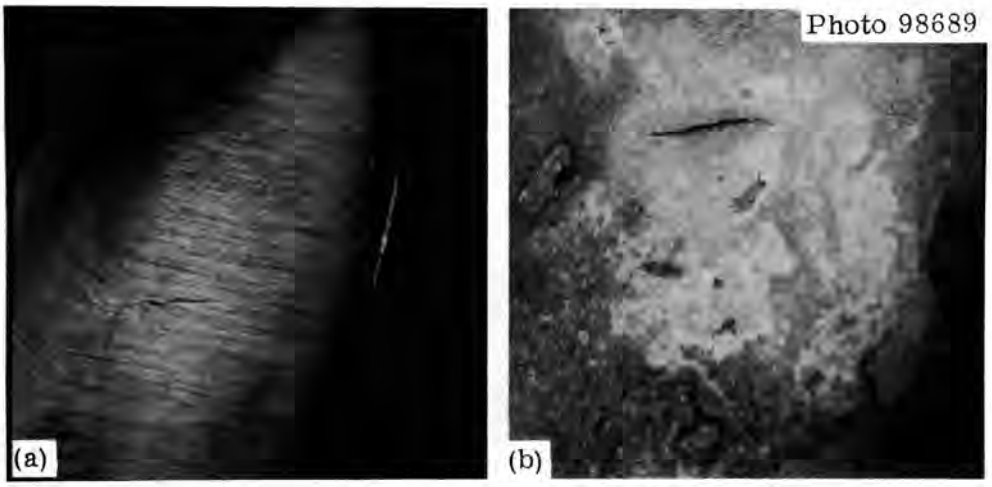

Fig. 10.1. Appearance of Defect in Type 304L Stainless Steel Tube Used to Study Effect of Sodium Leakage on Oxidation Behavior. 15×. (a) Before test. (b) After test.

The insulation surrounding the leak in test 3 was of the colloidal silica type[13] and was in block form.

Sodium was admitted to the tube at about 760°C. Basing our judgment on the work of Brainard,[14] we expected that the defect would immediately become plugged with sodium oxide and would remain plugged so long as there was not a significant pressure differential across the defect. Monitoring of the cover gas confirmed that plugging did occur. An internal Ar pressure of 250 psig was applied to the Na inside the tube, and after about 2 hr we observed the first evidence of Na leaking through the defect. After the crack was unplugged, a total of 6 g of Na leaked through the crack in about 30 min. The leak then became plugged with corrosion products as had occurred in test 2. We continued the test for an additional 50 hr with an internal Ar pressure of 250 psig but observed no further leakage of Na or Ar through the defect. Examination of the tube after this test showed no corrosion products inside the tube; however, there were yellow patches of sodium peroxide on the outside of the tube. After we removed the scale in hot 15% HNO_3–1% HF, we found that the width of the leak (crack) had increased [Fig. 10.1(b)]. The insulating material used in this test was penetrated to a depth of about 3/8 in., and the penetrated material closely resembled the product formed with the silica-alumina insulating material in the previous tests.

References

1. R. L. Klueh, Fuels and Materials Development Program Quart. Progr. Rept. Sept. 30, 1969, ORNL-4480, pp. 118–119.
2. R. L. Klueh and J. H. DeVan, The Oxidation of Vanadium and Vanadium Alloys in Sodium, ORNL-TM-2827 (March 1970).
3. C. Wagner, Z. Elektrochem. 63, 772 (1959).
4. R. A. Rapp and H. D. Colson, Trans. Met. Soc. AIME 236, 1616 (1966).
5. R. L. Wagner, Fuels and Materials Development Program Quart. Progr. Rept. Sept. 30, 1969, ORNL-4480, pp. 122–124.
6. D. H. Jansen, Fuels and Materials Development Program Quart. Progr. Rept. Sept. 30, 1969, ORNL-4480, p. 120.
7. On loan from Reactor Chemistry Division.
8. H. P. Maffei, Establishment of Preliminary Requirements for FFTF Cover Gas Purity, BNWL-1143 (October 1969).
9. P. L. Surman and J. E. Castle, Corros. Sci. 9, 771 (1969).
10. C. D. Bopp, Fuels and Materials Development Program Quart. Progr. Rept. March 31, 1969, ORNL-4420, pp. 92–100.
11. C. D. Bopp, Fuels and Materials Development Program Quart. Progr. Rept. Sept. 30, 1969, ORNL-4480, pp. 124–128.
12. Kaowool, a product of Babcock and Wilcox Company.
13. MIN-K 2000, a product of Johns-Manville Company.
14. J. P. Brainard and D. C. Kirkpatrick, Quarterly Status Report on the Advanced Plutonium Fuels Program April 1 to June 30, 1969 and Third Annual Report, FY 1969, LA-4284-MS, pp. 23–26.

11. DEVELOPMENT OF FAST-REACTOR NEUTRON-ABSORBER MATERIALS

G. M. Adamson, Jr. W. R. Martin G. W. Keilholtz [1]

The prime candidate material for the safety and shim rods in the Fast-Flux Test Reactor (FTR) and liquid-metal-cooled fast breeder reactor (LMFBR) is B_4C pellets in a stainless steel cladding. In spite of the widespread use of B_4C as a neutron absorber in thermal reactors, basic data have never been obtained. The material has never been fully characterized for structure, homogeneity range, effect of fabrication variables, and the effects of varying composition. The objective of our work is to characterize the material sufficiently to provide measurable control parameters to properly evaluate fabrication techniques, compatibility experiments, and the effects of irradiation. The irradiation studies will emphasize basic effects of materials variables in both thermal and fast-reactor environments. A secondary effort of this program will be the preliminary characterization of alternate materials that possess possible advantages over B_4C for use in fast reactors.

Characterization of Boron Carbide

Structural Changes That Result From Annealing of Powders (G. L. Copeland)

Further work is in progress on defining the changes that occur during high-temperature annealing of B_4C powders. The formation of the polyhedral voids and the dependence of their size on annealing temperature was confirmed. The pores are just barely visible at 1000× after annealing at 1450°C and range up to 3 μm in diameter after annealing at 2000°C. The increase in toluene density reported previously[2] may have been an anomalous result. The toluene pycnometer density of these powders is very sensitive to impurities and other variations. Results during this reporting period have indicated that up to 5 vol % pores may be generated during 2000°C annealing of Norbide 325F that has a B:C ratio of 3.62. The pore size and powder density are now being checked under carefully controlled conditions as a function of annealing temperature from 1350 to 2000°C.

Vacuum Hot Pressing of Pellets (G. L. Copeland)

Cylindrical pellets 0.4 in. in diameter by 0.4 in. long of several densities were prepared by vacuum hot pressing in graphite dies at 0.9 tsi. Higher densities are obtained when the powder is precompacted at 50 tsi in steel dies lubricated with stearic acid. A zirconia mold wash on the graphite minimizes reaction with the B_4C. The density obtained under these conditions varies with the pressing temperature from 60% at about 1650°C to near the accepted theoretical density of 2.52 g/cm^3 at about 2300°C. The pellet density appears to be reproducible under constant pressing conditions.

Boron Carbide Phase Equilibria (G. L. Copeland)

We previously reported[3] unidentified phases in an experimental B_4C produced in a button arc-melting furnace with a W electrode and Cu hearth. These phases have since been shown to be due to W and Cu contamination. Figure 11.1 shows the microstructure of a button produced by arc melting

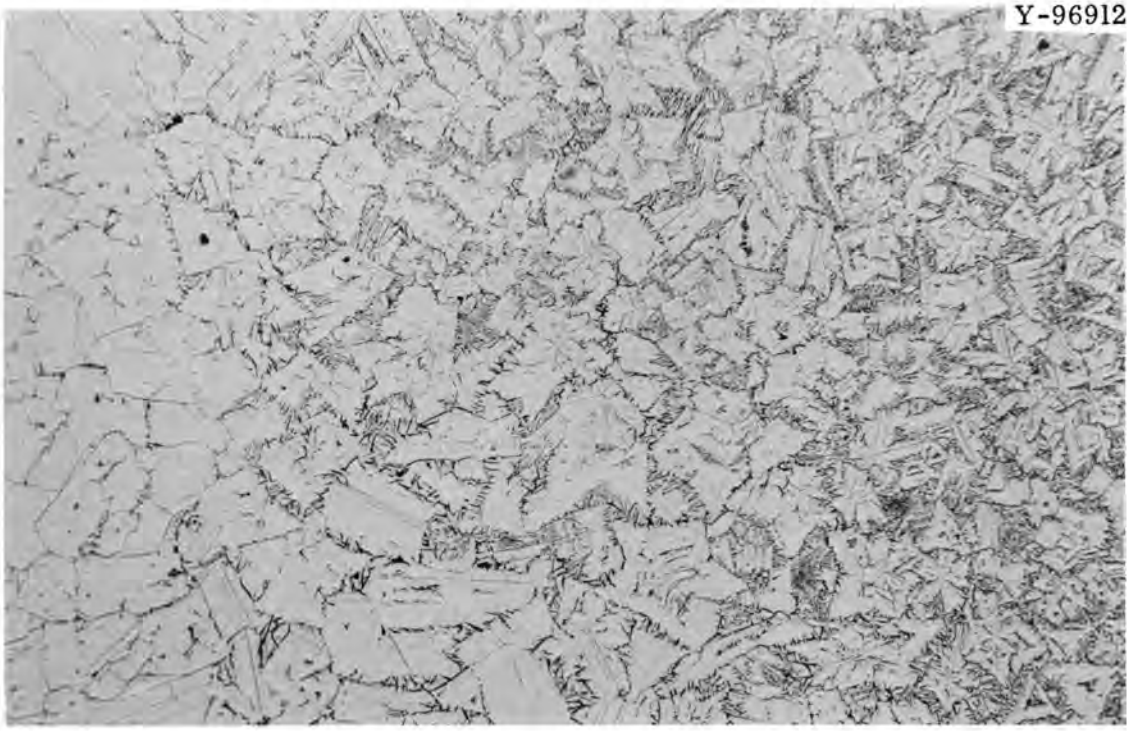

Fig. 11.1. Microstructure of Boron Carbide Arc-Melted with Graphite Electrode and Hearth. Electrolytically etched with 10% chromic acid solution. 100×.

Norbide 325F with a graphite electrode and graphite hearth. Graphite flakes are abundant in areas of the sample. X-ray diffraction shows that the sample consists of stoichiometric B_4C and graphite but no other phases. The B_4C grains are heavily twinned.

Irradiation Behavior of Boron Carbide

Thermal-Reactor Tests (G. L. Copeland)

The objectives of these tests are to examine the basic irradiation behavior of B_4C and to determine the influence of material variations such as the B:C ratio, grain size, and particle density. The thermal flux will allow high burnups in a short time, and the sample size will be kept small to minimize self-shielding.

The first three of a series of samples have been irradiated three weeks in the Oak Ridge Research Reactor. The capsules (see Fig. 11.2) were designed to reach about 450°C through gamma heating. The three powders irradiated were Norbide 325F as received and after annealing at 1500 and 2000°C. The powders are being evaluated by measurements of gas release, metallography, scanning electron microscopy, x-ray diffraction, pycnometer density, and analysis of burnup. The irradiation temperatures are being determined by evaluation of the SiC monitors.

Fast-Reactor Tests (G. L. Copeland, G. W. Keilholtz[1])

Fast-neutron irradiation tests in a reactor environment are necessary to correlate information gained from more basic tests to expected performance in a fast reactor. Pellets produced from some of the same materials used in the thermal-neutron irradiations will be tested in the Experimental Breeder Reactor-II (EBR-II). Capsule designs were completed for row 8 of the EBR-II, but the capsules are being redesigned for anticipated insertion into row 7 of EBR-II when the power is increased sometime near the end of FY 1970.

ORNL-DWG 70-575

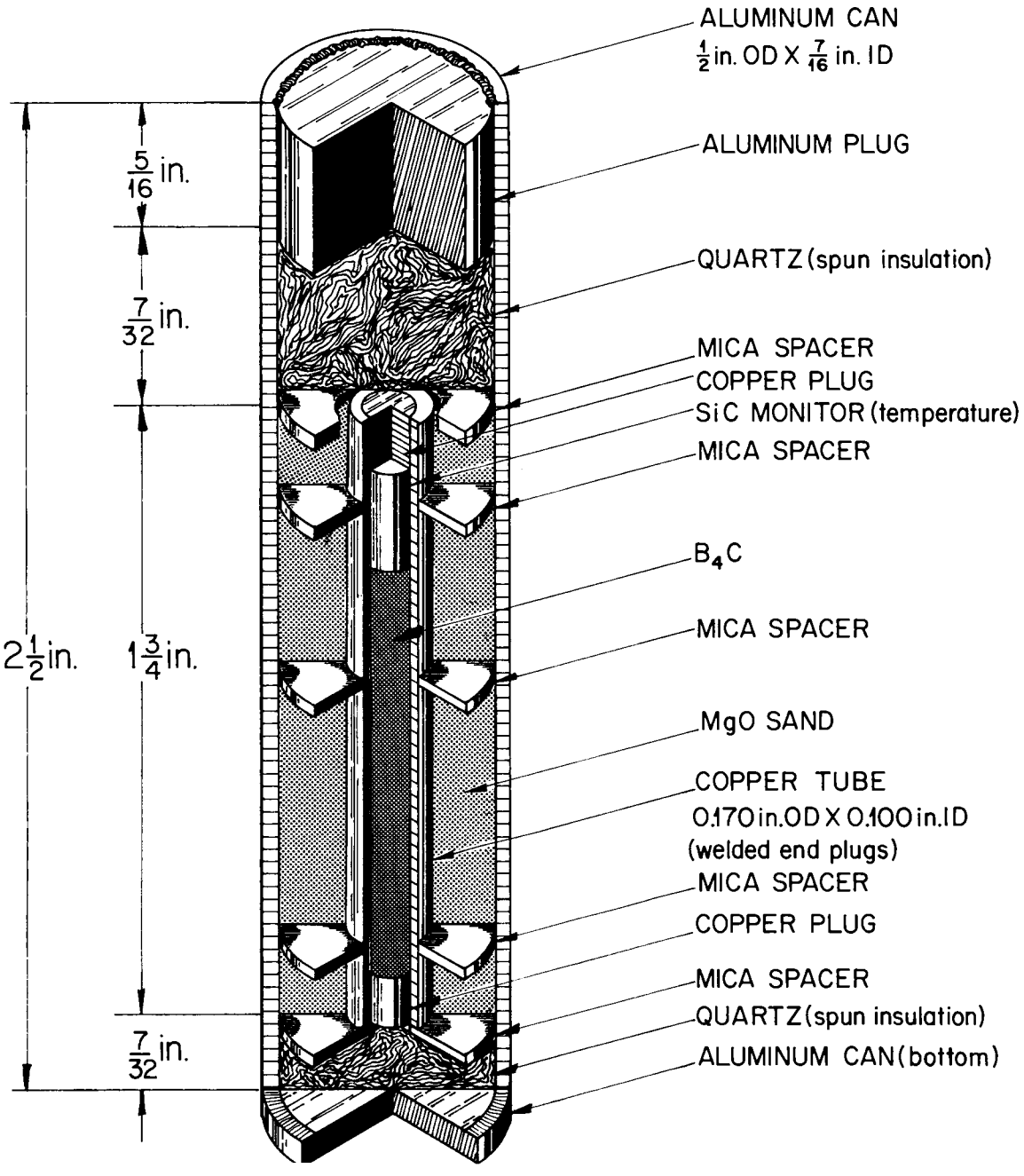

Fig. 11.2. Capsules for Irradiation of Boron Carbide in Isotopes Stringer in the Oak Ridge Research Reactor.

References

1. Reactor Chemistry Division.
2. R. S. Mateer and G. L. Copeland, Fuels and Materials Development Program Quart. Progr. Rept. Sept. 30, 1969, ORNL-4480, pp. 133–140.
3. R. S. Mateer and G. L. Copeland, Fuels and Materials Development Program Quart. Progr. Rept. Sept. 30, 1969, ORNL-4480, pp. 142–145.

PART II

SPACE POWER TECHNOLOGY

FUELS

12. DEVELOPMENT OF URANIUM MONONITRIDE FUELS

J. L. Scott

Uranium mononitride (UN) is potentially attractive as fuel for space nuclear reactors because of its excellent stability at high temperatures, high thermal conductivity, and good irradiation stability to 1000°C. The purpose of this program is to determine the basic mechanisms of fuel swelling and gas release above 1000°C. Results will be used to develop a model for predicting the performance of UN as a function of temperature, burnup, and cladding restraint.

Irradiation Testing

T. N. Washburn

The basic objective of the ORNL program[1,2] for irradiation testing of UN is to investigate the performance capability of this fuel material at temperatures of 1000 to 1500°C at the fuel center and 900 to 1400°C on the outside surface of the cladding and at linear heat ratings from 5 to 10 kw/ft. Fuel properties of most interest are swelling rate, release of fission gas, and compatibility with the cladding materials. The irradiation tests are conducted in the poolside facilities of the Oak Ridge Research Reactor (ORR). These facilities allow adjustment of the position of the test capsule relative to the reactor face, thereby providing a constant temperature at a selected reference point on the test specimen as the flux profile in the reactor changes and/or as the fissile content of the test fuel is diminished.

Postirradiation Examination of Capsule UN-3 (D. R. Cuneo[3])

The irradiation of capsule UN-3, which began in January 1969, was terminated November 18 after 5807 hr of operation. During a routine check of the NaK blanket gas at a midcycle shutdown, a high quantity of fission products (^{133}Xe and ^{135}Xe) was found, indicating that one of the

fuel pins had failed. The capsule was placed in the retracted mode, and operated at about 10% of design power until the next major shutdown (Dec. 7, 1969), when the capsule was removed and disassembled to determine which of the fuel pins had failed.

Visual examination revealed several short cracks in the middle fuel pin. Generally, these cracks were parallel to the long axis of the pin. Figure 12.1 shows the axial location and visual appearance of these cracks. Both fuel pins with T-111 cladding (middle and bottom) appeared rather shiny in the fueled (hot) regions. In these regions it was possible to see grains distinctively outlined; this is indicative of an etching effect by the NaK. The W–25% Re cladding on the top fuel pin

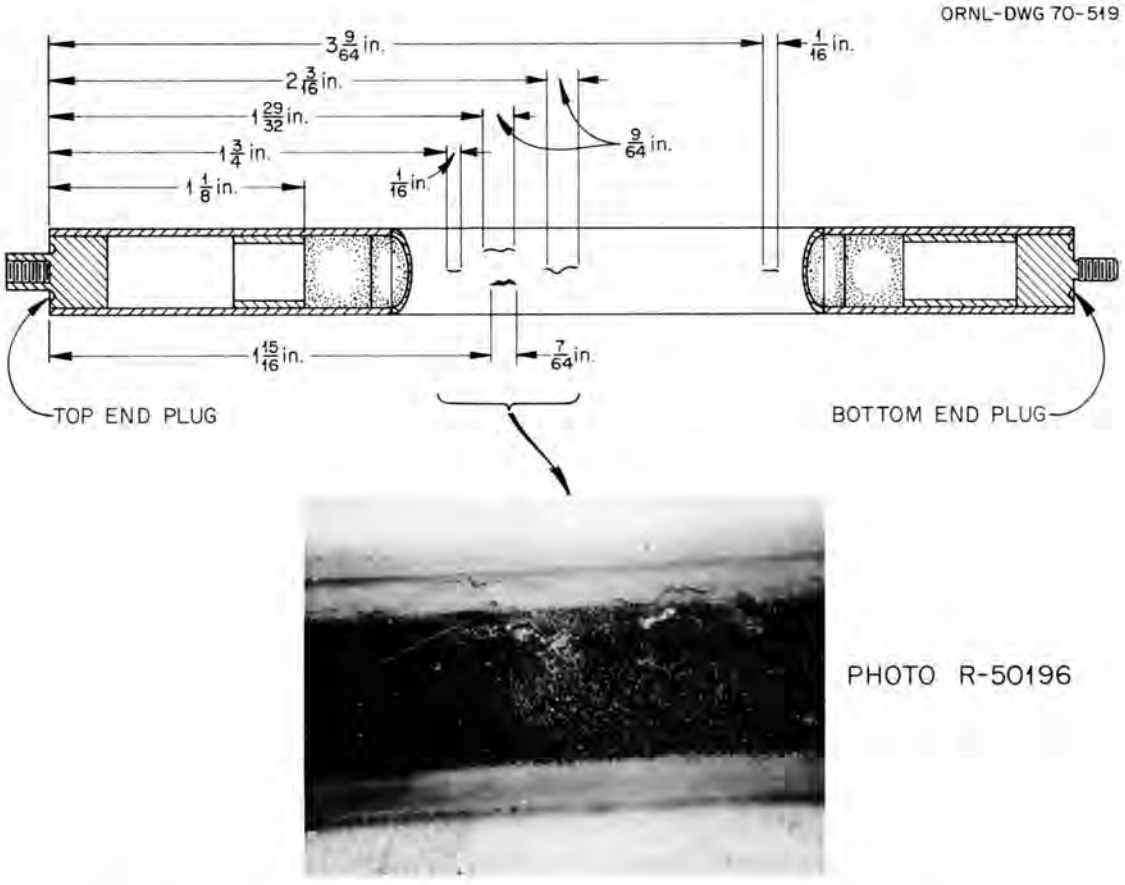

Fig. 12.1. Location and Appearance of Cracks in Cladding of Middle Fuel Pin of Capsule UN-3.

did not show this effect. The locations of some of the thermocouple sheaths were evident due to varying appearances of the cladding in localized regions. By visual examinations and dye-penetrant checks, we determined that the claddings of the top and bottom fuel pins remained sound during the irradiation test.

Each of the three fuel pins was examined by gamma scan; no unusual characteristics were revealed. The scan of the top fuel pin showed no activity other than in the fueled portion because the W-Re cladding and end plugs do not have activation products with sufficient half-lives to be found this long after removal from reactor flux. Activated nuclides could be distinguished clearly in the T-111 (Ta-W-Hf) cladding and end plugs, as illustrated in the scan of the middle fuel pin shown in Fig. 12.2. These scans were taken in the energy range 0.75 to 0.85 Mev,

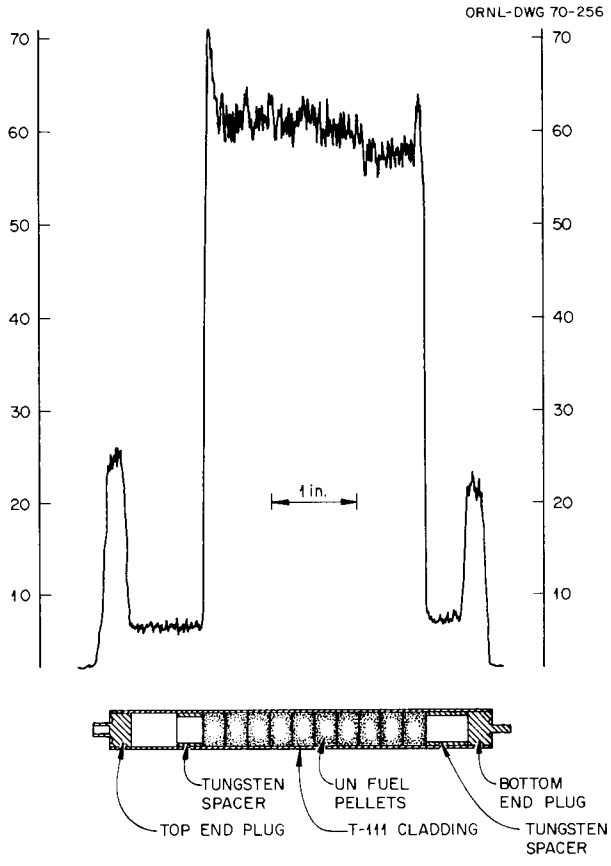

Fig. 12.2. Activity Indicated by Gamma Scan of Middle Fuel Pin — Capsule UN-3 (0.75 to 0.85 Mev).

which is particularly sensitive to ^{95}Zr-Nb. Scans made at a wide range of energy (0.5 Mev and greater) show very high peaks for the end plugs (^{182}Ta = 1.12, 1.22 Mev). Scans were made at various energies in both fueled and unfueled regions of the fuel pins. The findings were normal. In the fueled regions we found ^{134}Cs, ^{95}Zr-Nb, and indications of Ru. Cesium-137 cannot be detected by use of NaI spectrometry in the presence of ^{140}Ba-La and ^{95}Zr-Nb. The unfueled regions showed the possible presence of ^{134}Cs and ^{181}Hf and definitely indicated the presence of ^{182}Ta (the last two are activation products). The scans of the gas plenum at the bottom region of the top fuel pin showed the possible presence of ^{140}La, but this scan may have been made so close to the fuel column that the scanner responded to the high-energy (1.6 Mev) gamma radiation of ^{140}La from the fuel itself.

Preliminary measurements of the diameters of the fuel pins by means of an opposed dial gage profilometer yielded the data plotted in Figs. 12.3 and 12.4. The correlation between postirradiation measurements of the fuel pins over the end plugs and the preirradiation measurement of the diameters of the tubes indicates there is no significant difference between the results from the two measurement techniques. It is interesting to note that each of the fuel pins had some reduction in diameter during the irradiation test. This is most pronounced in the top fuel pin, which had a maximum decrease in diameter of 0.003 in. just below the end of the thermocouple well. The bottom fuel pin decreased in diameter by about 0.001 in. near the top of the fuel column but increased in diameter by about 0.0015 in. near the bottom of the fuel column. Correlation between diameter measurements at 0 and 90° orientations indicates that there is little or no ovality in the irradiated fuel pins.

In measuring the diameters on the middle (failed) pin, we selected the 0° orientation to obtain the maximum diameter at the largest crack. Therefore, the difference between readings at 0 and 90° orientations does not necessarily indicate ovality; it more likely indicates protrusion of the cladding in the failed region.

The diameters of each fuel pin will also be measured by air gage with continuous readout of the dimensions. This technique gives maximum

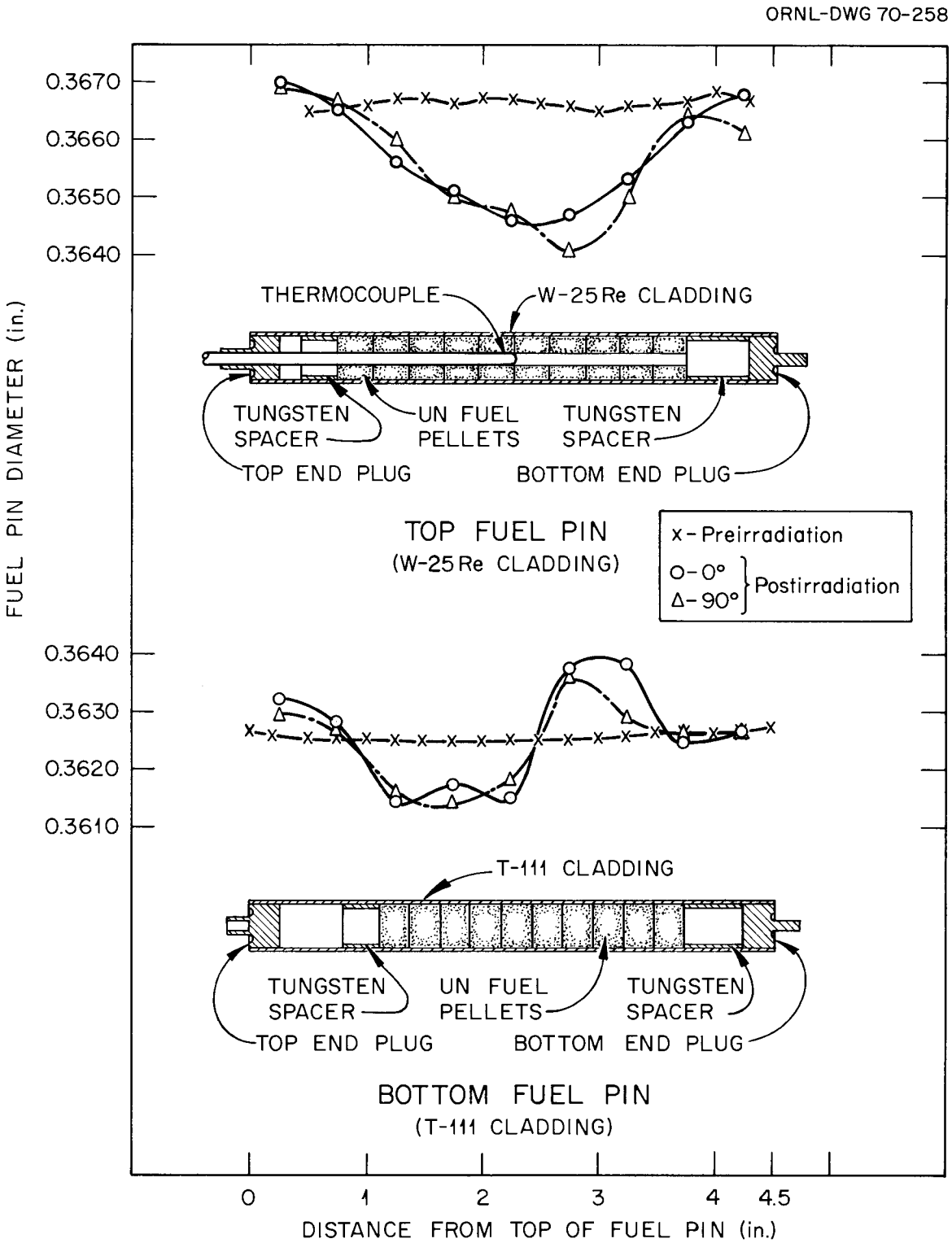

Fig. 12.3. Comparison of Diameters of Top and Bottom Fuel Pins of Capsule UN-3 Before and After Irradiation.

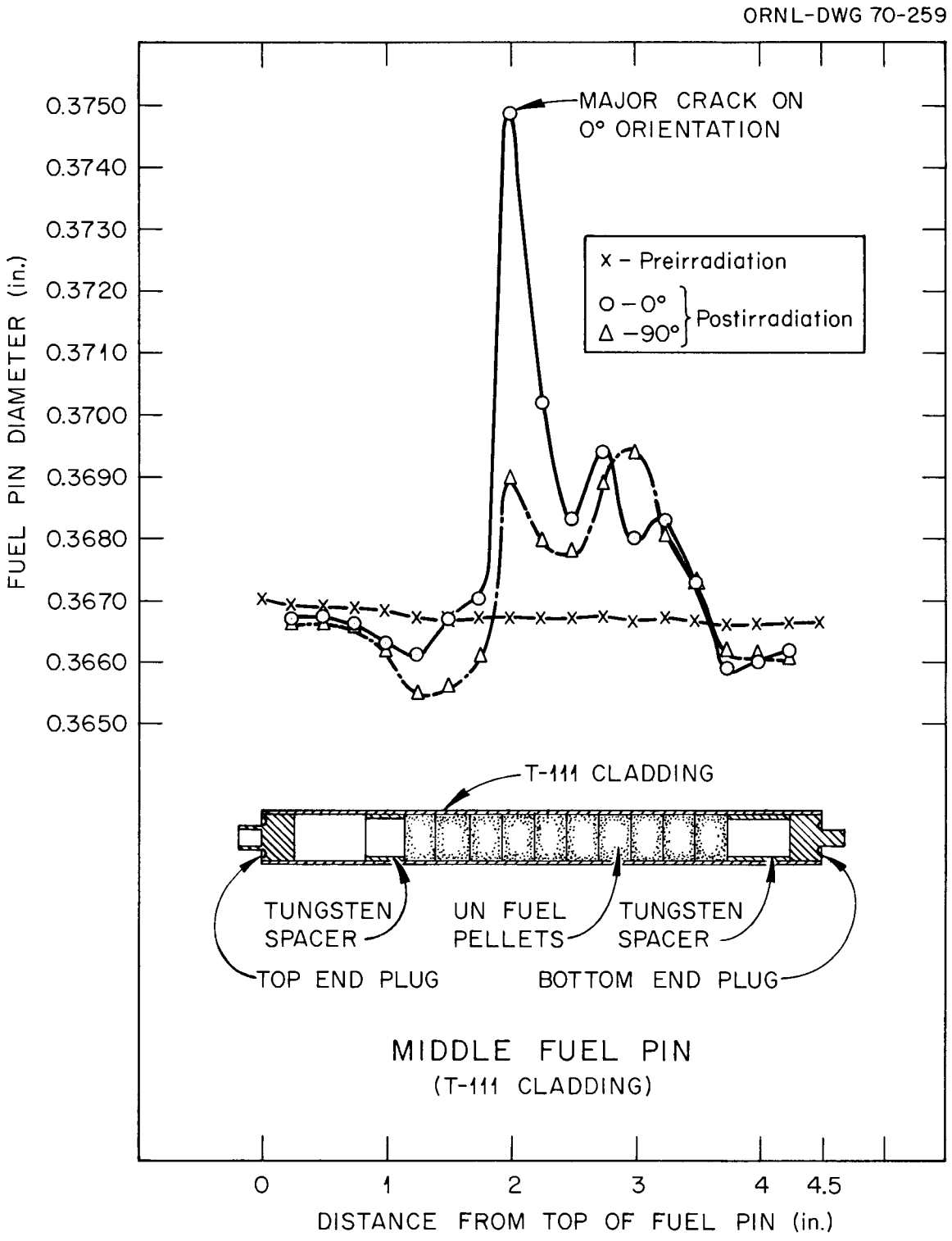

Fig. 12.4. Comparison of Diameters of Middle Fuel Pin From Capsule UN-3 Before and After Irradiation.

assurance of detecting maxima and minima and will also show ovality and bowing. This inspection will complete our nondestructive evaluation of the pins. We will then section the middle fuel pin to investigate the cause of failure.

References

1. The current program includes work sponsored by the Atomic Energy Commission (AEC) and work sponsored by the National Aeronautics and Space Administration (NASA) under Interagency Agreement 40-184-69, NASA Order C-54536-B. Specifically, capsules UN-1, UN-2, UN-3, and UN-6 are funded by AEC, and capsules UN-4 and UN-5 are funded by NASA.
2. T. N. Washburn, Fuels and Materials Development Program Quart. Progr. Rept. Sept. 30, 1969, ORNL-4480, pp. 149–150.
3. On loan from Reactor Chemistry Division.

CLADDING AND OTHER STRUCTURAL MATERIALS

13. CLADDING MATERIALS FOR SPACE ISOTOPIC HEAT SOURCES

P. Patriarca R. G. Donnelly

The immediate tasks of this program are (1) to evaluate the more promising superalloys that are available commercially and (2) to develop improved alloys and eventually qualify those that show greatest promise for containment of radioisotopes in space power systems. The superalloy tasks include evaluation of embrittling-aging reactions, determination of evaporation characteristics, and studies of the interaction of stress and vacuum on properties at elevated temperatures. Because of a change in program emphasis, the work reported for superalloys represents a closeout of these tasks. In the alloy development portion of the program, the strength, resistance to evaporation in vacuum, and resistance to oxidation in air are of primary concern.

Embrittling-Aging Reactions in Superalloys

H. Inouye

Impact Tests of Hastelloy N, Haynes Alloy No. 25, and Haynes Developmental Alloy No. 188 (D. T. Bourgette)

The objective of this study was to determine the effect of aging on the impact properties of superalloys. Charpy V-notch impact specimens of Hastelloy N (Ni–17% Mo–7% Cr–4% Fe–0.06% C), Haynes alloy No. 25 (Co–15% W–20% Cr–10% Ni–2% Fe), and Haynes developmental alloy No. 188 (Co–22% Cr–14% W–22% Ni–0.08% La) were solution annealed for 1 hr at 1150°C and then aged at 650, 700, 800, 850, and 900°C for 50, 100, 500, 2000, 4000, and 5000 hr. Only the Haynes alloy No. 25 specimens being aged 4000 hr and the Haynes alloy No. 188 and Hastelloy N specimens being aged 5000 hr have not yet completed the required aging time and are therefore yet to be tested.

The results of impact tests at room temperature and at 315°C show that the fracture toughness of Haynes alloy No. 25 is greater than 240 ft-lb for the solution-annealed state but decreases to 3 ft-lb after aging for 5000 hr at any of the temperatures investigated. Fracture toughness decreased most after a short aging time at any of these temperatures. Impact values of 49 ft-lb and 6 ft-lb were measured after 50 hr at 650 and 850°C, respectively. The intergranular fractures were attributed to the precipitation of a Laves phase (Co_2W) in the grain boundaries.

The impact behavior of Haynes alloy No. 188 after aging is, as expected, similar to that of Haynes alloy No. 25, since the alloys are quite similar in composition. Although the vendor states[1] that the ductility of alloy No. 188 after aging is greater than that of alloy No. 25, our results show that the difference is insignificant for aging times of 50 to 2000 hr and temperatures of 700 to 900°C. Longer aging times showed that the fracture toughness of alloy No. 188 is three to six times greater, depending on the aging temperature, than that of alloy No. 25. However, the fracture toughness is still low enough to consider the alloy exceedingly brittle. The impact value for both these Co-base alloys showed little dependence on the test temperature.

The impact results for Hastelloy N exhibited a significant dependence on test temperature and showed the least aging response. The impact value in the solution-annealed state was 175 ft-lb at room temperature, but it increased to 240 ft-lb at 315°C. The fracture toughness decreased with aging time at aging temperatures of 650, 800, and 900°C, but increased at 700°C. The reason for this behavior is presently unknown. The greatest embrittlement occurred after 4000 hr of aging at 400°C. An impact value of 29 ft-lb was measured at room temperature, but it increased to 70 ft-lb at 315°C.

Effect of Vacuum on Superalloys

H. Inouye

Evaporation of Hastelloy N and Haynes Developmental Alloy No. 188 (D. T. Bourgette)

Evaporation rates of Hastelloy N and Haynes developmental alloy No. 188 were measured at 800 to 1050°C and 10^{-9} torr to determine their suitability for use in high vacuum. Evaporation rates increased with concentration of the elements that have higher vapor pressures (i.e., Cr and Mn) but decreased with time at constant temperature. The time-dependent decrease in evaporation rate is influenced by the thickness of the specimen, at least to times of 1500 hr: the thicker the specimen, the less is the decrease in evaporation rate with time. We attribute this behavior to the greater availability of the evaporating elements at the surface as a result of bulk diffusion. Further, gradients in the bulk concentration resulted from selective loss of material. Material losses resulted in microstructural damage such as the formation of voids and solution of precipitates. The formation of voids in Haynes developmental alloy No. 188 was confined to grain matrices because grain boundaries are ineffective vacancy sinks when a continuous grain-boundary phase is present; in Hastelloy N, however, voids formed principally at the grain boundaries. Observations of evaporated surfaces with the scanning electron microscope indicate a complete change in surface morphology. Flat regions surrounded by ridges resulted from losses of about 2 mg/cm^2. This behavior suggests that initial evaporation of the alloy may be described by classical ledge theory[2] as applied to pure metals; when the surfaces become enriched with the elements that have lower vapor pressures, however, bulk diffusion will become the rate-controlling mechanism.

Weight losses in excess of 4.0 mg/cm^2 resulted in proportional precipitation of intermetallic phases at the surface. Continued evaporation causes the surface precipitates to stand in relief and become larger with time. Evaporation of the precipitates is evidenced by the rounding of initially sharp edges.

Development of Improved Alloys

H. Inouye

Creep Tests of Experimental Alloys (C. T. Liu)

Our efforts were concentrated on the development of Pt-base alloys with superior strength, oxidation resistance, and compatibility at high temperatures for use in containing radioisotopes in advanced thermoelectric generators for use in space.

A Pt-base alloy that contained 5% Mo (alloy S-22) was prepared by drop casting. The ingot was fabricated at room temperature without difficulty. Creep specimens 0.070 in. in diameter were machined from the prepared stock. Figure 13.1 shows the plot of the log of the steady-state creep rate, $\dot{\epsilon}$, as a function of the reciprocal of temperature at 5 and 10×10^3 psi. It is seen that the steady-state creep rate fits the empirical equation

$$\dot{\epsilon} = K\sigma^n \exp(-Q/RT) \ , \qquad (13.1)$$

where K and n are materials constants, σ is stress, R is the gas constant, and Q is the activation energy for creep. Like that of the other disordered alloy, S-3 (45% Ni–46% Co–9% V) (ref. 3), the steady-state creep rate of alloy S-22 is also sensitive to the applied stress; it has a stress exponent of $n = 5$. But the calculated value of the activation energy for creep from Fig. 13.1 is 84 kcal/mole, which is as high as that for the ordered alloy S-4 [$V(Ni,Co)_3$]. Fabrication technique affects the creep rate of alloy S-22. A specimen prepared from cold-swaged stock shows three times better creep resistance than that from cold-rolled stock.

Two alloys of the nominal composition Pt_3Cr (S-19) that contained different levels of interstitials, were arc melted and drop cast into 3/8-in.-diam ingots. The cast ingots were canned in Mo and extruded successfully at 1260°C at an extrusion ratio of 6.5. Specimens for tensile and creep tests were prepared from the extruded 0.145-in.-diam

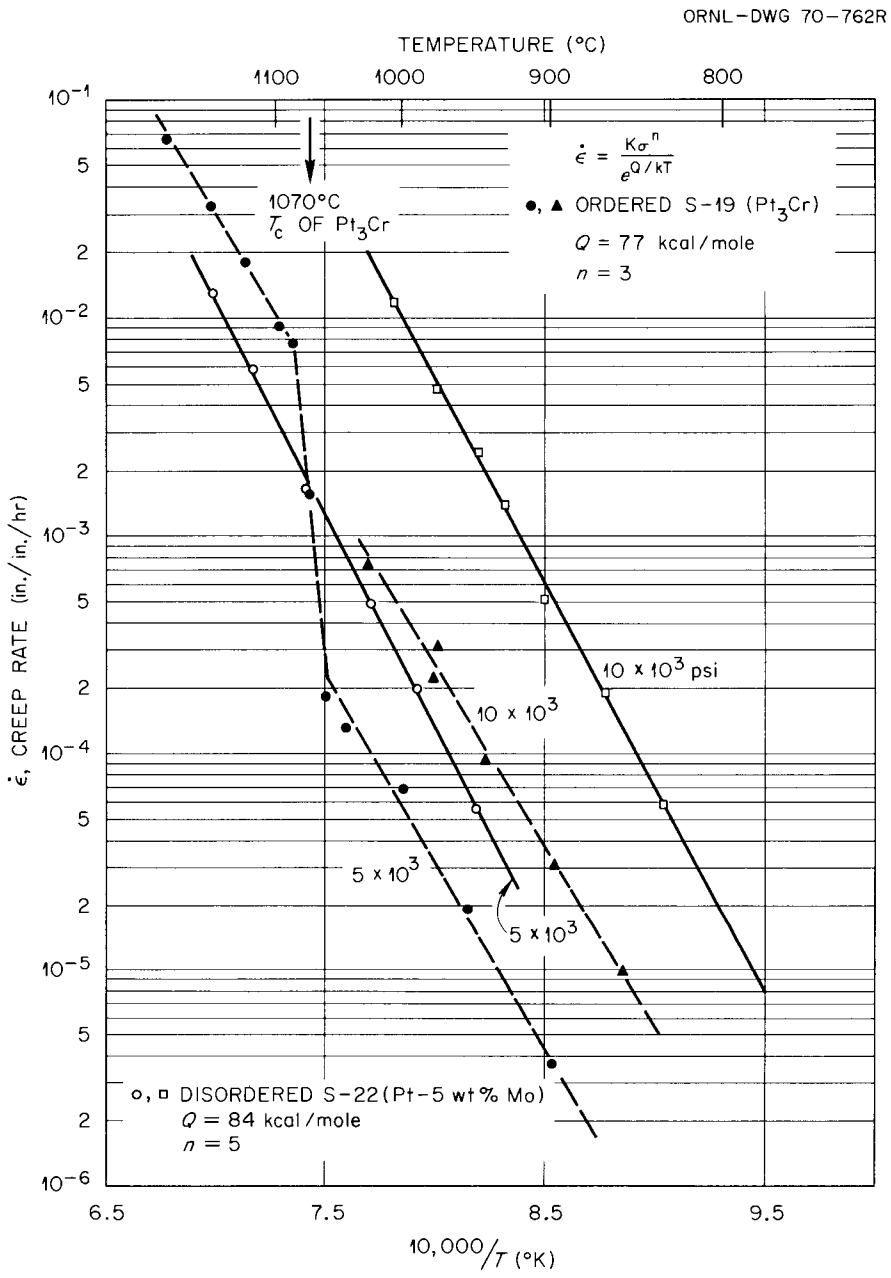

Fig. 13.1. Steady-State Creep Rate as a Function of Temperature for Alloys S-19 and S-22.

bars. The ordering reaction, as determined from Debye-Scherrer x-ray diffraction patterns, can be suppressed by quenching the alloy in water from 1300°C. Thus, the control of the state of order is not a problem in this alloy. The desirable $AuCu_3$ type of superlattice structure forms after 4 hr of aging at 850°C. Measurements of microhardness show almost the same diamond-pyramid hardness (190 DPH) for both the ordered and disordered specimens. This result is different from what we observed in alloy S-4, in which the ordering reaction was accompanied by a large increase in hardness that resulted from a crystallographic transformation.

The effects of long-range order on the creep properties of ordered alloy S-19 are being determined as a function of temperature and stress. A plot of the log of steady-state creep rate at 5×10^3 psi versus the reciprocal of temperature (Fig. 13.1) shows a sharp, discontinuous change in creep rate around 1070°C. This temperature is in excellent agreement with the recently reported critical temperature (T_c) of Pt_3Cr, obtained from the measurements of specific magnetic susceptibility at temperature.[4] It is noteworthy that formation of long-range order among Pt and Cr atoms reduces the creep rate by as much as a factor of 25. This result clearly indicates the superior properties of the ordered structures. Figure 13.2 shows the characteristics of the creep curves of Pt_3Cr around the critical temperature and the tremendous increase in the creep rate upon destruction of long-range order with increasing temperature. Below the critical temperature (1057°C), the curve is characterized by an initial transition stage in which the creep rate is lower than the steady-state creep rate. There is no transition stage when samples are tested at temperatures around the critical temperature (1072°C) and above it (1084°C), and the creep curve assumes the usual shape with the attendant large first-stage creep generally observed in the disordered alloys. This low primary creep in ordered alloys is highly desirable in applications requiring limited creep strains.

Figure 13.1 shows that the steady-state creep rate of alloy S-19 also fits Eq. (13.1). Like the ordered alloy S-4 (ref. 3), alloy S-19 is also less sensitive to the applied stress; it has a stress exponent of $n = 3$. This lower value of the ordered alloys is desirable for

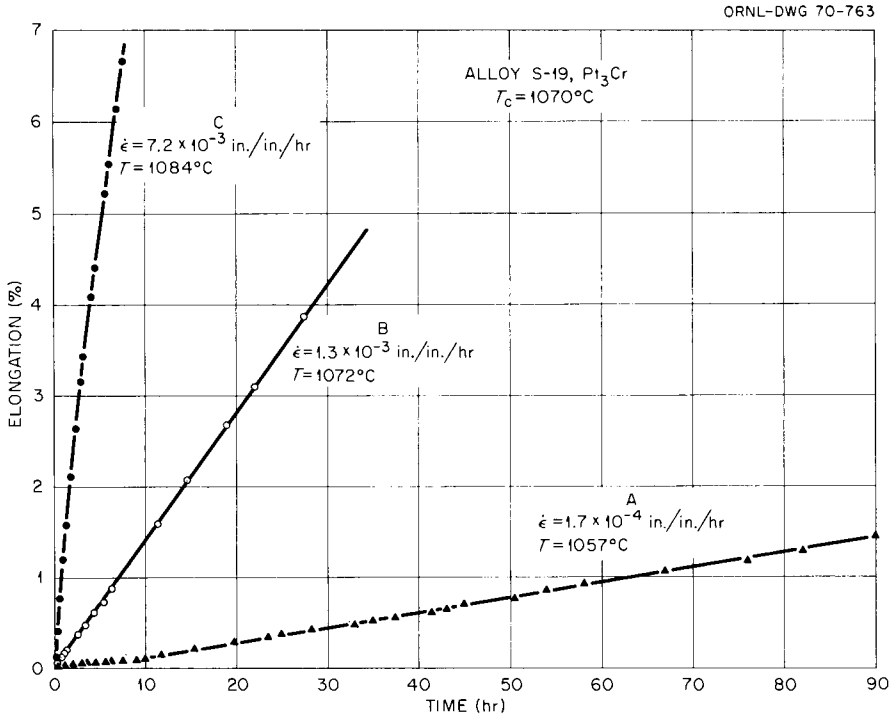

Fig. 13.2. Curves for Creep of Alloy S-19 (Pt_3Cr) Tested Around the Critical Ordering Temperature (1070°C) at 5 × 10^3 psi in a Vacuum of 10^{-8} torr.

resistance to high applied stress. The measured values for the activation energies for creep for both ordered and disordered states in Pt_3Cr are approximately the same, 77 kcal/mole. The creep rate of alloy S-19 in the ordered state is lower than that for alloy S-22 by factors of about 4 and 18 at 5 and 10 × 10^3 psi, respectively (Fig. 13.1). However, when the temperatures increase above the critical ordering temperature, disordered alloy S-19 that contains Cr is weaker than the alloy that contains Mo.

Table 13.1 lists the times required to produce 1% plastic strain for the experimental alloys together with that required for Haynes alloy No. 25 stressed at 10 × 10^3 psi in a vacuum of 10^{-8} torr. Alloy S-19 possesses the best creep resistance at 900°C. The time to produce 1% strain in ordered alloy S-19 is about two orders of magnitude less than that for Haynes alloy No. 25.

Because of the superior creep resistance of the ordered alloy S-19, we checked it further for resistance to oxidation and vaporization in

Table 13.1. Comparison of Creep Data for Experimental Alloys with that for Haynes Alloy No. 25 Stressed at 10×10^3 psi in a Vacuum of 10^{-8} torr

Alloy	Structure	Test Temperature (°C)	Time to Produce 1% Plastic Strain (hr)	Specimen Dimension
S-3	Disordered	900	1.5	0.07-in.-diam bar
S-4	Ordered	899	5.0	0.07-in.-diam bar
S-22	Disordered	900	14–28[a]	0.07-in.-diam bar
S-19	Ordered	897	450	0.07-in.-diam bar
Haynes alloy No. 25	Disordered	900	1.6	0.03-in.-thick sheet
Haynes alloy No. 25[b]	Disordered	900	11.0	0.06-in.-thick sheet

[a]Data depend on the fabrication technique.

[b]D. T. Bourgette, Fuels and Materials Development Program Quart. Progr. Rept. Sept. 30, 1969, ORNL-4480, pp. 152–153.

vacuum. The oxidation data obtained in air at 1000°C show weight losses that average 1.3×10^{-3} mg cm^{-2} hr^{-1} to 120 hr. As a comparison, the weight changes in Ta- (ref. 5) and Mo- (ref. 6) base alloys that contain 10% or less of alloying elements are about 10 and 400 mg cm^{-2} hr^{-1}, respectively, at this temperature.

The initial evaporation rate of Haynes alloy No. 25 in high vacuum is about 140 mg cm^{-2} hr^{-1} at 982°C, due to the preferential loss of Mn and Cr elements.[7] Our preliminary data show that although alloy S-19 contains 25 at. % Cr, the evaporation rate cannot be measured even after 200 hr of exposure in vacuum at 984°C.

References

1. Union Carbide Corporation, Materials Systems Division, "Haynes Developmental Alloy No. 188," New Product Data Sheet, F-30,361, August 1967.

2. J. P. Hirth and G. M. Pound, Condensation and Evaporation: Nucleation and Growth Kinetics, pp. 87–88, The MacMillan Company, New York, 1963.

3. C. T. Liu, Fuels and Materials Development Program Quart. Progr. Rept. Sept. 30, 1969, ORNL-4480, pp. 153–156.

4. A. Kussmann et al., Z. Metallude 59, 859 (1968).

5. F. F. Schmidt, Tantalum and Tantalum Alloys, DMIC-133 (1960).

6. J. A. Houck, Physical and Mechanical Properties of Commercial Molybdenum-Base Alloys, DMIC-140 (1960).

7. D. T. Bourgette, Evaporation of Iron-, Nickel-, and Cobalt-Base Alloys at 760–980°C in High Vacuums, ORNL-3677 (1964).

14. PHYSICAL AND MECHANICAL METALLURGY OF REFRACTORY ALLOYS

P. Patriarca R. G. Donnelly

The purpose of this program is to provide a broad, base-technology evaluation of high-temperature alloys for use in high-performance nuclear reactors and isotopic heat sources for advanced space, terrestrial, and civilian power applications. Principal emphasis is placed on materials problems that involve Ta-, Nb-, Mo-, and V-based alloys for systems that use alkali metals as thermodynamic working fluids and heat-transfer media.

Physical Metallurgy

H. Inouye

Effect of Interstitial Reactions on the Behavior of Refractory Alloys (H. Inouye)

The isotopic heat sources being developed for future thermoelectric devices are designed to be multilayered structures consisting of a graphite heat shield, a cladding of Pt alloy for resistance to oxidation, a fuel liner and strength member of refractory alloys, an oxide isotopic fuel, and oxide diffusion barriers. During this period we attempted to identify materials problems for such heat sources so that we can direct development work toward their solution. We defined the potential problems summarized below.

The selection of refractory alloys on the basis that their high melting point would increase the chances for intact impact and survival of the heat source in a fire abort neglected the possibility that phases with low melting points might form. Tantalum reacts with UO_2 to form $U(TaO_3)_4$, which has a melting point of about 1850°C (ref. 1). Tantalates that have low melting points also form with the oxides of Cm and Pu (ref. 2). Thus, the justification for the use of refractory alloys, which was based on the survival of a Ta alloy in a simulated fire test, might have been the result of simulating an oxide fuel with W–40% Mo (ref. 3). A liquid phase with a melting point of about 800°C forms between Mo and UO_2 in an oxidizing environment.[1]

The degassing of the graphite heat shield and the interaction of the O in the fuel with the C in the fuel creates a capsule environment consisting of CO, CH_4, and numerous other gases.[4,5] The reactions $2\ CO \leftrightarrows CO_2 + C$ and $CH_4 \leftrightarrows 2\ H_2 + C$ could deposit C in the pores of the nonselective vent and cause restricted flow or plugging.[6] Because this factor was not considered (as evidenced by tests only in pure He), the conclusions regarding the operational success of vents[7] cannot be taken at face value.

The capsule environment is expected to have an effect on the mechanical properties of refractory alloys. It is also expected that the concentration of active gases will be too low to cause a surface reaction to form a product. However, concentrations of active gas as low as 10^{-7} torr cause significant changes in the interstitial content of TZM, Ta, and Nb alloys.[8] The mechanical properties of contaminated refractory alloys under normal operating conditions or under abnormally high heating rates and high impact velocities have not, to the author's knowledge, been documented. Uncontaminated and unaged refractory alloys apparently meet the requirements for intact impact.[9,10]

Since more than 80% of the random reentries of heat sources will occur over oceans,[11] the probability that a heat source will experience an environment of water or water vapor is also high. Either the use of nonselective vents or failure of the Pt alloy cladding would subject all structures made of refractory alloys to H_2O. Although oxidation of refractory alloys in H_2O is expected to be superficial due to low temperatures, the H_2 generated by the reaction will be absorbed by alloys based on Ta or Nb, may form hydrides, and under certain conditions may cause catastrophic fragmentation.[12]

Effect of Nitrogen Interaction on the Creep Properties of Tantalum Alloys (D. T. Bourgette)

The objective of this research is to determine the creep behavior of Ta alloys while they are undergoing interactions with interstitial environmental impurities and the products of the decomposition of nuclear fuels. We believe that existing creep data from tests under ultrahigh

vacuum conditions are not representative of the properties under conditions that expose the alloys to low concentrations of interstitial impurities.

We designed an apparatus to test the creep properties of Ta alloys in low-pressure N_2 to simulate their interaction with the N_2 that results from nitride fuels. Vacuum components and temperature control devices were ordered.

Development of Age-Hardening Refractory Alloys (C. T. Liu)

This task is related to the development of particle-strengthened refractory alloys for use at elevated temperatures. Because of the high aging response observed in the Ta-Hf alloy system,[13] the current effort is concentrated on this alloy system.

Three Ta-base alloys containing 65, 50, and 30 wt % Hf were examined by x-ray powder diffraction after aging at 600 to 1750°C and 1 to 55,000 min. The data are summarized in Fig. 14.1, where the aging temperature is plotted against a_β, the lattice parameter of body-centered

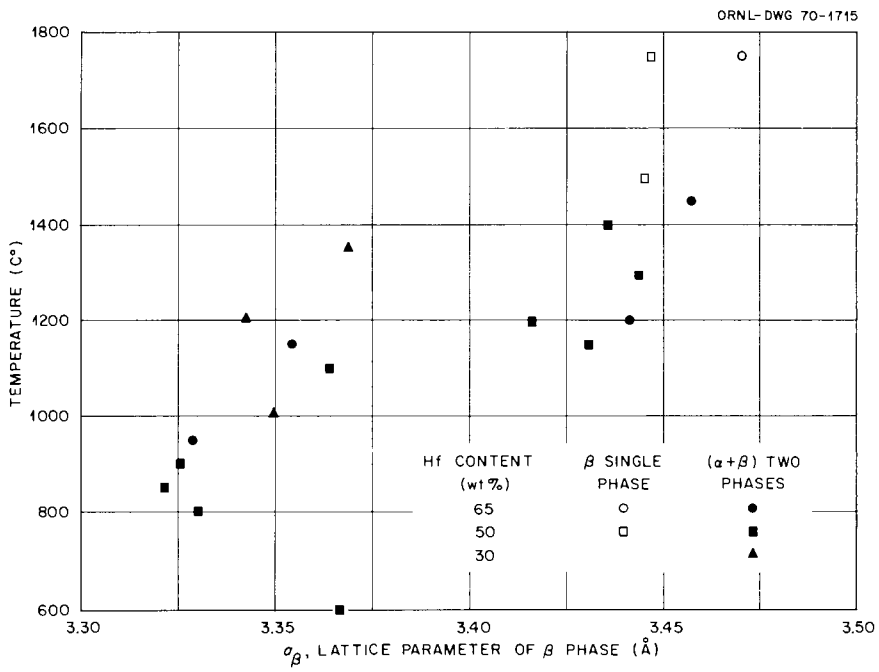

Fig. 14.1. Aging Temperature Versus Lattice Parameter of the β Phase for Three Tantalum-Hafnium Alloys.

cubic (bcc) matrix. Since the value of a_β directly reflects the Hf content in solution, Fig. 14.1 is similar to a phase diagram. All alloys show either a simple bcc pattern or a two-phase bcc plus hexagonal close-packed (hcp) pattern that is not in accord with the reported existence of a miscibility gap associated with bcc β phases.[14,15] Instead, the data suggest a simple β, (β + α), α sequence of phases at low temperature for increasing Hf content, as observed in the Nb-Hf system.[13] The estimated positions of two-phase boundaries for Ta alloyed with 65, 50, and 30 wt % Hf are roughly located at 1500, 1450, and 1400°C, respectively.

The newly obtained data for the hardness of Ta–50 wt % Hf alloy isothermally aged between 850 and 1300°C are plotted in Fig. 14.2 together with those reported previously.[13] The specimens aged at 1030°C or below sharply increase in hardness in the early stage of precipitation, while those aged at 1150°C or below initially drop in hardness. X-ray diffraction shows tremendous line broadening in the two phases that are present after aging a short time at 850°C. This suggests that the hardness peak on the 850°C curve (Fig. 14.2) results from precipitation of coherent Hf-rich α particles and that the rapid drop in hardness after 10^3 min aging is due to the loss of coherency. The crystallographic relation between the phases is $(0002)_\alpha \| (110)_\beta$. The peak hardness

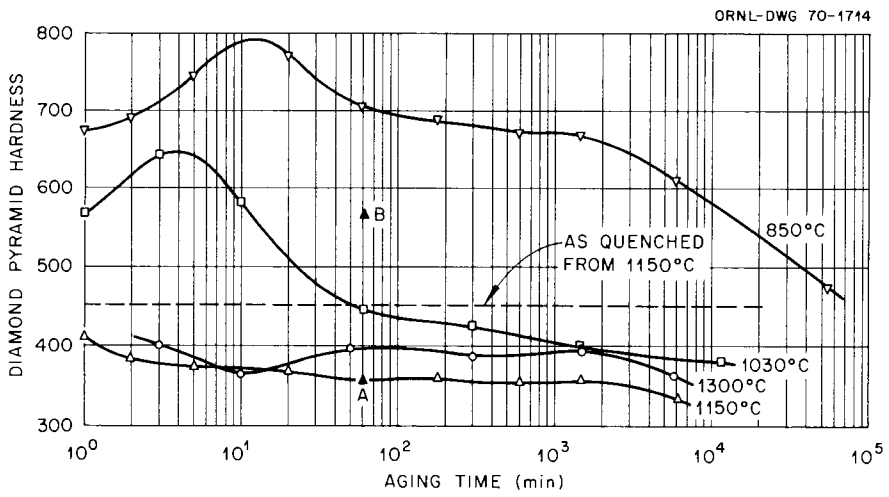

Fig. 14.2. Diamond Pyramid Hardness at Room Temperature Versus Aging Time for Ta–50 wt % Hf Alloy.

in the 1030°C curve is also related to the transition from coherent to incoherent precipitation. The high-temperature aging treatment produces incoherent precipitates that continuously coarsen with time. The eutectoid temperature (about 1020 to 1050°C), which has not been confirmed by this study but was reported in the Ta-Hf system by Svechnikov et al.[14] and Oden et al.,[15] coincides with the temperature at which a change is observed in the mechanism of precipitation.

Hardness increases from 355 (point A in Fig. 14.2) to 565 DPH (point B) when the cooling rate is reduced from oil quenching to radiation cooling after 1 hr aging at 1150°C. X-ray diffraction shows line broadening of the bcc β-matrix reflections in specimen B. This indicates that slow cooling from 1150°C causes further decomposition of the matrix.

Thermodynamics of Spinodally Decomposed Alloys (C. T. Liu, B.T.M. Loh)

Previously[16] we derived an expression for the free energy of mixing, ΔG_m, in a binary solid solution in which the nonrandomness of atomic arrangement or clustering of the atoms is considered. Since a constant interaction energy of solution was assumed, the clustering model predicted only a symmetrical miscibility gap. However, asymmetric gaps are generally observed in real solutions. In order to fit such gap, ΔG_m is modified by introducing concentration-dependent potential energies between first and second nearest neighbor atoms:

$$\Delta G_m = NZc(1-c)V_1/2 - NkT\{(Z-1)[c\ell nc + (1-c)\,\ell n(1-c)] - (Z/2)[c\ell n(c-p) + (1-c)\ell n(1-c-p)]\}\,, \quad (14.1)$$

where

$p = 2c(1-c)/(1+f^{1/2})$,

$f = 1 + 4c(1-c)(e^{2V_2/kT} - 1)$,

V_1, V_2 = the concentration-dependent interaction energies,

N = the total number of atoms,

Z = coordination number,

k = Boltzmann's constant, and

c = concentration of β atoms.

This modified clustering model includes the nonrandom configurational entropy, and we are trying to apply the model to real solutions.

According to Cahn's theory of spinodal decomposition,[17] in the absence of strain effects, the features of the kinetic parameters such as the fastest growing wavelength of the decomposition modulation, λ_m, and the time required for a given fraction of decomposition, t_d, can be determined from the value of $\Delta G_m''$ alone. Thus differentiating Eq. (14.1) twice with respect to c gives

$$\Delta G_m'' = NZ[-V_1 + (1 - 2c)V_1' + c(1 - c)V_1''/2] + NkT[1 - (Z/2)(1 - 1/f^{1/2})]/c(1 - c) + NZ\{2(1 - 2c)V_2'/f^{1/2} - 2[pV_2' \exp(V_2/kT)]^2/kTf^{1/2} + pV_2''\} . \quad (14.2)$$

In order to demonstrate the applicability of the model, we assume a hypothetical solution with interaction energies $V_1 = k(30 - 10c)$ and $V_2 = k(210 + 110c - 30c^2)$, which gives a critical temperature, T_c, of 1531°K at a concentration, C_c, of 0.6 for the solution. Since these values are the critical conditions of the miscibility gap in the Au-Pt system, qualitative comparisons between theoretical and experimental results may be possible. With the information above, computer programs were set up to calculate the miscibility gap, λ_m, and t_d.

Figure 14.3(b) indicates that when the interaction energies are dependent on concentration, the miscibility gap and the spinodal region are asymmetrical. For comparison, Fig. 14.3(a) shows the symmetrical miscibility gap obtained from the simple clustering model and regular solution model.[16] Figure 14.4(b) shows a distinctive feature due to clustering and potential energies dependent on concentration. At a low temperature ($T/T_c = 0.25$) the curve for λ_m versus c bows upward near c_c; this makes the minimum sharper and pushes it toward the β-component end. With increasing temperature, the curve for λ_m gradually assumes the simple U-shape, as predicted by the model for a simple, regular solution. These features provide a useful way to check the model experimentally.

Carpenter[18] measured the wavelength of the structural modulation in the Au-Pt system as a function of Pt concentration and temperature. The measured wavelength, λ, is plotted against c in Fig. 14.5. Note that the measured values of λ vary with c and T in qualitative agreement with the prediction of the modified clustering model (Fig. 14.4). This agreement strongly suggests that this model is realistic.

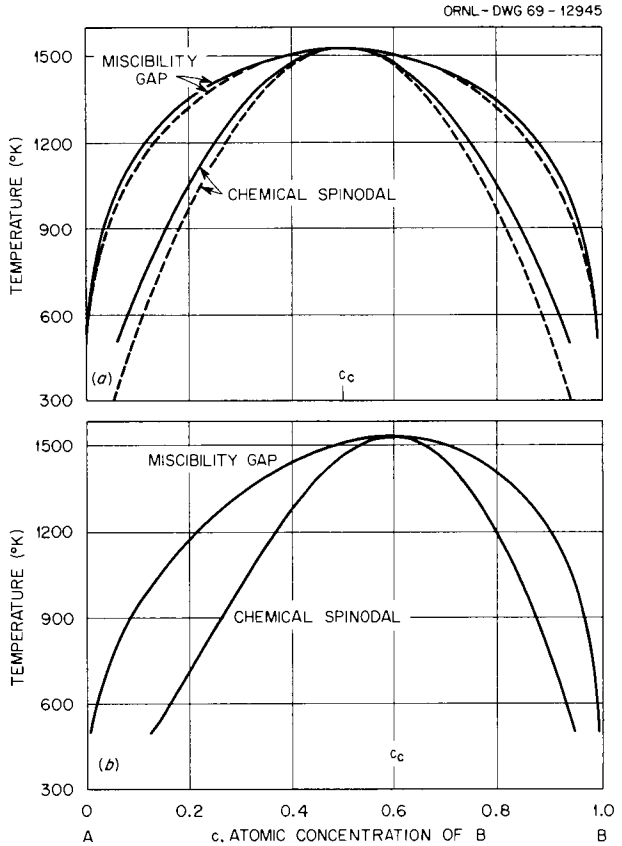

Fig. 14.3. Miscibility Gaps and Chemical Spinodals for Three Solution Models. (a) Solid curves derived from simple clustering model; dashed curves derived from simple, regular solution model. (b) Curves derived from modified clustering model.

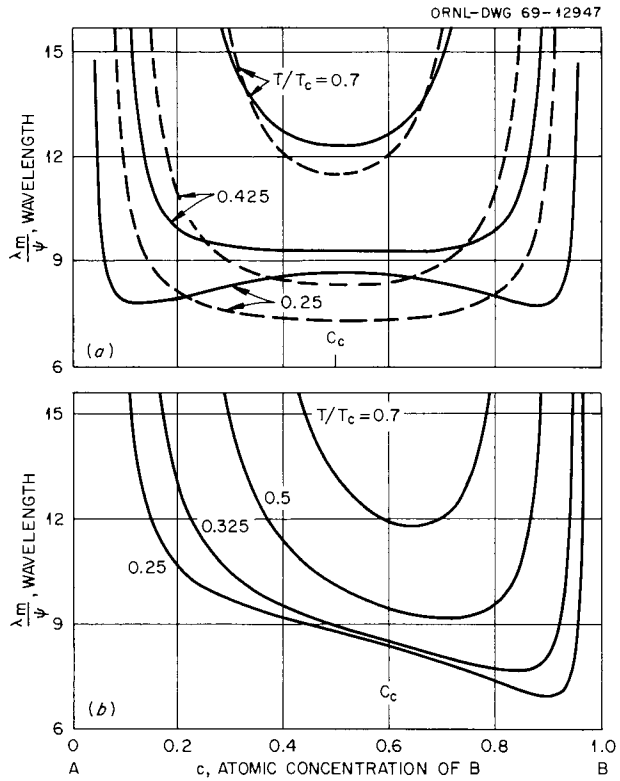

Fig. 14.4. Variation of the Fastest Growing Wavelength of Composition Modulations, λ_m (in Units of the Interaction Distance, ψ), with Atomic Concentration. (a) Solid curves derived from simple clustering model; dashed curves derived from simple, regular solution model. (b) Curves derived from modified clustering model.

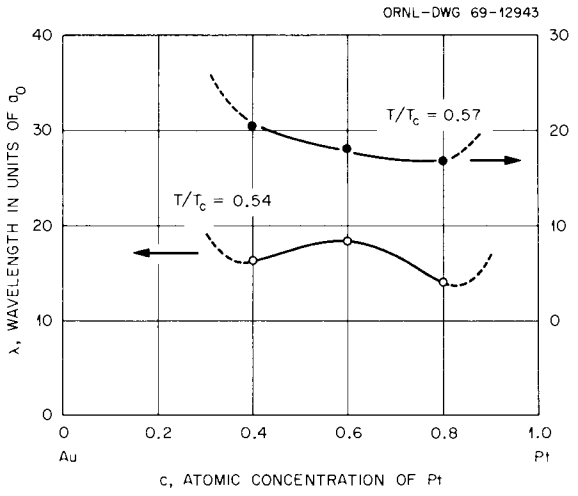

Fig. 14.5. Variation of Wavelength, λ, Measured in Units of a_o, the Lattice Constant for the Quenched Single-Phase Gold-Platinum Alloys with Atomic Concentration of Platinum.

The time-temperature-transformation curves typical for the reaction controlled by diffusion are shown in Fig. 14.6(b). The nose temperature of the curve, T_n, varies with T_s, the spinodal temperature, according to the equation $(T_s - T_n)/T_n = 2kT/Q$, where Q is the activation energy for solute diffusion.[17]

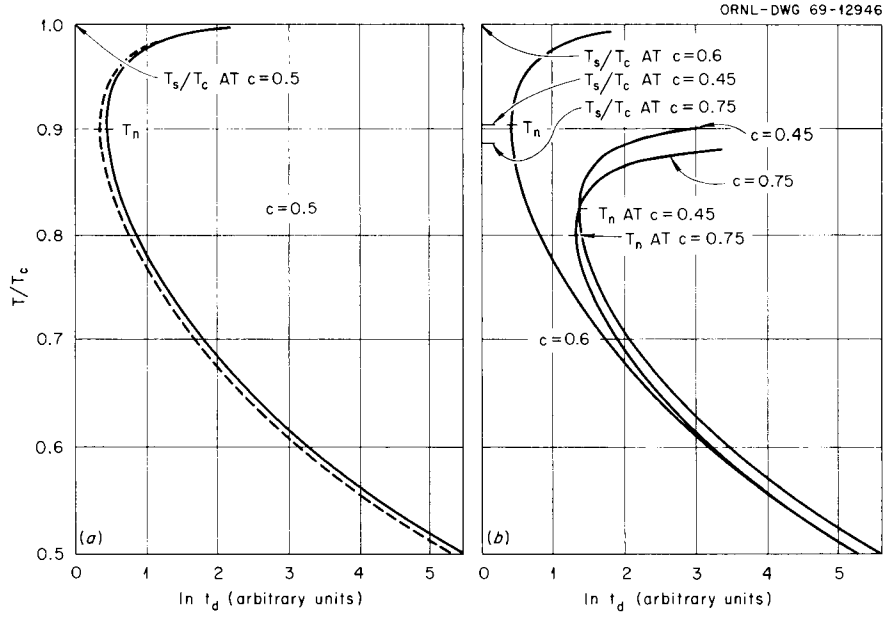

Fig. 14.6. Time-Temperature-Transformation Diagram for an Arbitrary Fraction of Spinodal Decomposition. (a) Solid curves derived from simple clustering model; dashed curves derived from simple, regular solution model. (b) Curves derived from modified clustering model.

Mechanical Properties of Commercial Refractory Alloys

H. E. McCoy, Jr.

Mechanical Properties of Welds in Refractory Alloys (R. L. Stephenson)

Since most practical devices require joining, we consider the creep properties of welds to be of critical importance in evaluating a high-temperature material. We are studying the creep properties of welds in TZM, W–25% Re, Ta–10% W, T-111, and T-222. The results to date on TZM and W–25% Re are shown in Figs. 14.7 and 14.8, respectively. The rupture time of transverse electron-beam welds in TZM appear to be essentially identical to those of control specimens. Such welds are only slightly weaker than the controls in W–25% Re.

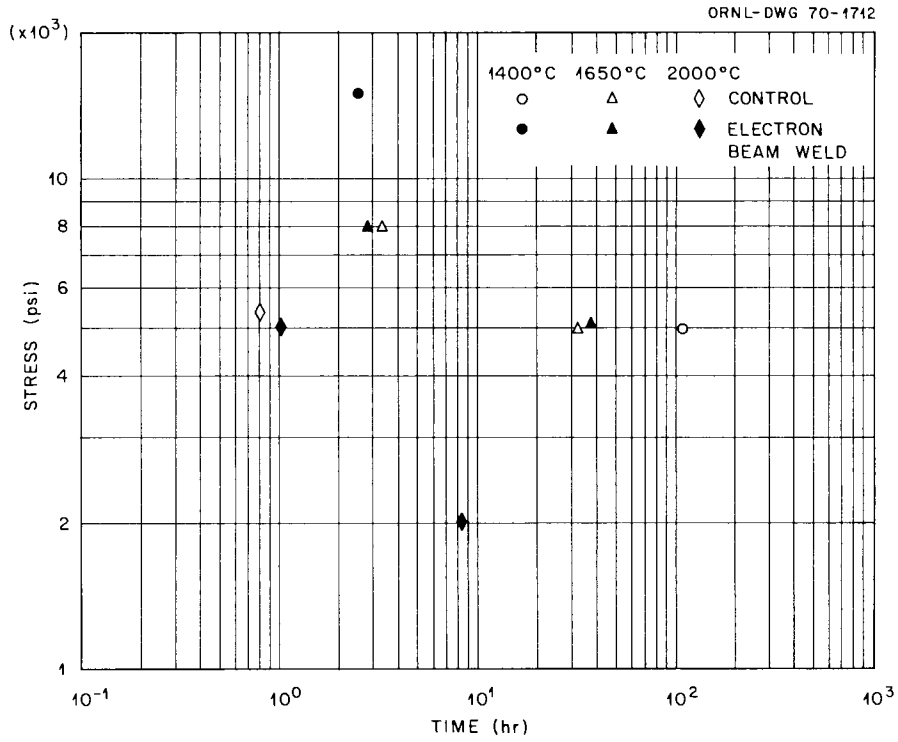

Fig. 14.7. Comparative Stress-Rupture Properties of Transverse TZM Welds.

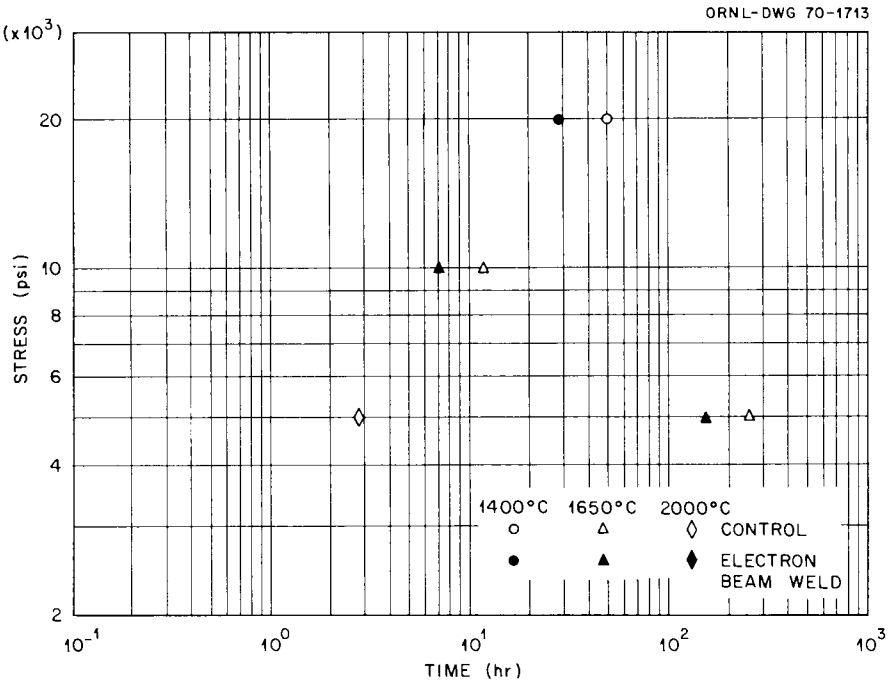

Fig. 14.8. Comparative Stress-Rupture Properties of Transverse W–25% Re Welds.

Welding and Brazing

G. M. Slaughter

Studies of Brazing Alloys (D. A. Canonico)

We began an investigation of the remelt temperature of brazed joints, made with filler metals developed at ORNL, in refractory materials. Remelt temperature, as we define it, is the temperature at which the brazement is incapable of sustaining an appreciable stress.

The brazing cycle may promote alloying of the filler metal and base metal; for example, the solution of refractory elements into the filler metal may promote an increase in the melting point of the filler metal. Moreover, the brazes in this study are made in a vacuum, and this, too, due to the volatilization of one or more of the elements that constitute the filler metal, may result in a remelt temperature higher than the original brazing temperature.

The subject of remelt temperature has been discussed often, but very few quantitative data applicable to design conditions have been

reported. We are now studying this subject with three brazing alloys, Ti–48% Zr–4% Be, Ti–46% Zr–8% Ge, and Ti–21% V–25% Cr, that have initial melting points of 985, 1377, and about 1600°C, respectively.

A high-temperature brazing furnace in the Welding and Brazing Laboratory was modified to permit the observation of a brazement during its brazing cycle and later during the remelt experiments. Miller-Peaslee tensile-shear specimens were brazed at the applicable temperature for each brazing filler metal under study and in a vacuum of 10^{-6} torr. For the remelt studies, the specimens were stressed to 60 or 160 psi with W weights to overcome surface tension. The specimens were kept under observation during reheating, and their failure temperature was determined.

Table 14.1 summarizes our results to date on the Ti–48% Zr–4% Be and Ti–46% Zr–8% Ge alloys. The Ti–48% Zr–4% Be filler metal had a remelt temperature about 75°C below its original melting temperature. The Ti–46% Zr–8% Ge alloy indicated a slight increase (about 20 to 40°C) in remelt temperature. The brazed joint will be analyzed with an electron-beam microprobe to determine the reason for the change in the melting point of the brazement.

Table 14.1. Results of Studies of the Remelt Temperature of Tantalum Brazed Joints[a]

Filler Metal Composition (wt %)	Average Melting Temperature[b] (°C)	Load On Brazed Joint (psi)	Remelt Temperature (°C)
Ti–48 Zr–4 Be	985	60	910
			910
		160	935
			915
Ti–46 Zr–8 Ge	1377	60	1395
			1425
		160	1410
			1430

[a]Time at original brazing temperature was about 5 min.

[b]Brazing alloy on Ta pad.

Joining Platinum to Refractory Metals (D. A. Canonico, Nancy C. Cole, G. M. Goodwin)

The initial phase of the program for joining Pt to Ta–10% W was completed. As previously described,[19] the objective was a joint that was leaktight after extended periods of time in a vacuum at elevated temperatures.

Six methods for making the joint were devised. Five of these techniques were described previously.[19] Table 14.2 lists the joining techniques investigated and the results of the first phase of the investigation. The coextrusion process did not form an acceptable joint. Joints made by three other processes (brazing, Swagelok, and pressure bonding) failed the leak test after aging for 100 hr at 1200°C. The joint made by electron-beam welding passed the 100-hr test but failed after 500 hr.

The technique that proved the most encouraging was the three-tube transition joint that we developed during this report period. Since metallographic studies of the Swagelok and pressure-bonded specimens revealed the presence of Kirkendall voids in the Pt where an intimate contact existed between the Pt and Ta–10% W, we investigated the use of

Table 14.2. Results of Experimental Joining of Platinum and Tantalum Alloys

Joining Technique	As Joined	After Aging[a]		
		100 hr	500 hr	1000 hr
Coextrusion	NA[b]			
Brazing	A[c]	NA		
Swagelok	A	NA		
Electron-beam welds	A	A	NA	
Pressure bonded	A	NA		
Braze weld (three-tube transition)	A	A	A	NA

[a]Aging at 1200°C in a vacuum.

[b]Not acceptable; excessive leak rate.

[c]Acceptable; leak rate less than 1×10^{-10} cm^3/sec.

a transition material to avoid this diffusion couple. Tungsten was selected. Electron-beam welds were made between W and Ta—10% W and between W and Pt; the W served as the buffer material. This joint was acceptable after a 500-hr age at 1200°C; however, after 1000 hr, its leak rate was unacceptable. A metallographic examination revealed the presence of Kirkendall voids at the interface between the Pt and W.

Physical Properties

D. L. McElroy

Development of Electrical Heating Method (R. K. Williams, K.-H. Bode)

The direct-heating apparatus constructed[20] for measurements of thermal conductivity, electrical resistivity, and Seebeck coefficient on metals at higher temperatures is now being evaluated. Measurements of electrical resistivity and Seebeck coefficient obtained on a Nb—10% W sample between 700 and 1200°K agree with measurements from our operational apparatus for electrical resistivity and Seebeck coefficient within the combined uncertainties.[21]

The smoothed values obtained for electrical resistivity and Seebeck coefficient from the latter experiments are given in Table 14.3. Preliminary results for thermal conductivity obtained near 950°K on the Nb—10% W rod are at least 15% higher than values obtained in our radial heat-flow apparatus.[22] However, the new measurements have a ±0.2% repeatability. This indicates that the significant positive error in measurements of thermal conductivity is systematic, and this is under investigation. The lack of early success in measurements of thermal conductivity is probably offset by the fact that a majority of the components of the direct-heating system are yielding performances ultimately needed to obtain an operational device. The Varian power supply is stable to better than ±2 ppm at 100 dc amp. The Guildline direct-current comparator, a seven-dial potentiometer, can be read to 0.1 μv at 2 v. The temperature distribution of the specimen is stable to better than ±0.05°K due to the performance of the five systems for temperature control. These combined performances are yielding surprisingly good

Table 14.3. Electrical Resistivity and Absolute Seebeck Coefficient of a Nb–10% W Alloy

Temperature (°K)	Electrical Resistivity[a] (μΩ-cm)	Absolute Seebeck Coefficient[b] (μv/deg)
300	16.23	−1.5
400	20.49	−2.5
500	24.43	−2.8
600	28.15	−3.0
700	31.65	−3.0
800	35.02	−2.8
900	38.37	−2.4
1000	41.63	−1.8
1100	44.72	−1.1
1200	47.75	−0.2
1300	50.74	+0.7
1400	53.66	+1.6
1500	56.54	+2.3
1600	59.44	+2.9
1700	62.35	+3.2

[a]Values not corrected for thermal expansion. Data above 1500°K are probably high by about 0.9 μΩ-cm due to contamination of the sample.

[b]Calculated from S_{Pt} values tabulated by N. Cusack and P. Kendall, Proc. Phys. Soc. (London) 72, 898–901 (1958).

auxiliary data (for example, electrical resistivity values with a precision of about ±0.005% and $d\rho/dT$ values to ±0.1%).

Temperature Distributions in an Electrically Heated Wire (K.-H. Bode, P. H. Spindler)

Methods involving electrically heated wire are often viewed as the panacea for measuring thermal conductivity at high temperatures. We have not yet confirmed this. One difficulty is the lack of a closed solution to the general equation that describes the steady-state temperature distribution. Numerous solutions exist in the literature, but all involve assumptions that may deviate from reality. We began a computer study of this problem that yielded universal dimensionless curves valid for all possible pertinent physical properties and geometries. This

calculation showed the shape of the temperature-distance curve as well as the maximum temperature of a number of experimental studies to have larger deviations than rough estimates would lead one to believe. Basic to this work was the calculation of a complex integral by the computer. We used a Gaussian mechanical quadrature integration method that failed to converge by as much as 3% after using 512 terms. This is important, for most analyses only use 16 terms and assume convergence. Later in these calculations, we considered linear temperature dependencies for thermal conductivity, electrical resistivity, and the total hemispherical emittance and a modified integration that obtains convergency using Simpson's rule. These calculations not only point out deficiencies in the literature but offer possibilities of new ways to use this method of measurement.

References

1. D. Vollath, Compatibility of High-Melting Metals with UO_2, EURFNR-569 (April 1968).
2. J. R. DiStefano, Oak Ridge National Laboratory, private communication.
3. Large-Radioisotope Heat Source Capsule Fire Test, AI-AEC-12841 (May 29, 1969).
4. L. G. Overholser and J. P. Blakely, Outgassing Characteristics of Various Graphites, ORNL-3396 (February 1963).
5. K. E. Spear, A. R. Olsen, and J. M. Leitnaker, Thermodynamic Applications to $(U,Pu)O_{2\pm x}$ Fuel Systems, ORNL-TM-2494 (April 1969).
6. F. E. Harris, Metal Progr. 47, 84 (1945).
7. Transit RTG Design Review Report, TWR(A)-11404-167, 4 of 5, 7-65/73 (March 21, 1969).
8. H. Inouye, "The Contamination of Refractory Metals in Vacua Below 10^{-6} Torr," pp. 871–883 in Refractory Metals and Alloys III: Applied Aspects, Vol. 30, Part 2, Gordon & Breach Science Publishers, New York, 1963.
9. Transit Heat Source Program Review, undocumented TRW Report (Oct. 23, 1969).
10. "Intact Impact Heat Source Program Review," undocumented Isotopes, Nuclear Systems Division Report (Oct. 23, 1969).
11. G. P. Dix, "Safety Considerations for Radioisotope Power Systems," p. 57 in Symposium on Materials for Radio-Isotope Heat Sources, Nucl. Met. 14, ed. by D. E. Thomas, W. O. Harms, and R. T. Huntoon, American Institute of Mining, Metallurgical and Petroleum Engineers, New York, 1969.

12. W. T. Chandler and R. J. Walter, "Hydrogen Effects in Refractory Alloys," p. 197 in Refractory Metals and Alloys, Plenum Press, New York, 1968.

13. C. T. Liu and P. G. Marden, Fuels and Materials Development Program Quart. Progr. Rept. Sept. 30, 1969, ORNL-4480, pp. 157–160.

14. V. N. Svechnikov et al., Phase Equilibrium Diagram of the Hf-Ta System, NASA TT F-10,280 (September 1966).

15. L. L. Oden et al., The Hafnium-Niobium Equilibrium Diagram, BMRI-6521 (February 1964).

16. C. T. Liu and B. T. Loh, Fuels and Materials Development Program Quart. Progr. Rept. Sept. 30, 1968, ORNL-4350, pp. 298–302.

17. J. W. Cahn, Trans. Met. Soc. AIME 142, 166 (1968).

18. R. W. Carpenter, Acta Met. 15, 1567 (1967).

19. D. A. Canonico, Nancy C. Cole, G. M. Goodwin, and R. E. McDonald, Fuels and Materials Development Program Quart. Progr. Rept. Sept. 30, 1969, ORNL-4480, pp. 163–164.

20. K.-H. Bode, "Possibilities to Determine Thermal Conductivity Using New Solutions for Current-Carrying Electrical Conductors," p. 317 in Thermal Conductivity, Proc. 8th Conf., ed. by C. Y. Ho and R. E. Taylor, Plenum Press, New York, 1969.

21. W. Fulkerson, J. P. Moore, and D. L. McElroy, J. Appl. Phys. 37, 2639–2653 (1966).

22. J. P. Moore and R. S. Graves, Metals and Ceramics Div. Ann. Progr. Rept. June 30, 1966, ORNL-3970, p. 79.

15. TUNGSTEN METALLURGY

P. Patriarca A. C. Schaffhauser

The objective of this program is to provide the base technology on W alloys for advanced power applications in space. We are developing fabrication processes for W alloys based on modification of conventional extrusion and warm-drawing techniques, direct chemical vapor deposition, and welding. Since the primary criterion for the use of W alloys is based on the creep-rupture properties, we are conducting extensive long-time tests at the temperatures of interest. We are also determining the mechanisms that control the creep behavior and the effect of interactions with the vapor species from an isotope or reactor fuel.

Chemical Vapor Deposition of Tungsten Alloys

J. I. Federer

Chemical Vapor Deposition of Tungsten-Rhenium Sheet and Tubing (J. I. Federer)

We continued to deposit W-Re alloys on resistance-heated substrates by H_2 reduction of WF_6 and ReF_6. Nominal W–5% Re alloys can be deposited as tubes or sheet with a compositional uniformity of ±0.5% Re over a length of 16 in., but nodules are usually observed when the deposit becomes 0.010 to 0.015 in. thick. The nodules grow much faster than adjacent columnar-grained material and soon protrude from the surface. Although nodules could be ground flush with the surface, the porosity associated with these growths is a serious microstructural defect that cannot be removed.

Many attempts have been made to minimize nodules by adjusting such deposition conditions as variations in gas composition and mass flow of gases. We have also prepared deposits by pulsing or interrupting the gas flows.[1] These experiments were based upon the observation that nodules grow from dense, smooth deposits; therefore, pulsing or interrupting the gas flows was intended to cause periodic nucleation of new growth to

avoid the condition that causes nodules. So far, none of these methods has been successful.

Recent experiments to minimize nodules in sheet deposits were based upon the renucleation principle. In one experiment a nominal W–5% Re alloy was deposited for 30 min, and then the flow of WF_6-ReF_6 was stopped. The deposit was cooled to room temperature and then reheated to the deposition temperature (about 700°C), and the WF_6-ReF_6 flow was started again. This cycle was repeated about 30 times. The resulting deposit, which had a maximum thickness of about 0.032 in., contained scattered nodules.

In two experiments the WF_6 and ReF_6 flows were alternately pulsed. The WF_6 flowed for 3 min, then was off for 1 min. The ReF_6 flowed during the 1-min interval when the WF_6 was off. In two other experiments the WF_6 flowed continuously, while the ReF_6 was pulsed 2 min on and 2 min off. These deposits also contained scattered nodules in an otherwise smooth surface.

A 3/4-in.-ID × 0.015-in.-wall-thickness tube of W–5% Re was deposited in about 5 hr. After nodules were ground flush with the surface, an additional 0.015-in.-thick layer was deposited. The second deposit was more nodular than the first. Apparently, some nodules in the first layer continued to grow, and new nodules formed in the second layer.

Tubes with a 1/8-in. inside diameter and 0.025-in.-thick wall were also deposited. A W–5% Re tube prepared by periodic reversal of the WF_6-ReF_6 flow had scattered nodules protruding from a smooth surface. A W–25% Re tube prepared with continuous, unidirectional flow of WF_6-ReF_6 and another prepared by pulsing the WF_6-ReF_6 flow were very nodular and porous.

Thus, none of the attempts to eliminate nodules by depositing layers was completely successful. As mentioned previously, grains frequently grow through laminations caused by pulsing or interrupting gas flows.[1] A distinct stop and start does not occur. Other methods being considered for causing renucleation include deposition of an impurity layer, such as a carbide or nitride, and mechanical working of the surface during deposition. The dependence of nodule formation on the Re content of W-Re deposits is also being investigated.

Metallurgical Properties of Tungsten Alloys

H. Inouye

Effect of Low-Pressure Oxygen on the Creep Properties of Tungsten (H. Inouye)

The creep behavior of W in low-pressure O_2 is being determined at thermionic temperatures to simulate the effects of an interaction between an oxide fuel and its cladding. Previously,[2] we reported that the steady-state creep rate of W was always higher in an atmosphere of 10^{-5} torr O_2 than at the base pressure of about 10^{-7} torr. The effects of O_2 pressure were attributed to the sublimation of W as volatile oxides and to the effect of O either in solution or in causing an increased rate of growth of creep cavities.

During this quarter, the creep behavior of powder-metallurgy W was determined as a function of the O_2 pressure at 1800°C and at a stress of 1000 psi. The results in Fig. 15.1 show that the creep rate of W increases with the O_2 pressure at about 10^{-5} torr and is significantly higher than at a base pressure of 10^{-7} torr. Under the test conditions,

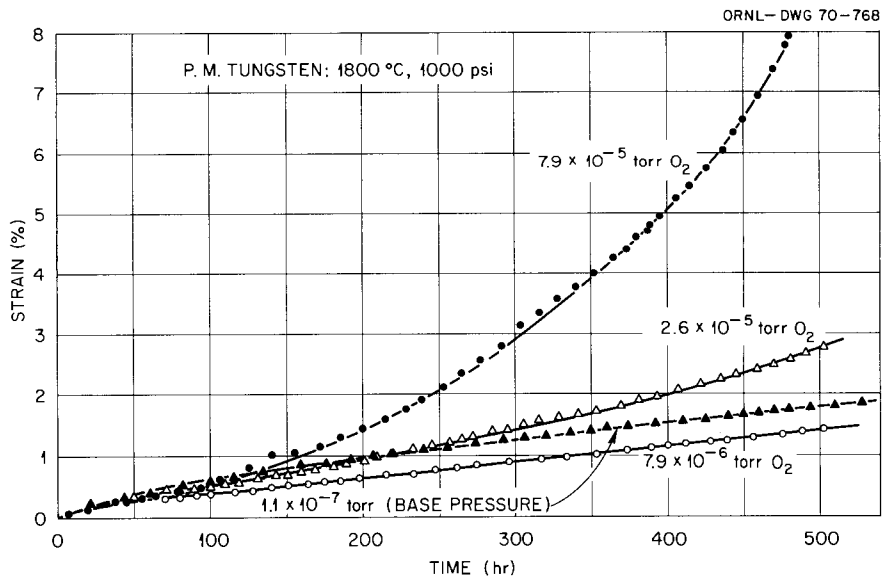

Fig. 15.1. Creep Properites of Powder Metallurgy Tungsten as a Function of Oxygen Pressure.

the specimens were in third-stage creep early in the test, and consequently did not exhibit a definable steady-state creep stage. Although the creep curve at 8×10^{-6} torr O_2 lies below the curve at the base pressure, the steady-state creep rates after 500 hr were the same in both tests. The difference between the total strains is attributed to a shorter period for primary creep of W in the O_2 environment.

The increased creep rate at O_2 pressures above 10^{-5} torr is primarily due to a reduction in the cross section of the specimen by sublimation of volatile oxides. Table 15.1 shows that sublimation increases with the O_2 pressure as expected. However, it should also be noted that an unstressed specimen sublimes at about 1/3 the rate of a specimen stressed to 1000 psi at about 3×10^{-5} torr O_2 (0.06 vs 0.22 mg cm^{-2} hr^{-1}). The microstructures of W specimens subjected to different stresses at a constant O_2 pressure of 7×10^{-5} torr are shown in Fig. 15.2. The increase in the surface roughness with stress apparently increases the surface area, and therefore, the sublimation rate. Thus, the destructive sublimation process at a particular temperature is a function of both stress and the O_2 pressure.

Table 15.1. Sublimation Rates and Oxygen Content of Tungsten After Creep Testing in Low-Pressure Oxygen at 1800°C

Oxygen Pressure (torr)	Stress (psi)	Sublimation Rate (mg cm^{-2} hr^{-1})	Oxygen Content[a] (ppm)
7.9×10^{-5}	1000	0.48	36
2.6×10^{-5}	1000	0.22	48
7.9×10^{-6}	1000	0.01	37
1.1×10^{-7}[b]	1000	Not measurable	13
3×10^{-5}[c]	0	0.06	5

[a]Oxygen content of specimens as received was 9 ppm.

[b]Base system pressure at temperature, no oxygen added.

[c]R. L. Wagner, "Sublimation of W–25% Re Between 1550 and 1950°C in Low-Pressure Oxygen," paper presented at IEEE 1969 Thermionic Conversion Specialist Conference, Carmel, Calif., Oct. 21–23, 1969. To be published in the proceedings.

Y-94521

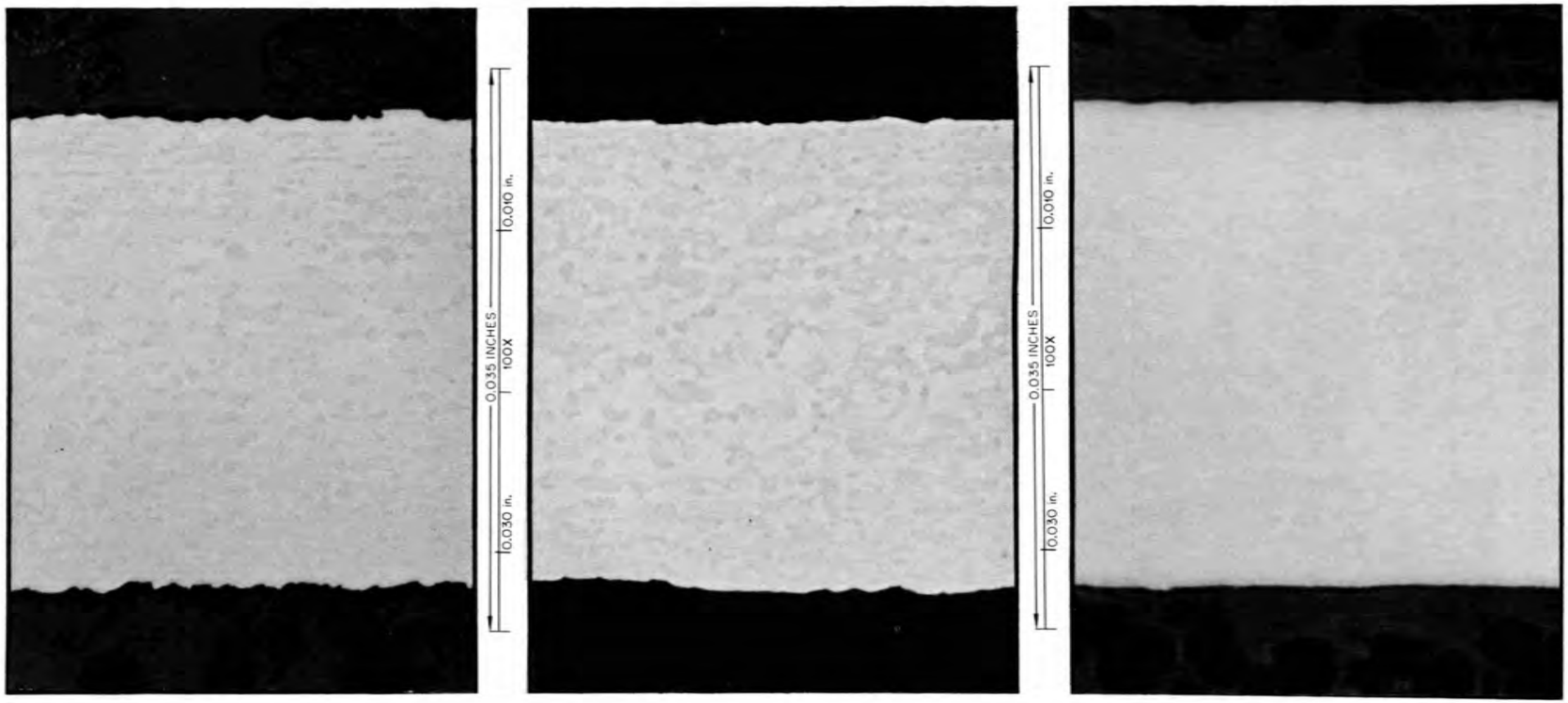

Fig. 15.2. Microstructures of Tungsten Creep Tested in 7×10^{-5} torr Oxygen. Temperature, pressure, and sublimation rates are, respectively, (a) 1500°C, 4000 psi and 0.98 mg cm^{-2} hr^{-1}; (b) 1650°C, 2000 psi, and 0.43 mg cm^{-2} hr^{-1}; and (c) 2000°C, 500 psi, and 0.06 mg cm^{-2} hr^{-1}.

Analyses after the tests showed an increase of about 40 ppm O that was independent of O_2 pressure above 8×10^{-6} torr (Table 15.1). Because solid oxide phases of W are unstable under these test conditions, it appears that the solubility limit of O in W at 1800°C is about this value.

Long-Time Creep Properties of Tungsten Alloys

H. E. McCoy, Jr. J. O. Stiegler

Creep and Stress-Rupture Properties of Arc-Melted and Chemically Vapor Deposited Tungsten-Rhenium Alloys (R. L. Stephenson)

We are continuing our study of the creep- and stress-rupture properties of W-base materials. Stress-rupture curves for several materials were presented previously. We are now gathering data on the times to low strains in these materials. The times to selected strains and to rupture at 1650°C are shown for arc-melted unalloyed W, W–5% Re, W–26% Re, W–25% Re–30% Mo, and chemically vapor deposited W in Figs. 15.3 to 15.7, respectively.

Design stresses are usually chosen on the basis of some primary design criterion along with the consideration of one or more secondary design criteria. In the case of a thermionic capsule or a reactor fuel

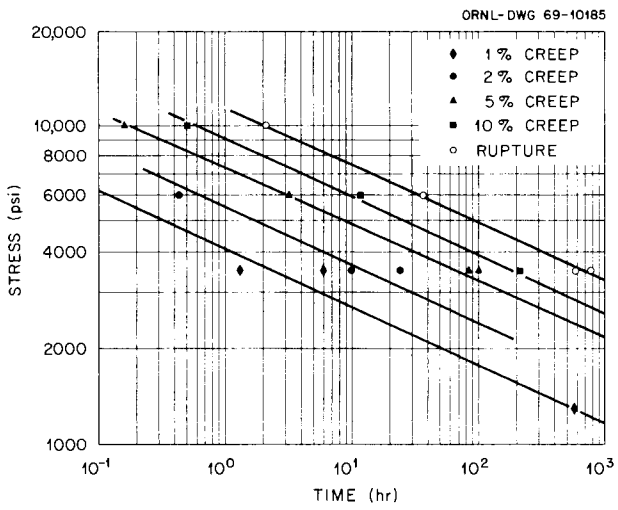

Fig. 15.3. Creep-Rupture Properties of Unalloyed Tunsten at 1650°C.

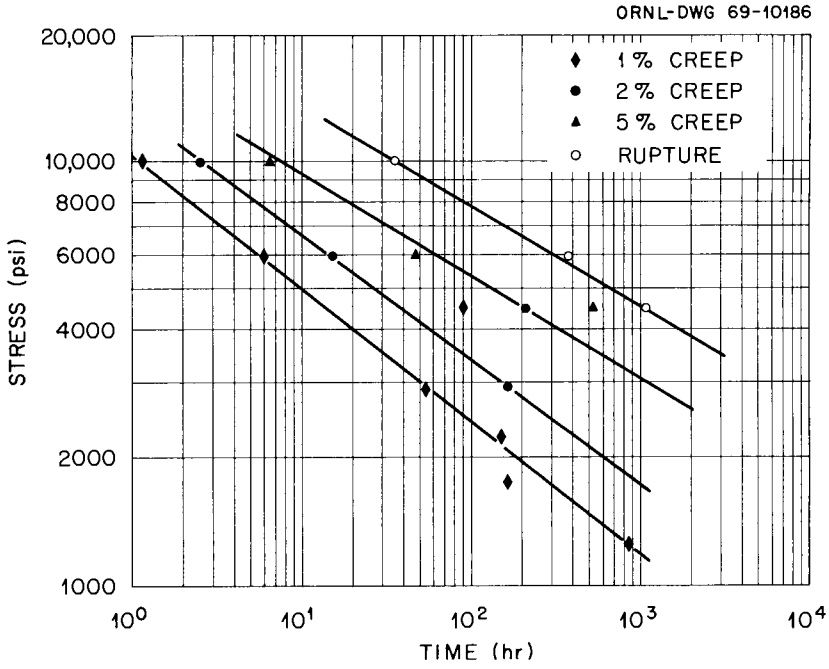

Fig. 15.4. Creep-Rupture Properties of W–5% Re at 1650°C.

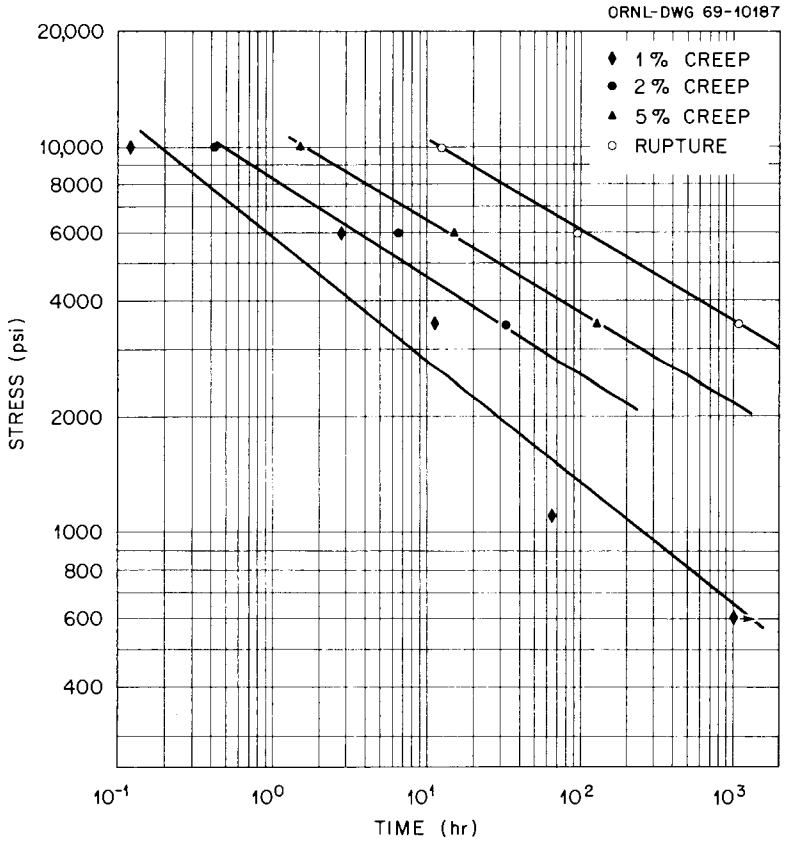

Fig. 15.5. Creep-Rupture Properties of W–26% Re at 1650°C.

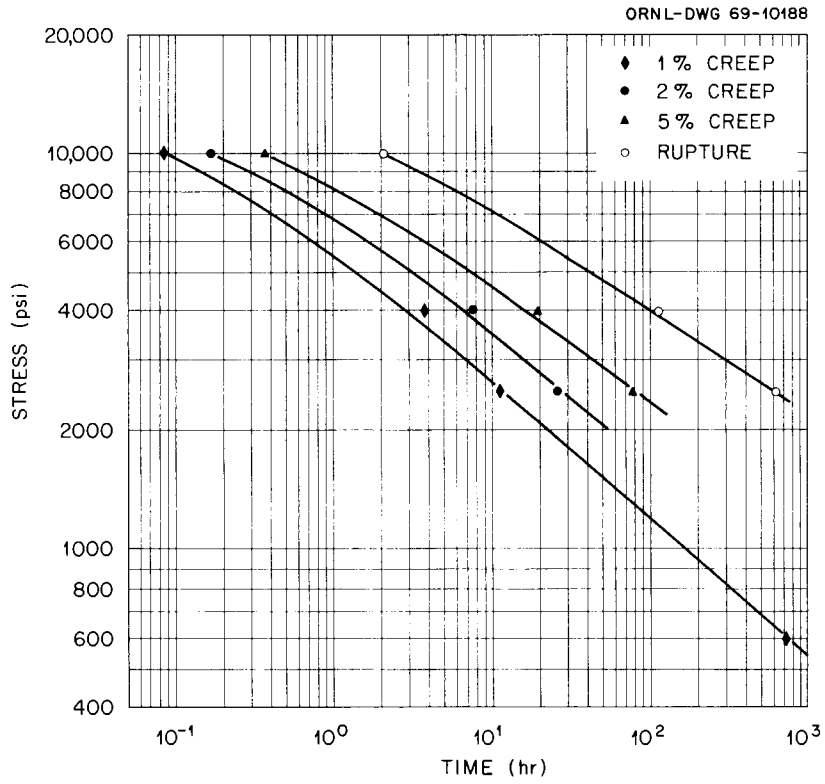

Fig. 15.6. Creep-Rupture Properties of W–25% Mo–30% Re at 1650°C.

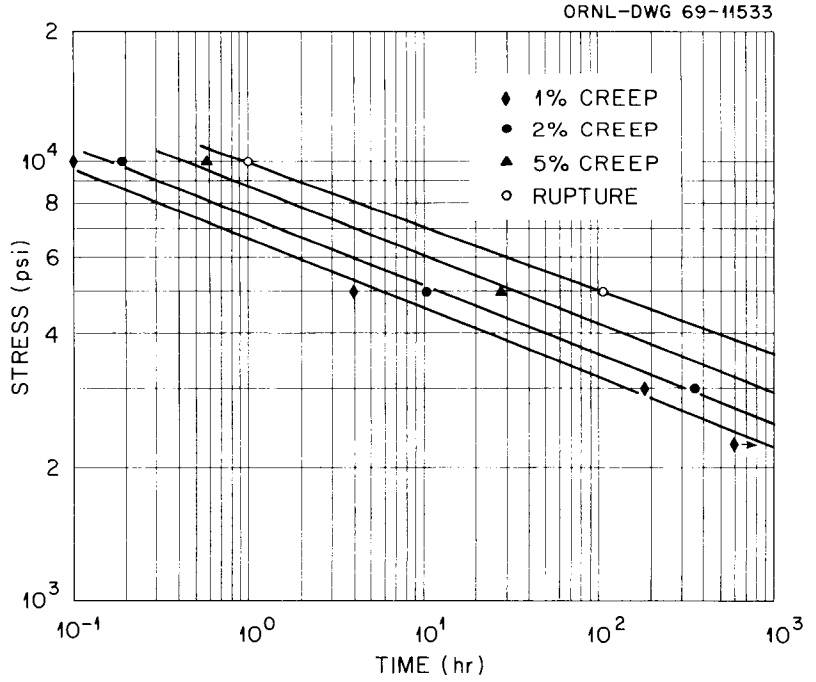

Fig. 15.7. Creep-Rupture Properties of Chemically Vapor Deposited Tungsten.

element, the primary design criterion would be the stress to produce some specified strain during the design life. A secondary design criterion might be that the design stress must not exceed some fraction of the rupture stress. These criteria interact to such an extent that a design stress cannot be selected on the basis of one without consideration of the others. This point can be illustrated with the experimental data presented.

Let us assume that the primary failure criterion for a thermionic capsule is the attainment of 1% creep. Since we must avoid the release of radioactive material, let us establish the additional condition that the design stress must not exceed 50% of the stress to produce rupture in the design life.

Figure 15.8 compares the stress to produce 1% creep in 1000 hr for each of the materials listed above. On this basis chemically vapor

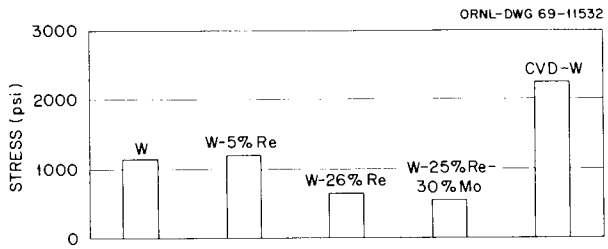

Fig. 15.8. Stress to Produce 1% Creep in 1000 hr for Selected Tungsten-Base Materials at 1650°C.

deposited W seems superior, followed by W–5% Re and then unalloyed W. One is able to visualize the interaction of failure criteria much better, however, when the materials are compared using isochronous stress-strain curves, such as those in Fig. 15.9.

In an isochronous stress-strain curve, the stress is plotted as a function of strain at constant time and temperature. Each curve is constructed from data from a number of creep tests performed at different stresses at a given temperature. It is apparent that the stress to produce 1% creep in chemically vapor deposited W exceeds 50% of the rupture stress. This stress is still above the stress to produce 1% creep in W–5% Re, but the margin is reduced. If we decide that we can tolerate

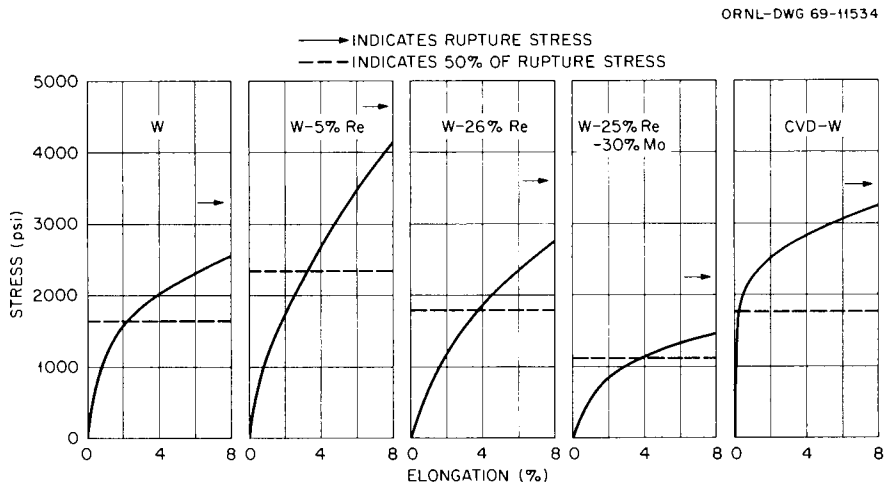

Fig. 15.9. Isochronous (1000 hr) Stress-Strain Curves for Selected Tungsten-Base Materials.

2 or 3% strain, the allowable stress for chemically vapor deposited W does not increase, since it is already limited by 50% of the rupture stress. The allowable stress for W–5% Re can be increased, however, making it the most attractive alloy under these conditions. On the other hand, if we decide that 50% of the rupture stress is too conservative and that 80% is more reasonable, the chemically vapor deposited W becomes most attractive again.

Attention must not be focused on one aspect of material behavior to the exclusion of others. A complete understanding of the behavior of a particular material at various stresses and temperatures is necessary before safe design is possible. This is particularly important in isotopic capsules, since they will see changing temperatures and stresses.

Comparative Creep-Rupture Properties of W–25% Re Consolidated by Arc-Melting and Powder-Metallurgy Techniques (R. L. Stephenson)

We have performed additional tests on powder-metallurgy W–25% Re sheet to confirm the anomalous creep behavior reported previously.[3] The secondary creep rates of arc-melted and powder-metallurgy material at 1650 and 2200°C are shown as a function of stress in Fig. 15.10. If the curves for the powder-metallurgy material were extrapolated to lower stresses it appears that they would cross. This would mean that at the lower stresses the material would actually creep faster at 1650°C than

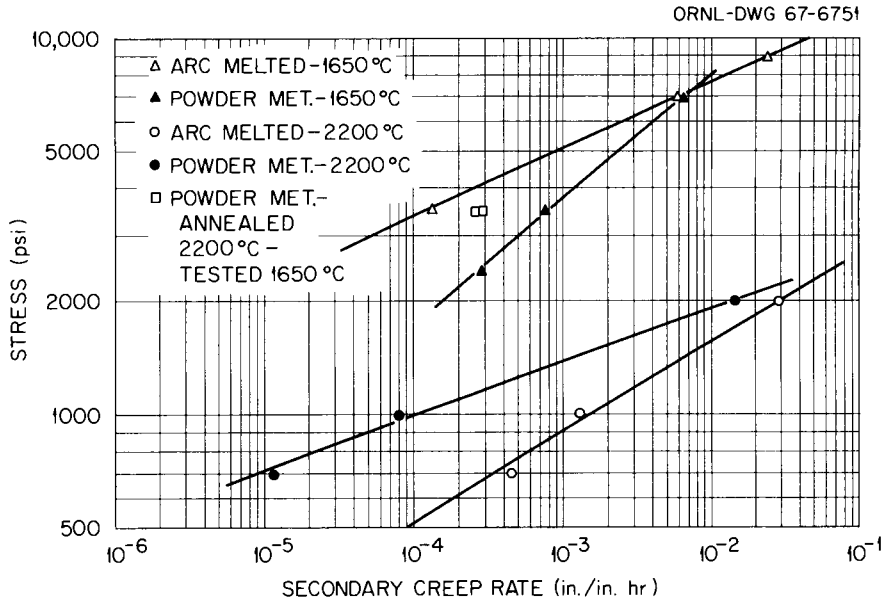

Fig. 15.10. Secondary Creep Rate Versus Stress for W–25% Re.

at 2200°C. In order to determine whether this implausible event would actually occur, a specimen was loaded to 500 psi at 1650°C and measurements were made until the secondary creep rate was established. Without changing the load, we abruptly changed the temperature to 2200°C. The creep rate as a function of time (i.e., the slope of the creep curve at any given time) is shown in Fig. 15.11. After about 50 hr at 1650°C a creep rate of 6×10^{-6} hr^{-1} was established. When the temperature was increased to 2200°C, the creep rate increased by several orders of magnitude, but over a period of about 10 hr it decreased to 3×10^{-5} hr^{-1}. Specimens annealed at 2200°C and tested at 1650°C showed that more than 1 hr but less than 20 hr is required to establish the large grain size characteristic of the higher temperature.[3]

When a small grain size is stable for long times at temperatures up to a critical temperature above which secondary recrystallization takes place, as is the case for powder-metallurgy W (ref. 4) and if most of the observed creep deformation is due to the growth of voids at grain boundaries,[3] then it is plausible that the creep rate at a certain stress could be lower at 2200°C than at 1650°C. A lower creep rate and less total strain occur at the higher temperature simply because there are fewer grain boundaries on which voids can grow. When the temperature

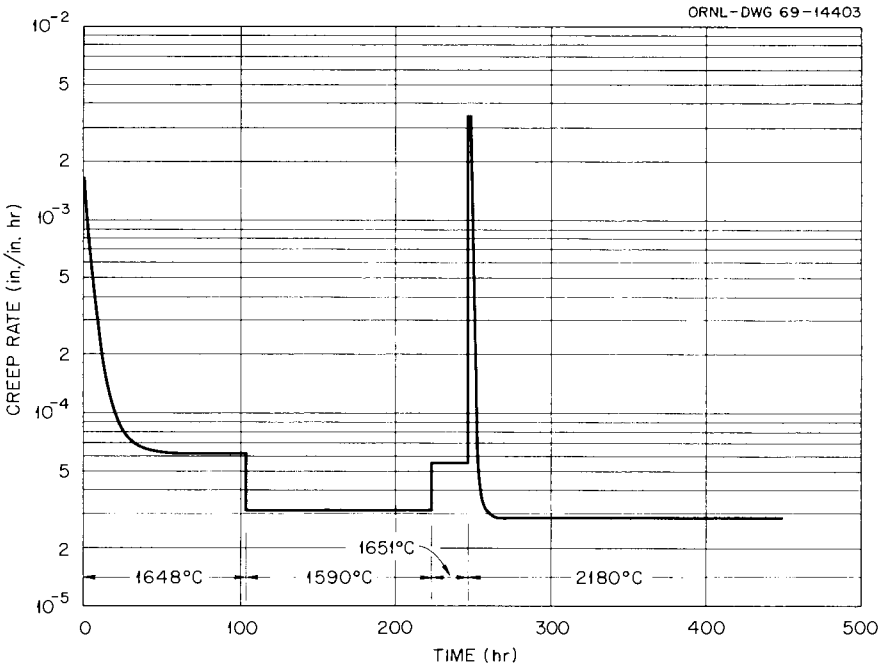

Fig. 15.11. Creep Rate Versus Time for Powder-Metallurgy W–25% Re at 500 psi.

of the specimen shown in Fig. 15.11 was reduced to 1650°C again after having been exposed to a temperature of 2200°C, the creep rate decreased far below that observed for the fine grain size that prevailed before exposure to the higher temperature.

Before raising the temperature to 2200°C, we cycled the temperature between 1648 and 1590°C to permit the calculation of the apparent activation energy for creep. The value thus obtained was about 40,000 cal/mole. This value is surprisingly low; however, Vandervoort and Barmore[5] observed a more or less systematic decrease in apparent activation energy with decreasing stress for this alloy. If their results are plotted as a function of stress, a value of 40,000 cal/mole at 500 psi is in reasonable agreement.

The only known processes in W that have activation energies this low are the diffusion of interstitials or divacancies. Since the growth of voids seems to be important in the creep of these W materials, the diffusion of divacancies may have some relevance. In view of the stress dependence of the activation energy, however, it seems clear that the creep process is quite complex.

Growth of Large Creep Cracks in Powder-Metallurgy Tungsten

(J. O. Stiegler)

We are following the progressive development of cracks formed at grain boundaries in powder-metallurgy W under creep deformation. We believe that these studies will help clarify the mechanisms involved in the nucleation and growth of cracks and allow us to understand reasons for the strikingly different behavior shown by W and W alloys processed by different means.

The present experiments were conducted at 1600°C at stresses between 4500 and 12,000 psi. Tests were interrupted at various points along the creep curve to permit observation of stages in the nucleation and growth of the cracks. After the tested specimens were cooled to room temperature, they were fractured brittlely. The brittle fracture surfaces generally ran along grain boundaries, where they bisected and thus exposed the creep cracks formed at high temperature. Replicas of the surfaces containing the cracks were then examined by means of the electron microscope.

Studies with an optical microscope allowed creep cracks to be classified into two categories:[6] at high test temperatures and low stresses they appear equiaxed and lie predominantly on grain boundaries perpendicular to the applied stress; at low test temperatures and high stresses they appear wedgelike, spreading from triple grain junctions. Previous work,[7] which used the electron fractography technique for powder-metallurgy W, showed that both types of cracks were nucleated on grain interfaces but that the conditions of test temperature and stress determine whether they grow in an equiaxed manner or primarily along the surface of the boundaries.

During the past quarter, effort has been concentrated on examination of the features of large cracks extending several grain diameters in length. Nearly all such cracks have rumpled surfaces, and small, isolated cracks appear to be growing in the region immediately in advance of the main crack, as can be seen in Fig. 15.12. From these observations we conclude that these cracks, which would be classified as the wedge type by optical metallography, do not grow by the simple advance of the main crack front, but rather by the merger with large numbers of small voids

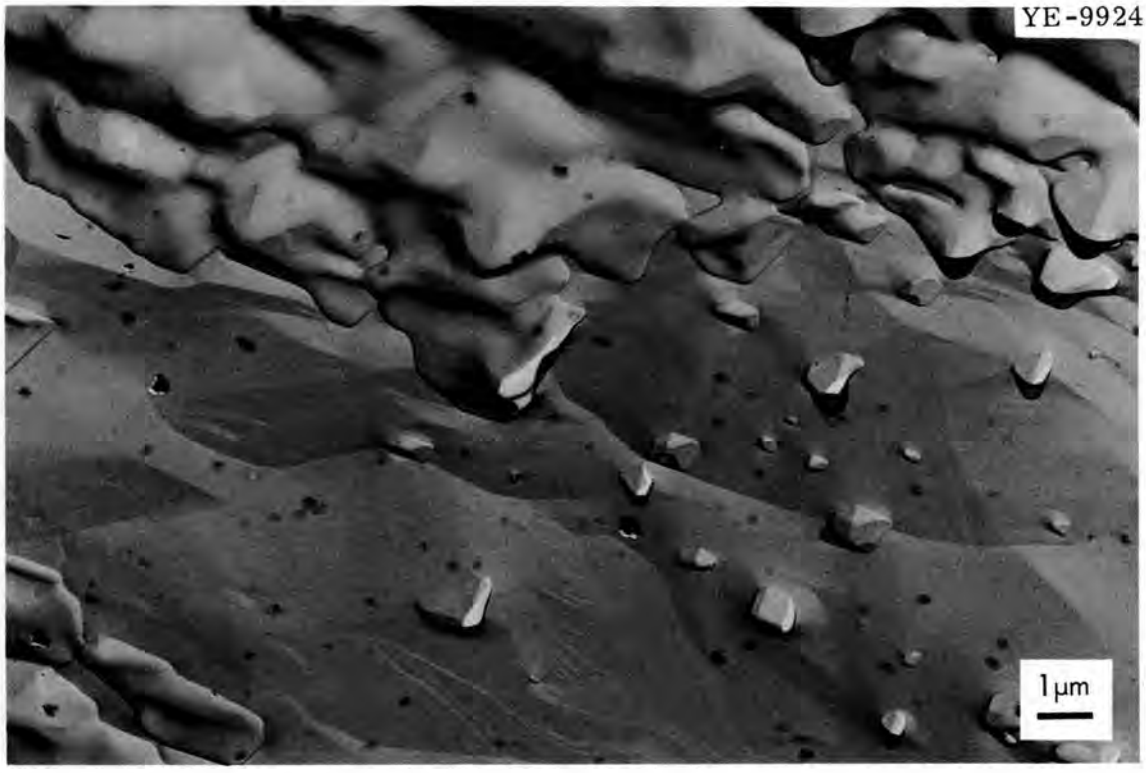

Fig. 15.12. Small Creep Cavities Opening in Front of a Large Crack. Note the rumpled appearance of the crack, which indicates that it has advanced by merger with small cavities.

formed in front of the main crack. A few instances of uniform crack growth from a triple grain boundary junction were observed (Fig. 15.13), but these were rare and isolated observations. The common mechanism of crack growth is by the merger of small voids.

The method by which the material was originally consolidated appears to be an important variable that influences the creep behavior of W. For example, material prepared by powder-metallurgy techniques exhibits failure by growth of intergranular cracks with little reduction in area; arc-melted material necks extensively and fails ductilely.[3,8] Optical and electron fractographic studies[3] showed few cracks at grain boundaries in the arc-melted material. In addition, grain sizes after testing under identical conditions are much larger in arc-melted material than in powder-metallurgy material.

Observations by transmission electron microscopy showed that, for the grade of powder-metallurgy W used in the present tests, an annealing

Fig. 15.13. True Wedge Type of Crack Spreading from a Triple Grain Junction. Compare the smooth appearance and relatively uniform front of this crack with the rumpled and irregular nature of the crack shown in Fig. 15.12. This type of crack is very rare.

treatment of 1 hr at 1600°C produces a moderate concentration of cavities ($> 10^{11}$ cavities/cm^3), probably gas bubbles, both within the grains and on the grain boundaries. Preliminary observations of arc-melted material of comparable purity failed to reveal any bubbles.

We believe that many of the differences between these materials are due to the small gas bubbles present in the powder-metallurgy product. Such bubbles could favor the development and growth of intergranular cracks in two ways: (1) by providing suitable nuclei for the formation and growth of cracks by the merger process and (2) by promoting grain stability to prevent boundaries from migrating away from existing cracks. Bubbles within the grains may also affect the scale and extent of the substructure and thereby influence creep strength.

Evaluation of Methods for Joining Tungsten Alloys

G. M. Slaughter

Development of Filler Metals with Low Melting Points (Nancy C. Cole)

This quarter we have concentrated on the gas W-arc welding of 0.030-in. arc-melted W–25% Re sheet. We are determining the optimum welding conditions for bead-on-sheet and butt welds between two sheets. Using no preheat and maintaining the travel speed at 10 in./min and the arc gap at 1/16 in., we found that a 200-amp welding current produced full-penetration welds. Care was taken to assure high purity in the Ar welding atmosphere. Restraint from the clamping fixture was minimized to prevent cracking. Figures 15.14 to 15.16 show photomacrographs of the three types of joints produced. Figures 15.14 and 15.15 are welds for which no filler metal was used. Figure 15.16 is a bead-on-sheet weld with Mo–50% Re filler wire.

A narrow weld with no cracks was successfully produced by the bead-on-sheet (no filler wire) joint design (Fig. 15.14); however, crater cracking was encountered with the wider butt weld (Fig. 15.15). The

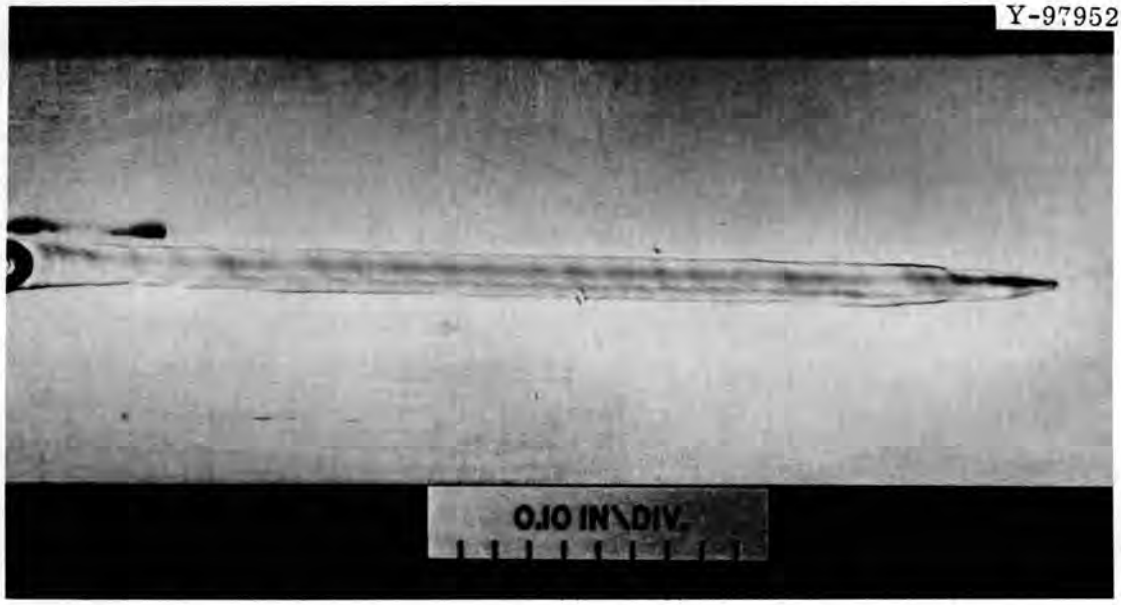

Fig. 15.14. Bead-On-Plate Weld of W–25% Re with No Filler Metal.

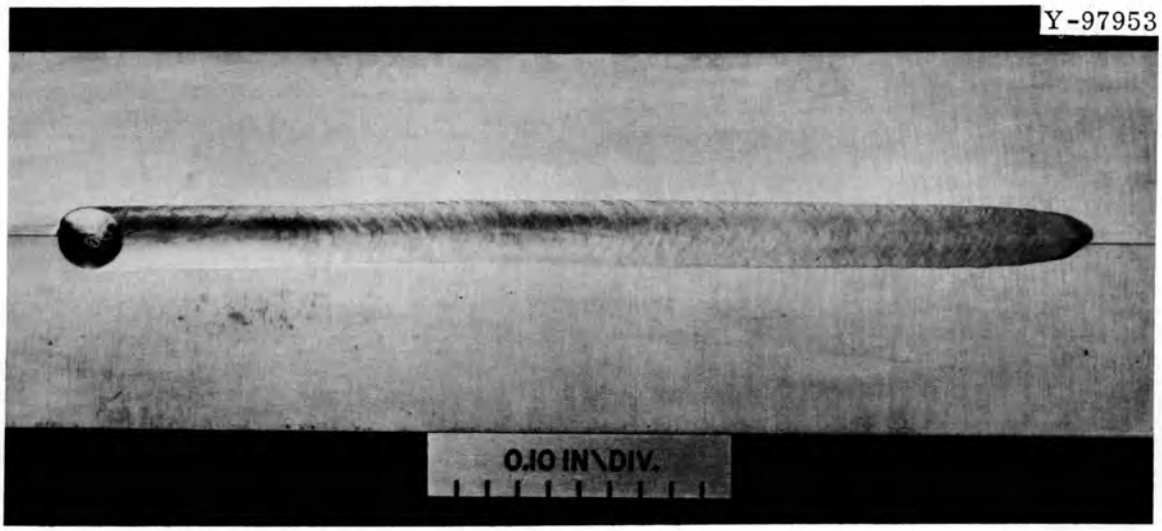

Fig. 15.15. Butt Weld in W–25% Re with No Filler Metal.

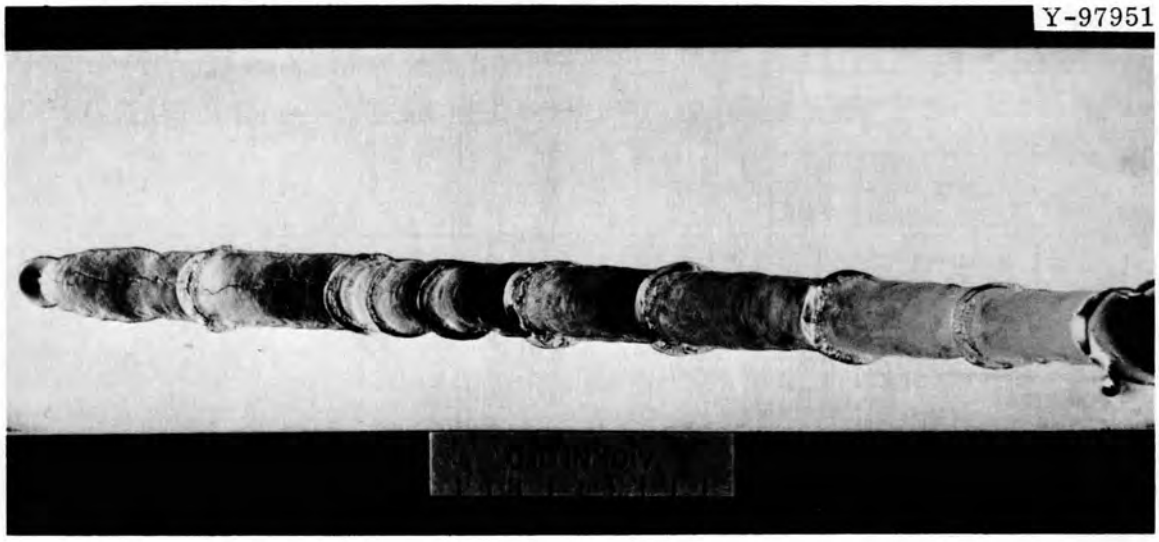

Fig. 15.16. Bead-On-Plate Weld in W–25% Re with Mo–50% Re Filler Metal. Some hot cracking is evident.

addition of Mo–50% Re filler metal caused a considerable widening of the weld bead (Fig. 15.16). Apparently, the alloying with the filler wire, which had a lower melting point, was sufficient to lower the overall melting temperature and cause a larger weld pool. Hot cracking is evident at the beginning of the weld.

In future experiments, heat input will be reduced in the latter two types of welds. Others[9] have shown difficulty in obtaining gas W-arc welds that are free of cracks in W–25% Re, but narrow electron-beam welds were free of cracks. We postulate that if the heat input is lowered to achieve narrow welds the gas W-arc process may also produce welds without cracks.

References

1. J. I. Federer, Fuels and Materials Development Program Quart. Progr. Rept. Sept. 30, 1969, ORNL-4480, pp. 170–173.
2. H. Inouye, Fuels and Materials Development Program Quart. Progr. Rept. Sept. 30, 1969, ORNL-4480, pp. 176–180.
3. R. L. Stephenson, Comparative Creep-Rupture Properties of W–25% Re Consolidated by Arc-Melting and Powder-Metallurgy Techniques, ORNL-TM-2651 (September 1969).
4. K. Farrell, A. C. Schaffhauser, and J. O. Stiegler, J. Less-Common Metals 13, 144 (1967).
5. R. R. Vandervoort and W. L. Barmore, "Elevated Temperature Deformations and Electron Microscope Studies of Polycrystalline Tungsten and Tungsten-Rhenium Alloys," pp. 108–137 in 6th Plansee Seminar, ed. by F. Benesovsky, Metallwerk Plansee AG., Reutte/Tyrol, 1969.
6. D. McLean, J. Inst. Metals 85, 468 (1956–1957).
7. J. O. Stiegler, K. Farrell, B.T.M. Loh, and H. E. McCoy, Jr., Trans. Am. Soc. Metals 60, 494 (1967).
8. R. C. Rau and F. T. Williams, Jr., Creep Failure Modes in Arc-Cast and Powder Metallurgy Tungsten, GEMP-640 (1967).
9. G. G. Lessman and R. E. Gold, The Weldability of Tungsten Base Alloys, WANL-SP-020 (May 9, 1969).

16. FAST-NEUTRON IRRADIATION EFFECTS ON ELECTRICAL INSULATORS

G. M. Watson[1] G. W. Keilholtz[1]

The purpose of this program is to establish the effects of fast neutrons on the mechanical, physical, and electrical properties of materials suitable for use as electrical insulators in thermionic converters and to evaluate the mechanisms of neutron damage in these materials up to 1100°C.

General Survey of Fast-Neutron Effects on Electrical Insulators

R. E. Moore[1] D. A. Dyslin[2] H. E. Robertson[1]

We are investigating four advanced materials that are excellent electrical insulators and that may have an advantage over polycrystalline alumina with respect to separation at grain boundaries. One of these, silicon oxynitride (Si_2ON_2), was irradiated in the Engineering Test Reactor (ETR) at low temperature (70 to 90°C). The results, which were reported previously,[3,4] were very encouraging. The other three advanced materials are now being irradiated in the ETR at low temperature. These are (1) synthetic sapphire, (2) high-purity, single-crystal MgO, and (3) zirconia-doped transparent Y_2O_3 (General Electric). We are planning to irradiate all four materials, as well as polycrystalline alumina, in row 8 of the Experimental Breeder Reactor-II (EBR-II) in an assembly designed for specimen temperatures of 400 and 800°C.

Irradiation of High-Density Commercial Al_2O_3 Products Considered for Thermionic Insulators

R. E. Moore[1] D. A. Dyslin[2] H. E. Robertson[1]

Four commercial alumina products of high density are being investigated to establish their behavior in a fast-neutron flux over a broad temperature range. These materials, which are listed in Table 16.1, are considered for actual use as electrical insulators in nuclear-powered

Table 16.1. Commercial Alumina Products Under Investigation

Type	Trade Name	Grain Size (μm)	Impurities, wt %				
			Total[a]	Major			
				Mg	Si	Fe	Other
I	Coors AD-995	13	0.42	0.1	0.06	0.06	(Cu, 0.06) Cr, 0.1)
II	Wesgo AL-995	23	0.25	0.1	0.1	0.03	
III	GE Opaque Lucalox	6	0.06	0.02	0.007	0.01	(Ni, 0.01)
IV	GE Translucent Lucalox	25	0.14	0.08	0.02	0.003	

[a]Summary of spectrographic analyses performed by C. Feldman and Anna M. Yoakum, Analytical Chemistry Division.

thermionic converters. Most of the irradiations were carried out in the ETR. Some of the results were reported previously.[3,4] These data, as well as more recent data, are summarized in the sections below.

Low-Temperature Irradiations in the ETR

Figure 16.1 shows the expansion in the volume of type IV alumina over two ranges of low temperatures. A curve representing the expansion of a total of 28 specimens of all four types over a very low range of fluence (0.2 to 0.7 $\times 10^{21}$ neutrons/cm^2) is also shown.

The great difference between the two curves of Fig. 16.1 means that the effect of temperature[3,4] on neutron damage to alumina begins to become increasingly important at temperatures above about 100°C. The point determined by Wilks *et al.*[5] for a single crystal at 150°C agrees with our data. The expansion of the single crystal at 150°C after exposure to a fluence of 1.25 $\times 10^{21}$ neutrons/cm^2 was isotropic. It might have become anisotropic at this temperature, however, on exposure to higher fluences. Metallographic examinations of specimens irradiated at the higher temperatures (110 to 325°C) shown in Fig. 16.1 showed that separation at grain boundaries begins at a fluence of about 2.3 $\times 10^{21}$ neutrons/cm^2 and contributes increasingly to the volume expansion with increasing fluence. This indicates that anisotropic

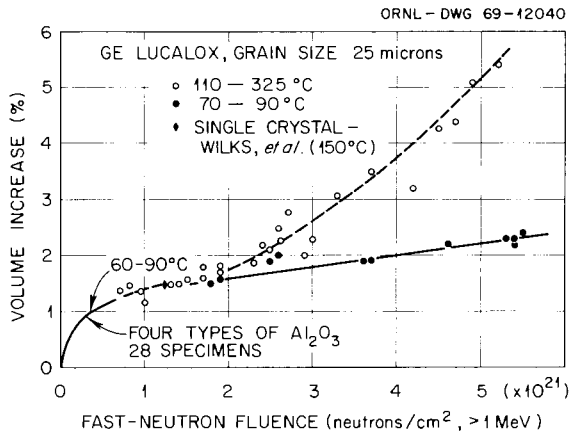

Fig. 16.1. Volume Increase of Commercial Alumina after Irradiation at Low Temperatures. [Ref. R. S. Wilks et al., The Irradiation-Induced Macroscopic Growth of α-Al_2O_3 Single Crystals, AERE-R-5460 (May 1967).]

crystal expansion occurs over this temperature range at high fluences. Metallographic examinations have not yet been completed on the specimens irradiated at 70 to 90°C.

Results of a Short-Term, High-Temperature Irradiation in the ETR

Tables 16.2 and 16.3 list, respectively, the gross damage to solid cylinders and to thin-walled cylindrical shells of alumina that were irradiated in the ETR in an instrumented high-temperature assembly designated ORNL-41-38. A greater percentage of shells fractured than of solid cylinders, probably because short fractures would penetrate completely through the shells. Based on an examination of the data for solid cylinders in Table 16.2, we concluded that purity is the most important factor in determining gross fracture over the ranges of conditions for this assembly. None of the specimens of types III and IV, the two purest types, fractured; type I, the least pure type, fractured most severely.

Separation at grain boundaries is an important result of neutron damage to alumina. Under the conditions of this experiment, it was not found to be related to gross fracturing; nevertheless, it unquestionably weakens the structure and contributes to swelling of the specimens.

Table 16.2. Gross Damage to Solid Cylindrical Alumina Specimens[a] Irradiated in ORNL-41-38

Fast-Fluence Range [neutrons/cm^2 (> 1 Mev)]	Irradiation Temperature (°C)	Types of Specimens[b]	Gross Damage Resulting from Irradiation
$\times 10^{21}$			
0.4–0.6	400	I,II,III,IV	None
1.0–1.3	710	I,II,III,IV	None
1.4–1.7	1070	I,II,III,IV	Type I, small crack
1.65–1.8	910	I,II,III	Type I, very thin crack Type II, very thin crack
1.75–1.95	750	II,III,IV	Type II, very thin crack
2.05–2.25	630	I,II,III	Type I, small crack
2.25–2.4	1230	I,II,III	Type I, crack
2.35–2.5	580	II,III,IV	Type II, crack
2.8–2.95	930	I,II,III	Type I, large crack
2.8–2.9	790	I,II,III	None
3.1	1100	I,II,III,IV	Type I, broken in half Type II, broken in half

[a] Diameter: 0.493 in.

[b] Types of alumina:

I, Coors AD-995, 13-μm grain size.

II, Wesgo AL-995, 23-μm grain size.

III, GE Opaque Lucalox, 6-μm grain size.

IV, GE Translucent Lucalox, 25-μm grain size.

Table 16.3. Gross Damage to Cylindrical Shells[a] of Alumina Irradiated in ORNL-41-38

Fast-Fluence Range [neutrons/cm^2 (> 1 Mev)]	Irradiation Temperature (°C)	Gross Damage Resulting from Irradiation[b]
$\times 10^{21}$		
0.7–0.8	430	Types I,II, broken
1.4–1.6	910	All broken
2.0–2.2	1230	All broken
2.6–2.8	550	None
2.6–2.8	930	Types I,III, broken
2.9–3.0	790	None
3.0–3.1	1200	None

[a]Outside diameter: 0.493 in.
Wall thickness: 0.020 in.

[b]Types of alumina:

I, Coors AD-995, 13-μm grain size.

II, Wesgo AL-995, 23-μm grain size.

III, GE Opaque Lucalox, 6-μm grain size.

Figure 16.2 shows separation at grain boundaries in the four types of alumina irradiated under comparable conditions. Type III alumina is clearly superior to the other types, probably because of the smaller grain size of this type of alumina.

The volume expansion of the irradiated specimens is shown in Fig. 16.3. The temperature range is 580 to 1230°C except for the four low-fluence points at 400°C. The data fall above the low-temperature data of Fig. 16.1 for the range 110 to 325°C, but the effect of temperature over the range 580 to 1070°C appears to be minimal. Apparently, in-reactor thermal annealing of displacements produced by fast neutrons reduced the damage to the specimens irradiated at 1100°C. Irradiation at much higher temperatures (1230°C), however, caused severe grain-boundary separation with a concomitantly large volume expansion of types I and II.

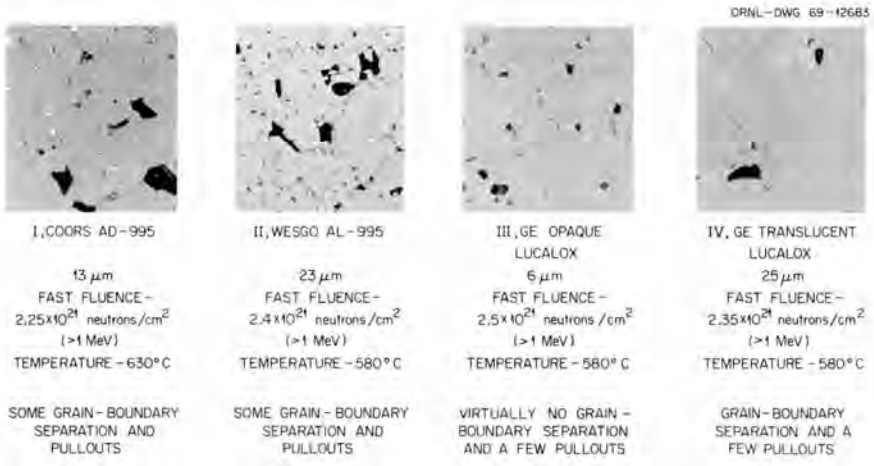

Fig. 16.2. Four Types of Commercial Alumina Irradiated under Comparable Conditions Showing Grain-Boundary Separation and Pullouts Resulting from Polishing (As-Polished Photomicrographs, 500X).

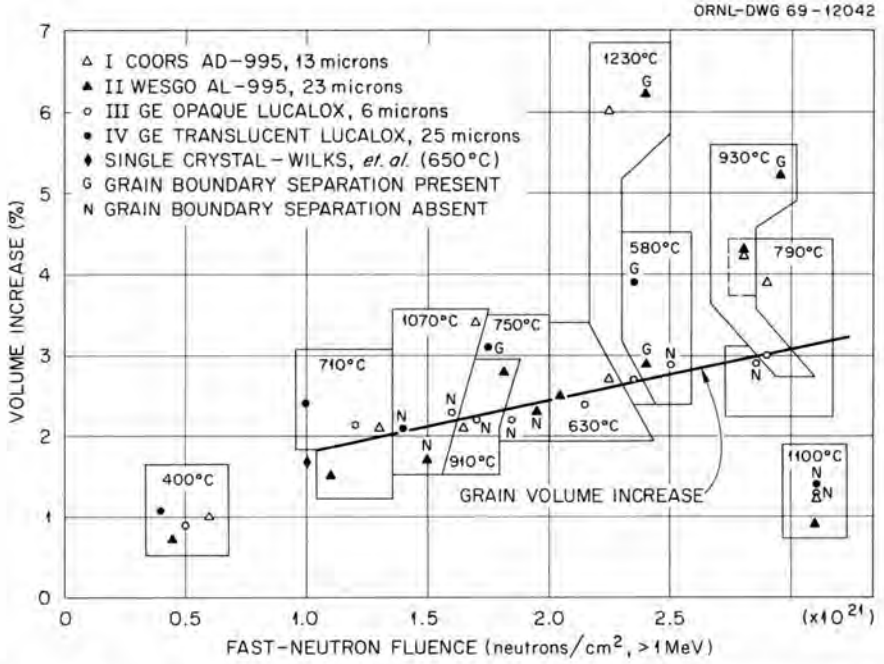

Fig. 16.3. Volume Increase of Four Commercial Types of Alumina after Irradiation at High Temperatures.

The specimens indicated by the symbols G or N in Fig. 16.3 were examined metallographically. No separation at the grain boundaries was found in the type III alumina. The line of Fig. 16.3 is drawn through the points where grain-boundary separation was absent. It is, therefore, representative of the increase in grain volume of alumina over the temperature range 580 to 1070°C as a function of fast fluence.

The datum point determined by Wilks et al.[5] for a single crystal of alumina at 650°C agrees with our line for grain volume increase. The single-crystal expansion at this temperature was anisotropic; the c axis of the crystal expanded much more than the a axis. The separation at the grain boundaries that was found for many of the polycrystalline specimens can be explained, therefore, by stresses on the grain boundaries that resulted from anisotropic expansion of the grains.

We concluded from these results that alumina to be used as a thermionic electrical insulator in a fast-neutron flux should be of high purity to minimize fracturing and of small grain size to minimize or eliminate separation at the grain boundaries.

Results of a Long-Term, High-Temperature Irradiation in the ETR

Irradiation assembly designated ORNL-41-39 was identical in every respect to assembly ORNL-41-38 except that it was irradiated in the ETR J-12 core position for a much longer period of time. The fast fluences received by specimens in ORNL-41-39 were about 2.4 times those received by corresponding specimens in ORNL-41-38.

Both the solid cylinders and the cylindrical shells in ORNL-41-39 were fractured to a greater extent than those in ORNL-41-38. Like those in ORNL-41-38, however, the specimens of higher purity alumina (types III and IV) were damaged less than those of the lower purity alumina (types I and II), and the least pure alumina (type I) was damaged more than the other three types.

The expansion in volume of specimens from ORNL-41-39 was about twice that of corresponding specimens from ORNL-41-38. A part of this additional expansion undoubtedly was due to an increase of grain volume

(i.e., an extension of the line for grain volume increase shown in Fig. 16.3). Some of it, though, is probably a result of additional separation at the grain boundaries caused by this increase in grain volume.

Irradiation in EBR-II

Solid cylinders and thin-walled shells of alumina of types I, II, and III were irradiated in row 4 of the EBR-II. The neutron flux in the EBR-II is nearly a pure fast flux in contrast to that of the ETR, which has a thermal component slightly greater than the fast component. The purpose of this irradiation was to separate the effects of fast- and thermal-neutron damage to these specimens of commercial alumina. Irradiation temperatures and neutron fluences for the specimens in this irradiation will be determined from analyses of temperature monitors and flux monitors that were included within the assembly.

The assembly, designated O-1, contained five solid cylinders and five shells each of the three types of alumina. Three solid cylinders and one shell of type I alumina fractured. All other specimens survived intact. The results for gross fracture are consistent with the results of the irradiations in the ETR in a mixed thermal and fast flux.

Type III alumina, as was the case in the ETR irradiations, expanded less than the other two types of alumina. The average volume expansion of alumina irradiated in the O-1 assembly was greater than in ORNL-41-38. A definitive interpretation of the results from assembly O-1 must await additional analytical and hot-cell work.

Metal-Clad Al_2O_3 Specimens

R. E. Moore[1] D. A. Dyslin[2] H. E. Robertson[1]

The present status of the irradiations of bilayers and trilayers is given in Table 16.4. Some of the results from the ORNL-41-40 irradiation experiment in the ETR were reported previously.[3] Experiment O-3, for irradiation in row 8 of the EBR-II, is being constructed.

Table 16.4. Irradiations of Bilayers and Trilayers

ORNL Experiment Number	Supplier	Design Temperatures (°C)	Fast Fluence [neutrons/cm^2 (> 1 Mev)]	Status
			$\times 10^{21}$	
41-40	NASA-Lewis Fairchild-Hiller Thermo Electron	600, 800, 1000, 1100	0.6–2.8	Complete except for metallography
41-42	Thermo Electron Gulf General Atomic	600, 800	(0.6–2.8)	Undergoing irradiation
0-3	Thermo Electron	700–800		Under construction

References

1. Reactor Chemistry Division.
2. General Engineering Division.
3. R. E. Moore, D. A. Dyslin, and H. E. Robertson, Fuels and Materials Development Program Quart. Progr. Rept. Sept. 30, 1969, ORNL-4480, pp. 188–195.
4. G. W. Keilholtz, R. E. Moore, D. A. Dyslin, and H. E. Robertson, Fuels and Materials Development Program Quart. Progr. Rept. June 30, 1969, ORNL-4440, pp. 114–116.
5. R. S. Wilks et al., The Irradiation-Induced Macroscopic Growth of α-Al_2O_3 Single Crystals, AERE-R-5460 (May 1967).

17. CORROSION STUDIES OF ADVANCED REFRACTORY METALS

W. O. Harms J. H. DeVan A. P. Litman

Requirements for auxiliary electricity or ion propulsion for space vehicles necessitate power plants of high efficiency that will operate at high temperatures. For these applications, nuclear power systems have been proposed in which alkali metals are used to transfer heat, drive a turbogenerator, and lubricate rotating components. Accordingly, we are investigating the corrosion properties of candidate alkali metals, primarily Li, K, and Na, under conditions of interest for space applications. Because of the relatively high temperatures (> 1000°C), the investigation is concerned largely with refractory-metal container materials.

Lithium Studies

J. H. DeVan A. P. Litman

Lithium Forced-Circulation Loop Experiments (W. R. Huntley,[1] C. W. Cunningham,[1] B. Fleischer)

Our program of forced-circulation Li loops is designed to gain information on cladding materials for fuel elements and containment materials for Li-cooled power systems. The first loop in this series (FCLLL-1) began operation this quarter and has completed 344 hr of the projected 3000 hr design life. The loop is constructed of T-111 and incorporates T-111 test specimens that will provide information on mechanical properties and mass transfer. Analysis of the Li immediately before operation of the loop showed < 5 ppm N and about 15 ppm O. The Li bulk-fluid temperature limits are 1370°C (2500°F) maximum and 1205°C (2200°F) minimum. These test temperatures are the highest that have been reached in any test with an alkali metal under forced circulation. The velocity of Li past internal stringers of corrosion specimens is about 15 ft/sec. The vacuum atmosphere surrounding the loop is now at a pressure of 6×10^{-8} torr.

We are constructing a replacement test section for the present loop that will permit us to investigate metal interactions between T-111, Li, and candidate W-base cladding materials. In this second test (FCLLL-2), the surface area of W-base materials will be small with respect to that of T-111, thus maximizing the corrosion of the W-base materials if interaction of dissimilar metals by migration of W-base materials is an important factor. This test will be run at the same temperatures and velocities as FCLLL-1.

Two field welds will be required to substitute the new test section into the test bed of the loop. To prepare for installation of the FCLLL-2 test section, we made a mockup of the field weld. A 1/2-in.-OD × 0.065-in.-wall thickness Li-filled tube oriented with its axis vertical was cut, and Li was cleaned out of the lower portion of the tube to a depth of about 2 in. from the cut edge with a manual drill and a scraper. The last trace of Li was removed from the inner wall by wiping with a damp cloth. No sparking or smoke was observed. A backup ring, which serves both as an alignment device and a filler material, was put in place, and a clean upper tube was then welded to the lower tube by means of automatic field-welding equipment. There was no evidence of Li contamination of the weld as determined by visual and metallographic examination of the weld. Visual examination of the Li 2 in. from the weld zone indicated that no melting had occurred during the welding process. To evaluate the resistance of this weld to corrosion, we shall expose it to static Li at 815°C (1500°F) for 100 hr.

The tubing material for fabrication of FCLLL-2 was included as part of the material order for FCLLL-1. To ensure that sufficient T-111 tubing of each size would be available, the extra 1-in.-OD × 0.065-in.-wall-thickness tubing that remained after fabrication of FCLLL-1 was converted to 7/8-in.-OD × 0.060-in-wall-thickness and 1/2-in.-OD × 0.060-in.-wall-thickness tubing by the Materials Processing Group of the Metals and Ceramics Division.

Manufacture of the specimens and specimen holders is about 90% complete. We have received all the T-111 specimen holders and shims and are bright etching them to remove burrs. The ASTAR 811C and T-111 specimens were machined and inspected and are awaiting bright etching. The

chemically vapor deposited W tubular specimens were bright etched and annealed and are ready for marking and characterization. The remainder of the W-base specimens are being machined and are expected to be delivered early in January.

References

1. Reactor Division.

PART III

GENERAL REACTOR TECHNOLOGY

FUELS

18. FISSION-GAS RELEASE AND PHYSICAL PROPERTIES OF FUEL MATERIALS DURING IRRADIATION

O. Sisman[1]

The purpose of this work is to measure the variables that control the release of fission gas from highly characterized nuclear fuels and to evaluate these variables in terms of a generalized model for predicting release from operating fuel materials. Thermal diffusivity is measured in-reactor in analogous experiments.

Measurements of Thermal Diffusivity in UO_2 During Irradiation

R. M. Carroll[1] R. B. Perez[1]

Our last report on this subject was somewhat pessimistic.[2] The general prospects now, however, look good. The problem was that the temperature response to a step change in fission rate could not be entirely fitted to a curve described by two constants and a single exponential. A reasonable fit could be obtained if the first 2 min of the heating curve were ignored, but we found that the correction factors that had to be applied were then so large that they outweighed the data.

The entire data curves (except for the first several seconds) could be fitted by an equation containing three constants and two exponentials. There are, however, a number of different combinations of constants and exponentials by which a given data curve can be fitted. We had a collection of data that looked very good, but our mathematical processes for extracting values of thermal diffusivity had not worked.

A method of obtaining a unique fit to the heating curve has now been devised by P. R. Coleman of the ORGDP Computing Center. Since we had already obtained a fit with two constants and a single exponential for each heating curve, ignoring the first 2 min, we used a stripping process on the ignored portions of the heating curve and a second fit

with a single exponential equation for the first 2 min of the curve. A combination of the two equations results in a fit of the data with two exponents. All the data curves have now been fitted in this manner; for a typical example, see Fig. 18.1.

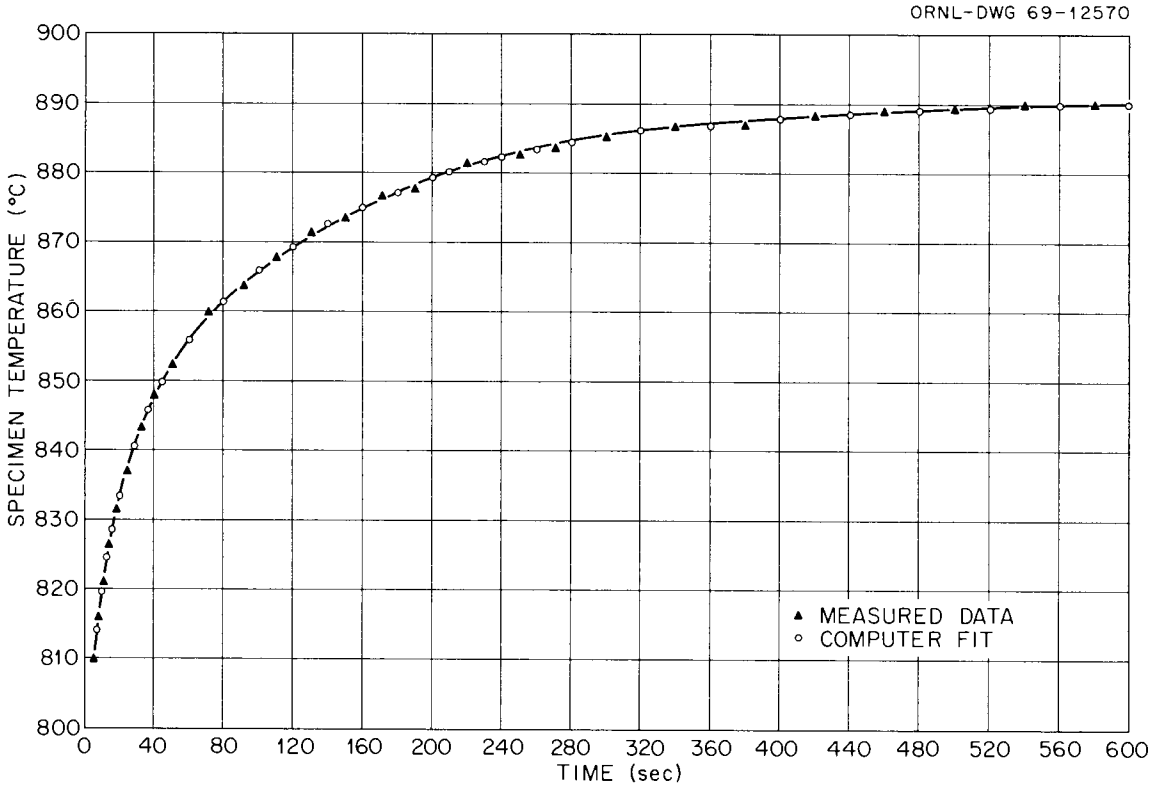

Fig. 18.1. Typical Computer Fit to Heating Curve.

In the meantime, a general theory of time-dependent heat-diffusion phenomena was developed.[3] This shows the feasibility of measuring the thermal diffusivity with a single temperature measurement and without the necessity of measuring the power input. For the general case, the value of the thermal diffusivity is obtained by iteration of three transcendental equations. The parameters needed for the calculation are the two lowest time-eigenvalues observed in the temperature-time curves and the material properties of the region surrounding the specimen.

The computer program for obtaining the values of thermal diffusivity is now being debugged. We are optimistic that the method will work and

that the accumulated data can be evaluated to obtain relative changes in the thermal diffusivity as a function of both temperature and irradiation level.

Release of Fission Gas From UO_2

R. M. Carroll[1] R. B. Perez[1]

A cylindrical specimen of large-grained UO_2 (ref. 4) was used primarily to obtain data on thermal diffusivity. However, the fission-gas release was also measured whenever it was feasible. The fission gas was released from the specimen in a manner typical of high density UO_2; that is, there was a slight reduction in the amount of fission gas released as burnup progressed, and the gas was released by a coupled trapping-diffusion process.

While the thermal data were being obtained, the specimen was irradiated to a burnup of 1.7×10^{19} fissions/cm^3 at temperatures from 500 to 1150°C. There was no cracking during this period. We wished to irradiate the specimen at higher temperatures to see the effect of grain growth on the release of fission gas from this type of specimen, but the specimen began to crack when the temperature was raised to 1350°C. The cracking of a specimen during irradiation is evidenced by bursts of released gases of long half-lives and by an increased surface area, which can be detected by low-temperature gas release. Since the subsequent gas release was a function of the amount of cracking rather than the fuel characteristics, the specimen was removed from the experimental facility.

Behavior of Sol-Gel $(U,Pu)O_2$ During Irradiation

R. M. Carroll[1] R. A. Bradley H. E. Robertson[1]

About 100 crack-free microspheres were selected from batch PUM-4-1,3 by use of an inspection microscope and vacuum tweezers. The microspheres were radiographed, and 50 of the particles were measured on a microscope with a Cooke image-splitting eyepiece. The mean diameter was 546.4 μm; the standard deviation was 17.4 μm.

The microspheres were heat treated in a W crucible at 1450°C for 11 hr in an Ar–4% He atmosphere. Three pellets, heat treated along with the microspheres, had O:metal ratios of 2.012, 2.006, and 2.007. A photograph of the treated microspheres is shown in Fig. 18.2.

Fig. 18.2. Sol-Gel Microspheres. 17×.

These spheres are 17.35% Pu and 71.61% U by weight. The U is 99.3% ^{238}U, and the Pu is 90.52% ^{239}Pu, 0.828% ^{241}Pu, and 8.58% ^{240}Pu. The spheres have a density of 10.8 g/cm^3.

Capsule C1-27 was loaded with 51 of the microspheres arranged to form a hollow cylinder as shown in Fig. 18.3. This specimen was inserted into the Oak Ridge Research Reactor (ORR) during the November midcycle shutdown.

The mixed oxide specimens we have irradiated in the past[4,5] have had small, interconnected passages that allowed the fission gas to trickle out. As irradiation progressed these passages would, to some extent,

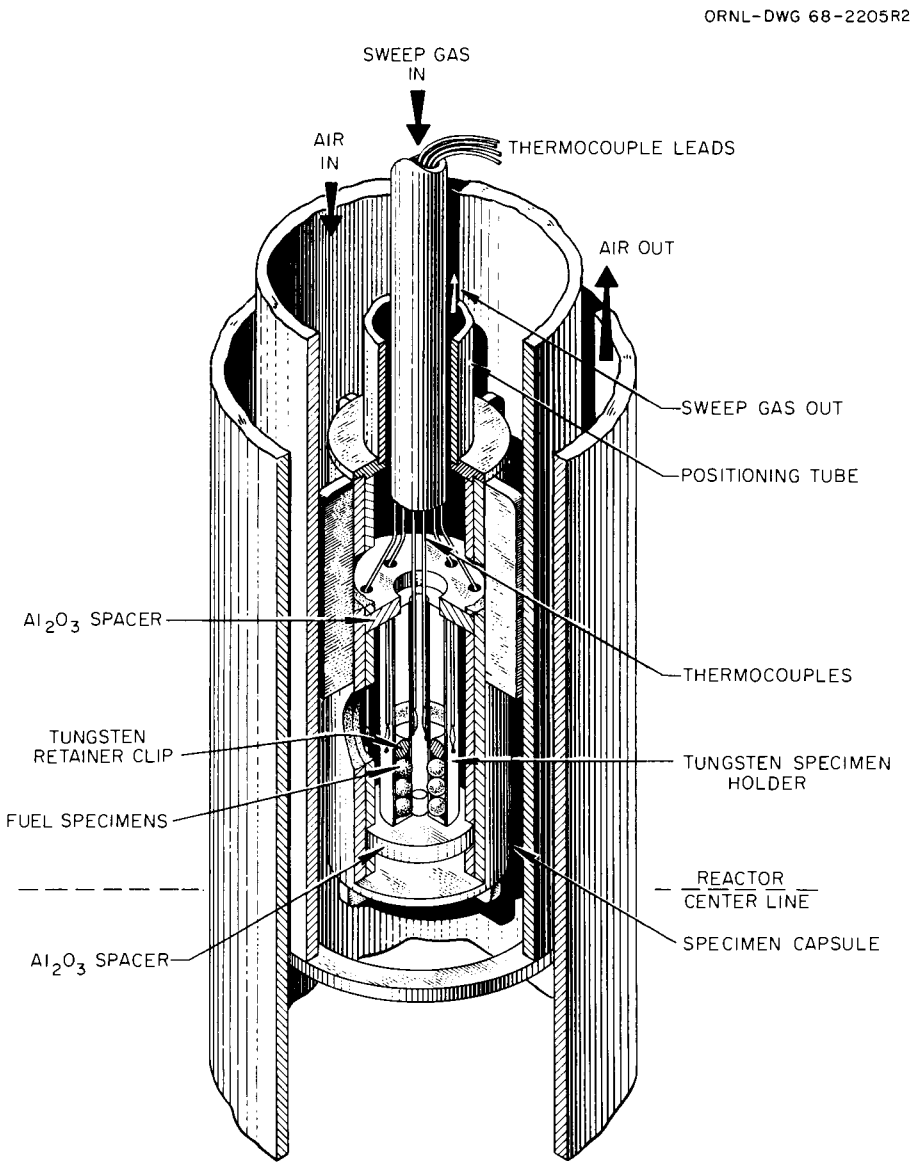

Fig. 18.3. Schematic of Sol-Gel Irradiation Capsule.

become sintered closed by fission spike sintering. This resulted in a greatly lowered rate of release of fission gas. The generated gas was trapped in closed pockets. The resultant fuel was fragile, and thermal shock caused by rapid heating or cooling would rupture some of the pockets and cause bursts of gas release. As burnup progressed, enough gas pressure developed within the fuel to cause breakaway gas release. At this point, swelling of the fuel is also presumed.

To determine whether the sol-gel specimens were as porous as the sintered specimens we previously examined, we started the present

irradiation at low temperatures at which most of the release is from surface fissions. Under these conditions, the amount of gas release gives the relative amount of interconnected surface area. Because of the low power level of the irradiation (and several long reactor shutdowns) the specimens have not accumulated much burnup or been at temperatures over 700°C. However, a preliminary evaluation of the data shows that the sol-gel fuel emits about four times as much fission gas as the sintered material at low temperatures. This has not been corrected for surface area or surface-to-volume ratio; however, the difference in these factors between the sintered and sol-gel material cannot account for the magnitude of the difference in the rate of gas release. The gas release is not dependent on temperature below 700°C and appears to be going down somewhat as irradiation progresses. There is no indication of the interconnected porosity that characterized the previous specimens, and no cooling bursts were caused by mild thermal shocks.

References

1. Reactor Chemistry Division.
2. R. M. Carroll and R. B. Perez, Fuels and Materials Development Program Quart. Progr. Rept. Sept. 30, 1969, ORNL-4480, pp. 209–211.
3. R. B. Perez, R. M. Carroll, and O. Sisman, The Theory of a Time-Dependent Heat Diffusion Determination of Thermal Diffusivities with a Single Temperature Measurement, ORNL-4478 (in press).
4. R. M. Carroll, Fuels and Materials Development Program Quart. Progr. Rept. March 31, 1969, ORNL-4420, pp. 72–74.
5. R. M. Carroll, Fuels and Materials Development Program Quart. Progr. Rept. June 30, 1969, ORNL-4440, pp. 56–58.

19. DEVELOPMENT OF FUEL ELEMENT FABRICATION

G. M. Adamson, Jr.

The purpose of these programs is to devise new combinations of materials or new fabrication techniques to advance the technology for fabricating fuel elements and components for research reactors. We are attempting to improve the performance of advanced research reactors, such as the High Flux Isotope Reactor (HFIR) and Advanced Test Reactor (ATR), by developing fuel elements with lower production cost, longer lives, increased safety or reliability, or all three. The studies include factors affecting both fabrication and irradiation performance. We must also develop sufficient knowledge of the processes used for fabricating Al-base dispersion fuel elements so that we can adequately assist commercial fabricators, purchasers, specification writers, and technical inspectors. Other studies are aimed at improving the reliability and reducing the cost of the required nondestructive inspection techniques.

Irradiation Studies

W. R. Martin

Evaluation and Design of Cermet Fuel-Plate Irradiation Experiments

(M. M. Martin, W. K. Crowley[1])

We have decided to use position VXF-17 of the HFIR for our irradiations of Al-base fuel. We previously reported[2] the pertinent conditions for the VXF-6 and -19 positions, which are located similarly to VXF-17 in reference to the center of the active core. Thus, our preliminary design and analyses apply directly to position VXF-17.

Precise flux profiles for the VXF-17 position are required, however, before we can complete the initial design of the holder for irradiating the test plates. We designed and fabricated a flux-wire holder assembly to measure the flux and fission density. The design allows us to determine both the axial and radial flux shapes.

The flux-wire measurements are scheduled for the reactor cycle following the shutdown January 28. Since the flux normally increases during the cycle, we plan to make three determinations to cover the beginning, middle, and end of the life of the reactor core. After the wires are exposed, the analysis will require one week. We anticipate that decisions on the final design of the flow channels and the flow rate for the coolant water can be made by the second week in March.

In the interim, we shall complete phase two of the design of the holders for the test plates and instrumented fuel plates. We have finished the conceptional design, phase one, using a modular assembly for the irradiation experiment. Each module will contain three test fuel plates arranged in layers from the center of the reactor core. Coolant water will flow between the plates. The assembly to be irradiated will consist of six such modules stacked vertically and attached to a thermocouple-holder channel that will hold three instrumented fuel plates.

Postirradiation Examination of Miniature Fuel Plates and Burnable-Poison Test Plates (A. E. Richt, M. M. Martin)

This quarter, 25 miniature fuel plates and 6 miniature burnable-poison test plates were returned to ORNL for postirradiation examination and evaluation. These specimens were from the ORNL 69-1, 69-2, 69-3, 70-1, and 70-2 irradiation test experiments that were exposed in the G-12 loop of the Engineering Test Reactor (ETR) to study (1) the effects of the size of fuel particles on the irradiation performance of burned, high-fired, and sol-gel U_3O_8-Al dispersions, (2) the behavior of electrolessly deposited Ni coatings on fuel plates clad with types 6061 and 2219 Al, and (3) the irradiation performance of Al-clad B_4C-Al dispersions.[3] Although the examination programs are as yet incomplete, some preliminary results are summarized in the following sections.

Visual examination of the fuel plates from the ORNL 69-1 and 69-2 experiments showed all eight test plates to be in excellent physical condition. No indications of blistering or other gross damage were apparent. The six uninstrumented plates have been chemically cleaned of film, measured to determine the changes in the volume of the fuel

core, and prepared for metallographic examination and burnup analysis. Metallographic examination of sections of these specimens was delayed by budgetary restrictions, but results of the other examinations are summarized in Table 19.1. In general, these results indicate that the size of the fuel particles (the fines content) has little or no effect upon the swelling induced by irradiation in either the burned or high-fired U_3O_8-Al dispersions. As expected from consideration of the initial content of voids, plates fueled with the burned grade of U_3O_8 swelled significantly less than plates fueled with the high-fired type of U_3O_8, even though the burned U_3O_8 plates were exposed to slightly higher levels of burnup.

Table 19.1. Summary of Test Results[a] on Miniature Fuel Plates Irradiated for 9995 Mwd in the G-12 Loop of the Engineering Test Reactor

Specimen Number	Core Loading (wt %)	Fines Content (%)	Initial Core Voids (%)	Specimen Burnup (fissions/cm^3)	Change in Core Volume, %	
					Measured	Predicted
				$\times 10^{20}$		
			High-Fired U_3O_8			
0-67-974	40	10	3.2	17.9	+4.71	+8.1
0-67-982	40	25	2.8	18.0	+5.05	+8.6
0-67-986	40	51	2.8	18.0	+6.15	+8.7
			Burned U_3O_8			
0-68-997	49	10	9.8	19.7	+3.57	+2.6
0-68-1605	49	26	10.0	19.9	+3.04	+2.6
0-68-1607	49	54	10.0	19.5	+3.11	+2.3

[a] ORNL experiments 69-1 and 69-2.

Examination of the eight fuel plates from the ORNL 69-3 experiment revealed that one of the fuel plates (0-68-1635) was warped and had a small crack along one side of the cladding and frame. This damage apparently resulted from difficulties in unloading the specimens from the loop holders and not from irradiation. The other seven specimens appeared to be in excellent condition except for the almost complete

loss of the electrolessly deposited Ni coatings originally applied to the surfaces of six of these plates. Only small traces of the Ni coating remained along the sides of the plates protected from the coolant by the specimen holders. Changes in the weight, volume and core volume of the specimens, and analytically determined values for burnup for the six uninstrumented plates in this experiment are summarized in Table 19.2. The changes in weight and volume indicate the loss of the Ni coatings from the four coated plates. The measured swelling of the fuel core appears consistent with the expected swelling if we consider the initial content of voids in the cores and the levels of burnup. Some uncertainty remains as to when the Ni coatings spalled from the surfaces of these six plates. Since all the plates in this experiment were exposed to an accidental temperature excursion shortly after the test loop was shut down,[4] it is possible that the spalling occurred at that time. However, analysis of the temperature histories of the two instrumented plates in this test strongly indicates that the coatings spalled soon after the reactor reached full power at the start of irradiation.

The eight miniature fuel plates and six burnable-poison plates from the ORNL 70-1 and 70-2 experiments received an exposure of only 168 Mwd before the G-12 loop facility was ordered to shut down. Consequently these specimens received essentially no significant burnup. Recently, however, we have become interested in the behavior of fuel and absorber dispersions in the early stages of irradiation. Idaho Nuclear Corporation has reported some large decreases in volume in fuel dispersions that had high initial void content and were irradiated to relatively low levels of burnup under certain irradiation conditions.[5] Therefore, we decided to examine our specimens nondestructively to obtain additional data about the swelling behavior of dispersion fuels in the early stages of irradiation. The 12 uninstrumented plates from these two experiments were chemically cleaned of film, and the changes in core volume were determined by immersion density methods. The results shown in Table 19.3 indicate no significant changes in core volume in the B_4C-Al dispersions. Plates fueled with the sol-gel type of U_3O_8 showed less shrinkage of the core volume than plates fueled with

Table 19.2. Summary of Test Results[a] on Miniature Fuel Plates[b] Irradiated for 4430 Mwd in the G-12 Loop of the Engineering Test Reactor During Cycle 102A

Specimen Number	Type Aluminum Cladding	Initial Core Voids (%)	Specimen Burnup (fissions/cm^3)	Specimen Weight Change (g)	Change in Volume, %		
					Specimen	Core	
						Measured	Predicted
			$\times 10^{20}$				
0-68-1633	6061	9.3	12.7	+0.047	+0.94	+0.43	−1.3
0-68-1635	6061	9.4		+0.017	+0.09		
0-68-1636	Ni-coated 6061	9.4		−1.290	−2.34		
0-68-1638	Ni-coated 6061	9.4	12.7	−1.324	−2.82	+0.38	−1.3
0-68-1642	Ni-coated 2219	7.3	12.7	−1.270	−2.29	+1.66	+0.7
0-68-1643	Ni-coated 2219	7.5		−1.275	−2.34		

[a] ORNL experiment 69-3.

[b] All specimens fueled with 49 wt % burned U_3O_8 dispersed in Alcoa type 101 Al. Weight of Ni initially on fuel-plate surfaces was calculated to range from 1.23 to 1.25 g.

Table 19.3. Summary of Test Results[a] on Mini-Type Fuel Plates Irradiated for 168 Mwd in the G-12 Loop of the Engineering Test Reactor

Specimen Number	Core Loading (wt %)	Fines Content (%)	Initial Core Voids (%)	Change in Core Volume, %	
				Measured[b]	Predicted
		B_4C-Al Compacts			
0-83-1677	0		0.32	−0.12	−0.32
0-84-1681	0.52		0.29	−0.12	−0.29
0-85-1687	0.78		0.29	−0.04	−0.29
0-86-1691	1.05		0.34	−0.01	−0.34
0-87-1697	1.75		0.32	−0.04	−0.32
0-88-1901	3.00		0.34	−0.16	−0.34
		U_3O_8-Al Compacts			
0-89-1647	51[c]	0	3.61	−0.36	−3.6
0-89-1657	51[c]	50	4.40	−0.42	−4.4
0-89-1907	51[c]	10	3.34	−0.31	−3.3
0-90-1662	53[d]	11	9.64	−0.99	−9.6
0-90-1666	53[d]	26	9.37	−1.02	−9.4
0-90-1671	53[d]	54	9.64	−1.74	−9.6

[a] ORNL experiments 70-1 and 70-2.

[b] Assuming essentially zero burnup.

[c] Sol gel.

[d] Burned.

the burned grade of U_3O_8. The size of the fuel particles (the fines content) appears to have no effect upon shrinkage of the sol-gel dispersions, but increasing the amount of fines in the burned U_3O_8 dispersions apparently results in a greater or more rapid decrease in core volume in the early stages of irradiation. All 12 specimens were placed in temporary storage pending the projected continuation of the irradiation test program in the HFIR.

Fuel plate 0-56-957 from the ORNL 68-1 experiment was also received this quarter. It was fueled with 50 wt % high-fired U_3O_8, of which 3% was fines, and originally contained 3.7% voids. This plate received an exposure of 16,676 Mwd and achieved a burnup of 22.4×10^{20} fissions/cm^3. The fuel plate appeared to be in excellent physical condition with no

indications of actual or incipient failure. The fuel core increased 7.6 vol % as compared to a predicted 10.4 vol %.

As reported previously,[6] differences in the swelling behavior of a large number of miniature fuel plates irradiated in the G-12 loop of the ETR could be explained by differences in their initial void content. We have calculated the amount of swelling that should have occurred in this most recent group of fuel plates in the same manner and compared these calculated values with the measured values. As shown in Fig. 19.1, agreement between the calculated and measured values is relatively good;

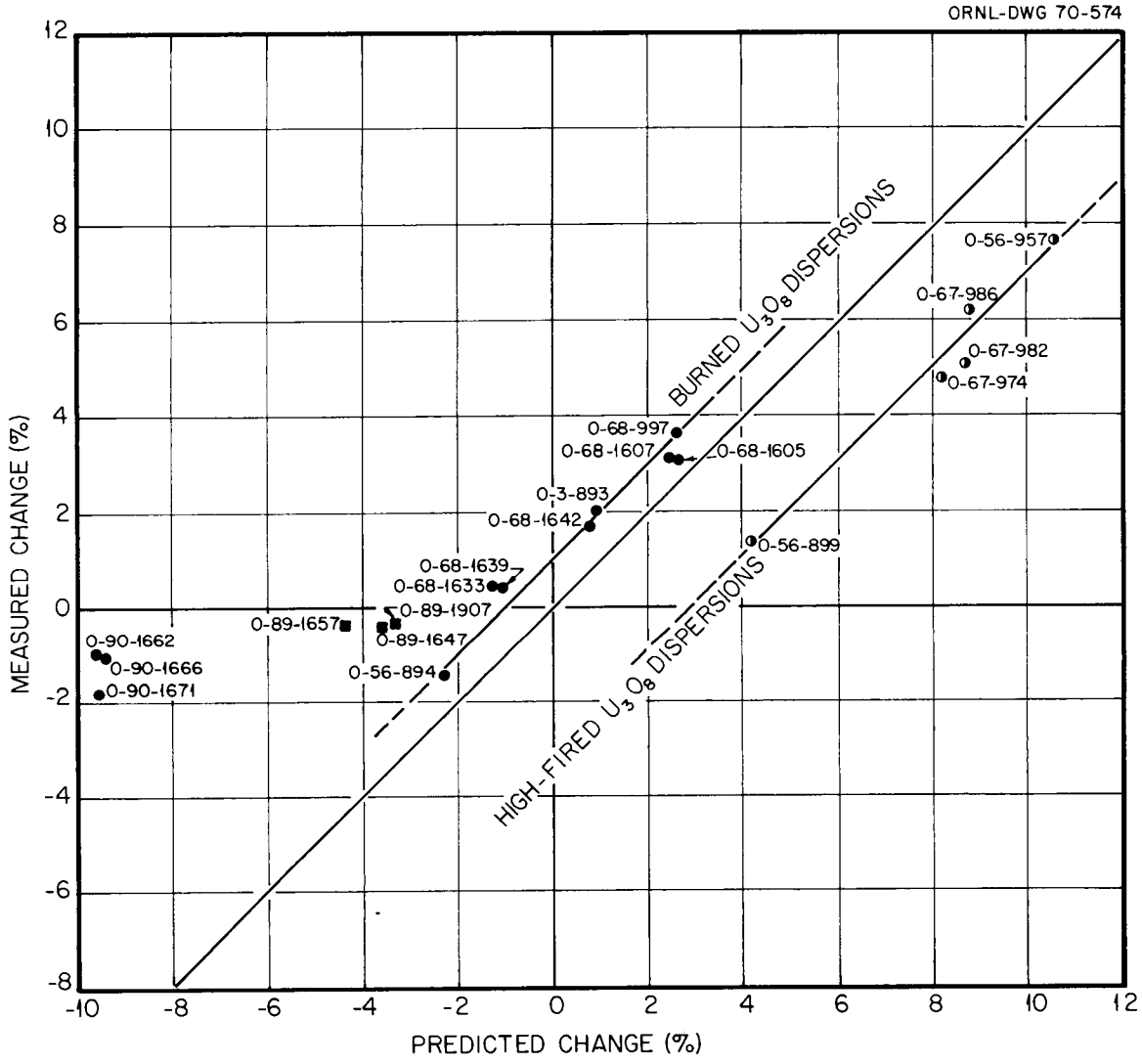

Fig. 19.1. Comparison of Predicted and Measured Changes in Core Volume in Irradiated Miniature Aluminum-Dispersion Fuel Plates.

however, plates fueled with the burned type of U_3O_8 consistently swelled about 0.8% more than predicted, whereas plates fueled with the high-fired type of U_3O_8 consistently swelled about 2.5% less than predicted. The cause of this discrepancy is unknown. The fact that the swelling lines for both types of oxide are parallel to the normal curve indicates that the assumed intrinsic swelling rate of these fuels is correct. This suggests that the assumed void content of the dispersions is in error. If one assumed that the initial void content of the burned U_3O_8 dispersions were 1% less than the calculated values, the values calculated and measured for swelling would be in almost perfect agreement. Since the burned U_3O_8 dispersions generally contain about 10% voids, it is conceivable that 1% of the voids might be present in the matrix of the fuel core and thus unavailable to accommodate fuel swelling. However, such an explanation is not applicable to the high-fired U_3O_8 dispersions. To obtain good agreement between calculated and measured swelling values for these dispersions, it is necessary to assume that these dispersions initially contained about 5.5% voids instead of the measured 3% voids. Additional work will be required to resolve this problem.

Technical Assistance for Commercial Manufacturing and Inspection Problems

W. R. Martin

Chemical Preparation of Type 6061 Al Surfaces for Roll Bonding (J. H. Erwin)

We are evaluating a process of chemical cleaning for preparing the surface of unclad type 6061 Al for the roll bonding of reactor fuel plates. After all grease is removed from the Al parts, they are submerged for 2 min in a solution of 10 oz Oakite 160 per gallon of water at about 74°C and then rinsed in water and cycled through 60 to 65% HNO_3 and water to remove all traces of smut. An alcohol rinse is then used to remove the water.

Since this chemical process is being used more frequently in the commercial preparation of unclad type 6061 Al parts for roll bonding and since process limits have not been published, we investigated the effects of the following variations from the standardized procedure on the resultant roll-bonded interface:

Etching Solution	
Ratio of Oakite 160 to water, oz/gal	2.5–10.0
Temperature, °C	54–82
Time of treatment, min	2–15
Inhibition, g dissolved Al/gal	0–170
Deoxidizing Solution	
Agent	Nitric acid or Oakite 34 deoxidizer
Nitric acid solution	
Strength, %	28–70
Bottle strength, %	40–100
Time of final treatment, min	2–15
Exhaustion, ft^2 of Al treated	0–1500
Temperature of water rinse, °C	24–74
Billet storage after cleaning, weeks	1 or 2
Rolling temperature, °C	400 or 500

We prepared ten billets for evaluating each variable. These billets were rolled into plates under fabrication conditions similar to the standards adopted for the production of HFIR fuel plates. Each plate was inspected for blisters and sampled for interfacial grain growth. The following procedures were used.

1. Simulated, unpunched frames, 1/4 in. thick, and cover plates, 1/8 in. thick, were sheared to 5 in. wide by 8 in. long from commercial type 6061-T6 Al plate.

2. Contamination in the form of a thin Ni coating on the surface of the as-received 1/4-in.-thick plates was removed by a 1/2-min submersion in the Oakite etching bath followed by a rinse in hot water and a rinse in nitric acid.

3. The stock was then heated 2 hr at 490°C, air cooled, and inspected for blisters.

4. Ten 1/4-in.-thick plates and twenty 1/8-in.-thick cover plates were chemically cleaned in six batches of five plates per batch.

5. The cleaned 1/4-in. plates were heated 35 min at 490°C in a furnace.

6. A 1/8-in.-thick cover plate was applied to either side of each hot frame, and the assembly was then tungsten-arc welded around the edges to within about 3/4 in. of each corner under an Ar atmosphere.

7. The billets were heated 45 min and rolled with a 12-in. two-high mill to a thickness of 0.065 in. at mill settings that produced reductions of 13, 15, 20, 24, 25, 25, 25, 21, 10, and 5% per mill pass. The billets were reheated after each mill pass.

8. The hot-rolled plate was annealed 1 hr at 490°C and cold rolled to 0.052 in. thickness using 6 mill settings and 24 mill passes.

9. The cold-rolled plate was annealed 2 hr at 490°C and furnace cooled to 100°C.

10. When cold, the plates were thoroughly inspected for blisters. The locations of all blisters were noted.

11. Each plate was divided into three approximately equal lengths for sampling. From opposite ends of the central plate section, two 1-in.-long samples were cut to examine the bond interface transverse and parallel to the rolling direction.

12. The polished samples were anodized to obtain color distinction with the use of half-wavelength light.

13. With the aid of a 0.040-in.-long micrometer in an eyepiece on a standard metallograph, we obtained the relative length of interface with and without grains common to the cladding and frame. From the 40 in. of sample representative of each process condition, we obtained about 950 measurements.

A summary of the number of blistered plates and the data for grain growth are shown in Table 19.4. Several blisters developed on the plates from billets deoxidized with Oakite 34, but only four plates blistered from the billets treated with nitric acid. These four plates

Table 19.4. Evaluation of Interfacial Bonds of Type 6061 Aluminum in Simulated Fuel Plates Rolled from Chemically Cleaned Frames and Cover Plates

Experimental Variables	Number of Plates with Blisters	Interfacial Grain Growth, %			Distribution of Grain-Growth Values						
		Average All Samples	Individual Samples		Number of Measured Increments	Percent of Total with Indicated Value					
			Maximum	Minimum		Full	> 75%	> 50% < 75%	> 25% < 50%	< 25%	None
Etching condition											
2.5 oz Oakite 160/gal water	0	87	92	78	946	27.5	86.0	11.6	2.0	0.4	0.0
5 oz Oakite 160/gal water	0	86	92	79	946	30.8	83.5	13.1	3.0	0.4	0.0
10 oz Oakite 160/gal water[a]	0	91	100	69	941	74.0	89.5	6.9	2.2	1.4	0.7
2.5 oz Oakite 160/gal water, inhibited with 31 g Al/gal	0	82	92	64	948	23.6	73.2	19.8	5.9	2.1	0.7
10 oz Oakite 160/gal water, inhibited with 170 g Al/gal	0	76	82	68	510	16.7	63.2	23.9	9.8	3.2	0.4
10 oz Oakite 160/gal water, etching time extended to 15 min	0	88	96	81	955	43.5	84.7	11.4	3.3	0.4	0.0
10 oz Oakite 160/gal water, 54°C	1	75	85	67	927	19.1	64.5	20.5	11.1	4.0	1.3
10 oz Oakite 160/gal water, 82°C	1	75	87	63	945	19.7	61.5	24.3	10.0	4.1	1.3
Deoxidation conditions											
40% HNO_3 (bottle), 5 min	0	87	93	73	990	36.5	84.0	12.2	2.7	1.1	0.2
60% HNO_3 (bottle), 5 min[a]	0	91	100	69	941	74.0	89.5	6.9	2.2	1.4	0.7
100% HNO_3 (bottle), 5 min	0	82	93	76	963	29.1	73.6	18.9	5.6	1.9	0.6
60% HNO_3 (bottle), 15 min	0	82	91	69	935	40.0	76.8	14.2	7.4	1.6	0.5
60% HNO_3 (bottle), 2 min	0	85	94	71	966	41.4	80.9	13.0	4.2	1.9	0.5
60% HNO_3 (bottle), 2 min (previously used for 90 plates)	0	93	100	81	942	72.7	90.3	7.0	2.2	0.5	0.0
60% HNO_3 (bottle), 2 min (previously used for 250 plates)	0	87	92	80	920	37.4	83.2	14.1	2.0	0.7	0.1
10 oz Oakite 34/gal water	7	58	73	43	910	10.7	36.8	25.4	23.2	14.6	4.8
Rinsing											
Etchant removed by cold (rather than 74°C) water rinse	1	77	85	68	964	19.0	65.9	22.1	9.7	2.3	0.4
Storage of cleaned plates											
Plates cleaned and stored 1 week before rolling	0	86	91	77	959	31.6	85.0	12.1	2.6	0.3	0.0
Stored 1 week, welded, stored another week before welding	1	78	91	61	978	19.2	69.1	20.8	8.0	2.1	0.2
Rolling temperature											
400°C	0	88	98	73	960	33.1	86.1	11.0	2.1	0.8	0.1
450°C	0	87	96	70	940	40.4	84.9	10.2	4.0	0.9	0.2

[a]Standard procedure.

were from four groups: billets etched with Oakite solution at 54 or 82°C, billets rinsed with cold water, and billets stored for two weeks before rolling. The blistered plate groups exhibited an average interfacial grain growth of less than 80%, and only one other group that exhibited similarly low grain growth failed to produce blisters. Greater than 80% grain growth was found in all the other plates. The maximum and minimum percentages for the individual samples generally follow the same relationship as the average, as one would expect; however, the plates cleaned with etching solution at 54°C showed a minimum grain growth of 67%, and plates rinsed with cold water showed a minumum of 68%. Both of these plates blistered, while plates that exhibited about the same or less grain growth from other cleaning treatments did not blister. For further clarification of the effects of the process deviations, the distribution of values for individual measurements of grain growth is given. The plate groups that had greater than 75% grain growth in less than 70% of the individual measurements also produced blistered plates with the exception of the group cleaned with the 10:128 Oakite solution inhibited with 170 g Al/gal. The distribution of grain-growth values for the other plate groups is about the same if the comparison is made at the 75% level.

The average grain growth at the interface of two pieces of type 6061 Al compares favorably with the average value of 89% previously reported[7] for the interface between types 1100 and 6061 Al when the parts were processed in the same manner according to the standard process. Examination of the data for grain growth reveals some deterioration in the quality of bond produced as a result of (1) extended use of the etching solution, (2) extreme deviation in the temperature of the etching solution, (3) removal of the etching solution by a cold-water rinse, and (4) extended storage of the cleaned billets before rolling.

The strength of the etching solution appears to be important only from the standpoint of inhibition: the different concentrations of Oakite 160 perform equally well, but the accumulation of Al in solution diminishes the reactivity of the solution at a rate approximately

proportional to the concentration. Weak, new solutions clean better than strongly inhibited solutions that are two or three times more concentrated as shown by the manufacturer's recommended chemical tests.

The reactivity of the Oakite 160 solution is affected by the temperature. Temperatures below 74°C appear to increase etching time, but 82°C produces an extreme reaction rate that is hard to control and may make plates more difficult to deoxidize.

Cold water appears less effective than hot water for removing the Oakite residue. However, extreme caution must be taken to prevent any drying of the surface during transfer of the parts to the nitric acid treatment.

Since the surface produced on the cleaned parts is passive, reasonable storage does not appear to affect it significantly.

Parametric Study of the Deformation of U_3O_8- and UAl_x-Al Dispersion Fuel Plates (M. M. Martin)

We continued our investigation of nonuniform deformation (dogboning) and our parametric study of the densification of U_3O_8-Al and UAl_x-Al dispersions that contain about 41 vol % of fuel compound. During this reporting period, we roll bonded the 44 fuel compacts described previously.[8] As prepared for bonding, the compacts varied between 82.1 and 94.2% of theoretical density depending on the type of fuel compound, the compacting pressure, and the degassing treatment. To determine the effect of the various initial compact densities upon deformation, the cladding billets are being examined for (1) dogboning by x-ray attenuation after each hot-rolling pass and after the second, fourth and sixth mill setting of the cold-rolling schedule and (2) core density after hot rolling and annealing, cold rolling, and final annealing.

We roll bonded four identical compacts to type 6061 Al for each of the 11 combinations of fuel compound, pressing pressure, and degassing temperature.[8] Each group of compacts was assembled into a single rolling billet, and then all were simultaneously roll bonded into four fuel plates. Based on measurements of billet thickness at room temperature after each hot pass, their hot reductions per pass in chronological sequence averaged 15.1, 14.7, 23.5, 23.6, 24.4, 23.1, 16.7, 14.0,

and about 7.3%. At this stage in fabrication, the total hot reduction of 83.6% yielded plates about 0.0619 in. thick.

After we measured the density of the plates following the hot rolling and annealing, we reduced them an additional 18.9% in thickness at room temperature by means of four rolling passes at each of six mill settings of 0.059, 0.057, 0.055, 0.053, 0.051, and 0.050 in. To complete the fabrication, we annealed the cold-rolled plates 3 hr at 490°C and then slowly cooled them to produce the "O" temper condition in the type 6061 Al cladding.

The densities of the clad dispersions were determined at various stages of fabrication by conventional pycnometer techniques and calculated from the density of the type 6061 Al cladding. Based on the theoretical densities of 5.2261 and 4.3313 g/cm^3 for the 71.6 wt % U_3O_8-Al and 67.2 wt % UAl_x-Al cores, respectively, we then calculated their void contents, which are shown in Table 19.5. In general, the hot-rolling-and-annealing operation decreased the void content of the prepared compacts to about 7 vol % regardless of either the pressed or degassed densities. The subsequent cold-rolling reductions increased the void content. The compacts pressed at 50 tsi are the noted exceptions to the first generalization. Surprisingly, it appears that the equilibrium void content of these hot-rolled-and-annealed cores is slightly greater than that of the pressed compacts.

As shown in Table 19.5, the UAl_x-Al compacts pressed at 30 tsi and degassed at 500°C also deviate from the norm. These compacts consistently contained about 2 vol % more voids after the hot- and cold-rolling operations than would be expected. We note that the transformation of the UAl_x, induced by diffusion during the degassing operation, caused the large increase in the void content of the degassed compacts. Gregg *et al.*[9] demonstrated with the aid of a heating-stage metallograph that swelling of UAl_x-Al compacts begins with fine cracks in the fuel compound soon followed by the growth from the cracks of a striated structure that simply forces apart the unbonded particles of the Al matrix. The reactions produce a heavily fragmented and brittle fuel particle. It is possible that the fragmentation of the fuel particles during this

Table 19.5. Concentration of Voids in 71.6 wt % U_3O_8-Al and 67.2 wt % UAl_x-Al Dispersions at Various Stages of Fabrication

Pressing Pressure (tsi)	Degassing Temperature (°C)	Average Concentration of Voids, vol %					
		Compacts		Cores			
		Pressed	Degassed	Hot Rolled and Annealed	Partially Cold Rolled	Cold Rolled	Final Annealed
				U_3O_8-Al Dispersions			
20	None	13.5	a	7.2	9.3	10.0	9.6
30	None	9.7	a	6.7	9.1	9.8	9.6
50	None	6.7	a	7.4	9.5	10.3	9.9
30	400	9.5	11.2	6.9	9.3	10.0	9.7
30	500	9.4	11.2	6.8	9.1	9.8	9.5
30	600	9.6	11.4	6.5	8.8	9.6	9.3
				UAl_x-Al Dispersions			
20	None	13.8	a	7.0	8.8	9.5	10.0
30	None	9.2	a	6.8	8.8	9.5	9.9
50	None	5.8	a	6.9	8.7	9.4	9.8
30	400	9.0	9.9	6.8	8.7	9.4	9.9
30	500	9.0	17.9	8.7	10.4	11.2	11.0

[a]Compacts not degassed.

reaction and also during hot rolling gave rise to the additional 2 vol % void content of these compacts.

During cold rolling, the oxide and intermetallic fuel phases also fragment and form stringers. The high-fired U_3O_8 compound, however, appears to form a more friable particle than does arc-cast UAl_x. In Table 19.5, the column "Partially Cold-Rolled Cores" lists the void content of the fuel dispersions after a reduction in thickness of 13.1% at room temperature. This degree of working produced an increase in void content of about 2.3 and 1.8 vol % for the U_3O_8 and UAl_x-bearing cores, respectively. Further cold rolling to a total reduction of 18.9% produced an additional linear increase of about 0.7 vol % of voids for both types of dispersions.

The final annealing operation affects the void contents of the two types of Al-base dispersions differently. A comparison of the values for cold-rolled and final-annealed materials in Table 19.5 for the U_3O_8-Al cores shows an average decrease of 0.3 vol %. A similar change of 0.2 vol % can be noted for the UAl_x-Al cores pressed at 30 tsi and degassed at 500°C. We believe that this slight reduction in average void concentration denotes sintering of the cold-rolled materials. For the UAl_x-Al cores, it also implies that the reaction between the UAl_x fuel particles and the Al matrix is now complete. This is not so, however, for the remaining UAl_x-Al cores pressed at 20, 30, or 50 tsi or for those pressed at 30 tsi and degassed at 400°C. These clad dispersions increased about 0.4 vol % in average void content, probably from the transformation of UAl_x during the final heat treatment.

After the hot-rolling-and-annealing operation, we noted that the equilibrium void content of the 71.6 wt % U_3O_8-Al and 67.2 wt % UAl_x-Al compacts of various initial densities was about 7 vol %. During this stage of fabrication, the compacts pressed at 20 and 30 tsi densified while those pressed at 50 tsi became slightly less dense. To elucidate when the density change occurred during hot rolling, we derived the following relationship

$$\ell_i w_i = \left(\ell_o w_o t_o \rho_o / \rho_i\right)\left(1/t_i\right), \qquad (19.1)$$

where ℓ, w, t, and ρ equal, respectively, the length, width, thickness, and density of the fuel dispersion and the subscript o designates the initial condition of the fuel compact that is ready for billet assembly while i designates the condition of the rolled core at any particular hot-rolling pass.

Equation (19.1) has the form of $Y = A + BX$, where $A = 0$ and $B = \ell_o w_o t_o \rho_o / \rho_i$. Thus, the slope of Eq. (19.1) should become constant if an equilibrium void content is achieved during hot rolling. After each hot-rolling pass, we determined ℓ_i and w_i from radiographs of the rolled billet and also measured the billet thickness, T_i. By assuming that the core thickness, t_i, reduces proportionately to the billet reduction, t_i was calculated according to Eq. (19.2).

$$\hat{t}_i = t_o T_i / T_o \ , \tag{19.2}$$

where $\hat{t}_i$ represents the calculated core thickness for a particular pass, i.

For each of the dispersions characterized previously in Table 19.5, we calculated by the method of least squares the intercept A, the slope B, and the root-mean-square of the $\ell_i w_i$ deviations, S_y, for Eq. (19.1). The correlation was made for hot-rolling passes 1 through 8. As shown in Table 19.6, the standard error of estimate, S_y, is effectively zero and indicates that an excellent fit of the data to the linear equation was obtained. The intercept is also a small value of near zero, as predicted from Eq. (19.1). The slope of about 0.102 $in.^3$ is constant for the two types of dispersions of various initial densities. If pass 1 is excluded from the correlation, the slopes remain 0.102 $in.^3$. We conclude that both the U_3O_8-Al and UAl_x-Al cores achieved their equilibrium void content on the first rolling pass. Further hot rolling, at least through 83.6% reduction in thickness, elongates and widens the core without changing its density.

We are also concerned with formation of dogbone during each pass. To date, x-ray attenuation scans of the 44 clad cores have been obtained for each of the nine hot-rolling passes and the second and fourth mill settings of the cold-rolling schedule. However, the calibration curves

Table 19.6. Least-Squares Fit of $\ell_i w_i$ vs $1/\hat{t}_i$ for Hot-Rolled 41 vol % U_3O_8-Al and UAl_x-Al Fuel Dispersions

Pressing Pressure (tsi)	Degassing Temperature (°C)	Intercept A (in.^{2})	Slope B (in.^{3})	Standard Error of Estimate (in.^{2})
		U_3O_8-Al Dispersions		
20	None	0.052	0.101	0.015
30	None	0.055	0.102	0.011
50	None	0.070	0.102	0.010
30	400	0.062	0.102	0.007
30	500	0.058	0.102	0.005
30	600	0.061	0.102	0.006
		UAl_x-Al Dispersions		
20	None	0.068	0.100	0.000
30	None	0.071	0.100	0.007
50	None	0.066	0.102	0.008
30	400	0.062	0.100	0.006
30	500	0.089	0.101	0.010

of U content per unit area versus x-ray attenuation value needed to evaluate the scans are not yet available.

Fabrication Development

W. R. Martin

Effect of Dispersoid Concentration on Void Content of Composite Plates (M. M. Martin)

Voids introduced into composites during fabrication can enhance irradiation performance of dispersion fuel plates.[10] Our studies showed that the principal factors affecting the void content in Al-base composites are the type and concentration of the fuel compounds.[11] The core compositions investigated, however, were of immediate interest to HFIR and ATR and only encompassed 15 to 25 vol % U_3O_8-Al and 25 to 35 vol % UAl_x-Al dispersions. We also reported[12] the effect for 41 vol % dispersions of U_3O_8 and UAl_x in Al.

To provide more information in support of our findings and to examine the maximum fuel concentrations that can be incorporated in test plates, we are now investigating the effect of dispersoid content over the entire concentration range of 0 to 100 wt %. Our work includes dispersions of high-fired U_3O_8-Al, burned U_3O_8-Al, arc-cast UAl_x-Al and α Al_2O_3-Al. The α Al_2O_3-Al is being considered for the filler section of HFIR fuel plates. In this regard, it appears that increasing the void content to about 3 vol % in the filler section may significantly reduce rejections for bond defects.[13]

To date, dispersions of high-fired U_3O_8-Al and α Al_2O_3-Al have been fabricated by conventional powder-metallurgy techniques and then clad with type 6061 Al by roll bonding. The fabrication entailed (1) blending the component powders, (2) cold pressing at 30 tsi for 6 sec, (3) degassing the 0.73-in.-long × 0.96-in.-wide × 0.15-in.-thick green compacts at 500°C for 1 hr at less than 0.05 torr, (4) assembling the billets for rolling, and (5) rolling the billets to 84% reduction in thickness at 490°C in eight hot passes. After blistering annealing at 490°C, the plates will be reduced 40% in thickness at room temperature. The void content of the dispersions will be determined at seven stages of fabrication: after pressing, degassing, hot rolling, and cold rolling to 10, 20, 30, and 40% reduction in thickness.

Triplicate specimens were prepared for the U_3O_8-Al dispersions of 25.8, 44.2, 58.3, 69.6, 79.5, 88.2, 96.5, and 100.0 wt % U_3O_8. A lack of available materials limited us to duplicate specimens of 14.1, 27.3, 39.9, 52.6, 65.7, and 82.0 wt % Al_2O_3 for the α Al_2O_3-Al dispersions.

Figure 19.2 shows the effects of dispersoid concentration on the void content of the high-fired U_3O_8 and α Al_2O_3-bearing dispersions through hot rolling. In general, both types of compacts grew upon degassing and densified during hot rolling, but the magnitude of these changes depended on the material and concentration (see Fig. 19.2). The rate at which voids are produced in the hot-rolled α Al_2O_3-Al dispersions increases significantly above 40 vol % α Al_2O_3; and, above 50 vol % α Al_2O_3, these cores contain more voids than the plates of similar content of high-fired U_3O_8 dispersoid. Surprisingly, the 96.5

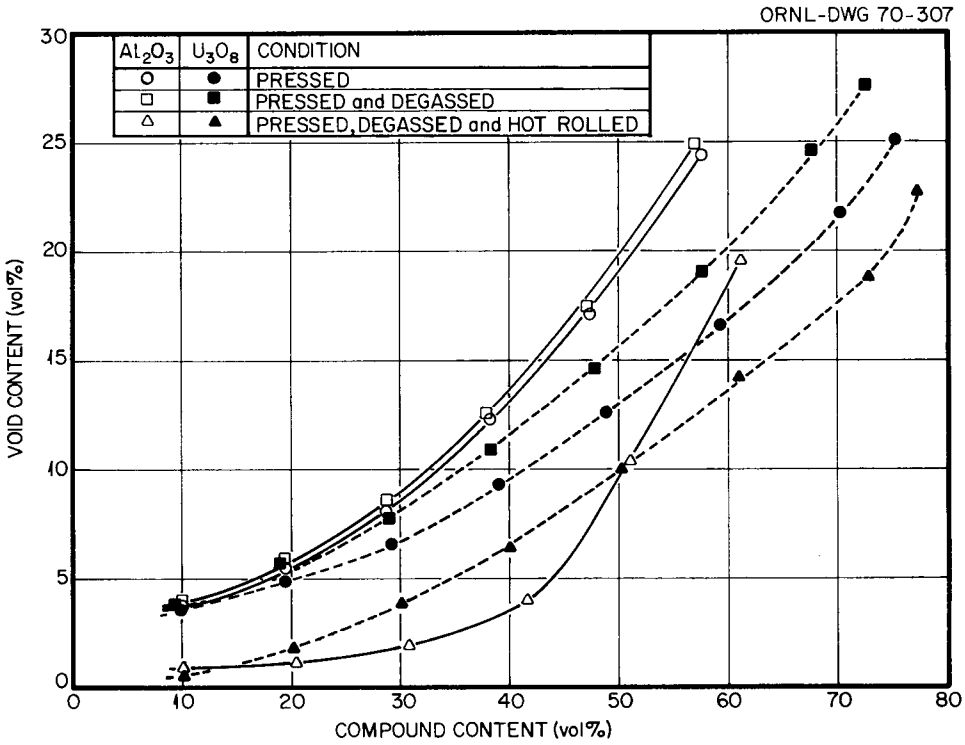

Fig. 19.2. Effect of Concentration on Void Content of U_3O_8-Al and Al_2O_3-Al Dispersions in the Pressed, Degassed, and Hot-Roll-Bonded Conditions.

and 100.0 wt % U_3O_8-Al dispersions had sufficient green strength after compacting to permit some handling without breaking. From radiographs and visual examination of the surfaces of the rolled plates, these compacts also appeared to roll satisfactorily, as is evident from the absence of internal cracks.

Our work has progressed to the point that we are able to form a generalization about the effect of deformation on the void content of dispersion fuel plates. For example, consider two Al-base dispersions, a and b. These may contain either two types of fuel compounds or the same fuel compound of differing dispersoid concentration. The dispersions are fabricated by the following procedures: (1) blending the component powders, (2) pressing to achieve sufficient green strength for handling, (3) degassing to reduce volatile contaminants, (4) assembling into rolling billets, (5) hot rolling to bond the cladding to the dispersion, (6) annealing to test for blisters, (7) cold rolling to

size, and (8) heat treating to achieve the "O" temper for the cladding and also to test again for blisters.

Figure 19.3 schematically illustrates the effect of deformation on a- and b-type dispersions at the various stages of fabrication into composite plates. The symbols a^V and b^V denote the void concentration of the a and b dispersions, respectively. Superscripts affixed to either a^V or b^V identify a particular stage of fabrication (D = pressing and/or degassing, HD = hot deformation, BA = blister anneal, CD = cold deformation, and F = final heat treatment). Our illustration starts with four vertically plotted points $\left(a^{V^{D_1}}, a^{V^{D_2}}, b^{V^{D_1}}, b^{V^{D_2}}\right)$ that represent the relative void levels of a and b dispersions after pressing at (1) 50 tsi and (2) 20 tsi. We note that V^D depends on the type and concentration of the dispersoid, the pressing pressure, and

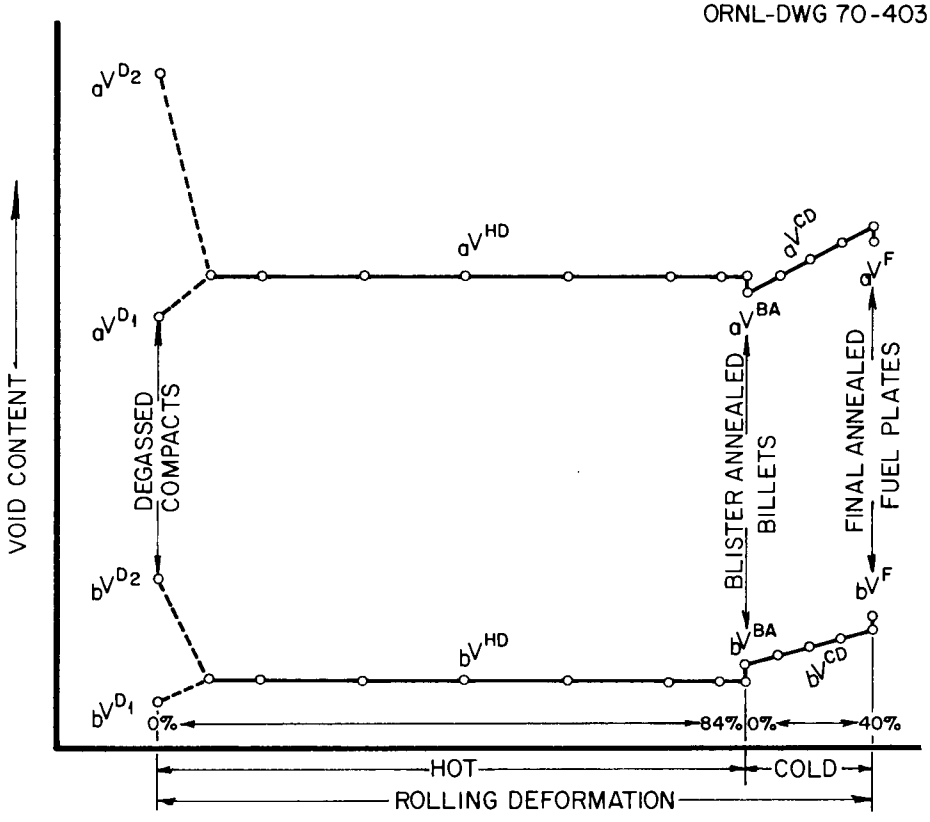

Fig. 19.3. Schematic Illustration of the Effect of Deformation on the Void Content of Two General Aluminum-Base Dispersions, a and b.

the degassing temperature. The particle size of the dispersoid, however, affects V^D only to the extent of changing the rate of reaction between the dispersoid and the Al matrix during degassing.

Based on our results to date, which are summarized in Fig. 19.3, we offer the following observations on the void content of Al-base dispersions at various stages of fabrication.

1. The V^{HD} may be either less than, equal to, or greater than V^D, depending on the pressing and degassing conditions for the powder-metallurgy compacts.

2. The V^{HD} is constant for all hot-bonding passes. In dispersions that are composed of chemically compatible materials, V^{HD} is also independent of V^D.

3. The blister annealing treatment given the plates after hot rolling produces little change in V^{HD}. However, V^{BA} can be either less than, equal to, or greater than V^{HD}. In Fig. 19.3 $a^{V^{BA}}$ depicts a slight degree of sintering in respect to $a^{V^{HD}}$ while $b^{V^{BA}}$ shows an increase because of a postulated reaction between the dispersoid and Al matrix.

4. Cold rolling increases the void content of dispersion-type fuels. The V^{CR} appears to depend linearly on the amount of deformation at room temperature. This observation presents us with another way to increase the void content of dispersion fuel plates.

5. The final void content of the dispersion, V^F, shows only a secondary dependency on deformation and heat treatment but depends principally on the type and concentration of the dispersions. However, it is recognized that the secondary influence of deformation and heat treatment on void formation could significantly influence the irradiation performance of dispersion plates.

Development of Nondestructive Inspection Techniques

R. W. McClung

X-Ray Attenuation (B. E. Foster, S. D. Snyder)

Study of Particle Variations. — We initiated a program for systematically checking the effect of size and surface area of particles on

the calibration curve for x-ray attenuation for both high-fired and burned U_3O_8 powders in fuel plates.[14] The 26 sets of plates (two identical plates per set) were scanned on the x-ray attenuation scanner at the normal x-ray energy of 50 kilovolts constant potential (kvcp) and also at an x-ray energy of 60 kvcp to increase the sensitivity to fuel change in the more heavily loaded plates. The attenuation data have not been processed. In addition, we measured the areas of the fuel cores from the radiographs of these plates. The average loading of U per 5/64-in.-diam spot, which will be related to x-ray attenuation, will be determined from the known content of U in the plate and the fuel area rather than by the previous method of chemical analysis of samples machined from the plate.

Homogeneity Evaluation of U_3O_8-Al, UAl_x-Al, and ZrO_2-Al Dispersions. — To aid the studies of dogbone formation, we have been systematically scanning 11 fuel plates after each rolling pass.[8] Six of these plates have cores of high-fired U_3O_8 in an Al matrix, and five plates have cores of arc-cast UAl_x in an Al matrix. Each plate contains four similar cores. We have scanned these plates on the x-ray attenuation scanner after each of the nine hot-rolling passes and two cold-rolling passes.

Four miniature plates with a filler section of 50 wt % ZrO_2-Al dispersion instead of the usual all-Al filler were received for evaluation of homogeneity. The fabricators were interested in the effects of this filler material on dogboning. The radiation attenuation scanning showed no evidence of dogboning, but the very high radiation absorption of the ZrO_2 relative to Al could have masked the dogboning.

Radiation Scattering[15] (B. E. Foster)

Measurement of Cladding Thickness. — We have continued preliminary investigation of the use of scattered and fluorescent radiation for measuring the thickness of the Al cladding on fuel plates.

The radiation source initially used was 1/2 curie of ^{241}Am. As a specimen for these studies we used a fuel plate clad with about 0.010 in. of Al and with a flat core dispersion of U_3O_8 in Al. The radiation beam was collimated to 3/8 in. in diameter and impinged on the surface of the

specimen at an angle of 40° from the normal. Changes in the thickness of the cladding are simulated by Al foils of different thicknesses. However, the count rate of the scattered radiation from both the cladding and core material varied with successive measurements with about ±1% uncertainty. At the energy of radiation being used, this uncertainty was greater than that caused by a significant change in the thickness of the cladding. This variation in count rate could have been caused by inhomogeneity in the core material as well as by radiation being scattered to the detector from the table under the specimen, since the radiation energy is high enough to allow considerable transmission through the entire plate.

We are investigating the use of ^{147}Pm (about 50 curies) as a radiation source. The lower energy (38 kev) and much greater intensity will probably reduce the fluctuations in count rate experienced with the ^{241}Am source. For preliminary work with the ^{147}Pm source we are using a piece of Pb as a substitute for U and adding Al shims to simulate cladding. We can readily detect the presence of a 0.00025-in. piece of Al on the Pb base.

We are apparently using the 12 kev L_{II} x ray from Pb fluorescence. If reasonable sensitivity to change in the thickness of the cladding is obtained through a 0.012-in. Al cladding, then further experimental work will be done using U as the base material.

Studies of Joining and Assembly

G. M. Slaughter

Joining Fuel Plates to Side Plates by Electron-Beam Welding (W. J. Werner)

We have been working toward characterization of the electron-beam process by statistical methods. Variables of primary importance are welding current, voltage, and beam focusing current. Both the welding speed and the distance between the welding gun and workpiece were constants in this particular study. The distance between the welding gun and workpiece was dictated by the clearance between our specially

designed gun and the inner side plate of the inner annulus of the HFIR fuel element. The choice of a 20 in./min welding speed was based on our initial studies of flat plates for process qualification.

Welds for the study were made on solid plates with the beam focused 1/8 in. below the work surface, on the work surface, and 1/8 in. above the work surface. Welding currents ranged from 65 to 85 ma, and voltages ranged from 16 to 24 kv. Data on weld width, depth, and width at half depth were obtained metallographically from the test plates. Our experimental design was such that the data for a given focus could be analyzed according to the following mathematical model:

$$Y = b_o + b_1x_1 + b_2x_2 + b_{12}x_1x_2 + b_{11}x_1^2 + b_{22}x_2^2 \qquad (19.3)$$

where

Y = response (weld width, depth, or width at half depth),
b_o = intercept,
b_1 and
b_2 = linear effects,
x_1 = voltage (kv),
x_2 = current (ma),
b_{12} = interaction, and
b_{11} and
b_{22} = quadratic effects.

Using the experimental data on weld width and depth, the parameters (coefficients) in the model were determined by the method of least squares. Using the statistically determined parameters, curves of constant weld width, depth, and width at half depth were obtained as a function of welding current and voltage for each focus. The plots obtained for a beam focused 1/8 in. below the work surface are shown in Figs. 19.4 through 19.6. The validity of this type analysis is determined by the ability of the model to fit the data. Figure 19.4 shows curves of constant weld width at the work surface as a function of welding current and voltage. Since weld width for a given heat input does reflect penetration and width at half depth, it may be an important visual measure of these items in welded assemblies. In

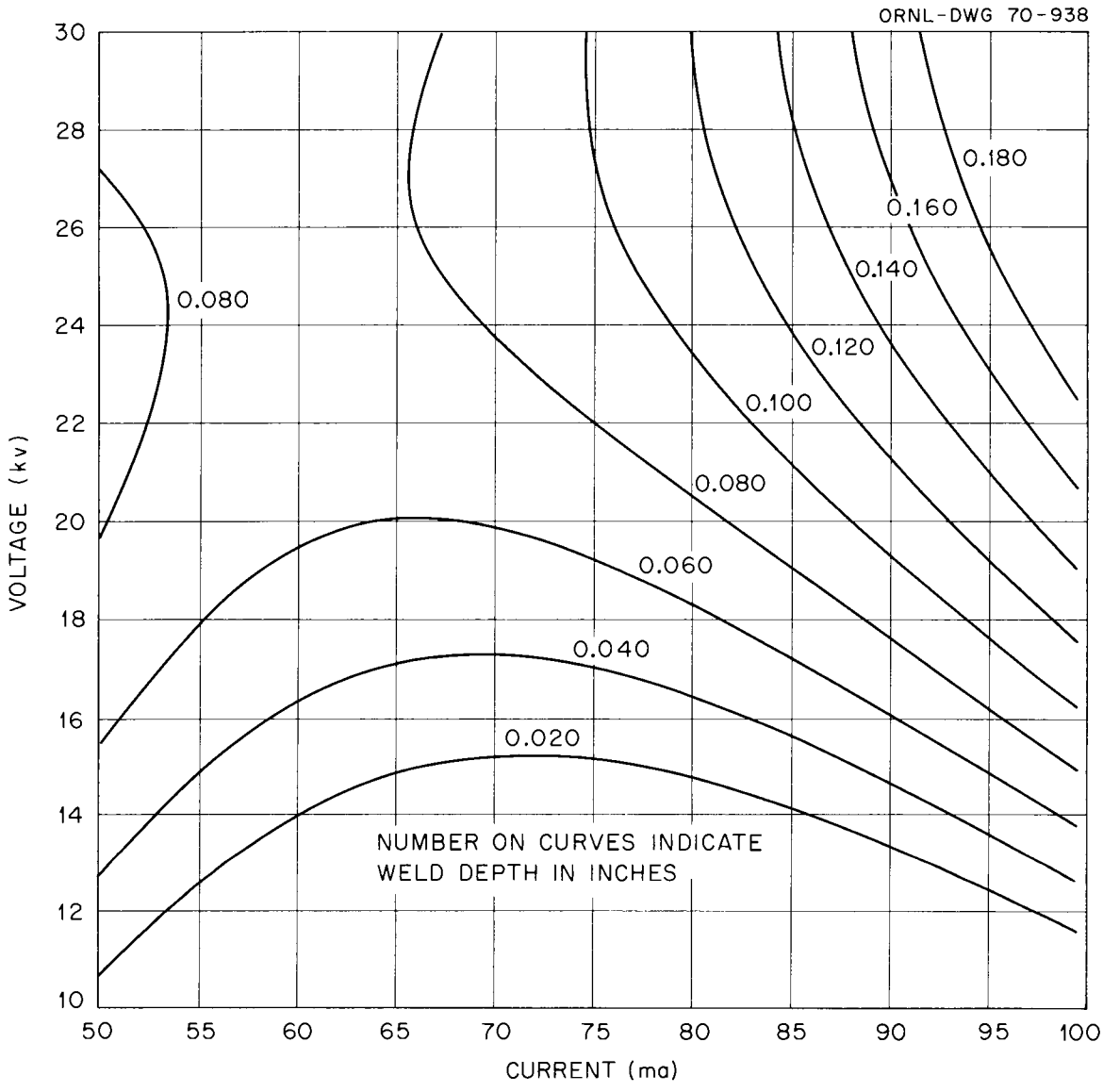

Fig. 19.4. Curves of Constant Weld Width at the Work Surface as a Function of Welding Current and Amperage for Beam Focus 1/8 in. Below the Work Surface.

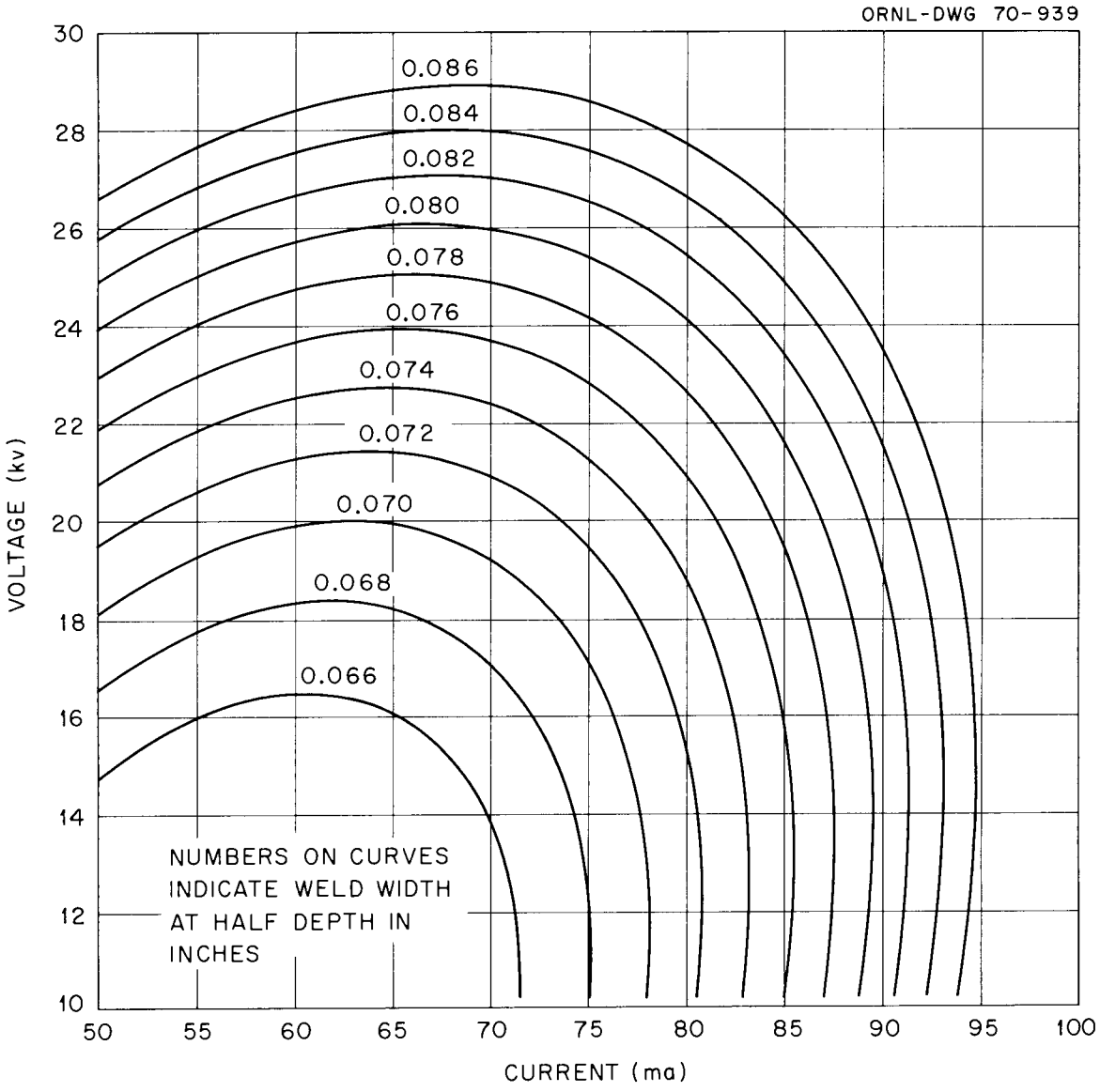

Fig. 19.5. Curves of Constant Weld Depth as a Function of Welding Current and Amperage for a Beam Focus 1/8 in. Below the Work Surface.

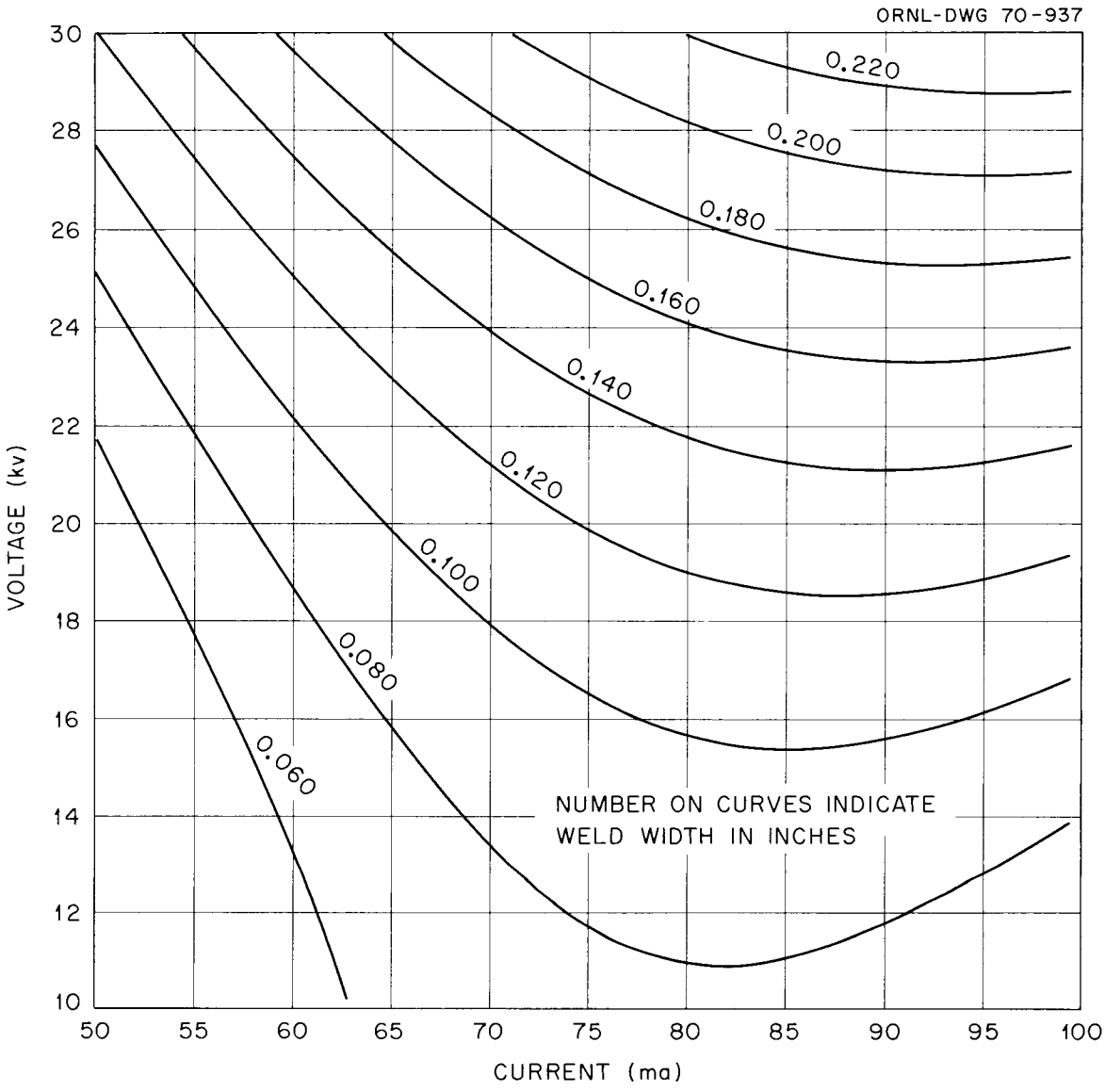

Fig. 19.6. Curves of Constant Width at Half Depth as a Function of Welding Current and Amperage for a Beam Focus 1/8 in. Below the Work Surface.

practice, we hope to choose the welding variables for a given fuel element on the basis of needed penetration (Fig. 19.5) and width of fusion zone (dictated by strength requirements) at the interface between fuel plate and side plate (Fig. 19.6).

There was not a good fit of experimental points on the curves, indicating that the experimental error was somewhat high. Examination of the data, however, showed excellent reproducibility within any given weld.

We believe that differences in preheating between the various welds account for the rather poor fit of the data points to the curve. For a given focus, the 14 different welds for a series were made on the same plate about 3/4 in. apart. We shall weld a new series and take added precautions to eliminate the variation in preheating.

References

1. Plant and Equipment Division.
2. M. M. Martin and W. K. Crowley, Fuels and Materials Development Program Quart. Progr. Rept. Sept. 30, 1969, ORNL-4480, pp. 213–215.
3. M. M. Martin, Fuels and Materials Development Program Quart. Progr. Rept. Sept. 30, 1969, ORNL-4480, pp. 214–218.
4. M. M. Martin and J. H. Erwin, Fuels and Materials Development Program Quart. Progr. Rept. June 30, 1969, ORNL-4440, pp. 205–206.
5. G. O. Haynes and G. W. Gibson, Idaho Nuclear Corporation, private communication, June 30, 1969.
6. A. E. Richt, Fuels and Materials Development Program Quart. Progr. Rept. Sept. 30, 1969, ORNL-4480, pp. 218–219.
7. J. H. Erwin, Metals and Ceramics Div. Ann. Progr. Rept. June 30, 1967, ORNL-4170, pp. 179–181.
8. M. M. Martin, Fuels and Materials Development Program Quart. Progr. Rept. Sept. 30, 1969, ORNL-4480, pp. 233–237.
9. J. L. Gregg, R. S. Crouse, and W. J. Werner, Swelling of UAl_3-Al Compacts, ORNL-4056 (January 1967).
10. M. M. Martin and A. E. Richt, Trans. Am. Nucl. Soc. 12, 98 (1968).
11. M. M. Martin, J. H. Erwin, and W. R. Martin, Trans. Am. Nucl. Soc. 11, 107 (1968).

12. M. M. Martin, "Parametric Study of the Deformation of U_3O_8- and UAl_x-Al Dispersion Fuel Plates," pp. 277–282, this report.

13. J. H. Erwin, M. M. Martin, and R. W. Knight, Fuels and Materials Development Program Quart. Progr. Rept. Sept. 30, 1969, ORNL-4480, pp. 228–229.

14. B. E. Foster, S. D. Snyder, and M. M. Martin, Fuels and Materials Development Program Quart. Progr. Rept. Sept. 30, 1969, ORNL-4480, pp. 239–241.

15. This work is jointly supported by the Nondestructive Testing Program and is also discussed in Chapter 22 of this report.

CLADDING AND OTHER STRUCTURAL MATERIALS

20. BEHAVIOR OF REFRACTORY MATERIALS UNDER IRRADIATION

G. M. Watson[1] G. W. Keilholtz[1]

The purpose of this program is to evaluate the effects of high fast-neutron fluences at temperatures up to 1100°C on the properties of refractory nuclear materials for both space and civilian power reactors. The present program has two major objectives: (1) the determination of the effects of He gas produced by fast neutrons in depleted UN fuels, and (2) investigation of the effects of fast neutrons on B_4C as part of a program for developing this material as a neutron absorber for control of reactivity in fast-flux reactors.

Irradiation Damage to Nonfissionable Refractory Materials

R. E. Moore[1] D. A. Dyslin[2] H. E. Robertson[1]

The work of this task is now entirely on the refractory-metal carbides, and it is nearly complete. Experiments still in progress are aimed at defining the mechanisms of neutron damage. This will aid in specifying types of carbides and fabrication conditions for possible applications in nuclear reactors and will contribute to a basic understanding of fast-neutron effects on materials.

A long-term, low temperature (< 150°C) assembly containing carbides of Ti, Zr, Ta, Nb, and W is still being irradiated in the Engineering Test Reactor (ETR). Specimens irradiated in an identical short-term assembly were examined and measured previously.[3] Out-of-reactor annealing of specimens irradiated in previous assemblies was continued during the past quarter. The data obtained for dimensional changes during annealing are helping to define damage mechanisms quantitatively.

Selected specimens from the short-term assembly mentioned above were annealed out-of-reactor at increasingly higher temperatures. None changed in dimensions by any significant amount at annealing temperatures

below 500°C. Therefore, displacements produced by fast neutrons are not eliminated by thermal annealing at irradiation temperatures below 500°C for any of the five carbides. Annealing at 700°C of specimens from another irradiation assembly caused shrinkage. The annealing studies will be continued to determine the annealing rates as functions of temperature. The annealed specimens will be examined by x-ray diffraction to measure the changes in the lattice parameters so that we may correlate these changes with the gross dimensional changes. This should aid in determining parameters for our damage model[3] in which we have assumed that easily annealed single displacements cause expansion in the lattice parameters but that clusters contribute only to the gross expansion.

Effects of Irradiation on LMFBR Fuels

R. E. Moore[1] D. A. Dyslin[2] H. E. Robertson[1]

This task is aimed at evaluating the effects of the generation of He gas through the $^{14}N(n,\alpha)^{11}B$ fast-neutron reaction within nitride fuels. Depleted fuels are used in the experiments to eliminate production of fission gas during irradiation.

A high-temperature (1000°C) instrumented assembly and a low-temperature (about 150°C) uninstrumented assembly are being irradiated in the J-12 core position in the ETR. The assemblies contain three types of specimens: UN, $U^{15}N$, and UN-UC (50-50 mole %). The effect of the (n,α) reaction will be measured directly by comparing the changes in properties of depleted UN and depleted $U^{15}N$, since the reaction does not occur in $U^{15}N$. Gas analyses of the capsules will measure the He release from both the UN and the UN-UC.

The low-temperature assembly will be removed from the ETR in January 1970, after receiving a range of fluences estimated at 0.5 to 2.0×10^{21} neutrons/cm^2 (> 1 Mev). Because of a delay in the insertion of the high-temperature assembly, it will continue to be irradiated until May or June 1970 to receive the same fluence as the low-temperature assembly will have received.

Fast-Neutron Effects on Materials for Neutron Absorption in Fast Reactors

R. E. Moore[1] D. A. Dyslin[2] H. E. Robertson[1]

The objectives of this task have been altered. The plans now call for all of the work to be centered on the development of B_4C as a neutron absorber for reactivity control of fast reactors. Instead of irradiating two assemblies containing B_4C pellets in row 8 of the Experimental Breeder Reactor-II (EBR-II), it has been decided to increase the number of assemblies to four, or possibly six, and to irradiate these assemblies in a higher flux position in row 7. The insertion will be delayed until the EBR-II goes to a higher power level in July 1970.

The addition of more assemblies to the experimental design will permit evaluation of more fabrication variables of B_4C. For example, the effect of voids within the grains on the He gas released during irradiation may be determined at several temperatures for different B:C ratios.

Preliminary design work on the irradiation assemblies of this comprehensive experiment was started. After July 1, 1970, the work under this task will be continued as part of another program that will encompass all phases of the development of B_4C neutron absorbers.

References

1. Reactor Chemistry Division.
2. General Engineering Division.
3. R. E. Moore, D. A. Dyslin, and H. E. Robertson, Fuels and Materials Development Program Quart. Progr. Rept. Sept. 30, 1969, ORNL-4480, pp. 245–254.

21. JOINING RESEARCH ON NUCLEAR MATERIALS

J. R. Weir, Jr. G. M. Slaughter

The purpose of this program is to gather the fundamental and applied data needed to understand the weldability of materials that are either being considered or are currently used for nuclear applications. Fundamental studies are concerned with the effects of minor constituents on the behavior of weldments. We are especially interested in the austenitic stainless steels and the alloys that are rich in Ni, such as Incoloy 800 and Inconel 600. In addition, a modest program concerned with the influence of weld defects will provide reference results in this much-talked-about but little-investigated field.

As a result of this broad-based program, we plan to suggest modifications in both alloy composition and procedures needed to improve the quality of weldments used in the various activities of the Commission.

The Effects of Minor Variations in Chemical Composition on Weldability

Our continuing investigation of the effect of minor variations in those elements usually present in structural material has included Inconel 600, Incoloy 800, and stainless steel.

Weldability of Incoloy 800 (D. A. Canonico, W. J. Werner)

We prepared filler wire from the specially melted and processed experimental heats that were used previously in tests with the Duffer's Gleeble[1] and in studies of ductility at intermediate temperature.[2] Samples from these heats were drawn to 1/16-in.-diam wire. Table 21.1 lists the experimental heats and their nominal chemical analyses. Three additional filler wires were studied. Two of these, Inconel 62 and Inconel 82, are commercial filler metals recommended for joining Incoloy 800. The third was prepared from electroslag remelted Incoloy 800 base plate. Commercially produced 1/8-in.-thick sheets of Incoloy 800 were obtained, cleaned, and welded to a strongback. The gas W-arc (GTA) welding process was used with the experimental heats serving

Table 21.1. Results of Nondestructive Examination of Welds in Incoloy 800

Identification	Nominal Chemical Analysis, wt %[a]									Nondestructive Test Results	
	Al	Ti	S	P	Fe	Ni	Cr	Nb	Mn	Dye Penetrant	Radiography
143	0.38	0.15								Acceptable	Acceptable
144	0.38	0.60								Acceptable	Acceptable
145	0.15	0.38								Acceptable	Acceptable
146	0.60	0.38								Acceptable	Acceptable
175	0.15	0.15								Acceptable	Acceptable
176	0.38	0.38								Acceptable	Acceptable
177	0.60	0.60								Acceptable	Acceptable
185	0.38	0.38	0.015							Cracks	Cracks
187	0.38	0.38		0.010						Porosity	Porosity
189	0.38	0.38		0.02						Acceptable	Acceptable
191	0.38	0.38	0.015	0.015						Cracks	Cracks
Incoloy 800[b]					46	32.5	21			Acceptable	Acceptable
Inconel 62					7.5	64	16	2.25		Acceptable	Acceptable
Inconel 82T					1	72	20	2.5	3	Acceptable	Acceptable

[a]Nominal base to which additions are made is Fe–16% Cr–31% Ni.

[b]Filler metal prepared from Incoloy 800 that had been electroslag remelted.

as filler wire. The welding conditions were within the following ranges: current, 30 to 65 amp; voltage, 10 to 14 v. The previous weld pass was allowed to cool to room temperature before the next pass was deposited.

Table 21.1 shows the results of nondestructive examinations of each weld. Specimens are being machined from these welds for tensile and bend tests. After these tests, an extensive metallographic examination will be conducted. These destructive examinations should prove much more definitive than the nondestructive tests for evaluation of the individual experimental alloys.

Weldability of Stainless Steels (D. A. Canonico, A. J. Moorhead, W. J. Werner)

Our study of austenitic stainless steels has centered about the effect of chemical composition on the quantity and morphology of the ferritic phase often present in stainless steel weld metals. The interest in this program is primarily in ferrite (body-centered cubic), a phase that is believed to occur early in the solidification of the weld metal. A second ferritic phase, martensite (body-centered tetragonal), may also be present, but its transformation from austenite occurs at considerably lower temperatures. The transformation kinetics of the two ferritic phases are entirely different, but there may be an interaction between them that is noteworthy. Further, the mechanical properties of a weld may be more dependent on the presence (or absence) of the martensitic phase than they are on the ferrite phase. We are continuing the program previously outlined[3] wherein we are studying the effects of various combinations of Ni, Cr, and Fe that should (according to a Schaeffler diagram) provide austenitic weld metals with similar quantities of ferrite but quite different chemical compositions. The alloys we are using in this study lend themselves to an investigation of the effect of temperature and strain on the transformation of austenite to martensite. Of considerable interest is the effect of the presence of the ferrite on the diffusionless transformation of austenite to martensite. There are a number of theories regarding the causes of the beneficial effect noted for ferrite, in particular, its ability to reduce the tendency toward hot cracking. It is possible

that its presence also influences the stability of the austenite by enriching it in those elements that tend to stabilize it. By so doing, it may prohibit the transformation to martensite, which, in turn, would assure a high level of toughness.

We have received 1-lb drop castings of each of the 13 alloys shown in Table 21.2. The riser and a section of the bottom were machined from each casting. The bars thus produced are 11/32 × 31/32 × 4 3/4 in. These bars were homogenized in H_2 at 1150°C for 1 hr and then cooled in the water-cooled zone of the tube furnace. Metallographic specimens from both ends of each bar are now being examined.

Table 21.2. The Effect of Homogenization[a] on the Magnetic Strength of the Experimental Alloys Being Studied

Casting Heat Number	Nominal Composition, wt %			Magne-Gage Reading[b]	
	Ni	Cr	Fe	Before Homogenization	After Homogenization
5408	12	19	69	111	WNA
5409[c]	12	19	64	102	153
5410	10	19	71	20	139
5411	14	19	67	WNA	WNA
5412	16	19	65	WNA	WNA
5415	12	21.5	66.5	8	102
5416	14	21.5	64.5	93	155
5417	16	21.5	62.5	155	WNA
5418	18	21.5	60.5	WNA	WNA
5419	14	24	62	9	92
5420	16	24	60	89	132
5421	18	24	58	144	WNA
5422	20	24	56	WNA	WNA

[a]Heated at 1150°C for 1 hr in H_2.

[b]All readings were taken with the No. 4 magnet. The higher the number, the lower the magnetic strength and ferrite content. WNA denotes that the magnet would not adhere to these specimens, so that no reading could be taken.

[c]This alloy contained 5% Mn.

In order to check for the presence of body-centered cubic phases (ferrite or martensite) in the castings, we measured magnetic response with a Magne-gage. These data are also reported in Table 21.2, in which it is possible to compare the magnetic strength (due to the amount of ferrite or martensite present) in a given casting before and after homogenization. The values are relative; higher numbers represent lower magnetic strength, which we attribute to the lower ferrite or martensite content. It is significant that those alloys whose compositions fall in the 5 to 10% ferrite region of the Schaeffler diagram (see Fig. 21.1) also had lower Magne-gage readings (greater magnetism) both before and after homogenization, probably because of the instability of the austenite in these compositions.

Our investigation of the effect of welding conditions on the quantity and distribution of ferrite in shielded metal-arc welds made with type 308 stainless steel electrodes is continuing. Previously,[4] we discussed the

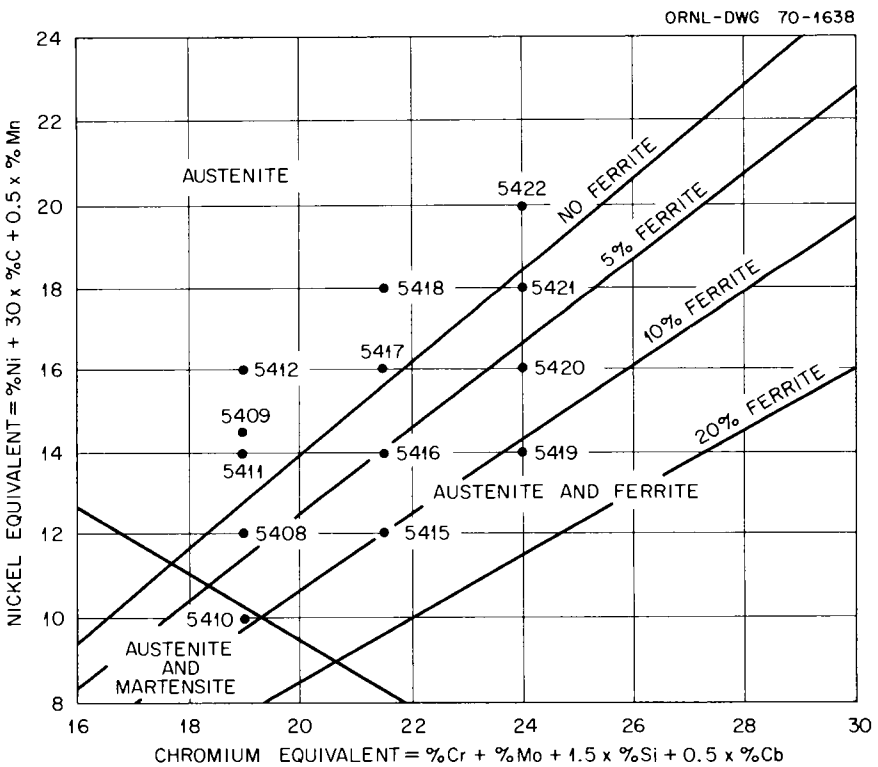

Fig. 21.1. Location of 13 Ternary Drop-Cast Alloys on the Schaeffler Diagram for Stainless Steel Weld Metal.

coated electrodes and welding technique used to obtain the welds for this study. During this quarter, we analyzed the weld metal in order to predict the ferrite content from a Schaeffler diagram. We also prepared specimens of weld metal for a metallographic examination. The quantitative television microscope is being used to measure the amount of ferrite present. The predicted ferrite contents of the weld metals, based on their chemical analyses, are given in Table 21.3, which also includes the heat input used for the various bead-on-plate welds. Similar heat inputs were obtained with variations in travel speed, current, and voltage. A cursory review of these data indicates that travel speed is a major contributor to the composition of the weld deposit. This is no doubt associated with the degree to which base metal is diluted in the weld metal. These data are being reviewed carefully and should provide some very useful correlations.

The Effect of Defects on the Mechanical Properties of Weldments

Tests of Electron-Beam Welds in Inconel 600 (C. D. Lundin[5])

We began testing specimens of base metal, weld metal, and composites of base metal and weld metal (transverse to the welding direction) from welds made in Inconel 600.

The test specimens of weld metal were obtained from electron beam welds in 1/8-in.-thick Inconel 600. The welding conditions were such that four overlapping passes provided a full-penetration weld fusion zone about 1/4 in. wide. The specimens were removed from this fusion zone with their longitudinal axes parallel to the welding direction. The specimens of base metal were machined from material adjacent to the heat-affected zone with their longitudinal axes parallel to the welding direction. Metallographic specimens from these and from other similar welds previously studied revealed very few discontinuities.

The results of the room-temperature tensile tests are shown in Table 21.4. It is evident that the yield strength of the samples of weld metal is about 10% higher than that of the samples of base metal and that the elongation and ultimate tensile strength are less than

Table 21.3. Percentage of Ferrite in Type 308 Austenitic Stainless Steel Welds as Predicted from a Schaeffler Diagram

Weld Identification	Nominal Ferrite in Electrode[a] (%)	Heat Input (kJ/in.)	Equivalents[b]		Predicted Ferrite[c] (%)
			Ni	Cr	
1-1	7	13	12.6	20.1	5
1-2	7	43	12.5	20.3	5
1-3	7	22	12.2	20.3	6
1-4	0	20	13.5	19.8	1
1-5	2	20	12.6	19.2	2
1-6	5	20	12.4	20.3	5
1-7	7	20	12.6	19.5	1
1-8	10	20	12.3	19.6	2
1-9	15	20	12.3	20.4	7
1-10	0	10	13.9	18.4	0
1-11	2	10	12.9	18.5	0
1-12	5	10	12.8	19.3	2
1-13[d]	7	10	12.5	19.4	3
1-14[d]	10	10	12.5	19.4	3
1-15[d]	15	10	12.4	19.4	4
1-16[d]	10	10	12.5	18.7	1
1-18	10	40	12.3	19.3	4
1-19[d]	15	40	12.4	19.7	4
2-1	0	40	13.9	19.1	0
2-2	2	40	12.7	19.0	1
2-3	5	40	12.3	19.4	3
2-4	7	40	12.2	20.4	7
2-5	10	40	12.1	19.9	6
2-6	15	40	12.1	21.5	9
2-7	0	60	14.2	19.4	0
2-8	2	60	13.1	19.4	0
2-9	5	60	12.6	20.0	5
2-10	7	60	12.6	20.5	6

Table 21.3. (continued)

Weld Identification	Nominal Ferrite in Electrode[a] (%)	Heat Input (kJ/in.)	Equivalents[b]		Predicted Ferrite[c] (%)
			Ni	Cr	
2-11	10	60	12.1	20.8	8
2-12	15	60	12.1	21.9	10
2-13	10	40	13.4	21.0	5
2-14[d]	0	40	13.7	19.1	0
2-15[d]	2	40	13.0	18.8	0
2-16[d]	5	40	12.7	19.6	3
2-17	7	40	12.0	19.0	4
3-1	7	20	12.4	19.8	5
3-2	7	40	12.9	20.2	5
3-3	7	60	13.0	20.8	7
3-4	7	20	12.9	20.8	2
3-5	7	40	13.5	20.2	2
3-6	7	60	13.4	20.0	2
3-7	7	10	13.7	20.5	3
3-8	7	20	13.9	20.3	2
3-9	7	40	13.6	19.9	1
3-10	7	10	13.6	20.3	2
3-11	7	20	14.1	19.9	0

[a]Shielded metal-arc coated electrodes were ordered to these ferrite levels.

[b]The Ni equivalent = % Ni + 30 × % C + 0.5 × % Mn; the Cr equivalent = % Cr + % Mo + 1.5 × % Si.

[c]Predicted from Schaeffler diagram.

[d]No analysis for C in the weld metal was made; the Ni equivalent is based on the estimated C level.

Table 21.4. Results of Room-Temperature Tensile Tests

Specimen	Origin	Strength, psi		Elongation in 1 in. (%)
		0.2% Offset Yield	Ultimate Tensile	
BM 2	Base metal	35,130	95,365	50
BM 3	Base metal	35,901	93,633	50
WM 2	Weld metal	39,289	86,049	46
WM 3	Weld metal	38,589	84,115	47
WM 4	Weld metal	36,105	75,666	31

those of the samples of base metal. This behavior was expected, and the data were specifically obtained to form a basis for comparison with the results from the specimens known to contain discontinuities. The lower values obtained from specimen WM-4 may reflect the presence of discontinuities. The fracture surfaces are being examined to determine whether discontinuities influenced the tensile behavior.

We began testing the previously described[6] welds that contain discontinuities. We attempted two testing procedures to reveal the effects of the discontinuities: (1) normal tensile tests at room temperature, and (2) short-time stress-rupture tests at 815°C. The short-time stress-rupture tests were conducted in the Duffer's Gleeble.

In general, whenever the radiographs showed the presence of discontinuities, the ultimate tensile strength and elongation were drastically reduced. Where water-clear radiographs were obtained, the ultimate strength and elongation decreased significantly but not catastrophically. These specimens always failed at the interface between the base metal and the fusion zone. Some cracks did develop in the weld metal during testing, but failure did not occur in the weld metal.

In the short-time stress-rupture tests at 815°C, the specimens in which x-ray examination revealed discontinuities were drastically reduced in stress-rupture life, while the specimens with water-clear radiographs showed little decrease in the stress-rupture time. Again, all failures were at the interface between the base metal and fusion

zone, even though cracks appeared in the fusion zone during testing. Thus, these results parallel those from the tests at room temperature.

References

1. D. A. Canonico, W. F. Savage, W. J. Werner, and G. M. Goodwin, "Effects of Minor Additions on Weldability of Incoloy 800," pp. 68–92 in Effects of Minor Elements on the Weldability of High-Nickel Alloys (Proceedings of a Symposium), The Welding Research Council, New York, July 1969.
2. W. J. Werner, Fuels and Materials Development Program Quart. Progr. Rept. Dec. 31, 1968, ORNL-4390, pp. 192–199.
3. W. J. Werner and D. A. Canonico, Fuels and Materials Development Program Quart. Progr. Rept. Sept. 30, 1968, ORNL-4350, pp. 252–254.
4. D. A. Canonico and W. J. Werner, Fuels and Materials Development Program Quart. Progr. Rept. Sept. 30, 1969, ORNL-4480, pp. 256–257.
5. Consultant from the University of Tennessee.
6. C. D. Lundin, Fuels and Materials Development Program Quart. Progr. Rept. June 30, 1969, ORNL-4440, pp. 161–165.

22. NONDESTRUCTIVE TESTING

W. O. Harms R. W. McClung

Our task is to develop new and improved methods of nondestructively testing reactor materials and components. We are studying various physical phenomena, developing instruments and other equipment, devising techniques, and designing and fabricating reference standards. Among the methods being studied for both normal and remote inspection are electromagnetics (with major emphasis on eddy currents), ultrasonics, penetrating radiation, and holography.

Electromagnetic Inspection Methods (Eddy Currents)

Design of Coil Systems for Detection of Defects (C. V. Dodd, W. G. Spoeri, W. E. Deeds,[1] W. A. Simpson)

We determined that the solution of the defect problem, which requires the solution of the inhomogeneous vector Helmholtz equation, can be performed using a modified Green's function. We are attempting to modify the Green's functions for infinite media to fit the boundary conditions between the defect and surrounding conductor.

We constructed a Micarta model, filled it with a column of Hg, placed two coils around it, and moved spherical "defects" past the coils. Preliminary measurements indicate that, as in the case of the coil above a conducting plane, our present theory is adequate for spherical defects. We have continued the computer study of the sensitivity to defects for systems with encircling coils. We varied such parameters as the shape and size of the coil and the spacing between the coils. The following general conclusions can be made about the ability of the coil system to resolve a defect.

1. The focus[2] is improved very little by decreasing the spacing between coils after the coils are moved closer together than the distance between the flaw and the surface.

2. The focus is not improved by decreasing the cross section of the coils as long as the distance between the defect and the surface of the specimen is greater than the cross section of the coils.

3. Small changes in the fill factor (the ratio of specimen diameter to coil diameter) cause relatively little change in the focus.

We improved our old computer programs and wrote a number of new ones, including programs for calculating coil impedance and voltage for two different conductors clad in layers on a third. We also wrote a program that calculates the response of a general eddy-current impedance bridge to a set of normalized impedance values from any impedance program. The program will automatically "balance" the bridge to give the same voltage for any two impedance values selected from the set. Any component in the bridge can be allowed to change its value slightly, and the new voltages and the voltage change for the particular drift will be displayed. This program has proven very valuable in designing eddy-current tests that use the impedance bridge. We modified an old program to aid in the construction of coils after we determine the general shape of the coil by means of other programs. We supply one of three things to the program – wire gage, number of turns, or inductance – and the program then calculates the other two values. It also calculates the number of turns per layer, the number of layers, and the resistance of the coil to direct current. This program will aid greatly in the actual design and winding of coils.

Ultrasonic Inspection Methods

Optical Visualization of Ultrasound (H. L. Whaley, Jr., K. V. Cook, L. Adler[1])

We established the necessary conditions for successfully making motion pictures from the display on the television monitor of the schlieren system. We made motion pictures of the interaction of ultrasound with the material under test in typical situations. The sample of chief interest was an Inconel plate (12.6 × 10.2 × 1.26 cm) that contained machined notches at various angles to the surface of the plate. The effect of these notches upon the propagation of ultrasonic pulses in the plate is made clear by the films.

Ultrasonic Frequency Analysis (H. L. Whaley, Jr., K. V. Cook, L. Adler[1])

We observed systematic variations in frequency spectra of ultrasonic pulses reflected from the flat, polished ends of metal rods as a function of reflector angle and size. The experimental apparatus for supporting and rotating the rods was described in the last report.[3] Figure 22.1 is a schematic representation of the experimental setup. The observed variations are quite reproducible under carefully controlled conditions.

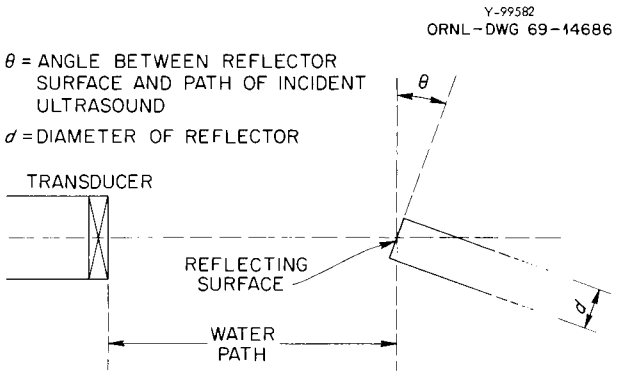

Fig. 22.1. Relative Positions of Transducer and Centered Reflector.

We are developing mathematical models to improve our understanding of these variations in frequency spectra. The first analytical model developed to explain the results obtained in the reflection experiments failed to account for an observed second-order effect that seems to be affected by the length of the water path between the source and reflector. An improved model was devised to account, both conceptually and numerically, for changes in water path and for those cases in which the center of the reflector is not on the axis of the source (that is, the system has not been "centered"). The success of this relatively simple model in describing the observed effects has been remarkable considering the complicated situation that actually exists experimentally. The basis of the model is an assumed interference of reflections from opposite extremes of the reflector.

Because spectral variations depend on "centering" or how closely the center of the reflector is aligned with the axis of the source, an experimental method to ensure adequate centering was necessary. This was simple enough when the angle θ in Fig. 22.1 was equal to zero (that is, when the sound beam was perpendicular to the reflecting surface), but centering was complicated whenever $\theta \neq 0$, as could happen if this technique were used to evaluate flaws in materials. We developed a simple experimental method of properly centering the system that ensures less than a 2% error from this source. Accurate centering is accomplished by finding the position at which the interference effects are most pronounced.

Further evaluation of the effect of the water path on frequency spectra in the "near field" or Fresnel zone of the transducer has now made it clear that an additional mechanism operates for very small water paths; therefore, our model does not apply very well to this special case. Because experimental results in the near field are extremely sensitive to small errors in centering and angular orientation, they are very difficult to repeat.

We found that the acoustic impedance of the reflector does not affect the results as it would in an amplitude-based system. Only the size and relative orientation of the reflector — and not the material of which it is made — are factors. This was demonstrated by comparing measurements of Plexiglas rods of two different diameters with those of brass rods of about the same diameters. Although the acoustic impedance of brass is ten times as great as that of Plexiglas, the accuracy with which the diameter of the reflector could be determined from the spectral data was about the same in both cases.

We also experimented on a number of noncircular flat reflectors made by flattening and shaping the ends of brass rods of various cross sections. Figure 22.2 shows the shape and dimensions and axis of rotation of each reflector. Only the end of the rod is used as a reflector; any ultrasound reflected from inside the rod or from the other end arrives later and is not processed. In each case, the dimension determined from the frequency analysis was that in the plane of

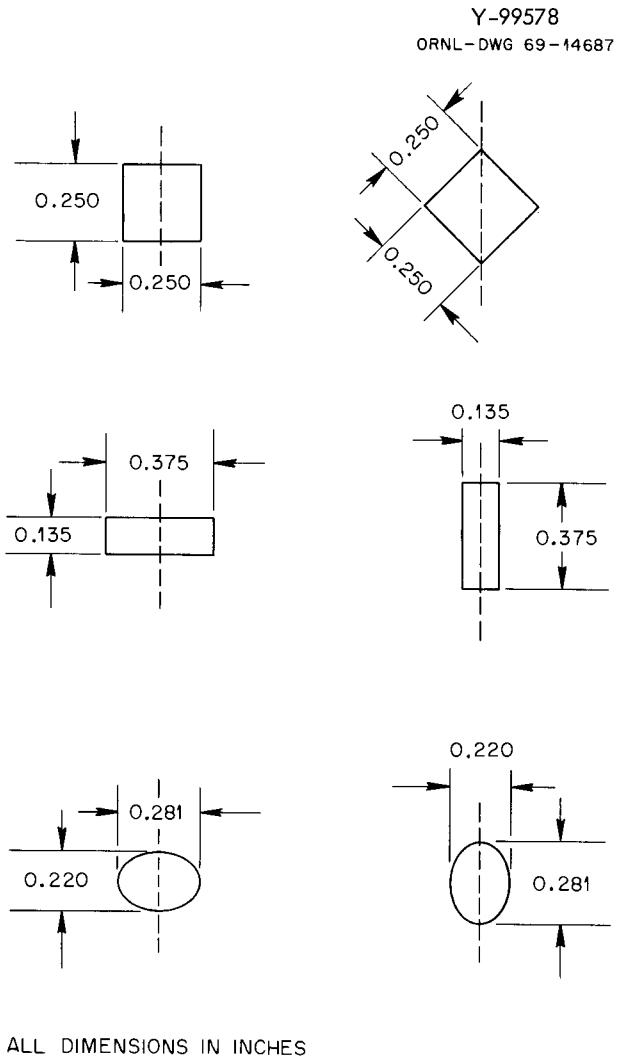

Fig. 22.2. Shapes and Dimensions of Reflecting Surfaces Used. The vertical, dashed line represents the axis of rotation.

rotation of the reflector (that is, the dimension perpendicular to the axis of rotation and passing through the center of the reflector). The results for the square reflector rotated about its diagonal were complicated and have not been completely explained. In all the other cases, the horizontal dimension was determined accurately from the data generated by rotating the reflector through an angle. The two main results from these experiments were that they showed (1) that our model

is applicable to any shape of flat reflector, and (2) that the effect is essentially one dimensional instead of, for example, involving surface area.

Reflection from a spherical surface produces only small spectral changes as a function of reflector size and, of course, reflector angle is not a meaningful term in this case. The two properties observed for changes possibly related to reflector size were the principal frequency and the spectral width. The principal frequency of the spectrum is the frequency component that has maximum amplitude, and the width is proportional to the total area under the normalized spectrum curve. Both of these showed some dependence on reflector size, but the changes were small compared to the experimental errors of transducer positioning; thus, no systematic dependence was found. It appears likely that information on changes related to reflector size could be obtained at lower frequencies.

Penetrating Radiation and Holographic Inspection Methods

X-Ray Attenuation (B. E. Foster, S. D. Snyder)

In continuing our studies of the use of x-ray attenuation for determining the homogeneity of graphite, we developed some preliminary calibrations that will provide direct measurement of the density of graphite as a function of attenuation. We have worked with 0.100- to 0.800-in.-thick AXF graphite, which has a density of about 1.8 g/cm^3, and with 2.8- to 6-in.-thick fiber-reinforced graphite composites[4] whose density is 1.2 to 1.8 g/cm^3.

For the AXF graphite, we operated our Be window x-ray tube unfiltered at 29 kilovolts constant potential (kvcp) and 8 ma; for the thicker fiber-reinforced graphite, we operated with a 0.163-in.-thick type 6061-T6 Al filter at 90 kvcp and 2.5 ma. The sensitivity of change in thickness, density, or the product of thickness and density to change in attenuation (recorder chart reading) was about 1.5% per chart division for the AXF graphite and about 0.4% per chart division for the fiber-reinforced graphite. Normally, we adjust the x-ray energy conditions and system electronics to display a change of thickness or density

of 1.5 times over the full range of the strip-chart recorder. However, for the AXF graphite, when we compressed the data so that a thickness variation from 0.100 to 0.500 in. could be displayed on the strip-chart recorder, we obtained poorer sensitivity than for the fiber-reinforced graphite. This sensitivity can be improved by further optimizing the x-ray energy conditions and adjustments to the electronics of the system or by limiting the span of thickness to be measured with a single instrument setting.

Radiation Scattering[5] (B. E. Foster, S. D. Snyder)

Our investigation of the use of scattered and fluorescent radiation for measuring the thickness of coatings or claddings on reactor components continued after additional repairs to the 1600-channel analyzer and digital printer.

Sensitivity to a 0.0025-in. piece of Al on a Pb base has been achieved. This sensitivity is apparently due to the 12 kev L_{II} x ray from Pb fluorescence. We are determining the maximum thickness of cladding through which useful sensitivity can be obtained.

The radiation source and detector were mounted on a goniometer to improve the mechanical arrangement. Accurate change and measurement of the angle of incidence of the radiation beam and simple interchange of radiation source and detector are now possible.

References

1. Consultant from the University of Tennessee.

2. C. V. Dodd, W. E. Deeds, J. W. Luquire, and W. G. Spoeri, Fuels and Materials Development Program Quart. Progr. Rept. March 31, 1969, ORNL-4420, pp. 188–192.

3. H. L. Whaley, Jr., and K. V. Cook, Fuels and Materials Development Program Quart. Progr. Rept. Sept. 30, 1969, ORNL-4480, pp. 268–269.

4. F. Lambdin, J. L. Cook, and G. B. Marrow, Fiber-Reinforced Graphite Composite Fabrication and Evaluation, Y-1684 (September 1969).

5. This work is jointly supported by the Fuel Element Fabrication Development Program and is also discussed in Chapter 19 of this report.

23. IMPROVEMENT OF HASTELLOY N AND RELATED COMPOSITIONS

J. R. Weir, Jr. H. E. McCoy, Jr.

This program is aimed at defining and understanding the metallurgical variables that affect the engineering performance of Ni-based structural alloys in reactor environments. Such alloys have been shown to have reduced stress-rupture properties and greatly reduced fracture strain after exposure to thermal-neutron fluences. Our work has concentrated on Hastelloy N. We have found that small additions of Ti, Zr, Hf, and Nb effectively reduce the deterioration of properties caused by irradiation. The end products sought by this program are a better understanding of the factors important to controlling irradiation damage in Ni-based alloys and development of a modified Hastelloy N with improved resistance to irradiation damage.

Mechanical Properties of Hastelloy N and Related Compositions

Aging and Irradiation of New Alloy Compositions (C. E. Sessions)

We are continuing our studies of the influence of alloy composition on aging behavior and irradiation damage of the Ni-base alloy Hastelloy N. We continue to look primarily at the elements Ti, Nb, and Hf added independently and collectively to the Ni–12% Mo–7% Cr base alloy. Previous studies have shown that the amounts of these elements needed to produce good thermal stability and good postirradiation creep-rupture properties is a strong function of the aging or irradiation temperature. We have previously shown that properties deteriorate at higher temperatures when the M_2C type of carbides[1] are precipitated. Outstanding properties are found when the alloy composition and heat-treatment temperatures favor precipitation of the MC type of carbide during aging or irradiation.

Recent studies have been aimed at determining the optimum concentrations of Nb, Hf, and Ti to produce an alloy with good postirradiation properties. Our results to date are fragmentary.

Aging Results. — A group of new alloys listed in Table 23.1 were aged 1000 hr at either 650 or 760°C and then tensile tested at 650°C at

Table 23.1. Tensile Properties[a] of New Alloy Compositions After Aging

Alloy Number	Alloying Addition,[b] wt %					Treatment[c]	Strength, psi		Total Elongation (%)
	Ti	Nb	Zr	Hf	Si		Yield	Ultimate Tensile	
							$\times 10^3$	$\times 10^3$	
285	0.08	0.5	0	0		46	40.5	91.9	43.7
						148	35.2	79.1	23.5
286	0.2	0.5	0	0		46	41.1	92.1	44.0
						148	36.5	81.9	25.1
287	0.1	0.6	0	0	0.1	46	40.9	100.7	41.1
						148	33.8	83.7	22.7
297	0.2	0.6	0	0		46	41.9	93.9	41.5
						148	35.5	87.2	25.7
299	0	0	0.04	0.5		46	47.9	92.6	36.3
						148	36.3	89.6	45.8
301	0	0	0.06	0.8		46	48.0	94.6	43.3
						148	39.2	90.4	39.1
304	0	0	0	0		46	36.8	84.8	32.1
						148	34.3	76.1	19.6
306	0	0.5	0.08	0	0.3	46	41.3	87.6	41.3
						148			
310	0.1	0.6	0.03	0.5		46	45.0	94.6	31.4
						148	42.6	80.4	18.3
312	0.2	0.6	0.03	0.4		46	48.3	97.9	39.1
						148	43.5	96.1	36.7
314	0.8	1.3	0.03	0.6		46	44.1	91.8	27.7
						148	43.7	89.2	25.4

[a]Tested at 650°C at a strain rate of 0.002 min^{-1}.

[b]All alloys have a base composition of Ni–12% Mo–7% Cr–0.06% C.

[c]Treatment 46 denotes an anneal of 1 hr at 1177°C and aging for 1000 hr at 650°C; treatment 148 denotes an anneal of 1 hr at 1177°C and aging for 1000 hr at 760°C.

a strain rate of 0.002 min^{-1}. Combined additions of Ti, Nb, Zr, and Hf – strong formers of the MC type of carbide – ranged from zero to 2.7% in the eleven alloys. The yield strength after aging at 650 or 760°C ranged from 33,000 to 48,000 psi. The yield strength was higher after aging at 650°C for each alloy except alloy 304, which contained none of these additions. For the three alloys that contained both Nb and Hf additions (alloys 310, 312, and 314), the yield strength even after 1000 hr at 760°C exceeded 40,000 psi. Thus, the yield strength after aging increases with increasing alloy content for aging at both 650 and 760°C.

The tensile ductility after aging ranged from 19 to 45%. For each alloy, the lowest ductility was found after aging at 760°C. This same trend was observed in a previous aging study on Ti-modified commercial alloys.[2] After aging at 650°C, each alloy except 314 had greater than 30% total elongation. Thus, alloy 314 shows that the greatest alloying additions do not correspond to optimum ductility after aging.

Four alloys – 285, 287, 304 and 310 – had less than 25% ductility after aging. Thus, relative to the other alloys, these four compositions undergo precipitation reactions on aging at 760°C that reduce the ductility. Alloy 304 did not contain any strong carbide formers (Ti, Nb, Hf, or Zr) and, on the basis of previous work, would be expected to lose ductility because of the tendency to precipitate the M_2C type of carbides. The other alloys that had low ductilities contained 0.5% Nb (alloy 285), 0.6% Nb–0.1% Ti–0.1% Si (alloy 287) and 0.6% Nb–0.5% Hf–0.1% Ti (alloy 310). Thus, one might infer that 0.6% Nb by itself or in combination with 0.1% Ti and 0.5% Hf does not produce a desirable type or distribution of carbide precipitate.

Effects of Irradiation. – Table 23.2 lists some results for new alloys that were recently tested for postirradiation creep-rupture properties. Each alloy has the base composition Ni–12% Mo–7% Cr–0.06% C with various minor additions of Ti, Nb, Zr, or Hf as listed in Table 23.2. The mechanical properties and phases present for unirradiated material after aging have not been determined; however, we can evaluate the relative benefit of a given combination of alloying elements by comparing the creep properties after irradiation.

Table 23.2. Postirradiation Creep-Rupture Properties of New Modifications of the Ni–12% Mo–7% Cr–0.06% C Base Alloys[a]

Alloy Number	Alloy Additions, wt %				Postirradiation Creep Properties			
	Ti	Nb	Zr	Hf	Stress (psi)	Rupture Life (hr)	Fracture Strain (%)	Minimum Creep Rate (%/hr)
					$\times 10^3$			
284	0	0	0	0	15	154.7	0.2	
286	0.2	0.5	0	0	40	9.4	0.9	0.0698
289	1.0	0	0	0	30	350	4.56	
290	1.05	0	0	0	30	> 350	> 6.2	
291	2.0	0	0	0	40	388.3	4.7	0.0085
292	2.4	0	0	0	40	> 690	> 0.7	
293	3.0	0	0	0	47	> 166	> 0.4	
301	0	0	0.06	0.8	40	339.6	10.8	
303	0.5	0.8	0	0	40	271	6.3	0.0194
315	0.5	0	0.05	0	40	48.1	4.4	0.0810
181	0.5	1.8	0	0	40	175.3	4.25	0.02
					35	666.2	4.28	0.008
					27	1580[b]	3.5[b]	0.002
184	1.2	0	0	1.2	47			
					35	2292	22.7	0.005
232	0	0	0	1.2	40	405.5	13.3	0.022
					27	2035.0[b]	6.9	0.002

[a]Alloys annealed 1 hr at 1177°C, irradiated at 760°C to 3×10^{20} neutrons/cm^2, and then creep tested at 650°C.

[b]Test discontinued before failure.

Figure 23.1 compares the results of stress-rupture testing for these new alloys with those for standard irradiated Hastelloy N. These data were obtained at 650°C after irradiation at 760°C to a thermal-neutron fluence of 3×10^{20} neutrons/cm^2. These particular test conditions have been shown to reflect the sensitivity of postirradiation properties to alloy content.[3]

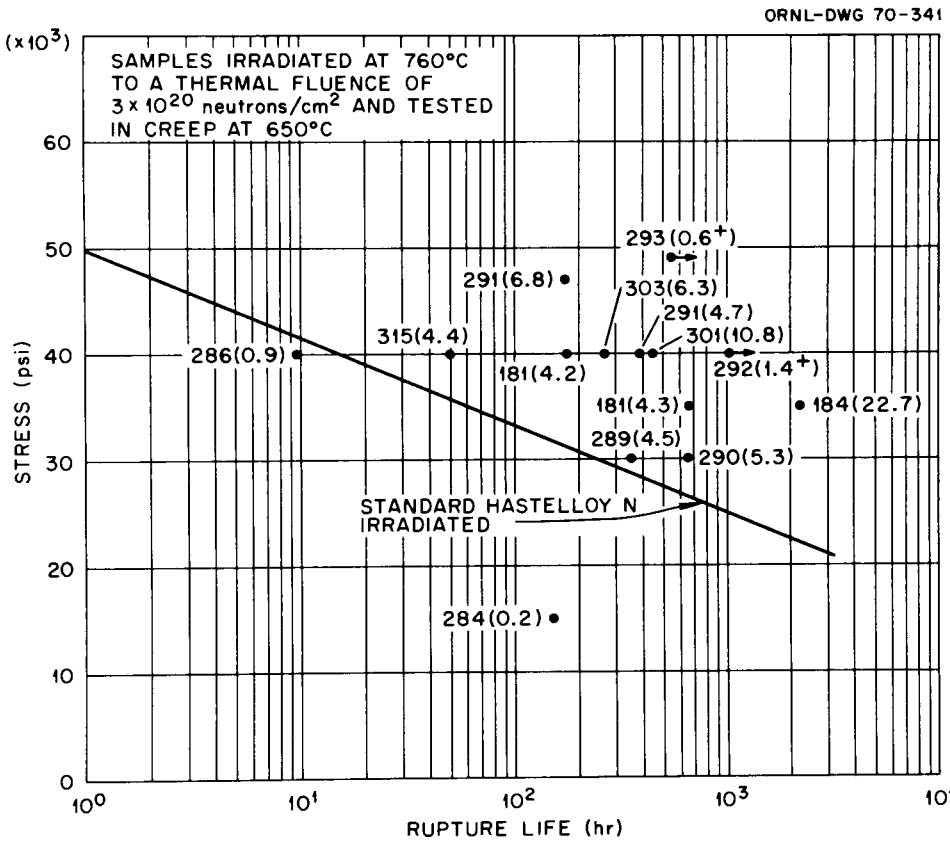

Fig. 23.1. Postirradiation Stress-Rupture Properties of Several Alloys of Modified Hastelloy N at 650°C. All materials were annealed for 1 hr at 1177°C and irradiated at 760°C to a thermal fluence of 3×10^{20} neutrons/cm^2. All alloys have a base composition of Ni–12% Mo–7% Cr–0.06% C, and the carbide-forming additions to each alloy are shown in Table 23.2. The numbers in parentheses indicate the fracture strain.

As expected from previous results, alloy 284, which contains no Ti, Nb, Zr, or Hf, had inferior properties compared to standard Hastelloy N. Alloy 286, containing 0.7% of additions (0.5% Nb + 0.2% Ti), is no better than standard Hastelloy N. However, alloy 301 (0.8% Hf) and alloy 315 (0.5% Ti + 0.05% Zr) both appear to be considerably better than the standard alloy in terms of rupture life and fracture strain.

Alloys 289 and 290 both contain about 1.0% Ti. The test specimens have not yet failed, as indicated by the arrows in Fig. 23.1. As discussed previously[3] the specimens with the 1.0% Ti addition show a large variation in creep properties after irradiation at 760°C that we do not yet fully understand. The properties of these two alloys at 30,000 psi

stress look very good, however. For increasing alloy content, alloy 232 (1.2% Hf) is particularly outstanding, with a 13% fracture strain in a creep test at 40,000 psi.

The alloys with about 2% total additions of strong carbide formers probably have the best postirradiation creep properties of the alloys shown here. Alloys 181 (1.8% Nb + 0.5% Ti), 184 (1.2% Ti + 1.2% Hf), and 291 (2.0% Ti) contain about 2% total additives, and the postirradiation creep properties are excellent. Of the three alloys tested to date, alloy 184 is far superior, with 23% fracture strain for creep at 35,000 psi. These recent results on alloys with 2% Ti are also quite encouraging and indicate that Ti additions alone can probably produce the desired mechanical behavior during service at 700°C.

Scale-up of Modified Hastelloy N (H. E. McCoy, Jr.)

Previous work on small, 2-lb laboratory melts revealed two alloys that had attractive postirradiation properties: alloy 181, with additions of 0.5% Ti and 2% Nb, and alloy 184, with additions of 1% Ti and 1% Hf. The next step with these alloys has been to obtain commercial experience by procuring two 50-lb melts of each from Allvac Metals Company. The alloys were vacuum melted twice, a practice used for making larger melts. The commercial alloy containing 1% Hf and 1% Ti was designated alloy 69-641. No difficulties were encountered during melting and fabrication to 1/2-in.-thick plate. The alloy containing 0.5% Ti and 2% Nb was designated 69-648. Some cracking was noted during fabrication; but the cracks were ground out, and a useful product was obtained.

The first test on these alloys was a weldability test in which the 1/2-in.-thick plates were welded to a carbon steel backing for restraint and joined with filler metal made from the same heat. Dye penetrant inspection of heat 69-641 showed several indications of small cracks, but these were very shallow and easily removed by rotary filing. Four side bends of weld metal were made from 1/8-in.-thick strips cut perpendicularly to the weld direction. Metallographic examination revealed some porosity in the weld metal, but the level was acceptable. Some cracks also appeared in heat 69-648 during welding, but these were

easily removed. Side bends were also made from weld metal of this heat, and only one of the four showed any flaws. However, metallography revealed that this one flaw was indeed a serious crack in the weld metal.

This difficulty in fabricating heat 69-648 (0.5% Ti, 2% Nb) was unexpected, and another commercial melt was made. A proprietary change was made in the deoxidation practice during melting, and the resulting ingot was easily fabricated. When this material is received, it will be tested for weldability.

Only limited tests of mechanical properties were run on these new heats of material. The following general observations were made.

1. The properties of the commercial heats are quite similar to those of our 2-lb laboratory heats.

2. The commercial heats, as well as the laboratory heats, have lower tensile strengths than standard Hastelloy N but higher creep strength.

3. Tensile tests show that welding increases the strength and decreases the ductility. The trends are equivalent to those noted[4] for standard Hastelloy N, but the fracture strains are higher for the modified alloys.

Property Changes of Hastelloy N During Irradiation (H. E. McCoy, Jr.)

The Molten Salt Reactor Experiment (MSRE) is constructed of standard Hastelloy N. Test samples for surveillance purposes were placed in the reactor core and outside the reactor vessel. The environment inside the core is a molten fluoride fuel salt consisting of 65 LiF–29.1 BeF_2–5 ZrF_4–0.9 UF_4 (mole %). The salt operates at about 650°C and corrodes the metal at a rate of less than 0.0001 in./year. Control samples are exposed to static barren fuel salt in another facility to measure the effects of the annealing on the properties. The samples outside the reactor vessel are exposed to an oxidizing environment of N_2 and 2 to 5% O_2. The same heat of material (Haynes-Stellite heat 5085) was used for both sets of samples so that it would be possible to follow the property changes with increasing fluence. The detailed examinations of these samples have been reported.[5–7]

The variation of the fracture strain with test temperature is shown in Fig. 23.2 for various sets of samples. The fracture strain is reduced over the entire range of test temperatures studied. The reduction in fracture strain at low temperatures is associated with carbide precipitation and could be recovered by postirradiation annealing.[7] The reduction in ductility above 500°C is due to the presence of He from the $^{10}B(n,\alpha)^{7}Li$ reaction and cannot be recovered by annealing. Some changes were noted in the properties of the control samples, but these changes were small compared to those for the irradiated samples. As shown in Table 23.3, only modest changes took place in yield strength. The reductions in ultimate tensile strength are due to the failure of the aged samples at lower fracture strains. The changes in the fracture strains are quite modest compared with the changes observed for the irradiated samples.

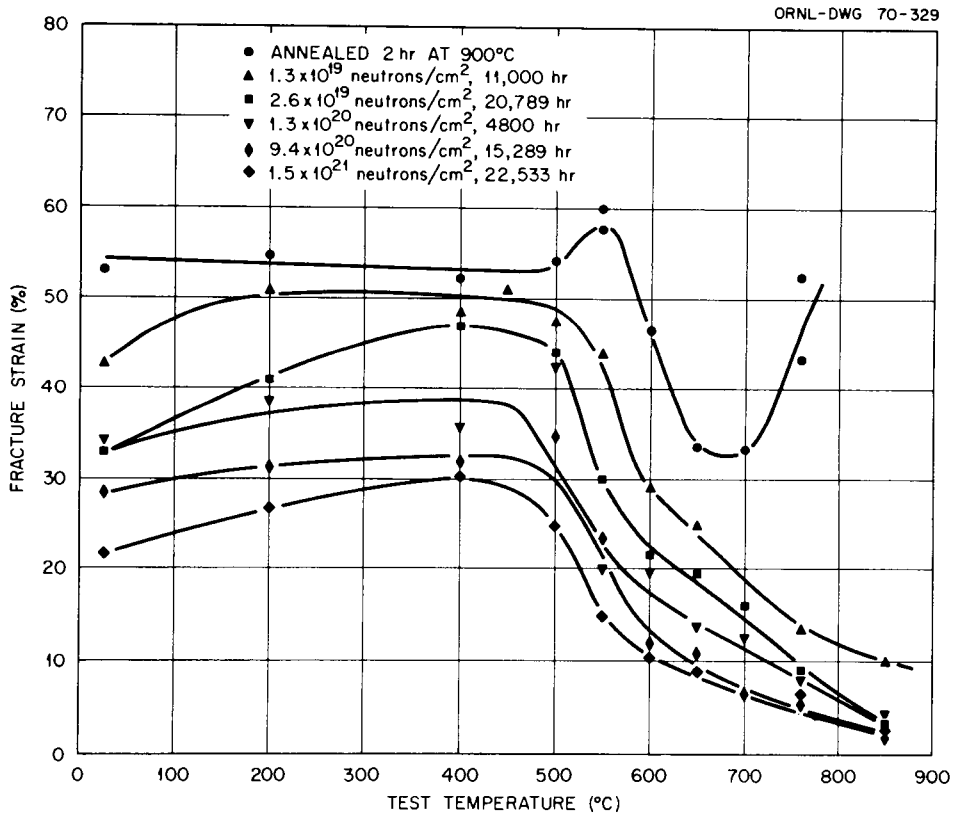

Fig. 23.2. Variation of Fracture Strain with Test Temperature for Hastelloy N. Samples were irradiated in the Molten Salt Reactor Experiment at 650°C to the indicated thermal fluence and then tested at a strain rate of 0.05 min^{-1}.

Table 23.3. Comparison of the Tensile Properties of Surveillance Samples for Molten Salt Reactor Experiment (Haynes-Stellite Heat 5085) Before and After Irradiation

Treatment	Stress, psi				Fracture Strain, %	
	Yield		Ultimate Tensile			
	at 25°C	at 650°C	at 25°C	at 650°C	at 25°C	at 650°C
Annealed 2 hr at 900°C	51,500	29,500	120,800	75,800	53.1	33.7
Annealed 2 hr at 900°C, Aged 22,533 hr at 650°C	48,100	32,600	108,500	75,200	40.6	32.0
Annealed 2 hr at 900°C, Irradiated for 22,533 hr at 650°C to a thermal fluence of 1.5×10^{21} neutrons/cm^2	53,900	36,400	89,000	50,800	22.1	9.3

Creep-rupture tests were run on these same samples; the results are shown in Fig. 23.3. The minimum creep rates are not changed appreciably by irradiation,[8] but the rupture life at a given stress level and the fracture strain are reduced. The progressive reduction in these properties with increasing thermal fluence is shown in Fig. 23.3. The most dramatic effects are on the fracture strains: thermal fluences of only 1 to 2 $\times 10^{19}$ neutrons/cm^2 reduce the fracture strain to values of 1 to 2%. This heat of material at this fluence contains only about 1 ppm He. The reduction in fracture strain at this low level of He indicates the extreme sensitivity of this material to the presence of He.

Further analyses of the results on irradiated Hastelloy N reveal a very distinct minimum fracture strain at a strain rate of about 0.1%/hr.[8]

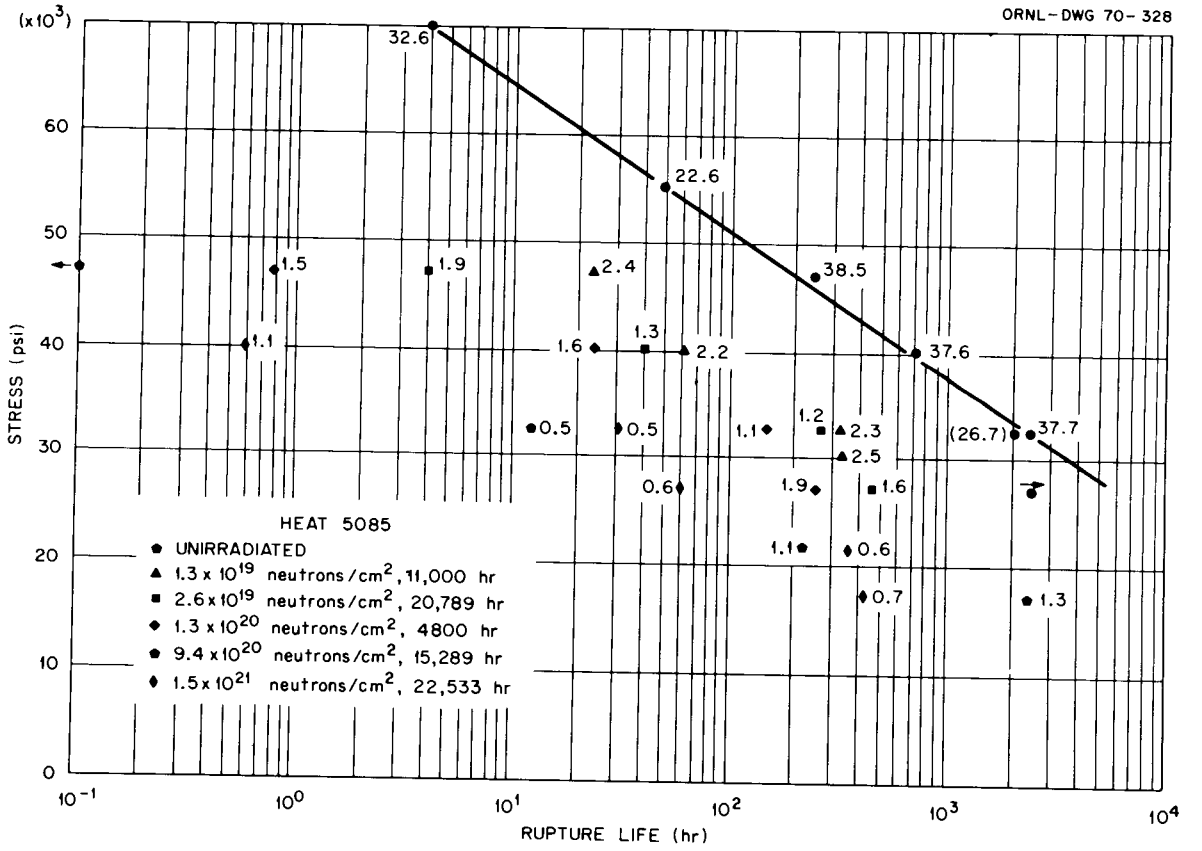

Fig. 23.3. Stress-Rupture Properties of Hastelloy N Surveillance Samples Exposed in the Molten Salt Reactor Experiment for Indicated Time at 650°C to Indicated Thermal Fluence. The number by each datum point indicates the fracture strain.

The dependence of the magnitude of this minimum strain on He content is shown in Fig. 23.4. Note that the fracture strains at higher strain rates are very dependent upon He content, but that the fracture strain at a strain rate of 0.1%/hr has already reached a very low value by the time the He content is only 1 ppm.

Samples exposed to the highest fluence of 1.5×10^{21} thermal and 1.1×10^{21} fast (> 50 kev) neutrons/cm^2 were examined by transmission electron microscopy. These samples contained numerous He bubbles, but no other types of damage were present.

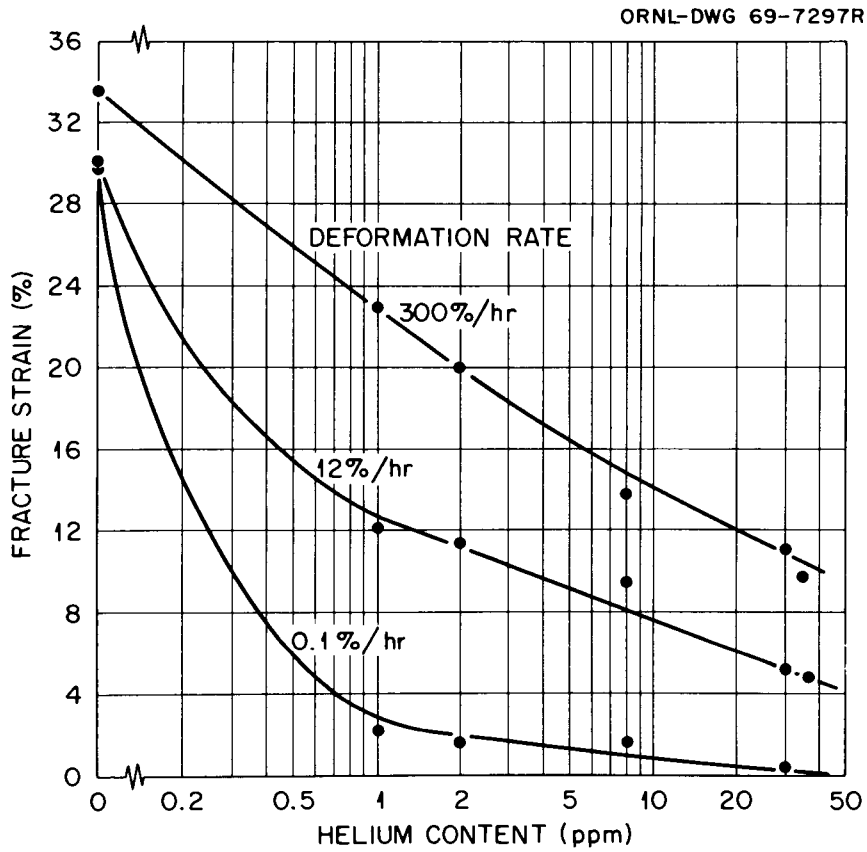

Fig. 23.4. Variation of Fracture Strain with Helium Content for Hastelloy N Irradiated in the Molten Salt Reactor Experiment at 650°C.

References

1. The symbol M here signifies the metal content of a carbide.
2. C. E. Sessions, Fuels and Materials Development Program Quart. Progr. Rept. Sept. 30, 1969, ORNL-4480, pp. 374–375.
3. C. E. Sessions and R. E. Gehlbach, Fuels and Materials Development Program Quart. Progr. Rept. Sept. 30, 1969, ORNL-4480, pp. 279–291.
4. H. E. McCoy and D. A. Canonico, Welding J. (N.Y.) 48(5), 203-s–211-s (May 1969).
5. H. E. McCoy, An Evaluation of the Molten Salt Reactor Experiment Hastelloy N Surveillance Specimens – First Group, ORNL-TM-1997 (November 1967).
6. H. E. McCoy, An Evaluation of the Molten Salt Reactor Experiment Hastelloy N Surveillance Specimens – Second Group, ORNL-TM-2359 (February 1969).
7. H. E. McCoy, An Evaluation of the Molten Salt Reactor Experiment Hastelloy N Surveillance Specimens – Third Group, ORNL-TM-2647 (January 1970).
8. H. E. McCoy, J. Nucl. Mater. 31(1), 67–85 (May 1969).

24. ADVANCED MATERIALS FOR STEAM GENERATORS

P. Patriarca G. M. Slaughter

The purpose of this program is to determine the corrosion resistance of welds in several high-temperature alloys being considered for use in steam generators for advanced high-temperature reactors. We need to know how well these weldments will resist both general and preferential corrosion in steam at 595 to 760°C.

The program includes four areas of investigation: (1) general corrosion (formation of a uniform scale) at 595 and 650°C, including an evaluation of the general weldability of various combinations of base and filler metals; (2) general corrosion at 705 to 760°C; (3) preferential corrosion (e.g., oxidation at the fusion line, pitting, and stress cracking); and (4) mechanical properties.

General Corrosion at 595 and 650°C and Weldability

Corrosion Studies (J. P. Hammond)

Specimens from welds of similar and dissimilar metals for studies of general corrosion by measurements of weight gain and scale thickness were exposed to superheated steam at 595 and 650°C for periods to 8000 hr, and interpretative analyses were made of them. The weldments under investigation were reported previously[1] but are listed again in Table 24.1 for convenience in interpretation of results.

Measurements of Weight Gains. — The corrosion results for the weldments between similar metals at 595 and 650°C are shown in Figs. 24.1 and 24.2; those for weldments between dissimilar metals are shown in Figs. 24.3 and 24.4. The linear portions of the curves were established from corrosion data by the method of least squares. Rather than fit curves of a parabolic form to the short-time data (3000 hr and less), we extrapolated to the coordinate to establish intercepts.

The results for the A16 weldments (2.25% Cr–1% Mo welded to Incoloy 800) are not included in these graphs, since at 595°C it was

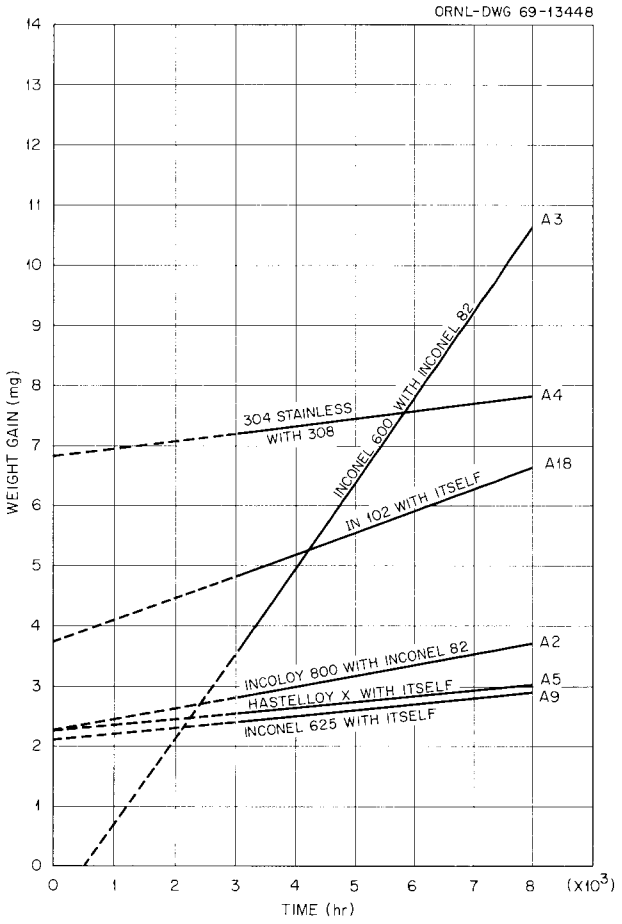

Fig. 24.1. Corrosion of Weldments Between Similar Metals in Superheated Steam at 595°C. The curves are a best fit to a linear rate law. Specimen surface area was 20 cm^2.

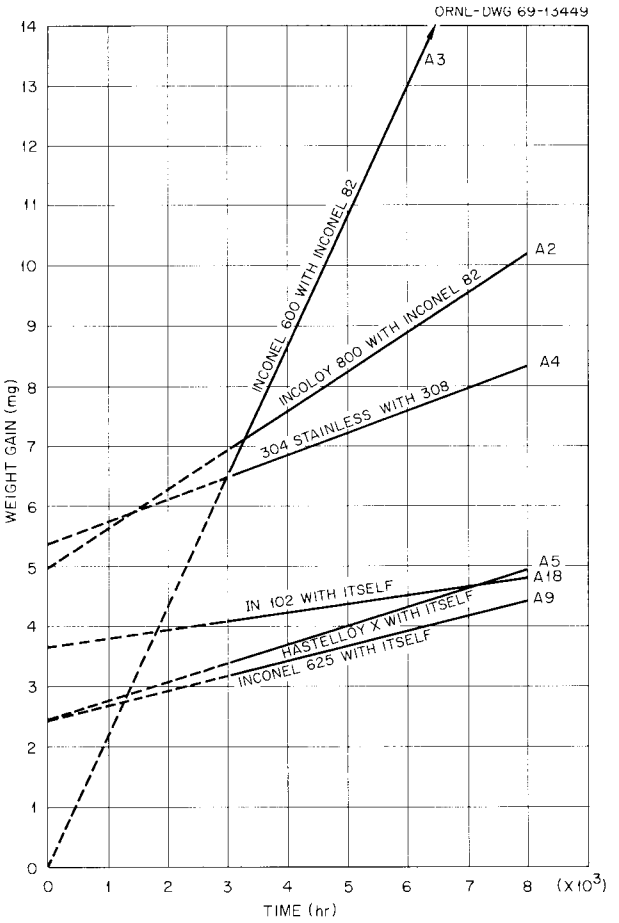

Fig. 24.2. Corrosion of Weldments Between Similar Metals in Superheated Steam at 650°C. The curves are a best fit to a linear rate law. Specimen surface area was 20 cm^2.

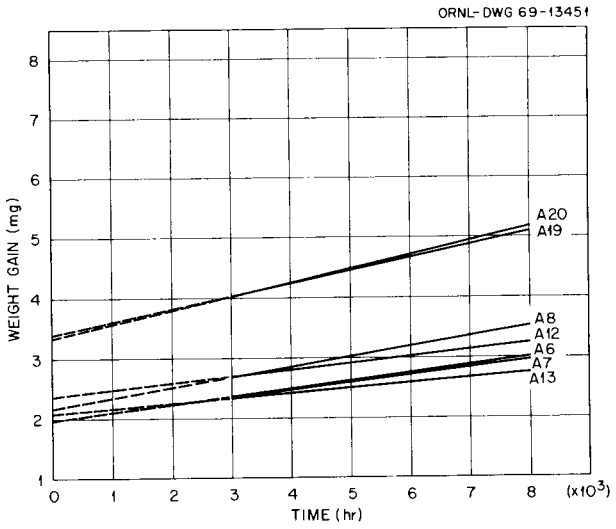

Fig. 24.3. Corrosion of Weldments Between Dissimilar Metals in Superheated Steam at 595°C. The curves are a best fit to a linear rate law. Specimen surface area was 20 cm^2.

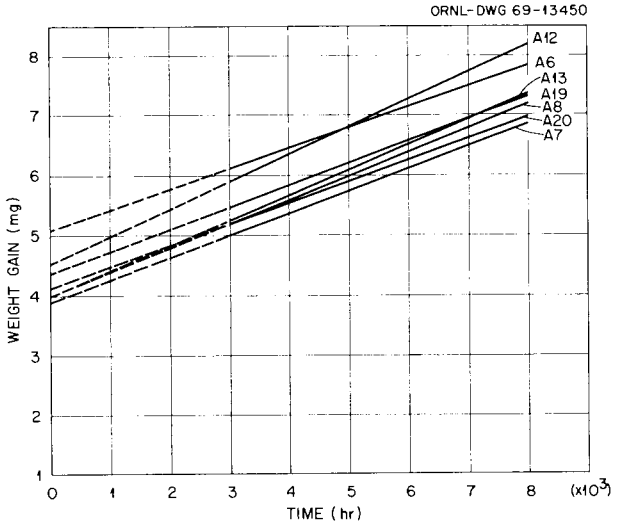

Fig. 24.4. Corrosion of Weldments Between Dissimilar Metals in Superheated Steam at 650°C. The curves are a best fit to a linear rate law. Specimen surface area was 20 cm^2.

Table 24.1. Alloy Combinations for Steam Corrosion Studies at 595 and 650°C

Identification Code	Base Metal	Base Metal	Filler Metal
A9	Inconel 625	Inconel 625	Inconel 625
A13	Inconel 625	Incoloy 800	Inconel 625
A12	Inconel 625	Incoloy 800	Inconel 82
A18	IN 102	IN 102	IN 102
A19	IN 102	Incoloy 800	IN 102
A20	IN 102	Incoloy 800	Inconel 82
A5	Hastelloy X	Hastelloy X	Hastelloy X
A6	Hastelloy X	Incoloy 800	Hastelloy X
A8	Hastelloy X	Incoloy 800	Hastelloy W
A7	Hastelloy X	Incoloy 800	Inconel 82
A2	Incoloy 800	Incoloy 800	Inconel 82
A3	Inconel 600	Inconel 600	Inconel 82
A16	2.25% Cr–1% Mo	Incoloy 800	Inconel 82
A4	Type 304 stainless steel	Type 304 stainless steel	Type 308 stainless steel

corroded 30 to 100 times more than the other weldments between dissimilar metals (over 30 mg after 8000 hr) and since at 650°C it was so corroded as to preclude testing.

Noteworthy features of the plots for the weldments between similar metals are the very low corrosion rates for the Inconel 625 (A9) and Hastelloy X (A5) weldments as contrasted to the higher rates for Inconel 600 welded with Inconel 82 (A3). Type 304 stainless steel welded with type 308 stainless steel (A4) shows high initial amounts of corrosion but surprisingly low linear rates. The linear rate of corrosion on all weldments is greater at 650°C than at 595°C, except that for the IN 102 weldment (A18), which decreases. Note also that the level of corrosion of the Incoloy 800 weldment (A2), as well as the rate, is substantially greater at 650°C than at 595°C.

The trends for the weldments between similar metals (Figs. 24.1 and 24.2) correlate with the results for the weldments between dissimilar metals (Figs. 24.3 and 24.4) and can be used to explain the close bracketing of curves for the exposure at 650°C and their separation into two groups at 595°C.

Metallographic Examination of Scale Thickness and Localized Corrosion. – A thorough examination of fusion lines and adjacent regions in the weldments failed to disclose any evidence of aggravated corrosive attack. The scale formed on the root pass of the weld deposits generally was similar to that associated with the remainder of the weld metal. The transition in scale microstructure from parent metal to filler metal after 2000 hr at 595°C was hardly discernible in some instances. With longer exposures, scale microstructures became distinctly different, but the transition from one scale structure to the next usually was gradual.

The scales that formed usually had two components: first, a continuous oxide layer of uniform thickness and, second, oxide protrusions (intergranular penetrations, transgranular Widmanstätten-type formations, or sporadic pit-type formations) that extended from the surface layer into the substrate.

Figure 24.5 illustrates the scales formed on weldment A8 (Hastelloy X welded to Incoloy 800 with Hastelloy W filler metal) after 4000 hr of exposure at 650°C. Figure 24.6 shows the scales on weldment A13 (Inconel 625 welded to Incoloy 800 with Inconel 625 filler metal) after 8000 hr at 650°C. The scale on Incoloy 800 after the 8000 hr of exposure is little different from that after 4000 hr and consists of protrusions into the base metal and a well-defined, uniformly thick surface component.

The Hastelloy W filler metal of weldment A8 had a protrusion component of thin Widmanstätten platelets that extended to considerable depths into the substrate. These oxide platelets were not as distinct on some specimens, and their prominence and depth appeared to depend upon the extent of cold work in the substrate induced during specimen preparation (milling to size and, subsequently, grinding). The cold working promoted the formation of Widmanstätten platelets.

Inconel 625, Hastelloy X, and IN 102 were used both as base metals and as filler metals. It appeared that these alloys formed slightly less scale when used as weld metals than as base metals. (For example, compare Inconel 625 as filler metal and base metal in Fig. 24.6.) The

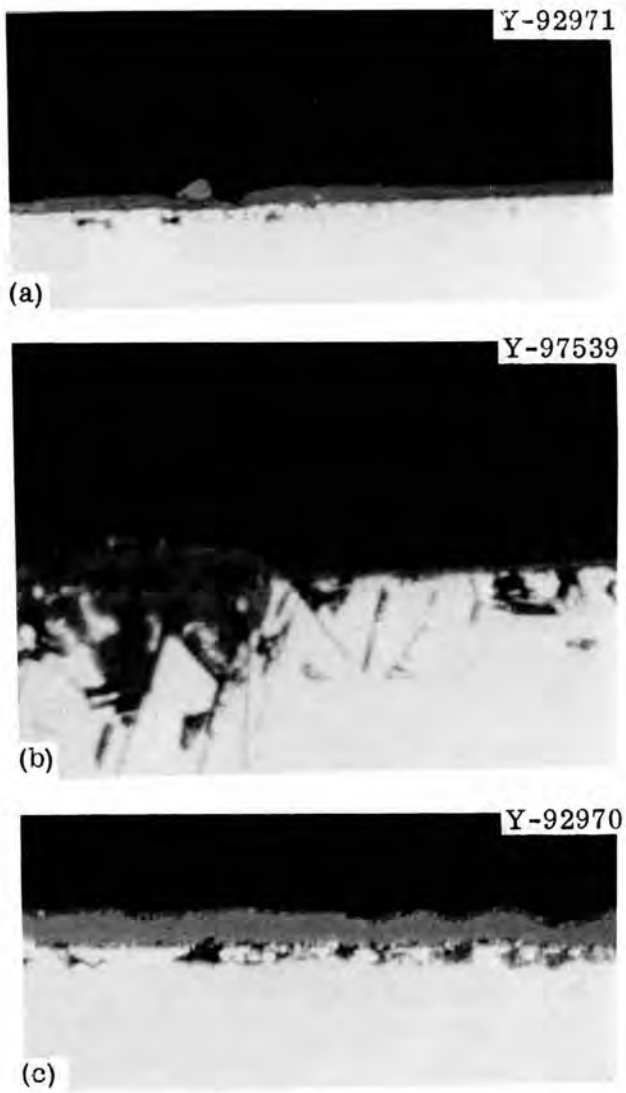

Fig. 24.5.1 Typical Scales on Weldment A8 after 4000 hr of Exposure at 650°C. From top to bottom are (a) plate (Hastelloy X), (b) filler metal (Hastelloy W), and (c) plate (Incoloy 800). 2000×.

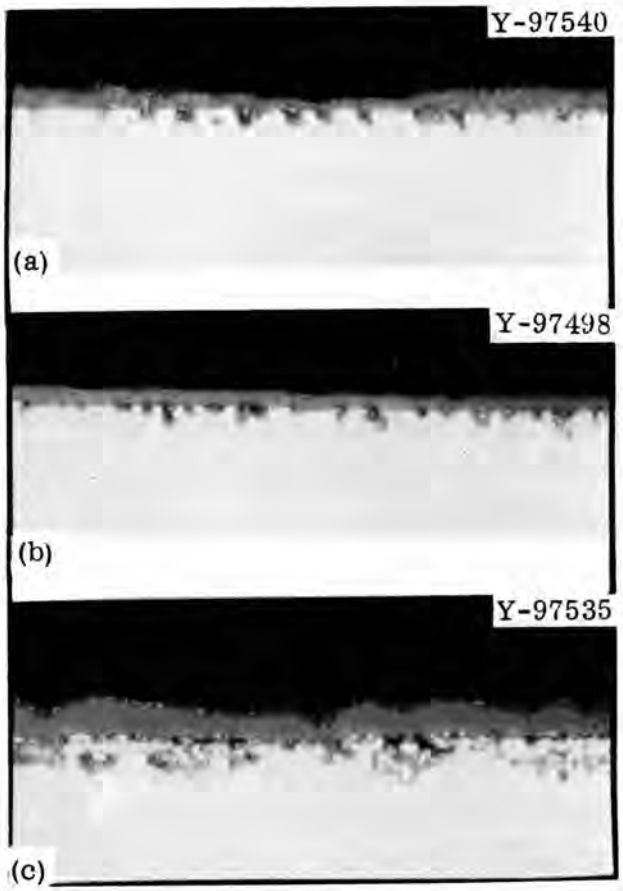

Fig. 24.6. Typical Scales on Weldment A13 after 8000 hr of Exposure at 650°C. From top to bottom are (a) plate (Inconel 625), (b) filler metal (Inconel 625), and (c) plate (Incoloy 800). 2000×.

scales that formed on Hastelloy X as filler metal and base metal were comparable to those of Inconel 625 except, possibly, for a smaller protrusion component.

Alloy IN 102, used as a base metal for weldments A18, A19, and A20, formed more scale (as surface layer plus pit-type substrate attack) at 595°C than at 650°C. This agrees with the measurements of weight gain (weldment A18 of Figs. 24.1 and 24.2). The scales formed on IN 102 when used as a filler metal were uniform, very thin, and about the same thickness after exposures at 595 and 650°C.

The scales formed on Inconel 82 filler metal at 595 and 650°C were quite similar, but those formed on Incoloy 800 at the two temperatures were different. The layer and protrusion components of the scale formed

on Incoloy 800 at the higher temperature were much more fully developed [Figs. 24.5(c) and 24.6(c)].

The scales formed on Inconel 600 used as a base metal were highly irregular and contained a very pronounced intergranular protrusion component that extended as much as 12 μm into the substrate of samples exposed at 650°C. The surface scale contained three separate and highly irregular layers, though one or two might be missing at any particular location. On the other hand, the scales that formed on type 304 stainless steel base metal and type 308 stainless steel weld metal (weldment A4) were characterized by a relatively thin layer component and almost no oxide protrusion into the substrate.

The scales (including protrusions) that formed on Inconel 625, Hastelloy X, and IN 102 as base metal and weld metal and on Incoloy 800 base metal at 595 and 650°C ranged from 1 to 5 μm thick. These scales were generally uniform and seemingly tenacious. The scales formed on Inconel 82 weld metal at 595 and 650°C were about 2 and 3 μm thick, while those on Hastelloy W were as much as 6.5 μm thick, depending upon the extent of cold work. Those on Inconel 600 ranged from about 10 to 14.5 μm thick, while the scales on types 304 and 308 stainless steel were usually 1 μm thick or less.

Evaluation of Scale Flaking. – Whereas it had been believed that alloy IN 102 spalled at 650°C, recent tests indicated that it does not. A reexamination of metallographic specimens and correlations of corrosion data for weldments between similar and dissimilar metals confirmed that this alloy does not flake at 650°C. Therefore, the cause of the superior corrosion resistance of IN 102 at the higher temperature (650°C as compared to 595°C) must be attributed to other factors and probably is related to a beneficial, diffusion-dependent alloying of the IN 102 scale at the higher temperature.

Table 24.2 summarizes the results of the experiments conducted on the various base metals to determine their relative propensities toward flaking. Comparison of the amount of scale theoretically associated with the weight gained during test (as O) with that associated with metal consumed (weight lost by scale removal in relation to original weight)

Table 24.2. Calculated Amounts of Flaking During Corrosion Tests at 650°C and Scale Remaining after Removal Treatment[a]

Alloy Specimens[b]	Weight Loss, Metal[c] (mg)	Weight Gain, Oxygen (mg)	Scale Calculated from		Scale Flaked Off[d] (%)	Scale Remaining[d] (%)
			Weight Loss Metal (mg)	Weight Gain Oxygen (mg)		
Inconel 625	10.7	4.7	14.2	19.6		27.8
Hastelloy X	11.0	4.2	14.8	16.2		8.7
IN 102	11.6	4.0	15.1	16.9		10.7
Incoloy 800	26.6	11.9	39.0	37.3	4.3	
Inconel 600	57.2	19.6	79.2	70.7	10.7	
Type 304 stainless steel	17.8	5.5	25.6	18.0	29.7	

[a]Calculations were based on the following calculated concentrations of metal in scales for the respective alloys: Inconel 625, 79.2%; Hastelloy X, 74.1%; IN 102, 76.7%; Incoloy 800, 68.1%; Inconel 600, 72.3%; type 304 stainless steel, 69.5%. Scales were removed by 2-hr immersion in a solution of boiling 20 wt % sodium hydroxide and 3 wt % potassium permanganate in water. Specimens were removed at 15-min intervals to remove rotted oxide with a soft-rubber eraser.

[b]Specimens had a surface area of 20 cm^2.

[c]Difference between original weight and weight after scale removal.

[d]Percent scale flaked off = $(A - B)/A \times 100$, where A is the scale calculated from weight loss (metal) and B is the scale calculated from weight gain (O). Percent scale remaining after scale-removal treatment = $(B - A)/B \times 100$.

provides a good indication of whether flaking occurred. Table 24.2 indicates that the specimens of Incoloy 800, Inconel 600, and type 304 stainless steel flaked to varying extents, whereas the scales on Inconel 625, Hastelloy X, and IN 102 could not be completely removed and probably had not flaked. However, the latter three specimens and Incoloy 800 appeared to be virtually free of scale except for perhaps inconsequential amounts of microscopic oxide particles embedded along their long edges or at washer-seating locations. An examination of

the microstructures of the scale on the Inconel 625 [Fig. 24.6(a)], Hastelloy X [Fig. 24.5(a)], and IN 102 samples used as base metals showed embedded particles protruding into the substrate; this explains why it was virtually impossible to remove all of the scale on these alloys.

When we consider the nature of the scale structure on the Incoloy 800 alloy [Fig. 24.6(c)], it should not be surprising that the test indicated slight flaking even if the specimen actually had not flaked. There were small metal particles enveloped in oxide at the base of the layer scale; these resulted from penetrations into the substrate. A small loss of metal during removal of the scale could account for this small indication of flaking, as could the effect of slight errors in weighing.

The specimens of Inconel 600 appeared "dirty" after the scale was removed, and, when the intergranular nature of the scaling attack is considered, there is little doubt that considerable metal was lost with the oxide during scale removal. If all the scale were to be removed from the sample, metal would probably continue to be removed in the process. The results would indicate an even higher propensity toward flaking that would be erroneous to the extent that metal was removed.

After treatment to remove the scale, the specimen of type 304 stainless steel still showed significant amounts of scale remaining in the areas where the spacer washer had seated and at the corners, yet this specimen disclosed a clear indication of flaking. The microstructure of the scale showed virtually no protrusion component and, clearly, no metal was removed with oxide to mollify this definite indication of flaking. The tendency for type 304 stainless steel to flake was confirmed by a "dusting off" behavior observed while weighing specimens of the A4 weldment.

The results of the flaking study validate our weight-gain technique as a method of corrosion evaluation. All of the base-metal alloys appeared to resist flaking with the exception of type 304 stainless steel (which spalled substantially) and possibly Inconel 600 (which spalled only moderately, if at all).

Preferential Corrosion

Development of High-Pressure Corrosion Loop (J. P. Hammond)

We are continuing our development of a high-pressure corrosion loop that will enable us to inject chloride and O_2 to levels of 20 ppm so that we may study stress-corrosion cracking of weldments under the influence of contaminants. This loop should be available for use by July 1970.

References

1. P. Patriarca and G. M. Slaughter, Fuels and Materials Development Program Quart. Progr. Rept. Sept. 30, 1969, ORNL-4480, pp. 297–300.

Previous reports in this series:

ORNL-4330	Period Ending June 30, 1968
ORNL-4350	Period Ending September 30, 1968
ORNL-4390	Period Ending December 31, 1968
ORNL-4420	Period Ending March 31, 1969
ORNL-4440	Period Ending June 30, 1969
ORNL-4480	Period Ending September 30, 1969

ORNL-4520
UC-25 — Metals, Ceramics, and Materials

INTERNAL DISTRIBUTION

1–3. Central Research Library
4–5. ORNL — Y-12 Technical Library Document Reference Section
6–35. Laboratory Records Department
36. Laboratory Records, ORNL RC
37. ORNL Patent Office
38. R. E. Adams
39. G. M. Adamson, Jr.
40. S. E. Beall
41. R. J. Beaver
42. M. Bender
43. R. G. Berggren
44. D. S. Billington
45. N. C. Binkley
46. E. E. Bloom
47. A. L. Boch
48. E. S. Bomar
49. C. D. Bopp
50. B. S. Borie
51. G. E. Boyd
52. R. A. Bradley
53. R. J. Breeding
54. R. B. Briggs
55. R. E. Brooksbank
56. D. A. Canonico
57. R. W. Carpenter
58. R. M. Carroll
59. J. V. Cathcart
60. D. L. Clark
61. G. W. Clark
62. Nancy C. Cole
63. K. V. Cook
64. W. H. Cook
65. G. L. Copeland
66. W. B. Cottrell
67. C. M. Cox
68. F. L. Culler
69. C. W. Cunningham
70. J. E. Cunningham
71. V. A. DeCarlo
72. W. E. Deeds
73. J. DeLuca
74. J. H. DeVan
75. J. R. DiStefano
76. C. V. Dodd
77. R. G. Donnelly
78. D. A. Dyslin
79. T. Eck
80. J. H. Erwin
81. K. Farrell
82. J. I. Federer
83. D. E. Ferguson
84. R. B. Fitts
85. B. Fleischer
86. B. E. Foster
87. A. P. Fraas
88. J. H Frye, Jr.
89. W. Fulkerson
90. L. C. Fuller
91. R. E. Gehlbach
92. T. G. Godfrey, Jr.
93. G. M. Goodwin
94. J. M. Googan (Y-12)
95. R. J. Gray
96. W. R. Grimes
97. A. G. Grindell
98. H. D. Guberman
99. L. L. Hall
100. D. G. Harman
101. W. O. Harms
102. R. F. Hibbs
103–107. M. R. Hill
108. D. O. Hobson
109. H. W. Hoffman
110. F. J. Homan
111. R. W. Horton
112. W. R. Huntley
113. H. Inouye
114. D. H. Jansen
115. J. D. Jenkins
116. W. H. Jordan
117. G. W. Keilholtz
118. R. T. King
119. R. L. Klueh
120. R. W. Knight
121. W. J. Lackey
122. C. E. Lamb
123. J. A. Lane
124. J. M. Leitnaker
125. B. C. Leslie

126. C. S. Lever
127. T. B. Lindemer
128. C. T. Liu
129. H. R. Livesey
130. B.T.M. Loh
131. E. L. Long, Jr.
132. A. L. Lotts
133. C. D. Lundin
134. J. W. Luquire
135. R. N. Lyon
136. R. E. MacPherson
137. M. M. Martin
138. W. R. Martin
139. R. W. McClung
140. H. E. McCoy, Jr.
141. H. C. McCurdy
142. R. E. McDonald
143. W. T. McDuffee
144. D. L. McElroy
145. C. J. McHargue
146. A. J. Miller
147. E. C. Miller
148. J. P. Moore
149. R. E. Moore
150. A. J. Moorhead
151. C. S. Morgan
152. J. G. Morgan
153. F. H. Neill
154. T. A. Nolan (K-25)
155. K. Notz
156. A. R. Olsen
157. M. F. Osborne
158. P. Patriarca
159. W. H. Pechin
160. R. B. Perez
161. A. M. Perry
162. S. Peterson
163. L. E. Poteat
164. R. A. Potter
165. R. B. Pratt
166. M. K. Preston
167. W. W. Proaps
168. R. E. Reed
169. C. R. Reese
170. G. A. Reimann
171. A. E. Richt
172. P. L. Rittenhouse
173. H. E. Robertson
174. M. W. Rosenthal
175. D. J. Rucker
176. C. F. Sanders
177. G. Samuels
178. A. W. Savolainen
179. J. E. Savolainen
180. A. C. Schaffhauser
181. J. L. Scott
182. J. D. Sease
183. C. E. Sessions
184. W. A. Simpson
185. O. Sisman
186. G. M. Slaughter
187. S. D. Snyder
188. I. Spiewak
189. J. E. Spruiell
190. W. J. Stelzman
191. R. L. Stephenson
192. J. O. Stiegler
193. D. A. Sundberg
194. R. W. Swindeman
195. V. J. Tennery
196. K. R. Thoms
197. D. B. Trauger
198. G. M. Watson
199. S. C. Weaver
200. M. S. Weschler
201. A. M. Weinberg
202. J. R. Weir, Jr.
203. W. J. Werner
204. H. L. Whaley, Jr.
205. G. D. Whitman
206. F. W. Wiffen
207. J. M. Williams
208. L. C. Williams
209. R. K. Williams
210. R. O. Williams
211. J. C. Wilson
212. R. G. Wymer
213. F. W. Young, Jr.
214. C. S. Yust
215. C. M. Adams, Jr. (Consultant)
216. Leo Brewer (Consultant)
217. L. S. Darken (Consultant)
218. Walter Kohn (Consultant)

EXTERNAL DISTRIBUTION

AIR FORCE MATERIALS LABORATORY, Wright-Patterson Air Force Base

219. C. H. Armbruster
220. H. M. Burte
221. G. Glenn
222. Technical Director

AIR FORCE WEAPONS LABORATORY, Kirtland Air Force Base

223. D. Brooks

AMES LABORATORY

224. O. N. Carlson
225. W. L. Larsen
226. M. Smutz
227. F. H. Spedding

ARGONNE NATIONAL LABORATORY

228. L. Baker
229. J. H. Kittel
230. M. V. Nevitt
231. P. G. Shewmon
232. R. C. Vogel

LMFBR PROGRAM OFFICE, Argonne National Laboratory

233. A. Amorosi
234. L. Burris
235. L. Kelman
236. J. M. McKee

AEC-RDT SITE REPRESENTATIVES

237. M. E. Jackson, Argonne National Laboratory
238. D. J. Wille, Atomic Power Development Associates
239. R. L. Morgan, Atomics International
240. J. V. Levy, General Electric, Sunnyvale
241. R. H. Ball, Gulf General Atomic
242. J. E. Hebert, Idaho
243. D. A. Moss, Idaho
244. K. A. Trickett, Idaho
245. D. F. Cope, Oak Ridge National Laboratory
246. C. L. Matthews, Oak Ridge National Laboratory
247. P. G. Holsted, Battelle-Northwest
248. J. Sako, Battelle-Northwest
249. Theodore Iltis, Westinghouse Advanced Reactor Division
250. Atomic Energy Commission Library, Washington

DIVISION OF NAVAL REACTORS, AEC, Washington

251. R. H. Steele

DIVISION OF REACTOR DEVELOPMENT AND TECHNOLOGY, AEC, Washington

252. J. C. Crawford, Jr.
253. G. W. Cunningham
254. A. Giambusso
255. H. G. Hembree
256. K. E. Horton
257. J. R. Hunter
258. E. E. Kintner
259. W. H. Layman
260. W. H. McVey
261. J. J. Morabito
262. R. E. Pahler
263. A. J. Pressesky
264. M. A. Rosen
265. J. M. Simmons
266. E. E. Sinclair
267. B. Singer
268. A. Taboada
269. A. N. Tardiff
270. A. Van Echo
271. C. E. Weber
272. M. J. Whitman

DIVISION OF RESEARCH, AEC, Washington

273. P. W. McDaniel
274. D. K. Stevens

DIVISION OF SPACE NUCLEAR SYSTEMS, AEC, Washington

275. R. E. Anderson
276. D. Beard
277. J. F. Griffo
278. F. D. Haines
279. C. E. Johnson
280. J. A. Powers
281. F. C. Schwenk

OAK RIDGE OPERATIONS OFFICE

282. W. J. Larkin
283. Laboratory and University Division

ATOMIC POWER DEVELOPMENT ASSOCIATES

284. E. C. Kovacic
285. A. A. Shoudy

ATOMICS INTERNATIONAL

286. H. Pearlman
287. J. G. Asquith

BABCOCK AND WILCOX COMPANY, Lynchburg, Virginia 24505

288. C. Baroch
289. S. P. Grant
290. C. Johnson
291. L. Weissert

BATTELLE MEMORIAL INSTITUTE, Columbus, Ohio

292. W. Berry
293. D. Keller
294. S. J. Paprocki
295. Defense Materials Information Center

BATTELLE-NORTHWEST, Richland, Washington

296. A. L. Bement
297. J. J. Cadwell
298. T. T. Claudson
299. D. L. Condotta
300. E. Evans
301. J. E. Hanson
302. B. R. Hayward
303. B. M. Johnson
304. W. E. Roake
305. D. W. Shannon
306. J. C. Tobin
307. R. G. Wheeler
308. Technical Information File

FAST FLUX TEST FACILITY, Battelle-Northwest

309. E. R. Astley

BROOKHAVEN NATIONAL LABORATORY

310. D. H. Gurinsky
311. C. Klamut

BUREAU OF MINES

312. Haruo Kato, Albany Metallurgy Research Center, P.O. Box 70, Albany, Oregon 97321
313. T. Sullivan, Bureau of Mines, Boulder City, Nevada 89005

COMBUSTION ENGINEERING

314. W. P. Chernock
315. S. S. Christopher

GENERAL ELECTRIC, Cincinnati

316. D. H. Ahmann
317. H. C. Brassfield
318. V. P. Calkins
319. E. Hoffman
320. J. McGurty
321. J. Moteff

GENERAL ELECTRIC, Nuclear Systems Programs, Cincinnati

322. E. E. Hoffman

GENERAL ELECTRIC, San Jose

323. R. Duncan
324. H. Klepfer

GENERAL ELECTRIC, Pleasanton

325. H. W. Alter

GENERAL ELECTRIC, Sunnyvale

326. K. P. Cohen
327. F. Comprelli
328. R. Skavdahl
329. C. Spalaris
330. E. L. Zebroski

GULF GENERAL ATOMIC

331. D. B. Coburn
332. A. J. Goodjohn
333. J. P. Howe
334. S. Jaye
335. J. F. Watson

IDAHO NUCLEAR CORPORATION

336. W. C. Francis
337. William Yuill

ILLINOIS INSTITUTE OF TECHNOLOGY RESEARCH INSTITUTE

338. D. J. McPherson

JET PROPULSION LABORATORY (NASA)

339. J. Davis

KNOLLS ATOMIC POWER LABORATORY

340. R. F. Wojciescak
341. Document Library

LOS ALAMOS SCIENTIFIC LABORATORY

342. R. D. Baker
343. D. B. Hall
344. J. A. Leary
345. R. Perkins
346. R. E. Peterson
347. Reports Library

MOUND LABORATORY

348. R. G. Grove

NASA HEADQUARTERS

349. J. J. Lynch

NASA, LEWIS RESEARCH CENTER

350. M. Ault
351. J.W.R. Creagh
352. J. J. Lombardo
353. T. P. Moffitt
354. T. A. Moss
355. F. E. Rom
356. L. Rosenblum
357. N. D. Sanders
358. N. Saunders
359. C. M. Scheuermann
360. H. Schwartz

NAVAL RESEARCH LABORATORY

361. J. R. Hawthorne
362. C. Serpan
363. L. E. Steele

NORTH CAROLINA UNIVERSITY, Raleigh, North Carolina 27607

364. J. Beeler
365. R. E. Dahl

NUCLEAR MATERIALS AND EQUIPMENT CORPORATION

366. C. Caldwell
367. K. Puechl

OHIO STATE UNIVERSITY, Columbus, Ohio 43212

368. M. G. Fontana
369. R. W. Staehle

RENSSELAER POLYTECHNIC INSTITUTE

370. W. Dickinson
371. W. F. Savage
372. C. B. Willingham, Jr.

SANDIA CORPORATION

373. J. Read Holland
374. J. Jacobs
375. D. R. Johnson

SAVANNAH RIVER LABORATORY

376. P. H. Permar
377. S. P. Rideout

TRW SYSTEMS (NASA), Redondo Beach, California 90278

378. H. Lurie

UNION CARBIDE CORPORATION, New York

379. J. A. Swartout

UNION CARBIDE CORPORATION, Materials Systems Division, Indianapolis

380. C. F. Leitten, Jr.

UNITED NUCLEAR CORPORATION

381. A. Strasser

UNIVERSITY OF CALIFORNIA, Lawrence Radiation Laboratory, Livermore

382. W. R. Holman
383. J. S. Kane
384. L. W. Roberts
385. A. J. Rothman
386. B. Rubin

U.S. NAVAL AIR SYSTEM COMMAND (AIR-52031B)

387. T. Kearns
388. I. Machlin

USAEC Scientific Representative, American Embassy, Box 40 FPO, N.Y. 09510

389. W.L.R. Rice

WESTINGHOUSE, Advanced Reactor Division, Waltz Mill Site

390. E. C. Bishop
391. A. Boltax
392. J.C.R. Kelly
393. P. J. Levine
394. P. Murray
395. W. E. Ray
396. G. A. Whitlow

WESTINGHOUSE, Astronuclear Laboratory

397. R. T. Begley
398. D. C. Goldberg

WESTINGHOUSE, Atomic Power Division

399. T. Stern

WESTINGHOUSE, Bettis

400. R. H. Fillnow
401. P. N. Gustafson
402. Westinghouse Bettis Laboratory Library

403–607. Given distribution as shown in TID-4500 under Metals, Ceramics, and Materials category (25 copies – CFSTI)